Magnesium-selective ligands in luminescence-based systems

Edward. R. H. Walter

A thesis submitted for the degree of Doctor of Philosophy

October 2017

Abstract

Magnesium is the most abundant divalent cation *in vivo*. Despite this, Mg^{2+} homeostasis remains poorly understood compared to other biologically relevant cations. Literature-based chelates lack structural variety, with a number of intrinsic problems limiting their applications *in vivo*. The *o*-aminophenol-*N,N,O*-triacetic acid (APTRA) chelate for example, is used extensively to sense Mg^{2+}, but displays a higher selectivity towards Ca^{2+} and Zn^{2+}, over Mg^{2+}.

The synthesis of a series of four binding chelates is described, containing both carboxylate and phosphinate ligating groups. A new phosphinate analogue of APTRA, *o*-aminophenol-*N,N*-diacetic acid phosphinate (APDAP) was synthesised with a much improved Mg^{2+} / Ca^{2+} selectivity, notwithstanding a 110-fold lower affinity for Ca^{2+}, compared to APTRA. All ligands are analogues of APTRA, and have been conjugated into naphthalene-, lanthanide(III)- and ruthenium(II)-based systems to study the affinity and selectivity of Mg^{2+}, Ca^{2+} and Zn^{2+}, via absorbance and luminescence spectroscopy.

The incorporation of the binding groups into an alkynyl-naphthalene fluorophore provided a model system to study the binding of Mg^{2+}, Ca^{2+} and Zn^{2+}. The APDAP-based naphthalene derivative displayed a significantly higher selectivity towards Mg^{2+} than the carboxylate analogues. A 10-fold weaker affinity for Ca^{2+} was reported, allowing the binding of Mg^{2+} to be investigated in a competitive medium, in the presence of biologically relevant cations at concentrations similar to those found in human serum.

A dramatically enhanced selectivity towards Mg^{2+} was observed in the metal-based APTRA analogues compared to the naphthalene series and literature APTRA sensors. Lanthanide complexes containing a pyridylalkynylaryl chromophore displayed the highest selectivity for Mg^{2+}, with a 28-fold reduced affinity for Ca^{2+}. The binding of Mg^{2+} in competitive media is described, using the first example of a europium-based luminescent probe to monitor 'free' Mg^{2+} in newborn calf serum. A dissociation constant of 0.6(1) mM was calculated, comparable to the 'free' Mg^{2+} concentration in human serum

Declaration

The work described in this thesis was undertaken at the Department of Chemistry, Durham University between October 2014 and October 2017. All of the work reported is my own, except where specifically stated otherwise. No part has previously been submitted for a degree at this any other university.

Statement of Copyright

Acknowledgements

Firstly, I would like to thank my supervisors Prof. David Parker and Prof. J. A. Gareth Williams for giving me the opportunity to pursue this PhD project, and for their support and guidance over the last 3 years.

Thanks to the Chemistry Department analytical services: Dr. Alan Kenwright, Dr. Juan Aguilar Malavia, Mrs Cathererine Heffernan and Dr. Raquel Belda-Vidal for solution-state NMR, Mr Peter Stokes and Dr. David Parker for Mass Spectrometry and Dr. Mark Fox for running my DFT simulations.

Thanks to the members of both the JAGW and DP group past and present: David, Emma, Mel, Jack, Joe for all the cinema, pizza and quiz nights, Raminder for all of the discussions in the office and the lab, for introducing me to music genres I thought never existed, but maybe wont ever be listened to again, Kevin, Alice, Laura, Mathieu, Andrew, Kanthi for Thursday pub nights, and Sergey for letting me stay in his spare room while writing up the final parts of this thesis.

Thanks to Carl, Chris, Jasmine and Mel for two great years at the 'the BRowans' for all the laughs and the many great moments together.

I would like to thank everyone I have met over the last three years while playing for Ustinov College Association Football Club. I've had many enjoyable moments, and made great friends. Special thanks to Alex, Angus, Matty, Matt, Rob, Adam, Dani, Menno, Jeroen and Peter for their friendship over the last 3 years.

Thanks to Elizabeth for her love, support and encouragement over the last 8 months, and throughout the writing of this thesis.

Finally, thanks to my family for all their support throughout my higher education.

Abbreviations

AAS	Atomic Absorption Spectroscopy
AC	Adenylyl cyclase
ADP	Adenosine diphosphate
AM	Acetoxymethyl esters
APDAP	*O*-Aminophenol-*N,N*-diacetic acid phosphinate
APTRA	*O*-Aminophenol-*N,N,O*-triacetic acid
ATP	Adenosine triphosphate
BAPTA	(1,2-bis(o-aminophenoxy)ethane-*N,N.N′,N′*-tetracetic acid
BODIPY	4-bora-3a,4a-diaza-s-indacene
bpy	2,2'-bipyridine
br	Broad
BSA	Bovine Serum Albumin
cAMP	Cyclic adenosine monophosphate
COSY	Correlation spectroscopy
CT	Computed Tomography
d	Day
dd	doublet of doublets
DME	Dimethoxyethane
DMF	Dimethylformamide
DMSO	Dimethyl sulfoxide
DNA	Deoxyribonucleic acid
DOTA	1,4,7,10-tetraazacyclododecane-1,4,7,10-tetraacetic acid
dq	doublet of quartets
dt	doublet of triplets
DTPA	Diethylene triamine pentacetic acid
E	Energy
e.g.	exampli grati (for example)
EDTA	Ethylenediaminetetraacetic acid
EDTMP	Ethylenediamine tetra(methylene phosphonic acid)
en	Ethylenediamine

ESI	Electrospray ionisation
ET	Energy transfer
et al.	et alia. (and others)
EtOH	ethanol
F	Fluorescence
FI	Fluorescent indicators
FRET	Fluorescence resonance energy transfer
h	Hour
HEK	Human embryonic kidney cells
HEPES	4-(2-hydroxyethyl)-1-piperazineethanesulfonic acid
HMBC	Heteronuclear multiple-bond correlation spectroscopy
HPLC	High Performance Liquid Chromatography
HRMS	High resolution mass spectrometry
HSAB	Hard-Soft Acid-Base theory
HSH	Hypermagnesaemia with secondary hypocalcemia
i.e.	Id est (that is)
ICP-MS	Inductively coupled plasma mass spectrometry
ICP-OES	Inductively coupled plasma optical emission spectrometry
ICT	Intramolecular Charge Transfer
in cellulo	within cells
in vivo	within a living organism
^{i}PrOH	*iso*-propanol
ISC	Intersystem crossing
J	Coupling constant
K_a	Association constant
K_d	Dissociation constant
LC	Ligand centered
Ln^{3+}	Lanthanide(III) ions
LRMS	Low resolution mass spectrometry
LUMO	Lowest unoccupied molecular orbital
m	multiplet
m.p.	Melting point

MC	Metal centered
MCLT	Metal-to-ligand charge transfer
MeOH	methanol
mg	milligram
min	Minute
mL	millilitre
mM	millimolar
mmol	millimole
MRI	Magnetic Resonance Imaging
MRS	Magnetic Resonance Spectroscopy
MW	Microwave
NCS	Newborn calf serum
nm	nanometre
nM	nanomolar
NMR	Nuclear Magnetic Resonance
NOESY	Nuclear overhauser effect spectroscopy
P	Phosphorescence
PET	Photo-induced electron transfer
PET	Positron Emission Tomography
phbpy	4,4'-biphenyl-2,2'-bipyridine
pK_a	Acid dissociation constant
pm	picometre
POPOP	1,4-bis(5-phenyloxazol-2-yl) benzene
ppm	parts per million
PPT	Photon-induced Proton Transfer
ppy	2-Phenylpyridine
q	quartet
r_1	Relaxivity
R_f	Retention factor
RNA	Ribonucleic acid
s	singlet
S_0	Singlet ground state

S_1	Singlet excited state
t	Triplet
$t_{1/2}$	Half-life
T_1	Longitudinal relaxation time
T_1	Triplet excited state
T_2	Transverse relaxation time
TBAF	Tetrabutylammonium fluoride
TBDMS triflate	*tert*-Butyldimethylsilyl trifluoromethanesulphonate
^{t}BuOH	*tert*-butanol
t_d	Delay time
TD-DFT	Time-Dependent Density Functional Theory
TN	Trimethylenediamine
TFA	Trifluoroacetic acid
t_g	Fixed gate time
THF	Tetrahydrofuran
TIPS	Triisopropylsilyl
TLC	Thin-Layer Chromatography
TOF	Time of flight
TRPM	Transient receptor potential ion channels melastatin
UV	Ultraviolet
wt.	weight
XMEN	X-linked immunodeficiency with magnesium defect
λ	wavelength
λ_{em}	Emission wavelength
λ_{ex}	Excitation wavelength
λ_{max}	Wavelength maximum
µL	microlitre
µM	micromolar
Φ	quantum yield

Table of Contents

1. Introduction

Slow and steady progress has been made over the years in the development of magnesium-selective probes since Hasselbach first published work indicating the importance of Mg^{2+} within cells in 1957.[1] This breakthrough was over half a century ago and yet there is still very little known about the homeostasis of Mg^{2+}. Other biologically relevant cations, for instance Ca^{2+}, H^+ and Na^+, have been studied in more depth, allowing detailed transportation and homeostatic information within mammalian cells to be acquired.

The slow progress made in this area led Wolf and co-workers to label Mg^{2+} as the 'forgotten cation', in a review article published in 2010.[2] In order for more information to be gained, more sensitive and selective methods are needed for its detection. Current methods such as Atomic Absorption Spectroscopy are inaccurate and impractical, while many of the current clinically available fluorescence probes have a number of selectivity issues with competing divalent cations, such as Ca^{2+}.

This introduction will outline the role of Mg^{2+} within cells, and what information is known about the transportation of Mg^{2+} *in vivo*. A summary of the current techniques used *in vivo* and *in vitro* to detect Mg^{2+} ions will also be critically discussed.

1.1 Cellular Mg^{2+} Distribution

Although Mg^{2+} is the second most abundant cation in most cells, it is the fourth in terms of body mass, behind Ca^{2+}, K^+ and Na^+.[3] A number of analytical techniques such as Atomic Absorption Spectroscopy (AAS) and Fluorescence Spectroscopy (FS) have been used to determine the concentration of Mg^{2+} within cells. The results from these techniques have indicated that the total intracellular concentration of Mg^{2+} in the majority of mammalian cells is within the range of 14 to 20 mM.[3]

Mg^{2+} is mineralised in bones and accumulates preferentially in the mitochondria and endo(sarco) plasmic reticulum because its positive divalent

charge allows it to preferentially bind to anionic species such as adenosine triphosphate (ATP) (**Figure 1.1**), polyphosphates and pyrophosphates, which are common in these compartments of the cell.[4] The majority of total cellular magnesium is present in the cytoplasm bound to ATP, due to its high abundance and binding affinity (K_d ~78 μM)[5]. The concentration of 'free' Mg^{2+} is therefore significantly lower, with values in the range of 0.8 to 1.5 mM being measured in the matrix of cardiac and liver mitochondria by commercially available Mag-Fura-2.[5-7] No such figure has yet been determined for the concentration of 'free' Mg^{2+} in the endo(sarco) plasmic reticulum because of the elevated levels of Ca^{2+} that are present. The majority of current commercially available fluorescence probes such as Mag-Fura-2 express a much higher affinity towards Ca^{2+} than Mg^{2+} (K_d= 50 μM vs. 1.5 mM).[5] Accurate Mg^{2+} concentrations in cellular compartments with Ca^{2+} concentrations above basal levels, therefore, remain challenging to obtain.

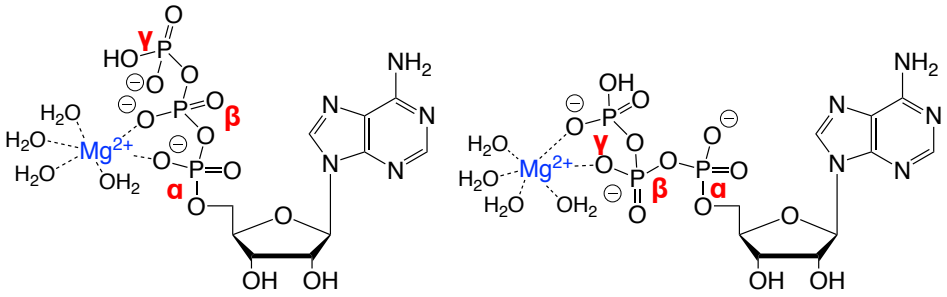

Figure 1.1 Mg^{2+} bound to ATP forming $MgATP^{2-}$. The β and γ phosphonate groups are primarily involved in Mg^{2+} ion coordination, forming the active species ready for hydrolysis to ADP.[8,9]

Within the cell, Mg^{2+} has a number of key and fundamental roles, for instance controlling channel regulation as well as the conformation of nucleic acids and proteins[10] (such as calmodulin, troponin, parvalbumin and the S100 protein) and the metabolic regulation of energy dependent mitochondrial and cytoplasmic pathways.[5] It is an essential cofactor for more than 600 enzymatic reactions.[11] Its catalytic nature is either direct or by modification of a substrate upon Mg^{2+} binding.[12] Of particular importance is the activation of ATPase, an enzyme that catalytically dephosphorylates ATP to ADP *in vivo* (**Figure 1.2**).[13] The process is essential to life, and for the generation of energy within the cell.

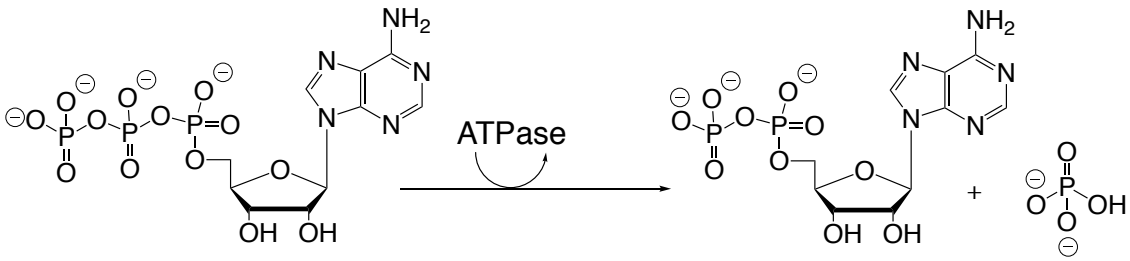

Figure 1.2 The dephosphorylation of ATP to ADP catalysed by ATPase.[13]

Magnesium also plays a key role in numerous stages of the cell cycle (**Figure 1.3**), a recognised model characterising the stages of cell growth and replication. The various phases of the cell cycle, along with a description of the role of each, is highlighted in **Table 1.1**. The effect of Mg^{2+} concentration on the cell cycle was first highlighted experimentally in 1980, where it was found that yeast cells incubated in low Mg^{2+} concentrations had limited growth, with a decreased percentage of cells in the S Phase, in comparison with cells incubated in high Mg^{2+} concentrations.[14]

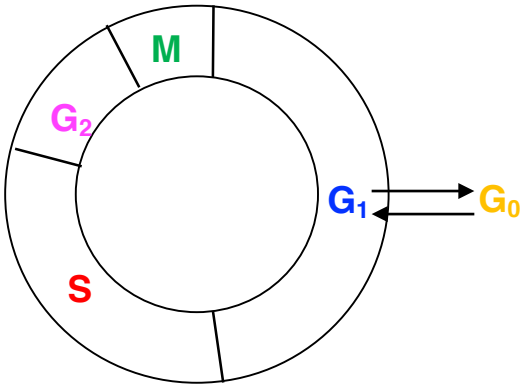

Figure 1.3 A schematic representation of the cell cycle**.** Where: G_0 = Gap 0 resting state, G_1 = Gap 1, S = Synthesis phase, G_2 = Gap 2 and M = Mitosis phase where cell division commences. A description of each phase is provided in **Table 1.1**.

Table 1.1 Highlighting the role of each stage within the cell cycle. The cycle is split into three states resting, interphase and cell division.

Phase	Description
Gap 0 (G_0)	Resting state where no cell division occurs.
Gap 1 (G_1)	Cells significantly increase in size in preparation for DNA synthesis.
Synthesis (S)	DNA replication occurs during the S phase.
Gap 2 (G_2)	The cell continues to grow, a gap between the S phase and mitosis.
Mitosis	Cell growth halts and cell division commences. A checkpoint in the mitosis phase allows the cell to complete cell division.

In mammalian cells, the ability of Mg^{2+} to bind to ATP^{4-} means it has a vital role in DNA duplication, as the phosphorylation of proteins by a kinase and ATP-activating proteins sends signals within the cell causing growth and proliferation.[15] Mg^{2+} therefore plays an important role in the S phase, where the DNA replication commences, and in the G_2 phase, the gap between the DNA synthesis and mitosis where the cell continues to grow. Studies in mammalian cells have shown that by increasing / decreasing the extracellular concentration

of Mg^{2+}, the rate of cell proliferation can be accelerated or retarded respectively, highlighting the fact that proliferating cells have higher Mg^{2+} concentrations than non-proliferating cells. Such a significant increase in proliferation is because magnesium stabilises the DNA structure, promoting an increase in DNA replication and transcription.[16]

Experiments involving smooth muscle cells have shown a 3-fold increase in DNA and protein synthesis in a 2 mM medium of Mg^{2+}. Touyz and co-workers deemed this to be a significant increase and attributed it to the specific activation of the ERK1 / ERK2 extracellular signal reduction kinase-dependent pathway, important in the regulation of mitosis.[16]

Across different mammalian cell types, however, the effect of extracellular magnesium concentration does not appear to show a consistent correlation with cell proliferation. A diverse range of cells are affected in a different manner. Tumour cells for instance, including HL-60 leukaemia cells, have shown an unchanged level of growth when extracellular Mg^{2+} concentrations were altered above or below their physiological values; their growth is therefore independent of Mg^{2+} intra- and extracellular concentrations.[17]

As the importance of Mg^{2+} within cells is evident, it is somewhat surprising that when compared to other biologically relevant cations including Ca^{2+} and Na^{+}, the mechanism by which eukaryotic cells regulate total and 'free' Mg^{2+} is still relatively unknown. Recent advances over the last two decades are, however, encouraging, with a greater understanding of the cellular importance of Mg^{2+} being gradually proposed.

1.2 Mg^{2+} in the Serum

The concentration of magnesium in the serum is relatively unknown, with no specific sensing mechanism in the circulatory system to measure concentration changes of Mg^{2+} being identified to date. Alterations in circulating Mg^{2+} ions are, therefore, commonly determined by a Ca^{2+} sensing receptor that can also detect changes in Mg^{2+}, because of the higher magnesium concentration

in the serum.[5] Using this approach it is believed that humans have between 0.7 and 1.1 mM of Mg^{2+} circulating around the body in the blood plasma.[18]

Maintaining a constant level of Mg^{2+} in serum is vital for health: elevated Mg^{2+} concentrations result in the onset of hypermagnesemia, causing muscle weakness and fatigue.[11] In contrast, a deficiency of Mg^{2+} in plasma is linked to the onset of hypomagnesemia, an electrolytic disturbance with an abnormally low Mg^{2+} concentration present in the blood. An electrolytic disturbance in the serum has been related to the development of a number of chronic diseases such as Type 2 diabetes[19], hypertension[20] and chronic kidney disease.[21] It is thought that hypomagnesemia affects up to around 15 % of the general population,[22] possessing little to no symptoms in its mild form making it difficult to detect and diagnose. Prescribed medication, an insufficient dietary intake of Mg^{2+} and genetic renal defects can all be linked to causing magnesium deficiency in the serum.

A review by Tilmann and Wolf in 2017 highlighted a number inherited and acquired disorders that arise from the development of Mg^{2+} imbalances in the serum.[11] The kidneys are the primary regulators of Mg^{2+} homeostasis, with 80 % of all serum Mg^{2+} being filtered in the glomerulus[11] (a cluster of small blood vessels around the end of a kidney tubule). Maintaining a constant Mg^{2+} concentration in the serum is, therefore, vital for maintaining healthy kidney function, preventing the onset of disease.

Tests have also been carried in conscious humans, where the administration of catecholamine-based hormones (e.g. adrenalin, norepinephrine and dopamine) over a time range of 30 min to 5 hours led to a variety of levels of hypomagnesia.[23] The administration of norepinephrine to perfused rat hearts was found to cause an extrusion of Mg^{2+} from the organs into the perfusate, increasing the serum Mg^{2+} levels.[23]

1.3 Mg^{2+} Transport in Mammalian Cells

Cellular cations such as Ca^{2+} are transported across the cell membrane and the membranes of cellular organelles via a series of well understood, highly selective mechanisms. Mg^{2+} is no different, with a series of selective channels for the accumulation of Mg^{2+} in cells (e.g. TRPM in the cell membrane) and organelles (Mrs2 in mitochondria) as well as selective exchange pathways for Mg^{2+} efflux (most notably the Na^+ dependent and Na^+ independent pathways).[24]

Romani and Scarpa have carried out extensive work in this area, making significant developments into Mg^{2+} homeostasis.[10,23,24] In 2002 Romani and Maguire reported that under resting conditions, Mg^{2+} flux on either side of the cell membrane is slow, taking place over a number of hours.[24] Such a slow turnover led many researchers to believe that the cellular changes in Mg^{2+} are too small in scale to be physiologically relevant or that cellular Mg^{2+} concentrations remain constant over a period of time.[5] The hypothesis proposed in 2002 was challenged after Romani and co-workers found that there were large fluxes of Mg^{2+} occurring either side of the cell membrane in a matter of minutes following hormonal or metabolic stimulation of mammalian cells.[5]

Since this publication, multiple examples of large fluxes of Mg^{2+} in cells following stimulation have been reported over a variety of mammalian cells. Wolf and co-workers recorded the extrusion of Mg^{2+} in rat spleen lymphocytes. It was found that 30 min after cell stimulation by cyclic adenosine monophosphate (cAMP) there was an efflux of Mg^{2+} which accounted for 15 % of the total Mg^{2+} content.[25]

1.3.1 Entry mechanisms of Mg^{2+} within cells

Mg^{2+} is transported across the cell membrane via a series of well-regulated channels including the transient receptor protein (TRPM) ion channels and MagT1. TRPM6 and TRPM7 are two members of the eight-protein TRPM subfamily; they are primarily responsible for the homeostasis of Mg^{2+}, and are famous for being the first Mg^{2+} channels identified in mammalian cells.[5] Although TRPM6 and TRMP7 are structurally similar, and are both predominantly

responsible for the transportation of divalent cations (Mg^{2+}, Ca^{2+} and to a lesser extent Zn^{2+} and Mn^{2+}), one fundamental difference remains. Unlike TRPM6 which is only involved in Mg^{2+} homeostasis in the kidney and the colon, TRPM7 is not localised to a particular cell type and is involved in Mg^{2+} homeostasis in an array of cells.[26]

Deficiencies in either the TRPM or MagT1 ion channel have been linked to a number of illnesses in humans, such as hypermagnesaemia with secondary hypocalcemia (HSH) and XMEN (X-linked immunodeficiency with magnesium defect, chronic Epstein Barr virus infections and Neoplasma).[27] In 2016 it was found by Gudermann and co-workers that by inactivating the TRPM6 ion channel a reduction of cellular Mg^{2+} occurred, leading to the development of hypomagnesemia in adult mice.[28] The disease was found to significantly reduce their lifespan and limit growth because of a reduced energy balance.[28]

Mrs2 is another family of magnesium transporters, and is responsible for the influx of Mg^{2+} into the mitochondria. Mrs2 is structurally similar to CorA, a protein in prokaryotes responsible for mediating the uptake and efflux of Mg^{2+}.[29] Its importance was first highlighted by Wiesenberger *et al.* where it was discovered to play a key role in RNA splicing in yeast mitochondria, a modification in pre-messenger RNA where introns are removed.[30] It was not until a number of years later that Bui *et al*. identified the importance of Mrs2 as a Mg^{2+} transporter in the inner mitochondrial membrane.[29] An under / over-expression of the Mrs2 gene presented a decreased and increased concentration of 'free' Mg^{2+} in the yeast mitochondria respectively. These findings have since been supported by findings in mammalian HEK 293 cells, where a reduced mitochondrial Mg^{2+} concentration was observed after an under-expression of the Mrs2 gene.[5]

1.3.2 Exit mechanisms: Mg^{2+} extrusion in living cells

In living cells there are two fundamental extrusion mechanisms for the efflux of cellular Mg^{2+}; the Na^+ dependent (Na^+/ Mg^{2+} exchange) and the Na^+ independent exchange pathways.

The first evidence for the Na^+ dependent Mg^{2+} exchange pathway was from work carried out by Gunther, Vorman and Forster in 1984.[31] The study found that when the extracellular Na^+ concentration is at a lower concentration than the physiological concentration, Mg^{2+} extrusion is inhibited, even after hormonal stimulation with isoproterenol and catecholamine. Subsequent work has been published since this breakthrough by the same group characterising Mg^{2+} efflux from chicken, rat and human erythrocytes supporting this Na^+ dependent exchange pathway.[32]

The Na^+ dependent exchange mechanism is activated by cAMP- mediated phosphorylation. cAMP is derived from ATP (**Figure 1.4**) and is used in signal transduction, regulating metabolism in a number of organisms.[33] The inhibition of the biological catalyst adenylyl cyclase with Rp-cAMP prevents the formation of cAMP and, therefore, blocks the extrusion of Mg^{2+} from mammalian cells, in turn increasing the intracellular concentration of Mg^{2+}.[33]

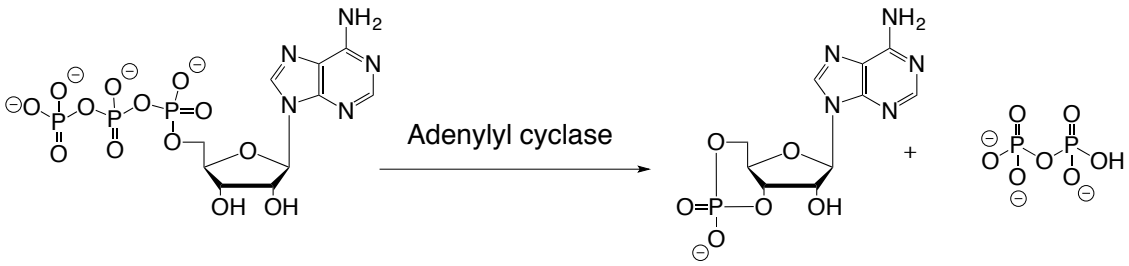

Figure 1.4 The cyclisation of ATP to cAMP catalysed by adenylyl cyclase (AC).

Wolf and co-workers found that rat spleen lymphocytes incubated in a HEPES (50 mM), $CaCl_2$ (1.3 mM), KCl (5 mM) and NaCl (130 mM) buffer expressed a 15 % extrusion of total cellular Mg^{2+} content after 30 mins.[25] Amiloride and imipramine, drugs used to treat hypertension, have been found to inhibit the Na^+/ Mg^{2+} exchange pathway of efflux of Mg^{2+}.[33] The pre-treatment of the rat spleen lymphocytes with amiloride and imipramine resulted in a 35 % and 29 % reduction in Mg^{2+} extrusion from the cells respectivly.[25] The replacement of NaCl with choline chloride in the incubation medium resulted in a 56 % reduction

in Mg^{2+} extrusion, further supporting the evidence of a complex Na^+ / Mg^{2+} exchange process.[25,33]

Mg^{2+} extrusion from living cells in the absence of physiological concentrations of extracellular Na^+ occurs via the Na^+ independent exchange pathway. In comparison to the Na^+ dependent pathway, the mechanism of the Na^+ independent pathway is poorly understood. It is less selective, with a wide variety of physiological monovalent and divalent cations (Ca^{2+}, Sr^{2+}, Mn^{2+}, and choline) and anions (HCO_3^-, Cl^-) reported in the literature to use this mechanism for Mg^{2+} extrusion.[34]

Garay and Feray have found evidence of a Mn^{2+} / Mg^{2+} (1:1) exchange mechanism, stimulating Mg^{2+} efflux from rat erythrocytes incubated in Na^+ free media. Efflux of Mg^{2+} was also measured when the concentration of extracellular Na^+ was raised; this reduced the efflux of Mg^{2+} via the Mn^{2+} / Mg^{2+} pathway, proving that the Na^+ / Mg^{2+} exchange mechanism is favoured.[35]

1.4 Intracellular and Extracellular Mg^{2+} Concentrations and Disease: Is there a link?

Mg^{2+} deficiencies in humans have been linked to a range of illnesses such as HSH, XMEN (**Section 1.3.1**), brain diseases such as Alzheimer's, Parkinson's and migraines, as well as hypertension. There is also a link between significant exposure to alcohol and a decrease in Mg^{2+} concentration in liver cells.[36] A large amount of research is devoted to understanding these processes, and looking into the potential of using magnesium as a therapeutic agent in the future to counteract these issues.

1.4.1 Mg^{2+} and Hypertension

Hypertension or high blood pressure is caused primarily by an increase in vascular resistance.[37] For the last two decades it has been thought that the prolonged reduction of intracellular and extracellular magnesium concentrations as a result of magnesium-deficient diets is related to the development of hypertension. There is increasing evidence supported from results of multiple

animal testing studies showing a direct correlation between Mg^{2+} dietary intake and the development of hypertension.[38] A study was carried out in which rats were subjected to a magnesium-deficient diet of 80 mg / kg. This resulted in an increase in the blood pressure and a reduction in the blood flow after 19 weeks, relative to the rats who maintained a healthy diet (960 mg / kg).[38] Similar results have been found in humans, where magnesium-rich diets have been seen to reduce blood pressure levels. The early stages of hypertension or pre-eclampsia are commonly treated with Mg^{2+} salts, in an attempt to increase vasodilation and improve the blood flow.[13]

Magnesium affects blood pressure by the modulation of vascular tone and reactivity. Low magnesium levels in the serum results in vasoconstriction, increasing vascular tone and reduction in the blood flow, resulting in the onset of hypertension. The exact mechanisms of action are relatively poorly understood, but it is believed that it occurs via two main processes. Firstly, Mg^{2+} acts as an antagonist for Ca^{2+} in smooth muscle cells, inhibiting extracellular calcium transport.[37] Ca^{2+} concentrations in comparison to Mg^{2+} have been seen to cause blood vessel contraction, reducing the blood flow and increasing the blood pressure.[13] Secondly, magnesium has anti-inflammatory properties and aids the release of nitric oxide and prostacyclin (PGI_2) from the epithelial cells. Prostacyclin is a vasodilation agent that inhibits platelet activation in blood vessels, preventing the formation of blood clots, improving blood flow and reducing the blood pressure. As a result, prostacyclin and prostaglandin based drugs are common oral medication to reduce the effects and treat patients with hypertension.[37]

The link between magnesium and diseases is evident; there is, however, still a great deal of work to be done in the area to develop a greater understanding, and to assess the potential of using Mg^{2+} therapeutically to treat hypertension and other chronic illnesses.

1.5 Techniques to Detect Mg^{2+} *in vivo*

Mg^{2+} cellular homeostasis is poorly understood because of the lack of methods for its detection *in vivo.* Calcium homeostasis in contrast has been at the centre of a great deal of research over the past two decades. Numerous methods have been developed for detection of Ca^{2+}, including the fluorescent probes Fura-2 and Indo-1 (**Figure 1.5**).[39-41] These ligands are prime examples of exceptionally selective Ca^{2+} chelators that have allowed researchers to develop a detailed understanding of Ca^{2+} homeostasis *in vivo*.

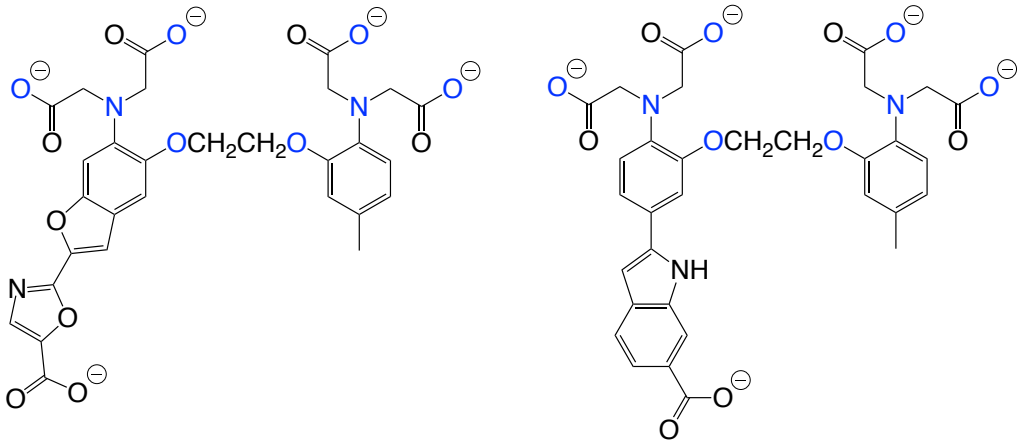

A) Fura-2 **B) Indo-1**

Figure 1.5 The structures of (**A**) Fura-2 and (**B**) Indo-1 APTRA developed by Tsien and co-workers.[40]

A vast array of analytical methods for the detection of Mg^{2+} have been designed in order to develop a greater understanding of the role of Mg^{2+} *in vivo*. The most common techniques include Atomic Absorption Spectroscopy (AAS), NMR techniques such as ^{31}P NMR and ^{19}F NMR, the use of unstable and stable radioactive isotopes (RI), and more recently the development of Fluorescent Indicators (FI) for use in Fluorescence Spectroscopy.

1.5.1 Atomic Absorption Spectroscopy (AAS)

Atomic Absorption Spectroscopy (AAS) has historically been an extensively used technique for measuring the concentration of magnesium in acidic extracts of biological samples. AAS has a number of limitations that restrict its use *in vivo*; firstly, the instrumentation is expensive and uncommon within

laboratories making its use impractical. Its major limitation, however, is that the technique is unable to differentiate between 'free' Mg^{2+} and Mg^{2+} bound to ATP^{4-} (the most abundant form of Mg^{2+}), with samples requiring dilution before measurements are taken.[10] More sensitive techniques such as inductively coupled plasma mass spectrometry (ICP-MS) have been used by Long and co-workers to determine K^+, Ca^{2+} and Mg^{2+} concentrations in human serum.[42] However, ICP-MS also requires expensive instrumentation, limiting its potential and widespread use for the measuring of Mg^{2+} concentrations in biological samples.

1.5.2 The use of Magnesium isotopes

The radioactive isotope ^{28}Mg (β^-, $t_{1/2}$ 20.9 h)[43] has been used as a tool to measure magnesium metabolism.[44] Its use as a tracer in humans is problematic, as its short half-life means that its administration is strictly forbidden in a large proportion of the population, including young children and pregnant women. Such problems restrict its scope and applications for *in vivo* studies.

Table 1.2 Isotope data for ^{24}Mg, ^{25}Mg, ^{26}Mg and ^{28}Mg.[43]

Isotope	Mass / Da	Natural abundance (atom %)	Half-life / h
^{24}Mg	23.9850423	78.99	stable
^{25}Mg	24.9858374	10.00	stable
^{26}Mg	25.9825937	11.01	stable
^{28}Mg	27.9838768	-	20.9

Stable magnesium isotopes ^{24}Mg, ^{25}Mg and ^{26}Mg have significantly longer half-lives than ^{28}Mg and have been used as safer, more cost-effective alternatives to the radioactive ^{28}Mg. Coudray and co-workers published a series of reports in which they have used ^{25}Mg to determine the size of exchangeable pools of magnesium in animals and humans.[45] The use of magnesium isotopes has also been developed to study the magnesium influx and efflux in erythrocytes of mice,

after it was determined that cancer patients have elevated erythrocyte Mg^{2+} concentrations.[46] A great deal of research is, however, required in this area in order to develop a better understanding into magnesium cellular exchange processes. The use of magnesium isotopes has become more feasible in recent years, with the development of more sophisticated mass spectroscopy techniques such as ICP-MS, allowing the isotope content to be established more accurately.[44]

1.5.3 The Use of Fluorescent Indicators (FI) in Fluorescence Spectroscopy

Roger Tsien first published work in 1980 concerning the use of fluorescent chelating ligands to measure cytosolic ion concentrations, primarily for the study of Ca^{2+}.[39] After this work was reported, fluorescence spectroscopy has become an extremely powerful and extensively used tool in cell biology.[47]

Fluorescence spectroscopy is an attractive technique because of its high temporal resolution and sensitivity, meaning that only a small concentration of the FI is required to provide a good signal-to-noise ratio.[48] The credibility of this technique has further increased in recent years through its coupling to optical microscopy allowing a better visualisation of living cells *in vivo*.[37] FIs can be subdivided into two main groups, either non-ratiometric or ratiometric. The latter class has a shift in the emission and / or excitation wavelength on binding of the desired metal ion in combination with a change (either increase – 'turn on', or decrease – 'turn off') in the fluorescence intensity. Ratiometric probes are highly desirable, because the ratio between two specific wavelengths provides quantitative information independent of the local concentration of the FI, the concentration of the metal ion, photo bleaching, uneven dye loading and instrumental effects. These particular characteristics make ratiometric probes highly advantageous for use in metal binding cellular studies.

1.5.3.1 APTRA-based Fluorescent Sensors

The development of a range of commercially available Mg^{2+} fluorescent indicators based on the *O*-aminophenol-*N,N,O*-triaceticacid (APTRA) structure

by London and co-workers in the late 1980's was seen as a significant breakthrough in the search for indicators suitable for detecting cytosolic 'free' magnesium *in vivo* (**Figure 1.6**). These chelates are analogues of ethylenediaminetetraacetic acid (EDTA, a known Mg^{2+} binding ligand) and are made up of an APTRA binding unit which is connected to an aromatic reporter group providing the fluorescent properties.[48-51]

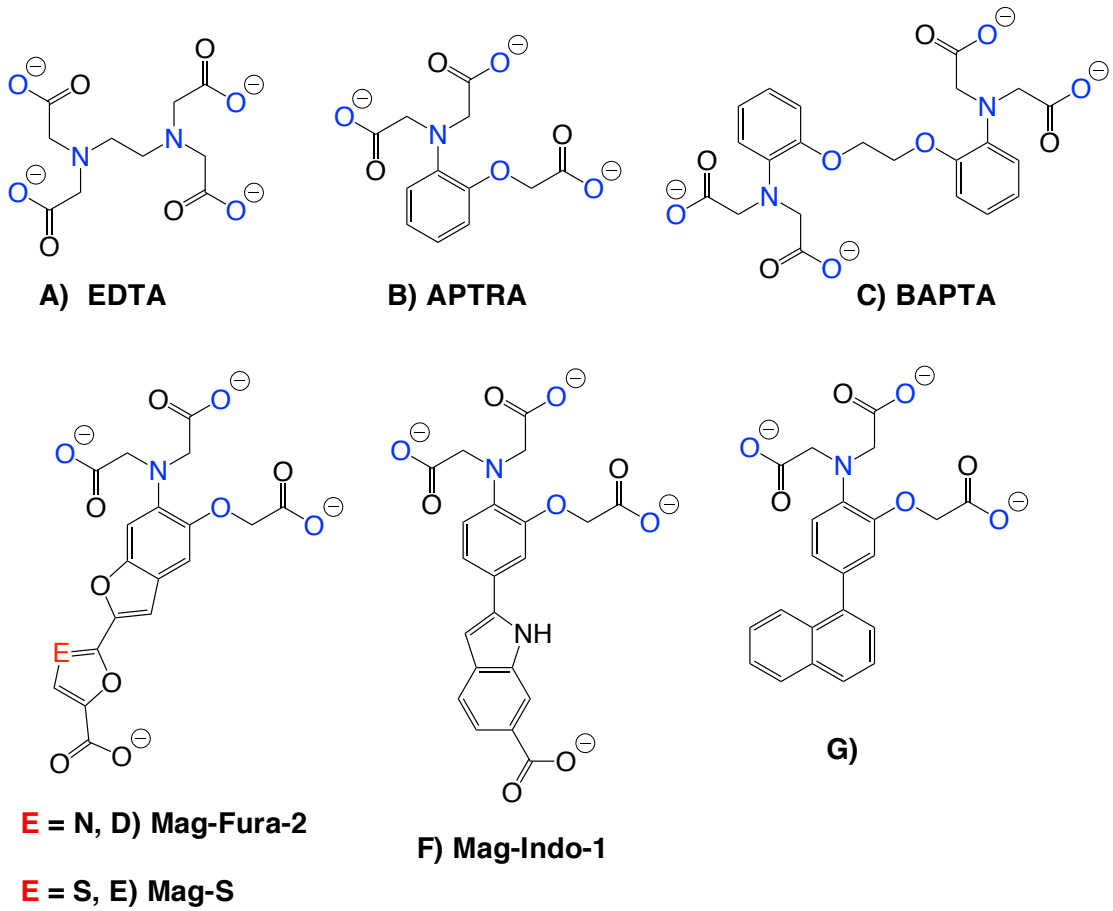

Figure 1.6 (**A**) EDTA, (**B**) APTRA, (**C**) BAPTA[39], (**D**) commercially available Mag-Fura-2 (λ_{ex} = 325 nm) [49], (**E**) Mag-S (λ_{ex} 392 nm) [50], (**F**) Mag-Indo-1 (λ_{ex} 340 nm)[43] and a later generation APTRA ligand (**G**) (λ_{ex} 325 nm) designed by London and co-workers.[51]

Mag-Fura-2 (also sometimes referred to as FURAPTRA) and Mag-Indo-1 were some of the first commercially available probes for Mg^{2+} with affinities in the low mM range (1.9 mM and 2.7 mM respectively).[49] They are composed of the same fluorophore developed to visualise selective Ca^{2+} binding via fluorescence spectroscopy, Fura-2 and Indo-1.[39] Their difference, however, arises with the introduction of an APTRA binding group at the expense of a BAPTA binding moiety used for Ca^{2+}. The APTRA moiety was introduced as the smaller ionic

radius of Mg^{2+} allows it to form stable complexes containing ligands with a lower denticity.

In 2001, an alternative synthetic approach to sp^2–sp^2 carbon-carbon bond formation was developed involving a palladium-catalysed cross-coupling reaction, allowing an array of different polyaromatic groups to be introduced onto the APTRA chelate to form a range of new APTRA fluorescent indicators (***Figure 1.6, 1.*6G**). From fluorescence measurements, it was found that naphthalene based **1.6G** acted as a 'turn on' ratiometric probe in the presence of Mg^{2+}: a 7-fold increase in the fluorescence intensity was observed at 358 nm with a 1.8-fold increase at 499 nm.[51]

Fluorescent indicators based around the APTRA framework are commonplace in the literature, but have a number of fundamental problems. Firstly, they are more selective towards Ca^{2+} than Mg^{2+} allowing them to be used as low affinity Ca^{2+} indicators. Secondly, commercially available Mag-Fura-2 and Mag-Indo-1 have relatively short emission and excitation wavelengths of 370 nm and 340 nm respectively. Low energy / high wavelength excitation is more favourable, reducing photo-damage and interference from background fluorescence in biological media.[50,52]

To overcome the issue of relatively high energy excitation, Buccella and co-workers have been working to increase the emission and excitation wavelengths of APTRA based chelators to make them more suitable for live fluorescence imaging (**Figure 1.6**)[50]. However, very few examples of Mg^{2+} indicators requiring low energy excitation are to be found in the literature. One such example, is the incorporation of heavier chalcogens (S, Se, Te) into the structure of numerous APTRA chelators to increase the emission and excitation wavelengths (**Mag-S, Figure 1.6**)[50]. The replacement of an oxygen by either a sulphur or selenium atom resulted in a greater Stokes' shift between the bound and unbound forms of the aromatic reporter group. Such a small and simple modification does not change the inherent ion selectivity; however, the affinity of the fluorescent indicators towards Mg^{2+} is slightly changed with K_d values of 2.2 mM and 3.2 mM observed for Mag-Fura-2 and Mag-S respectively.[50]

Following on from this work in developing low energy Mg^{2+} fluorescent sensors, in 2016, the Buccella group synthesised a range of bright red-emitting Mg^{2+} BODIPY (4-bora-*3a*,*4a*-diaza-*s*-indacene)-based fluorescence sensors MagB1 and MagB2 with absorption and emission maxima in the visible range (**Figure 1.7**).[53] This work was based on that of McClenaghan and co-workers in 2012, who developed two 'turn-on' BODIPY-BAPTA conjugates for the selective binding of Ca^{2+} ions.[54] The use of BODIPY fluorophores is highly advantageous, due in part to their high quantum yields, narrow emission and excitation profiles, low toxicity and the scope for structural modification. The introduction of groups onto the BODIPY core allows the possibility of colour tuning, while the introduction of binding moieties allows BODIPY based compounds to be utilised as metal binding fluorophores.[53-56]

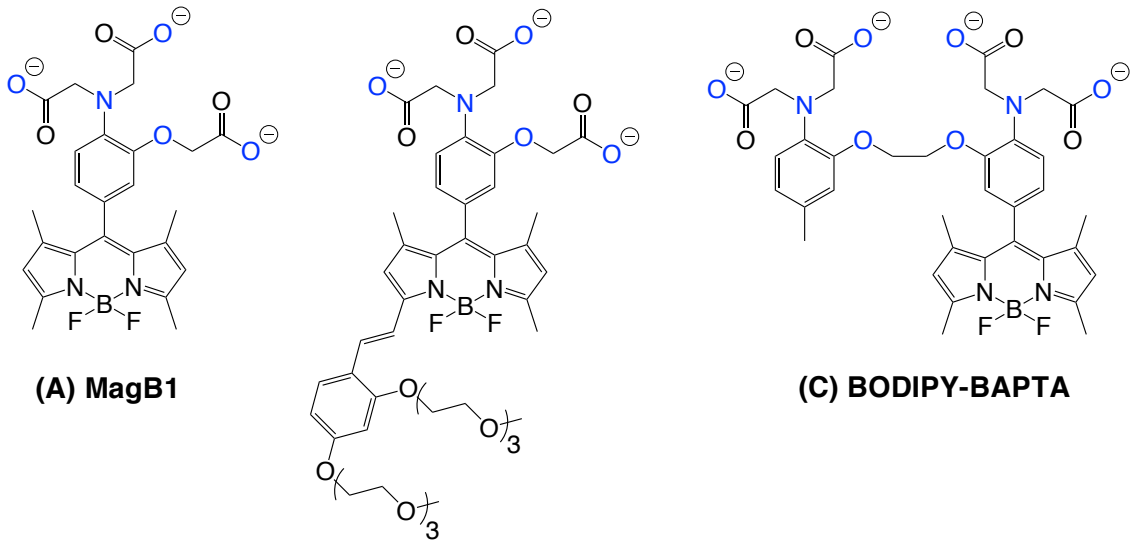

Figure 1.7 (**A**) MagB1 (λ_{ex} = 496 nm)[53], (**B**) Mag B2 (λ_{ex} = 575 nm)[53] examples of BODIPY-based Mg^{2+} sensors and (**C**) BODIPY-BAPTA, a Ca^{2+} sensor (λ_{ex} = 475 nm).[54]

Similarly to BODIPY-BAPTA, MagB1 and MagB2 are 'turn on' fluorescent probes with excitation in the visible range. A 15-fold and 58-fold increase in the fluorescence emission intensity was observed respectively. The 'turn on' nature of the probes is due to the fact that the coordination of Mg^{2+} eliminates the photo-induced electron transfer (PET) pathway that quenches the fluorescence of the unbound indicator in solution. A 'turn-on' response is highly advantageous and, coupled with binding constants in the low mM range (K_d = 4.3 mM for MagB1 and

2.1 mM for MagB2), make these probes potentially well suited for detecting 'free' or 'ionised' Mg^{2+} *in vivo*.[53] No shift in the emission or excitation spectrum is observed, however, after the addition of Mg^{2+} and Ca^{2+} in each instance. BODIPY- BAPTA, MagB1 and MagB2 are, therefore, non-ratiometic indicators for metal ions.[53,54]

The addition of specific targeting groups has allowed APTRA based fluorescent sensors to be used to detect 'free' Mg^{2+} in organelles with the development of Mag-mito-AM,[57] and HaloTag-Mg-S-Tz.[58] Mag-mito-AM is structurally similar to Mag-Fura-2, but contains a triazole linker between the APTRA binding unit and the mitochondrial targeting moiety (**Figure 1.8**). Acetoxymethyl esters (AM) are commonly introduced allowing indicators to enter cells, the ester groups are then hydrolysed to their resultant carboxylic acids within the cell. Mag-mito-AM has been used in ratiometric excitation imaging for the detection of Mg^{2+} in the mitochondria.[57] The use of Mag-mito has provided evidence of Mg^{2+} fluctuations specific to the mitochondria in the early stages of cell apoptosis in HeLa cells, induced by Staurosporine.[57] During apoptosis it was determined that there was an approximate 3-fold increase in 'free' Mg^{2+} to 2.6 mM, whilst the control experiment without the addition of Staurosporine resulted in a constant 'free' Mg^{2+} concentration of 0.8 mM.[57]

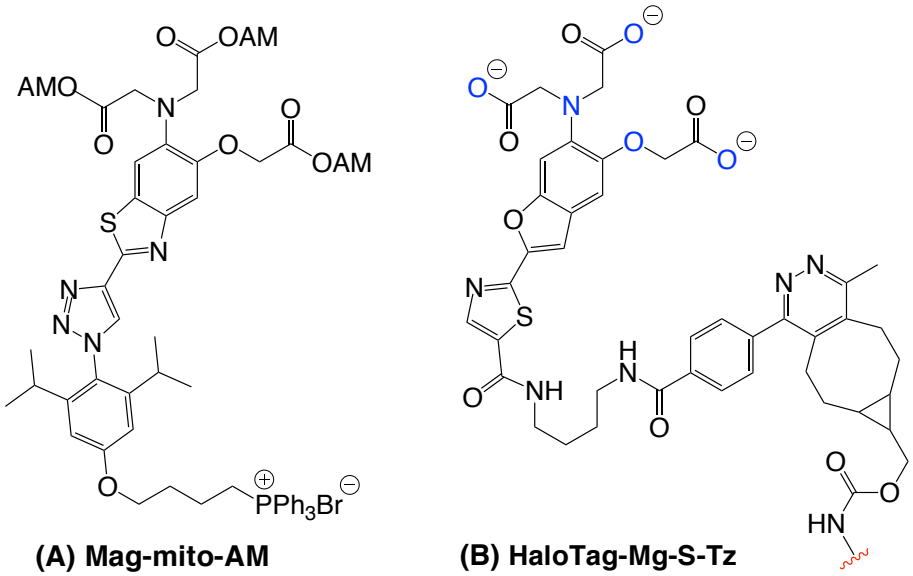

(A) Mag-mito-AM **(B) HaloTag-Mg-S-Tz**

Figure 1.8 (**A**) Mag-mito-AM, a mitochondrial targeted Mg^{2+} fluorescent sensor,[57] (**B**) HaloTag-Mg-S-Tz for imaging in the nucleus, Golgi apparatus and the mitochondria,[58] ~ indicates the start of the specific protein sequence enabling localisation within the cell.

HaloTag-Mg-S-Tz uses HaloTag protein labelling technology, and has been developed for ratiometric imaging of Mg^{2+} in specific cellular compartments including the nucleus, mitochondria and Golgi apparatus.[58] It achieves specific localisation within the cell by varying the protein sequence connected to the HaloTag domain.[58] It was found that the addition of the protein enabling localisation did not affect the sensor's affinity for Mg^{2+}, remaining in the mM range (K_d = 3.1 mM).[58]

1.5.3.2 β-Keto acid-based Fluorescent Sensors

Over the last decade, a number of probes as an alternative to the APTRA binding framework have been developed for the binding of 'free' Mg^{2+}. Examples include β-keto acids,[59-63] crown ethers,[64] porphyrin and the first genetically encoded fluorescent probe MagFRET-1, based on the high-affinity Mg^{2+} binding domain of human centrin 3 (HsCen3), with a Mg^{2+} affinity in the μM range (K_d = 148 μM).[65]

β-Keto acids have emerged in recent years as an alternative to the APTRA binding site. Suzuki and co-workers are at the forefront of this research and have developed a range of β-keto acids that selectively bind Mg^{2+} in a bidentate

manner (**Figure 1.9**). KMG-20 was the first of the series to be synthesised in 2002.[62] The charged bidentate β-diketone binding site and coumarin fluorophore showed promise, with a 200-times greater selectivity observed for Mg^{2+} over Ca^{2+} compared to commercially available probes, such as Mag-Fura-2 and magnesium green.[62] Nevertheless, KMG-20 has a number of significant disadvantages. The high dissociation constant (K_d) of 10 mM and the short wavelength absorption maxima observed meant that it was not excitable by the Ar^+ laser that is commonly used in confocal microscopy experiments. The group later developed a range of alternative probes in the series with longer wavelength maxima, including KMG-104[66] and KMG-301,[59] which have fluorescence emission that is independent of pH within the biological range,[66] allowing the binding of Mg^{2+} to be studied in the cytosol and the mitochondria.[59]

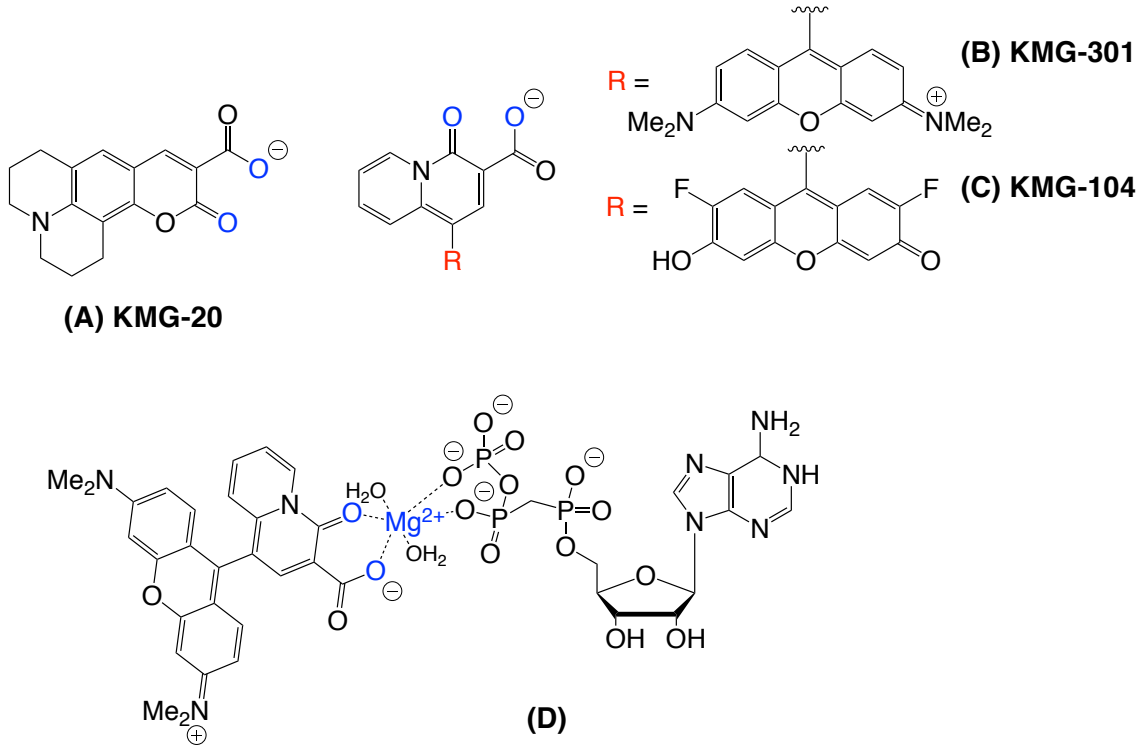

Figure 1.9 (**A**) KMG-20,[62] (**B**) KMG-301[59] and (**C**) KMG-104,[66] Mg^{2+} selective β-keto-acid fluorescent probes forming binary species with 'free' Mg^{2+}. (**D**) The binding of KMG-301 to $MgATP^{2-}$ forming a ternary complex.[60]

KMG-104 adopts a xanthene-based phore as an alternative to the coumarin group used for KMG-20, and has been used as a selective probe to model Mg^{2+} dynamics in the cytosol.[66] A PET quenching process is observed in

the ground state, instead of the internal charge transfer (ICT) mechanism observed with KMG-20. The elimination of the PET quenching mechanism upon Mg^{2+} binding resulted in an 8-fold 'turn-on' response upon the addition of Mg^{2+} ions, with a K_d of 2.1 mM.[66] No significant fluorescence response was observed with any competing biologically relevant metal ions including Ca^{2+}, K^+ and Na^+. A significantly increased Mg^{2+} / Ca^{2+} selectivity was observed, with the affinity for Ca^{2+} in the mM range (K_d = 7.5 mM), instead of the usual μM range of binding seen with the APTRA chelators in the literature.

The Ca^{2+} concentration in mammalian cells such as those in the brain is typically in the range of 50 to 100 nM, while extracellular Ca^{2+} concentrations are around 1.5 to 2.0 mM.[67] The K_d for Ca^{2+}, therefore, lies outside the range of intra- and extracellular Ca^{2+} concentrations.[67]

KMG-301 has a molecular design based on rhodamine, whose cationic charge is known to favour localisation in the mitochondria because of its negative membrane potential.[59] It was found that a 45-fold increase in the fluorescence emission was observed in the presence of 100 mM of Mg^{2+} with a K_d of 4.5 mM, an ideal range for the detection of Mg^{2+} *in vivo*.[59] A substantial improvement in the selectivity towards Mg^{2+} in comparison with the APTRA chelators was observed, with the fluorescence intensity remaining unaffected in the presence of biological concentrations of a number of cations including Na^+, K^+ and most notably Ca^{2+}.[59] Mitochondria typically possess a higher concentration of Ca^{2+} than other areas of the body, and it was, therefore, vital in this instance that the ligand has a low affinity towards Ca^{2+}, for the accurate measurements of Mg^{2+} dynamics to be measured.[59]

The use of KMG-104 in combination with KMG-301 has allowed a greater understanding to be developed into details about the accumulation and extrusion of Mg^{2+} in the mitochondria.[59]

β-Keto-acids have a number of significant advantages over APTRA based fluorescent sensors, primarily, their higher selectivity towards Mg^{2+} over Ca^{2+}. However, they too have a number of limitations to consider. Ligands in the KMG

series are non-ratiometric, unlike many of the APTRA based fluorescent sensors, meaning that upon binding of Mg^{2+} no shift in the emission and / or excitation wavelength is observed. The bidentate binding nature of the β-keto acids, occupying only two sites in the coordination sphere of Mg^{2+}, results in the formation of mixed species with Mg^{2+}.[60] Their low denticity means that β-keto acids can form both binary and ternary complexes with Mg^{2+}, i.e. forming complexes with 'free' Mg^{2+} and Mg^{2+} bound to ATP^{4-} respectively (**Figure 1.9D**).[60] Simple fluorescent measurements cannot be used to distinguish between the bound and unbound forms of Mg^{2+} that can be formed in the cell, because the K_d values for both species are in the low mM range (3.8 mM for Mg^{2+}, 14.2 mM for $MgATP^{2-}$).[60] Unless more sophisticated fluorescent measurements can be recorded, the ligands in the KMG series are not appropriate fluorescent indicators to develop a greater understanding of Mg^{2+} homeostasis *in vivo* and, therefore, a more accurate determination of intracellular concentrations of Mg^{2+} is required.

Compound	λ_{max} Absorption (nm)	λ_{max} Excitation (nm)	λ_{max} Emission (nm)	Quantum yield, Φ	K_d (Mg^{2+}) (mM)	K_d (Ca^{2+}) (μM)
Mag-fura-2[49,50]	369	370	511	0.24	1.9	25
Mag-S[50]	396	392	572	0.17(1)	3.2(1)	38(1)
Mag-Se[50]	412	410	584	0.09(2)	3.3(3)	41(2)
Mag-indo-1[43]	-	340	-	-	2.8	-
MagB1[53]	496	496	508	0.0051(2)	4.31(1)	25.2(2)
MagB2[53]	575	575	601	0.0050(2)	2.13(5)	15.4(7)
Mag-mito[57]	356	356	495	-	6.7(3)	71(4)
Mag-S-Tz activated[58]	404	404	595	0.100(4)	3.1(1)	40.6(8)
KMG-20[62]	425	-	485	-	10	30
KMG-301[59]	540	-	-	0.15	4.5	-
KMG-104[66]	502	502	523	-	2.1	7.5

Table 1.3 Summary of Mg^{2+} fluorescence probes in order as discussed in **Section 1.5.3.1** and **Section 1.5.3.2**. Measurements are recorded in H_2O, errors calculated for each measurement are included in parenthesis (mM binding affinity for Ca^{2+}).

1.5.3.3 Alternative Fluorescent Sensors to monitor Mg^{2+} binding

Crown ethers based upon diaza-18-crown-6-hydroxyquinoline are another example of ligands that have been used to bind Mg^{2+} selectively.[64, 68] Iotti and co-workers have synthesised a number of 8-hydroxyquinoline based probes, including DCHQ5, a fluorescent probe with a μM affinity for Mg^{2+} (**Figure 1.10**).[68] Such behaviour makes these 'turn-on' probes unsuitable for use *in vivo* for the detection of 'free' Mg^{2+}, because its concentration lies in the low mM range in mammalian cells. They can, however, provide an insight into the total intracellular Mg^{2+} concentration. No significant changes were observed in either the absorption or emission spectra upon the addition of a number of divalent cations, including Ca^{2+} and Fe^{2+},[64,68] highlighting their selectivity of binding Mg^{2+} over competing cations within this range.[68] The 'turn-on' response observed is due to the de-protonation of the phenol group of 8-hydroxyquinoline, on binding to Mg^{2+}, preventing an intramolecular photoinduced proton transfer (PPT) process occurring that is observed in the free ligand.[68]

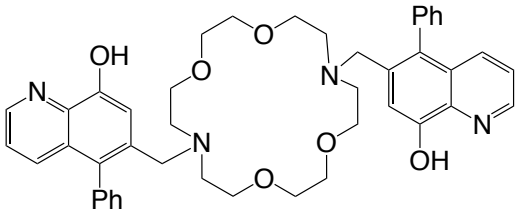

Figure 1.10 DCHQ5, an 8-hydroxyquinoline-based Mg^{2+} probe.[68]

In contrast, Duan and co-workers have developed a range of nano-sized lanthanide complexes that can act as luminescent chemosensors for the selective sensing of Mg^{2+} ions. Three ligands have been synthesised H_4DBOS, H_4DBDS and H_4DBBS that are selective towards the metal ions Mg^{2+} and Al^{3+} upon the addition of Ce^{3+} (**Figure 1.11**).[69] It was found from X-ray crystallography studies that in each instance the ligands bridge two homochiral Ce^{3+} ions forming 'lantern like' molecules with a stoichiometry of 2:3, metal:ligand. In the case of H_4DBDS and H_4DBBS upon the addition of Ce^{3+}, a cavity is formed allowing the selective binding of Mg^{2+}.[69]

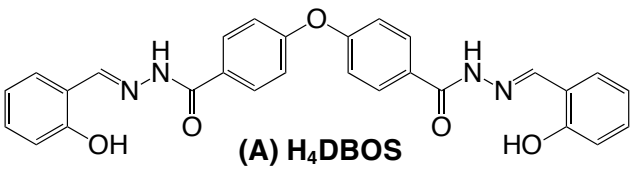

(A) H_4DBOS

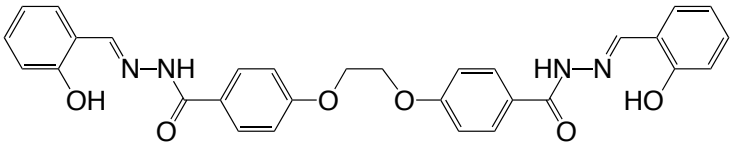

(B) H_4DBDS

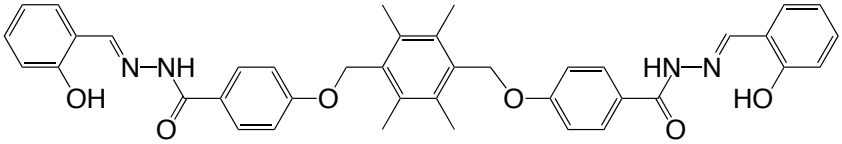

(C) H_4DBBS

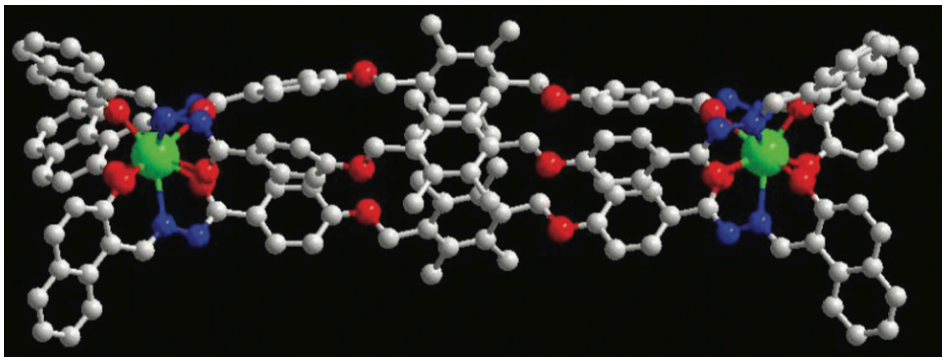

(D)

Figure 1.11 Ligands (**A**) H_4DBOS, (**B**) H_4DBDS and (**C**) H_4DBBS, (**D**) the crystal structure of H_4DBBS a cavity is formed upon the addition of Ce^{3+}, allowing metal ion binding to occur.[69]

A fluorescence titration with Mg^{2+} found that both $[Ce_2(DBDS)_3]^{2-}$ and $[Ce_2(DBBS)_3]^{2-}$ were highly selective towards Mg^{2+} while $[Ce_2(DBOS)_3]^{2-}$ was found to be selective towards Al^{3+}. $[Ce_2(DBDS)_3]^{2-}$ showed a 4.5-fold increase in the luminescence intensity after the addition of 10 equivalents of Mg^{2+}. In comparison, a negligible change in the fluorescence intensity was observed with other alkali earth metals and biologically relevant cations such as Ca^{2+}, Li^{+}, Na^{+} and K^{+}.[69] The high selectivity towards Mg^{2+} can be explained by the ionic radius of the cations in question. Mg^{2+} with a coordination number of six, has a significantly smaller radius than Na^{+} and Ca^{2+} (0.7 Å vs. 1.02 Å) making it an ideal

size to fit into the cavity of $[Ce_2(DBDS)_3]^{2-}$ and $[Ce_2(DBBS)_3]^{2-}$, resulting in a highly selective binding.[69]

1.5.4 ^{19}F NMR and ^{31}P NMR

London first used ^{19}F NMR to measure the concentration of cytosolic Mg^{2+} concentrations in 1988 by adapting the APTRA chelators and synthesising a range of fluorinated derivatives.[70] 4-Fluoro, 5-fluoro and 4-methyl-5-fluoro derivatives were made (**Figure 1.12**). Upon Mg^{2+} binding, a shift to higher frequency was observed for each of the three fluorinated derivatives in the ^{19}F NMR spectrum.[70] *In cellulo* experiments were carried out in human erythrocytes with the 4-methyl-5-fluoro derivative, where it was determined that the cytosolic 'free' Mg^{2+} concentration was 0.25 mM.[70]

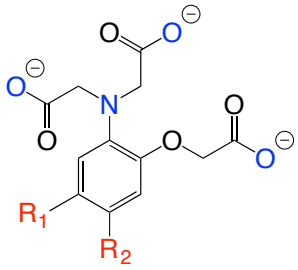

(A) R_1 = F, R_2 = H

(B) R_1 = H, R_2 = F

(C) R_1 = Me, R_2 = F

Figure 1.12 The structure of (**A**) 4-fluoro, (**B**) 5-fluoro and (**C**) 4 methyl-5-fluoro APTRA derivatives for the ^{19}F NMR studies.[70]

The vast majority of Mg^{2+} within the cell is bound to phosphorus-containing anions such as ATP, rendering ^{31}P NMR a more favourable technique for the measurement of the concentration of cytosolic free Mg^{2+} than ^{19}F NMR.

^{31}P NMR is a non-invasive technique that can be used to measure the concentration of 'free' magnesium in both cells and tissues.[10] Magnesium in its 'free' and bound states exist in a chemical equilibrium, allowing the chemical shift changes for the binding of magnesium to ATP to be related to the free Mg^{2+} concentration.[71] Upon magnesium binding, a shift in the NMR resonance is observed primarily at the β- and γ-phosphates in ATP as these phosphates play a key role in Mg^{2+} binding (**Figure 1.1**). The magnesium ion concentration can be determined from the separate ^{31}P resonances of ATP in its 'free' and unbound

forms. A slow exchange is observed between the free and unbound forms, allowing the magnesium concentration to be determined from **Equation 1.1**.[8,70]

$$Mg^{2+} = K_d \left(\frac{\delta_o - \delta_f}{\delta_b - \delta_o}\right) \quad \textbf{(Eq. 1.1)}$$

where: δ_o is the chemical shift for the observed resonance, δ_b is the chemical shift for the fully complexed ligand and δ_f is the chemical shift for the uncomplexed ligand.[8,70]

Other metabolites have been used in NMR studies as an alternative to ATP, such as ADP and citrate. ATP is favoured, however, because of its high concentration and broad distribution within cells.[8]

^{31}P NMR has been used to determine the 'free' Mg^{2+} concentration in muscle tissue, where a concentration of 0.6 mM was observed. Under different metabolic conditions, it was determined that during exercise the concentration of free Mg^{2+} increased from 0.33 mM to 0.56 mM.[71] The potential use of ^{31}P NMR commercially has a number of limiting factors. Firstly, no information can be derived on intracellular 'free' Mg^{2+} distribution because of its low sensitivity. ADP also represents a more attractive ligand than ATP because its K_d is similar to that seen with free Mg^{2+} ions; however, this is problematic because of the lower concentrations of ADP in relation to ATP within cells.[10]

1.5.5 Magnetic Resonance Imaging (MRI)

Since its introduction in 1980, Magnetic Resonance Imaging (MRI) has become one of the most important and recognised diagnostic techniques in clinical medicine.[72] It is non-invasive, delivering non-ionising radiation to the patient, making it a safer alternative to other imaging modalities such as X-ray Computed Tomography (CT).[73] The technique offers fast scan rates and exceptional resolution of images in the sub-millimetre (mm) range, producing a detailed visualisation of opaque organs and tissues *in vivo*.[72] MRI is based on the principles of Nuclear Magnetic Resonance (NMR) and visualises water protons in the body. A natural contrast is present between different mammalian tissue

types because they possess both; different concentrations of water molecules and contrasting proton relaxation times. A greater contrast between tissue is achieved, however, following the introduction of contrast agents. Contrast agents lower the relaxation times (T_1, T_2) of the surrounding water protons increasing the sensitivity and relaxivity (r_1- the ability of the contrast agent to enhance the rate of water proton relaxation per unit concentration).

Allegedly, 'smart' contrast agents induce a significant increase in relaxivity upon a change in pH or the binding of biologically relevant cations or anions. Numerous examples are present in the literature of MRI contrast agents for cation sensing, but are primarily limited to the detection of Ca^{2+} and Zn^{2+} ions. Meade and co-workers developed the first example of a Ca^{2+} responsive MRI contrast agent, DOPTA-Gd, containing two gadolinium based DO3A chelates and a modified BATPA binding site related to that developed by Tsien in 1980[39] (**Figure 1.13**). An 80 % increase in the relaxivity was observed upon the addition of Ca^{2+}.[74]

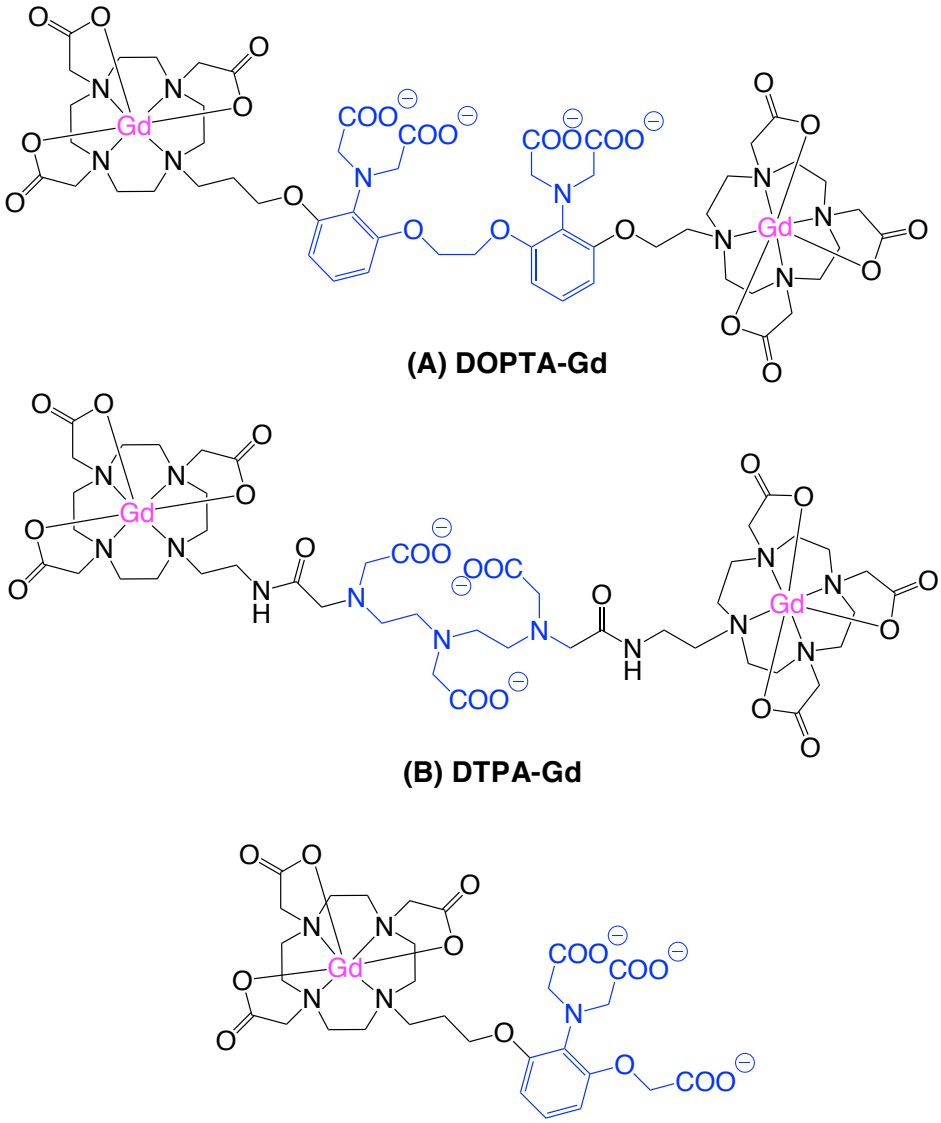

(A) DOPTA-Gd

(B) DTPA-Gd

(C) Gd-DOPTRA

Figure 1.13 (**A**) Ca^{2+} selective probe DOPTA-Gd,[74] (**B**) Ca^{2+} and Mg^{2+} probe DTPA-Gd,[75] (**D**) APTRA based probe Gd-DOPTRA [76] (Mg^{2+} binding site in blue, Gd^{3+} in pink).

MRI contrast agents for the detection of Mg^{2+} are much less developed with only a few examples present in the literature to date. The main reason for this is that there are very few commercially available ligands available to bind Mg^{2+} selectively. A gadolinium-based complex based upon a DTPA binding site was found to bind both Ca^{2+} (K_d = 0.25 mM) and Mg^{2+} (K_d = 2.0 mM).[75] Logothetis and co-workers incorporated an APTRA binding moiety into a DO3A-based gadolinium complex.[76] Synthesised to work predominantly as a low affinity Ca^{2+} responsive probe, relaxivity enhancements were also observed with Mg^{2+} and Zn^{2+}, reflecting the non-selective binding nature of the APTRA chelates,

highlighted first in the early work undertaken by London and co-workers.[49,51,70] A much more selective Mg^{2+} MRI based probe, however, has been reported by Suzuki and co-workers. They developed a novel gadolinium complex KMR-Mg, that is based on a well-recognised bidentate Mg^{2+} binding site, a β-keto acid moiety, that is known to bind Mg^{2+} selectively over Ca^{2+} (**Figure 1.14**).[77]

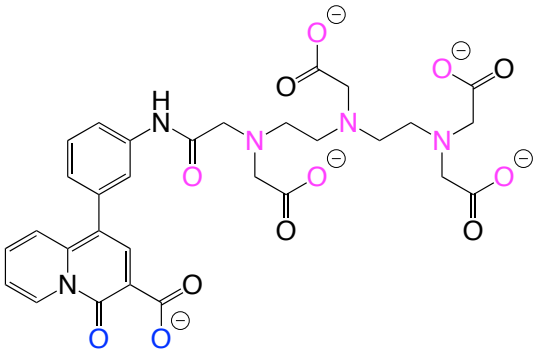

Figure 1.14 Mg^{2+} selective probe KMR-Mg for use in MRI. (Mg^{2+} binding site in blue, Gd^{3+} in pink).[77]

KMR-Mg is made up of a DTPA and β-keto acid framework for the binding of Gd^{3+} and Mg^{2+} respectively. A stable 9-coordinate complex with Gd^{3+} forms with the ninth coordination site occupied by an inner sphere water molecule.[77] It was found that the relaxivity decreased with increasing Mg^{2+} concentration, the addition of one equivalent of Mg^{2+} resulted in a 21 % decrease from 4.98 $mM^{-1}s^{-1}$ to 3.95 $mM^{-1}s^{-1}$.[77] The reduced relaxivity observed can be attributed to a change in the second sphere of hydration of Gd^{3+} on Mg^{2+} binding.

A relaxivity decrease was also observed in the presence of Ca^{2+}, meaning that KMR-Mg does not bind Mg^{2+} selectively. A reduced binding affinity was, however, observed with Ca^{2+} (log K 2.39 vs. 2.08), with a mM affinity reported for the binding of both Mg^{2+} and Ca^{2+}.[77] Such an affinity is analogous to fluorescence based probes in the KMG-series, showing a higher Mg^{2+} / Ca^{2+} selectivity over the APTRA series.[59-62]

In 2012, Charbonniere and co-workers developed a gadolinium-based smart contrast agent with a very high selectivity towards Mg^{2+} ions. Instead of the usual macrocycle framework to encapsulate the lanthanide ion, the complex is made up of a Gd^{3+} centre with a heptadentate polyphosphonate-based pyridyl

ligand (**Figure 1.15**). The complex $[Gd(H_2L)(H_2O)]^{3-}$ is thermodynamically stable with one bound water molecule in its primary hydration sphere, giving a total coordination number of eight.[78]

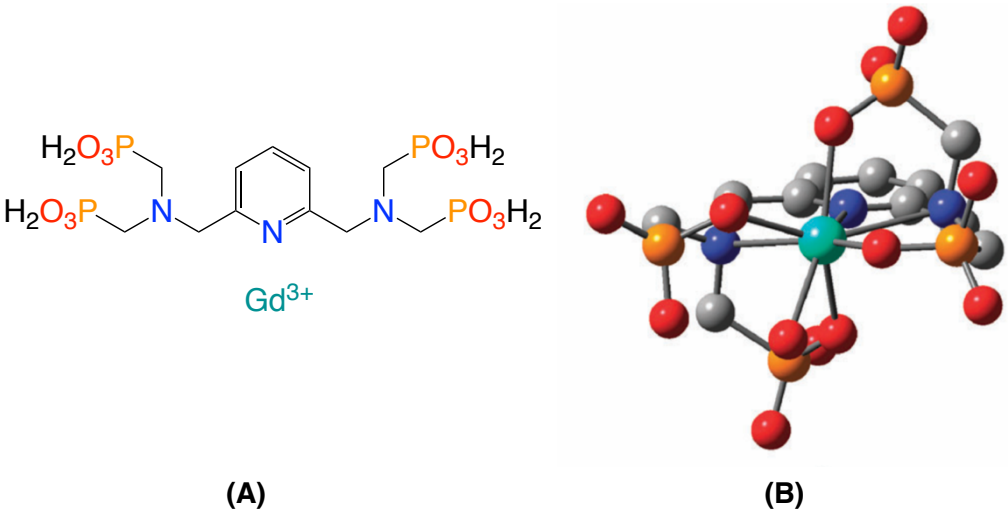

Figure 1.15 (**A**) The polyphosphonated pyridyl ligand, L, (**B**) DFT calculation of the stable 8-coordinate complex with Gd^{3+}, $[Gd(H_2L)(H_2O)]^{3-}$. [78]

From relaxivity measurements it is clear that the polyphosphonated pyridyl ligand is highly selective for the binding of Mg^{2+} over Ca^{2+}, with an increase in the relaxivity observed from 8.5 $mM^{-1}s^{-1}$ to 12 $mM^{-1}s^{-1}$ a 37 % enhancement upon the addition of 30 equivalents of $MgCl_2$.[78] The xylenol orange test was used in order to determine whether the increase in the relaxivity was because of gadolinium displacement. No colour change was observed, indicating that no lanthanide displacement occurs. It was instead thought that the addition of Mg^{2+} could result in the formation of polynuclear complexes, resulting in the increase of the rotation tumbling time of the complex and increasing the observed relaxivity.[78] The pH-dependence of the relaxivity of this system, however, is likely to inhibit any practicable utility.

1.6 Aims and Objectives

The overwhelming majority of Mg^{2+} sensors in the literature are based on either the APTRA binding framework, developed by London and co-workers, or the β-keto acid bidentate binding structure, developed by Suzuki *et al*. It is apparent from a literature search that there is very little variation in overall ligand design. The novelty in new sensors typically comes from modifications to the chromophore, or the use of different chromophores to report the fluorescence change upon binding of divalent cations. With the only structural variation of ligands coming from the chromophore used, the binding of Mg^{2+} and Ca^{2+} is similar in each instance, with a higher selectivity for the binding of Ca^{2+} over Mg^{2+}. The vast majority of APTRA-based probes in the literature, therefore, can also be used as low affinity Ca^{2+} sensors in the μM range.

The aims of the research detailed here can be sub-divided into two main categories. Firstly, one aim was to incorporate the ATPRA moiety into a range of new luminescence systems including naphthalene, lanthanide and ruthenium-based compounds to study Mg^{2+} binding. The primary objective, however, was to develop a range of new Mg^{2+} selective ligands containing both carboxylate and phosphinate binding groups. It was hoped that the introduction of a phosphinate group could influence the Mg^{2+} / Ca^{2+} selectivity while maintaining the desired low mM affinity towards Mg^{2+}.

Chapter 2 describes the synthesis of a series of carboxylate and phosphinate based ligands from commercially available starting materials. All analogues are based on the APTRA series, with an expected pentadentate $\mathbf{L^1}$, $\mathbf{L^2}$ and $\mathbf{L^4}$ and tridentate denticity, $\mathbf{L^6}$ (**Figure 1.16**).

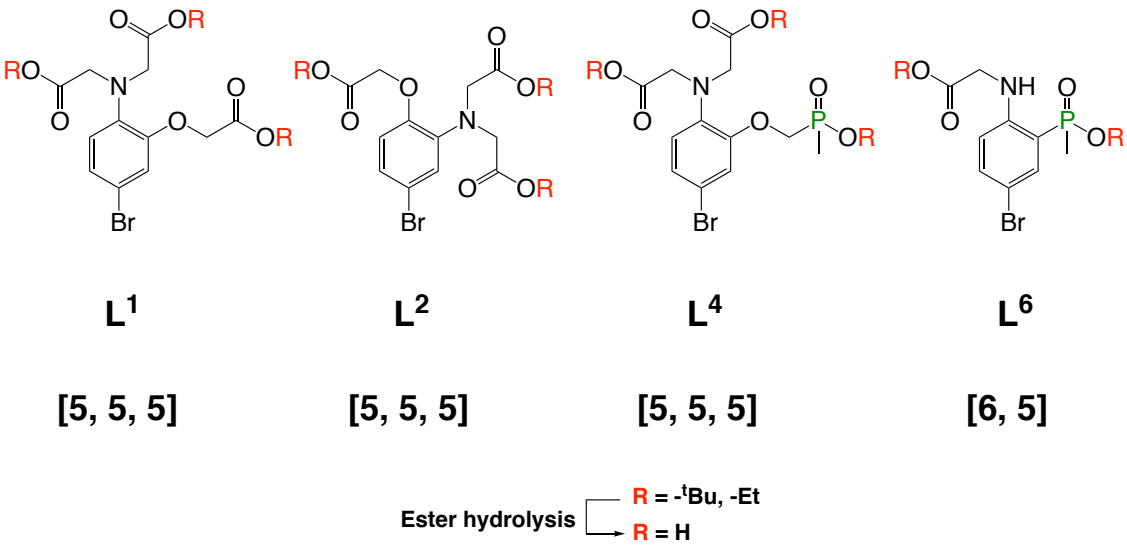

Figure 1.16 APTRA analogues $\mathbf{L^1}$, $\mathbf{L^2}$, $\mathbf{L^4}$ and $\mathbf{L^6}$

In **Chapter 3** a direct comparison between the binding properties of APTRA[48] with the newly synthesised phosphinate analogue APDAP is made via absorbance spectroscopy. **Chapter 4** outlines the incorporation of $\mathbf{L^1}$, $\mathbf{L^2}$, $\mathbf{L^4}$ and $\mathbf{L^6}$ into naphthalene based fluorescence systems. The binding properties of novel ligands $\mathbf{NapL^4}$ and $\mathbf{NapL^6}$ is reported, and directly compared to the APTRA analogues $\mathbf{NapL^1}$ and $\mathbf{NapL^2}$. Finally, **Chapter 5** details the incorporation of $\mathbf{L^1}$ and $\mathbf{L^2}$ into lanthanide(III) and $\mathbf{L^2}$ into ruthenium(II)-based systems to study the binding of Mg^{2+}.

1.7 References

[1] W. Hasselbach, *Biochim. Biophys. Acta.*, 1957, **25**, 562-572.

[2] V. Trapani, G. Farruggia, C. Marraccini, S. Iotti, A. Cittadini and F. I. Wolf, *Analyst.*, 2010, **135**, 1855-1866.

[3] A. M.P. Romani, *Arch. Biochem. Biophys.,* 2007, **458**, 90-102.

[4] V. Trapani, M. Schweigel-Rontgen, A. Cittadini and F. I. Wolf, *Methods Enzymol.*, 2012, **505**, 422-442.

[5] A. M. P. Romani, *Arch. Biochem. Biophys.*, 2011, **512**, 1-23.

[6] H. Ebel and T. Gunther, *J. Clin Chem Clin Biochem.*, 1980, **18**, 257-270.

[7] G. A. Rutter, N. J. Osbaldeston, J. G. McCormack and R. M. Denton, *Biochem. J.,* 1990, **271**, 627-634.

[8] R.E. London, *Annu. Rev. Physiol.*, 1991, **53**, 241-58.

[9] N. H. Williams, *J. Am. Chem. Soc.*, 2000, **122**, 12023-12024.

[10] A. Romani and A. Scarpa, *Arch. Biochem. Biophys.*, 1992, **298**, 1-12.

[11] M. Tilmann., F. Wolf, *Curr Opin Pediatr.*, 2017, **29**, 187-198.

[12] S. M. G. Alghamdi, E. C. Cameron and R. Sutton, *Am. J. Kidney Dis.*, 1994, **24**, 737-752.

[13] B. Sontia and R. M. Touyz, *Biochem. Biophys.*, 2007, **458**, 33-39.

[14] G. M. Walker and J. H. Duffus, *J. Cell Sci.*, 1980, **42**, 329-356.

[15] F. I Wolf, V. Trapani and A, Cittadini, *Magnes Res.*, 2008, **21**, 83-91.

[16] R. M. Touyz and G. Yao. *J. Cell Physiol.*, 2003, **197**, 326-335.

[17] J. A. M. Maier, D. Bermardini, Y. Rayssiguier and A. Mazur, *Biochem. Biophys. Acta.*, 2004, **1689**, 6-12.

[18] J. H. F. de Baaij, J. G. J. Hoenderop and R. J. M. Bindels, *Physiol Rev.*, 2015, **95**, 1-46.

[19] R. Taylor and L. Agius, *Biochem. J.*, 1988, **250**, 625-640.

[20] L. M. Resnick, *Am. J. Hypertens.*, 1993, **6**, 123S-134S.

[21] A. Tin and M.E. Grams, *Kidney Int.*, 2015, 820-827.

[22] H. F. Schimatschek and R. Rempis, *Magnes. Res.*, 2001, **14**, 283-290.

[23] A. M. P. Romani and A. Scarpa, *Front. Biosci.*, 2000, **5**, 720-734.

[24] A. M. P. Romani and M. E. Maguire, *Biometals.*, 2002, **15**, 271-283.

[25] F. I. Wolf, A. Di Francesco, V. Covacci and A. Cittadini, *Arch. Biochem. Biophys.*, 1997, **344**, 397-403.

[26] A. Fleig and R. Penner, *Trends Pharmacol Sci.*, 2004, **25**, 633-639.

[27] C. Schmitz, K. Brandao and A. L. Perraud, *Magnes Res.*, 2014, **27**, 9-15.

[28] V. Chubanov, S. Ferioli, A. Wisnowsky, D. G. Simmons, C. Leitzinger, C. Einer, W. Jonas, Y. Shymkiv, H. Bartsch, A. Braun, B. Akdogan, L. Mittermeier, L. Sytik, F. Torben, V. Jurinovic, E. P. C. van der Vorst, C. Weber, Ö. A. Yildirim, K. Sotlar, A. Schürmann, S. Zierler, H. Zischka, A. G. Ryazanov and T. Gudermann, *eLife.*, 2016, **5**, e20914.

[29] D. M. Bui, J. Gregan, E. Jarosch, A. Ragnini and R. J. Schweyen, *J. Biol. Chem.*, 1999, **274**, 20438-20443.

[30] G. Wiesenberger, M. Waldherr and R. J. Schweyen, *J.Biol. Chem.*, 1992, **267**, 6963-6969.

[31] T. Gunther, J. Vormann and R. Forster, *Biochen. Biophys. Res.*, 1984, 124-131.

[32] T. Gunther and J. Vormann, *Febs Letters.*, 1989, **250**, 633-637.

[33] T. Gunther, *Magnes Res.*, 2007, **20**, 89-99.

[34] H. Ebel, M. Hollstein and T. Gunther, *Biochim. Biophys. Acta.*, 2002, **1559**, 135-144.

[35] J-C. Feray and R. Garay, *J. Biol. Chem.*, 1987, **262**, 5763-5768.

[36] A. M. P. Romani, *Magnes Res.*, 2008, **21**, 197-204.

[37] R. M. Touyz, *Mol. Aspects Med.*, 2003, **24**, 107-136.

[38] C. M. Champagne, *Nutr. Clin. Pract.*, 2008, **23**, 142-151

[39] R. Y. Tsien, *Biochemistry.*, 1980, **19**, 2396-2404.

[40] G. Grynkiewicz, M. Poenie and R. Y. Tsien., *Bio. Chem.*, 1985, **260**, 3440-3450.

[41] C. Collet, B. Allard, Y. Tourneuer and V. Jacquemond, *J. Physiol.*, 1999, **2**, 417- 429.

[42] L. L. Yu, W. C. Davis, Y. N. Ordonez and S. E. Long., *Anal. Bioanal. Chem.*, 2013, **405**, 8761-8768.

[43] www.webelements.com

[44] C. Feillet-Coudray and C. Coudray, *Curr Nutr Food Sci.*, 2005, **1**, 63-70.

[45] C. Feillet-Coudray., C. Coudray., E. Gueux., A. Mazur and Y. Rayssiquier. *Magnes Res.*, 2002, **15**, 191-198.

[46] C. Feillet- Coudray, A. Nasulewicz, L. Jaffrelo, S. Thien, C. Coudray, M. Rambeau, E. Gueux, Y. Rayssiguier, A. Opolski, F. I. Wolf and A. Mazur, *Magnes Res.*, 2005, **18**, 103-108.

[47] E. Baggaley, J. A. Weinstein and J. A. G. Williams, *Coord. Chem Rev.*, 2012, **256**, 1762-1785.

[48] M. Brady, S. D. Piombo, C. Hu and D. Buccella, *Dalton Trans.*, 2016, **45**, 12458-12464.

[49] B. Raju, E. Murphy, L. A. Levy, R. D. Hall and R. E. London, *Am. J. Physical.*, 1989, **256**, 540-548.

[50] M.S. Afzal, J-P. Pitteloud and D. Buccella, *Chem. Commun.*, 2014, **50**, 11358-113361.

[51] P.A. Otten., R. E. London and L. A. Levy, *Bioconjugate Chem.*, 2001, **12**, 76-83.

[52] K. P. Carter, A. M. Young and A. E. Palmer, *Chem. Rev.,* 2014, **114**, 4564-4601.

[53] Q. Lin, J. J. Gruskos and D. Buccella, *Org. Biomol. Chem.*, 2016, **14**, 11381-11388.

[54] P. Batat, G. Vives, R. Bofinger, R-W. Chang, B. Kauffmann, R. Oda, G.Jonusauskas and N. D. McClenaghan, *Photochem. Photobiol. Sci.,* 2012, **11**, 1666-1674.

[55] J. L. Bricks, A. Kovalchuk, C. Trieflinger, M. Nofz, M. Büschel, A. I. Tolmachev, J. Daub and K. Rurack, *J. Am. Chem. Soc.,* 2005, **127**, 13522-13529.

[56] M. Baruah, W. Qin, R. A. L. Vallée, D. Beljonne, T. Rohand, W. Dehaen and N. Boens, *Org. Lett.*, 2005, **7**, 4377-4380.

[57] G. Zhang, J. J. Gruskos, M. S. Afzal and D. Buccella, *Chem. Sci.,* 2015, **6**, 6841.

[58] J. J. Gruskos, G. Zhang and D. Buccella, *J. Am. Chem. Soc.*, 2016, **138**, 14639-14649.

[59] T. Fujii, Y. Shindo, K. Hotta, D. Citterio, S. Nishiyama, K. Suzuki and K. Oka, *PLOS ONE.,* 2011, **6**, e23684.

[60] S. C. Schwartz, B. Pinto-Pacheco, J-P. Pitteloud and D. Buccella, *Inorg. Chem.*, 2014, **53**, 3204-3209.

[61] T. Fujii, Y. Shindo, K. Hotta, D. Citterio, S. Nishiyama, K. Suzuki and K. Oka, *J. Am. Chem. Soc.*, 2014, **136**, 2374-2381.

[62] Y. Suzuki, H. Komatsu, T. Ikeda, N. Saito, S. Araki, D. Citterio, H. Hisamoto, Y. Kitamuru, T Kubota, J. Nakagawa, K. Oka and K. Suzuki, *Anal. Chem.*, 2002, **74**, 1423-1428.

[63] P. A. Otten, R. E. London and L. A. Levy, *Bioconjugate Chem.*, 2001, **12**, 203-212.

[64] C. Marraccini, G. Farruggia, M. Lombardo, L. Prodi, M. Sgarzi, V. Trapani, C. Trombini, F. I. Wolf, N. Zaccheroni and S. Iotti, *Chem. Sci.*, 2012, **3**, 727-734.

[65] L. H. Lindenburg, J. L. Vinkenborg, J. Oortwijn, S. J. A. Aper, M. Merkx, *PLOS ONE.*, 2013, **8**, e82009-e82009

[66] H. Komatsu, N. Iwasawa, D. Citterio, Y. Suzuki, T. Kubota, K. Tokuno, Y. Kitamura, K. Oka and K. Suzuki, *J. Am. Chem. Soc.,* 2004, **126**, 16353-16360.

[67] D. M. Egelman and P. R. Montague, *J. Neurochem.,* 1998, **18**, 8580.

[68] A. Sargenti, G. Farruggia, N. Zaccheroni, C. Marraccini, M. Sgarzi, C. Cappadone., E. Malucelli, A. Procopio, L. Prodi, M. Lombardo and S. Iotti. *Nat. Protoc.,* 2017, **12**, 461-471.

[69] L. Zhao, Y. Liu, C. He, J. Wang and C. Duan, *Dalton Trans.*, 2014, **43**, 335-343.

[70] L. A. Levy, E. Murphy, B. Raju and R. E. London, *Biochemistry.*, 1988, **27**, 4041-4048.

[71] S. Iotti, C. Frassineti, L. Alderighi, A. Sabatini, A. Vacca and B. Barbiroli, *J Magn Reson Imaging*, 2000, **18**, 607-614.

[72] M Bottrill, L. Kwok and N. J. Long, *Chem. Soc. Rev.*, 2006, **35**, 557-571

[73] P Caravan, *Chem. Soc. Rev.*, 2006, **35**, 512-523.

[74] W-H Li, S. E. Fraser and T. J. Meade, *J. Am. Chem. Soc.*, 1999, **121**, 1413-1414.

[75] A. Mishra, P. Fouskova, G. Angelovski, E. Balogh, A. K. Mishra, N. K. Logothetis and E. Toth. *Inorg. Chem.,* 2008, **47**, 1370-1381.

[76] K. Dhingra, M. E. Maier, M. Beyerlein, G. Angelovski and N. K. Logothetis, *Chem. Commun.,* 2008, 3444 – 3446.

[77] H. Hifumi, A. Tanimoto, D. Citterio, H. Komatsu and K. Suzuki, *Analyst.*, 2007, **132**, 1153-1160.

[78] S. Abada, A. Lecointre., M. Elhabiri, D. Esteban-Gomez, C. Platas-Iglesias, G. Tallec, M. Mazzanti and L. J. Charbonniere. *Chem. Commun.*, 2012, **48**, 4085-4087.

2. Synthesis of Carboxylate and Phosphinate Ligands

2.1 Introduction

A number of factors must be considered when choosing and designing ligands for selective metal-binding applications. Some of these include the chelate effect, the Hard-Soft Acid-Base theory (HSAB) and ligand denticity.

The chelate effect highlights the greater stability of complexes formed with polydentate and macrocyclic ligands compared with those containing the equivalent number of monodentate ligands.[1] The higher stability arises from an enthalpic and entropic advantage of chelation, that makes the formation of metal complexes with bidentate ligands more thermodynamically favourable than complexes with the equivalent number of monodentate ligands. This can be demonstrated by comparing the reaction of Cd^{2+} with monodentate ammonia and bidentate ethylenediamine (en) (**Table 2.1**).[2]

$$[Cd(H_2O)_6]^{2+}_{(aq)} + 2NH_{3\,(aq)} \rightleftharpoons [Cd(NH_3)_2(H_2O)_4]^{2+}_{(aq)} + 2H_2O_{(l)} \text{ (Monodentate)}$$

$$[Cd(H_2O)_6]^{2+}_{(aq)} + en_{(aq)} \rightleftharpoons [Cd(en)(H_2O)_4]^{2+}_{(aq)} + 2H_2O_{(l)} \text{ (Bidentate)}$$

Table 2.1 Example of the chelate effect and the increase in stability of complexes formed when a polydentate ligand such as en is coordinated to a Cd^{2+} metal ion.[2] ΔG was calculated at 298 K using the equation: $\Delta G = \Delta H - T\Delta S$.

Complex	ΔG (kJ mol^{-1})	ΔH (kJ mol^{-1})	ΔS (J K^{-1} mol^{-1})
$[Cd(en)(OH_2)_4]^{2+}_{(aq)}$	–33.3	–29.4	+13.0
$[Cd(NH_3)_2(OH_2)_4]^{2+}_{(aq)}$	–28.3	–29.8	–5.2

5- and 6-membered rings are the most common chelate ring sizes formed. They are formed more favourably over 3- and 4-membered rings due to a more favourable bite angle around the metal ion generating less ring strain. Preference in chelate ring size varies from metal to metal, with larger metal ions of high coordination number favouring a 5-membered ring chelate, while smaller metal ions with a low coordination number have been found to favour 6-membered.[3]

Tuning the size of the chelate ring size can therefore improve metal binding selectivity.

The choice of donor group is also critical to the formation of stable complexes. The HSAB is a model that helps to rationalise ligand to metal binding affinities. It states that hard metals favour the binding of hard ligands; likewise, soft metals favour the binding of soft ligands. Mg^{2+} is a small, non-polarisable, hard, divalent cation that forms stable complexes with hard ligands or bases, such as oxygen and nitrogen donor groups. A selection of hard and soft acids and bases is highlighted in **Table 2.2**.

Table 2.2 Examples of hard and soft acids and bases, in the context of metal ions and ligands respectively.[4]

	Hard	**Soft**
Metal ions	Li^+, Na^+, Mg^{2+}, Ca^{2+}, Zn^{2+}	Ag^+, Au^+, Pd^{2+}, Pt^{2+}
Ligands	F^-, Cl^-, H_2O, COO^-, NH_3, RNH_2	I^-, HS^-, CN^-, PR_3

Ligand denticity is also an important factor to consider in ligand design, affecting the selectivity with which a ligand binds to metal ions. For example, Mg^{2+} (ionic radius = 72 pm in coordination number six)[2] commonly forms 5- and 6-coordinate complexes, while the larger Ca^{2+} ion (ionic radius = 100 pm in coordination number six, 112 pm in coordination number eight)[2] tends to form stable 8-coordinate complexes, e.g. those formed with the ligand BAPTA (**Figure 2.1**).[5]

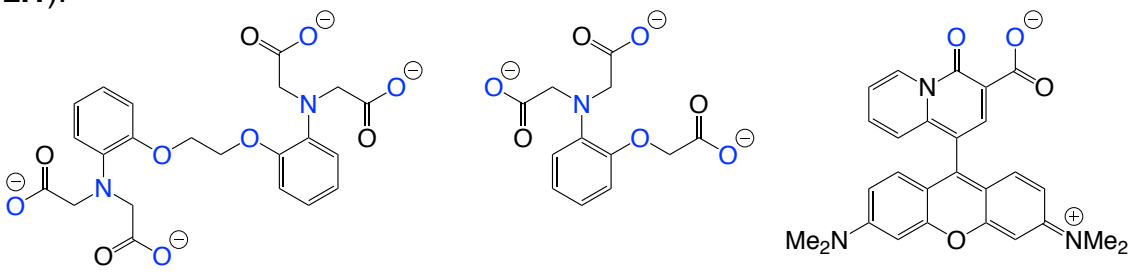

A) BAPTA **B) APTRA** **C) KMG-310**

Figure 2.1 Structures of (**A**) BAPTA (octadentate),[5] (**B**) APTRA (pentadentate)[6,10] and (**C**) bidentate β-keto-acid KMG-301.[7]

By changing the ligand denticity, it is possible to change the Mg^{2+} / Ca^{2+} selectivity. This is evident from the comparison of the APTRA binding site (pentadentate with Mg^{2+})[6] and the bidentate β-keto-acids (bidentate with Mg^{2+}) (**Figure 2.1**).[7] β-Keto-acids have been found to be more selective towards Mg^{2+}, due in part to the larger Ca^{2+} ion favouring binding to a ligand with a denticity greater than two. Buccella and co-workers further highlighted this idea in 2016, showing that Ca^{2+} ions prefer to form complexes with a higher coordination number than Mg^{2+}.[6] From X-ray crystallographic data it was found that APTRA binds Mg^{2+} in a pentadentate fashion with the sixth coordination site of Mg^{2+} in the solid state coming from a bridging carboxylate from an adjacent complex.[6] Ca^{2+} ions in contrast, form an 8-coordinate, dimeric species in the solid state $[Ca(OH_2)_3]_2\{[APTRA)Ca(OH_2)_2](\mu\text{-}H_2O)_2\}Cl_2$.[6] Ligands with a lower denticity inherently favour the binding of the smaller Mg^{2+} ion over the larger Ca^{2+} ion.

In this chapter the synthesis of a number of analogues of the APTRA binding framework will be discussed containing carboxylate and phosphinate binding groups. It was decided that ligands with a high denticity such as those in the APTRA series (pentadentate) would be studied throughout, in order to avoid the problems associated with formation of mixed species, which is characteristically observed with the bidentate β-keto-acids *in vivo* (highlighted in **Section 1.5.3**). It also presents the increased possibility of structural modification, allowing a range of ligands to be synthesised containing different binding groups.

2.2 Synthesis of Carboxylate Ligands

Carboxylate-based ligands have been used extensively in organic synthesis for selective ion binding. EDTA has been used to sequester metal ions such as Fe^{3+}, while Tsien and co-workers have developed numerous carboxylate based ligands such as BAPTA[5] and Fura-2[8] for selective binding to Ca^{2+}. Sensors for Mg^{2+} are no different, with the two main binding groups in the literature the APTRA chelators and the β-keto acids also containing hard carboxylate binding groups.

Target carboxylate ligands are based upon the APTRA binding unit, first developed during the late 1980's by London *et al.* which are thought to form [5, 5, 5] chelates with divalent metal ions (**Figure 2.2**). *tert*-Butyl and ethyl esters of ligands $\mathbf{L^1}$ and $\mathbf{L^2}$ vary only in the position of the nitrogen and oxygen donor atoms around the aromatic ring. Once conjugated into a luminescence system, and hydrolysed to their carboxylic acids, the difference in the position of the nitrogen and oxygen donor groups could potentially result in a different luminescence response, and differing selectivity and affinity towards different divalent cations such as Mg^{2+}, Ca^{2+} and Zn^{2+}.

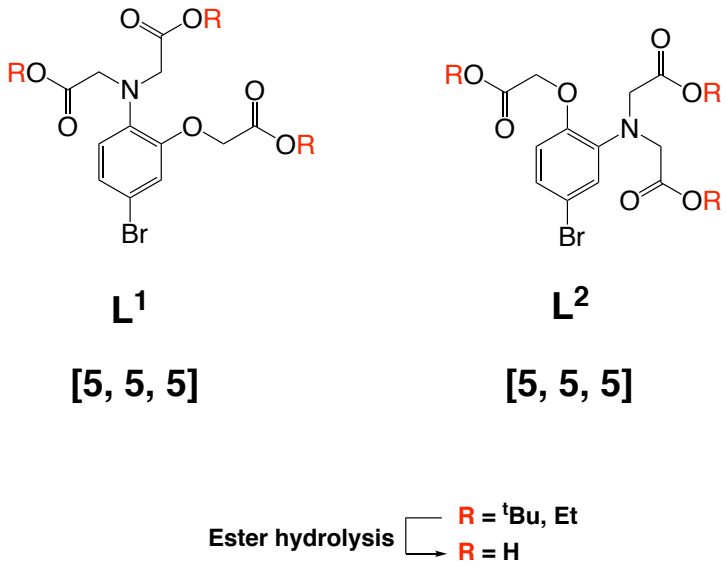

Figure 2.2 Target APTRA based *tert*-butyl and ethyl esters $\mathbf{L^1}$ and $\mathbf{L^2}$. The expected chelate ring size formed on coordination with Mg^{2+} is highlighted in bold. A pentadentate denticity of both ligands is expected around a divalent cation.

2.2.1 Synthesis of L^1 from *o*-aminophenol

A number of different methods are available for the synthesis of APTRA ligands, the method of choice being alkylation of an *o*-aminophenol precursor. A variety of conditions has been examined in the literature using a number of different bases and solvents. The original APTRA ligands synthesised by London and co-workers used alkylation conditions of methyl bromoacetate and proton sponge, heating under reflux in acetonitrile.[9-11] More recently, Dehaen *et al.* employed an alternative strategy, by alkylating *o*-aminophenol with chloroacetic

acid and sodium hydroxide in water (with a pH between 10 and 11), before re-esterifying with methyl- or ethyl bromoacetate.[12]

In the case of pro-ligands **L**^{1} and **L**^{2}, however, alkylation of *o*-aminophenols was carried out with both *tert*-butyl bromoacetate and ethyl bromoacetate heated at reflux in acetonitrile with *N,N*-diisopropylethylamine (Hünig's base), in a method adapted from Sando and co-workers.[13] The generation of both *tert*-butyl and ethyl esters allows both the acidic and basic ester hydrolysis to be carried out, subsequently.

Alkylation of commercially available *o*-aminophenol with *tert*-butyl and ethyl bromoacetate formed (**1**) and (**2**) after heating at reflux in acetonitrile for 4 days. Moderate yields were achieved after purification by silica gel column chromatography (**Scheme 2.1**).

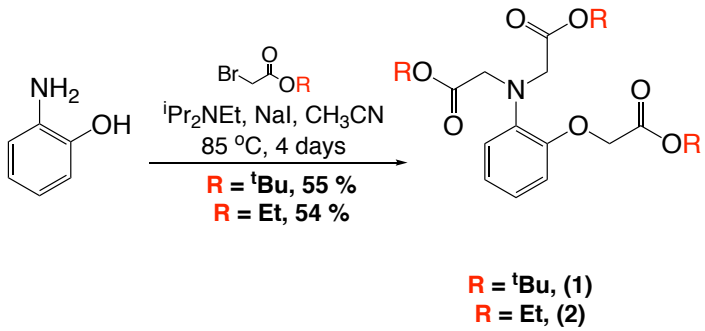

Scheme 2.1 General procedure for the synthesis of *tert*-butyl and ethyl esters (**1**) and (**2**).

Bromination of (**1**) and (**2**) was achieved with a unique tribromide salt of 18-crown-6, [K18-Crown-6]Br_3 (**3**). Compound (**3**) was formed in high yields from the reaction of 18-crown-6 with potassium bromide and Br_2 at room temperature, in a reaction first carried out by Ward and co-workers (**Scheme 2.2**).[14]

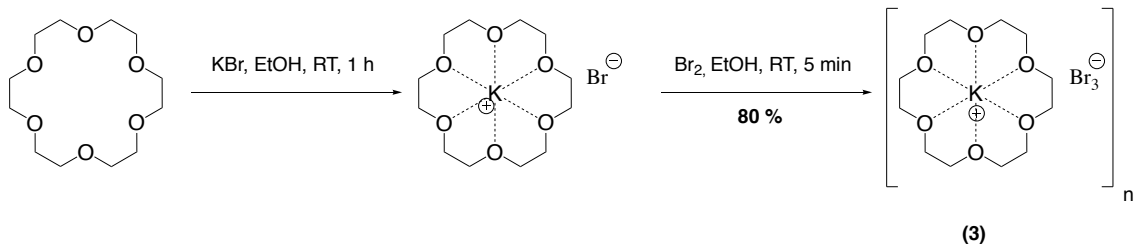

Scheme 2.2 The formation of [K.18-Crown-6]Br_3, (**3**) a tribromide salt used for the selective bromination of aromatic amines.[14]

Compound (**3**) can be used for the selective *para*-bromination of a range of aromatic amines, and is viewed as a safer alternative to the use of elemental Br_2 itself. The esters (**4**) and (**5**) were synthesised in moderate to high yields under mild conditions, with the reaction taking 1 to 2 h to reach completion (**Scheme 2.3**). Purification of (**4**) and (**5**) was achieved using an aqueous wash of a saturated solution of sodium bicarbonate to remove residual 18-crown-6, before purification by column chromatography.

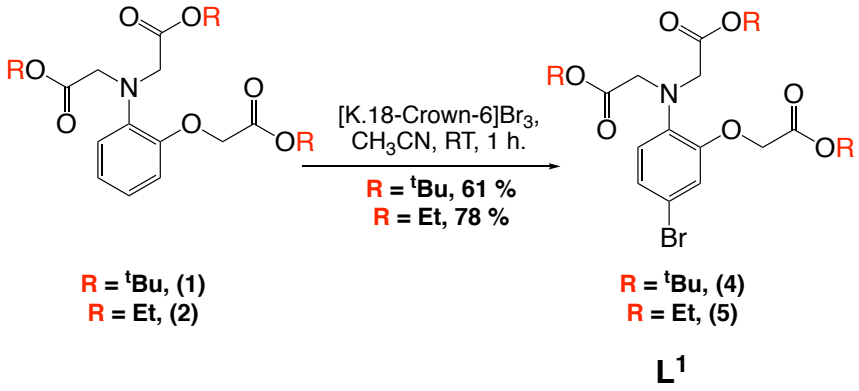

Scheme 2.3 General procedure for the selective bromination of *tert*-butyl and ethyl esters of $\mathbf{L^1}$ using [K.18-Crown-6]Br_3.

2.2.2 Synthesis of L^2 from 2-amino-4-bromophenol

The *tert*-butyl and ethyl protected esters (**7**) and (**8**) were synthesised in a similar manner to (**1**) and (**2**) under the same conditions, but starting from commercially available 2-amino-4-bromophenol (**Scheme 2.4**). In this instance, selective di-alkylation of the amine was achieved overnight forming (**6**), with no evidence of any O-alkylation after heating at reflux for 24 h as revealed by ESI-MS or ^{1}H NMR spectroscopy. Full conversion to (**7**) and (**8**) was achieved under the same conditions albeit with much longer reaction times of 5 to 7 days.

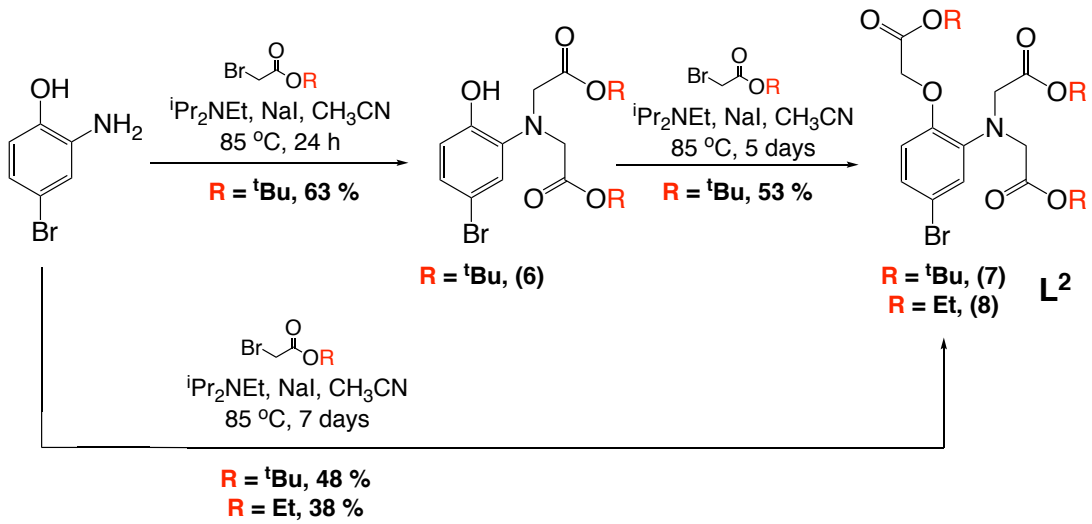

Scheme 2.4 General procedure for the synthesis of *tert*-butyl and ethyl esters of **L**^{2}.

It was observed with the formation of (**1**) and (**2**) that O-alkylation was slow under the conditions used (Hünig's base in acetonitrile). The formation of (**7**) and (**8**) is unsurprisingly no different with O-alkylation requiring several days even when 8-10 equivalents of the alkylating agent was used.

In order to increase the reaction rates and yields, other conditions were attempted. It was observed, however, for the O-alkylation of (**6**) with both sodium hydride in THF, and potassium carbonate in acetonitrile, that on heating cyclisation occurred to form a 6-membered lactone, with the loss of *tert*-butoxide. Under each set of conditions only the cyclised product (**9**) was detected, with no evidence of any O-alkylation taking place as deduced by either ESI-MS and ^{1}H NMR spectrometry (**Scheme 2.5**). The direct O-alkylation of (**6**) is apparently not feasible under these conditions.

The reaction was repeated at room temperature using the same equivalents of reagents to determine whether cyclisation could be prevented. Longer reaction times were expected, but, after two days at room temperature, only starting material was evident from ESI-MS, with no evidence of either (**7**) or (**9**) forming.

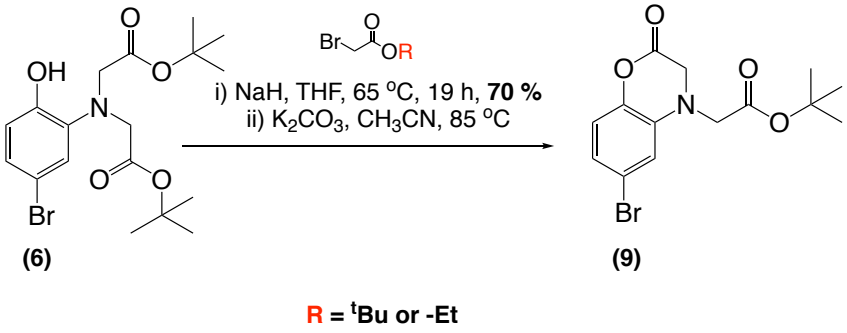

Scheme 2.5 The cyclisation of (**6**), upon attempted alkylation under the conditions: i) NaH, THF and ii) K_2CO_3, CH_3CN.

2.3 Synthesis of Phosphinate Ligands

A number of ligands bearing phosphinate groups have been used previously to study metal ion binding. Macrocyclic-based phosphinate ligands, developed by Parker and co-workers in the 1990's, were found to form complexes with a range of divalent cations (Zn^{2+}, Co^{2+}) and trivalent cations (Fe^{3+} and Ga^{3+}) (**Figure 2.3**).[15] Analogues of these macrocycles have been used as probes for $^{68}Ga^{3+}$ in positron emission tomography (PET).[16]

Phosphonate ligands have also been synthesised to bind to metal ions, in particular ethylenediamine tetra(methylene phosphonic acid) (EDTMP) an analogue of EDTA (**Figure 2.3**). Once coordinated to samarium-153, EDTMP has been used extensively as an anti-cancer drug to treat pain associated with bone metastases.[17]

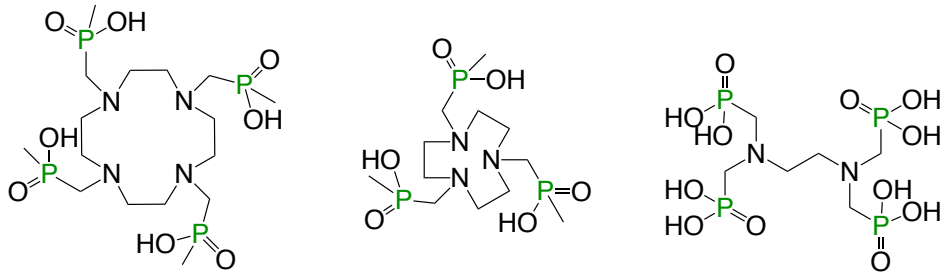

Figure 2.3 (**A**) and (**B**) phosphinate based macrocyclic ligands developed by Parker and co-workers for metal ion binding,[15] (**C**) EDTMP, the phosphonic acid derivative of EDTA.

Acyclic ligands containing phosphinate groups for metal ion binding are few and far between, and to our knowledge no fluorescence sensors containing a phosphinate binding moiety have been reported for the selective binding of Mg^{2+}. This is somewhat surprising, as phosphate groups such as those in ATP bind cellular Mg^{2+} strongly due to its high abundance and binding affinity (K_d ~78 μM).[18]

The synthesis of a number of phosphinate-based target ligands will be discussed here. Each contains one phosphinate binding group and the ability to adopt different chelate ring sizes on binding of divalent metal ions, and form complexes with a different ligand denticity (either tetradentate or pentadentate) on the binding of metal ions (**Figure 2.4**). After the incorporation into luminescence-based systems, a direct comparison will be made to the carboxylate-based ligands synthesised in **Section 2.2**. It will be determined what effect the introduction of a phosphinate group and changing the chelate ring size will have on the Mg^{2+} / Ca^{2+} binding affinity and selectivity.

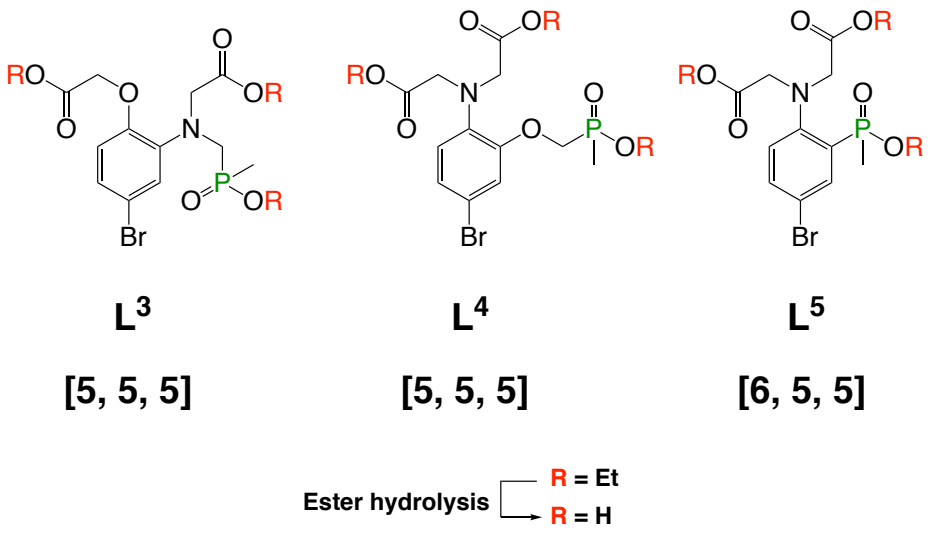

Figure 2.4 Target phosphinate analogues of APTRA $\mathbf{L^3}$, $\mathbf{L^4}$ and $\mathbf{L^5}$. The expected chelate ring size formed on coordination with Mg^{2+} is highlighted in bold. Pro-ligands $\mathbf{L^3}$ and $\mathbf{L^4}$ expected pentadentate binding, $\mathbf{L^5}$ expected tetradentate binding to Mg^{2+}.

2.3.1 Synthesis of a [5, 5, 5] phosphinate ligand by N-alkylation, L^3

The first step towards the synthesis of the ethyl ester of $\mathbf{L^3}$ is the synthesis of the phosphinate-based mesylate alkylating agent (**12**), which was formed from

a three-step procedure from diethyl methylphosphonite (**Scheme 2.6**). A reaction with one equivalent of water at room temperature formed ethyl methylphosphinate (**10**), with one equivalent of ethanol. Intermediate (**11**) was synthesised from a condensation reaction of (**10**) with paraformaldehyde in THF in a modest yield, before the alcohol was mesylated with methylsulfonyl chloride in the presence of triethylamine at room temperature to give (**12**) in quantitative yield.

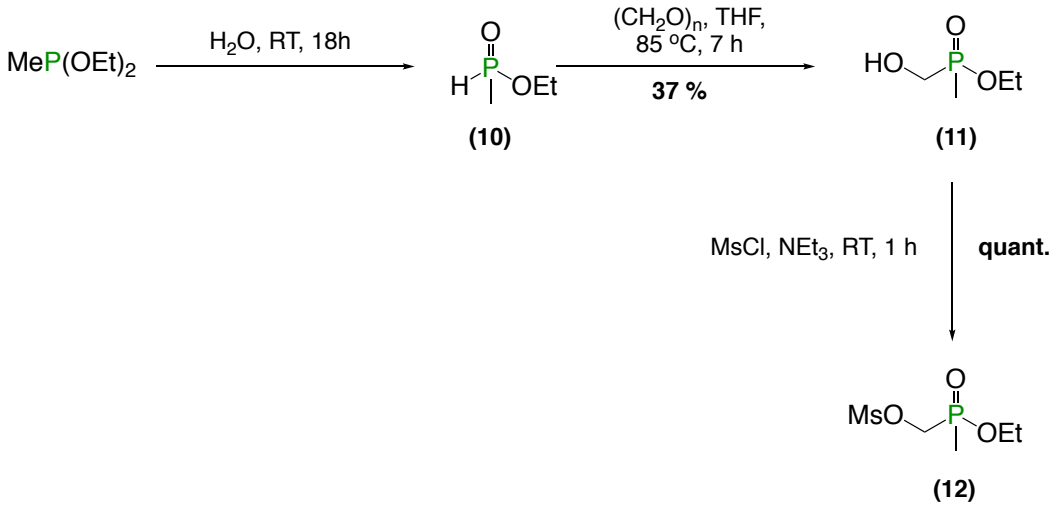

Scheme 2.6 The three-step synthesis of the mesylate (**12**), from diethyl methylphosphonite.

The introduction of the mesylate group allows (**12**) to be used as an alkylating agent in nucleophilic substitution reactions, providing the opportunity for the introduction of phosphinate groups onto aromatic systems.

Alkylation of 2-amino-4-bromophenol with (**12**) was very slow using the conditions that were reported for the alkylation of both 2-aminophenol and 4-bromo-2-aminophenol with *tert*-butyl and ethyl bromoacetate (**Scheme 2.7**). Evidence for mono-alkylation only was observed in ESI-MS and the ^{31}P NMR spectrum.

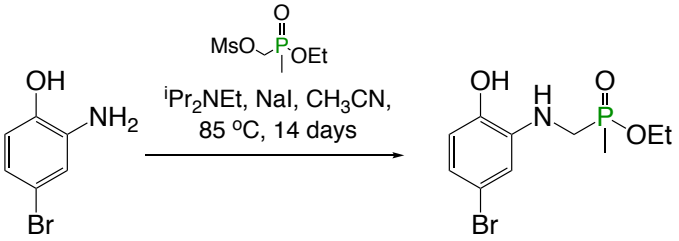

Scheme 2.7 The alkylation of 4-bromo-2-amino phenol with (**10**).

The hydrolysis of the mesylate (**12**) was observed over the course of the reaction, re-forming the alcohol (**11**) (**Figure 2.5**). The slow rate of mono-alkylation could be due to both competitive hydrolysis of the mesylate starting material and because (**12**) is a much weaker electrophile than the carboxylate based *tert*-butyl and ethyl bromoacetate.

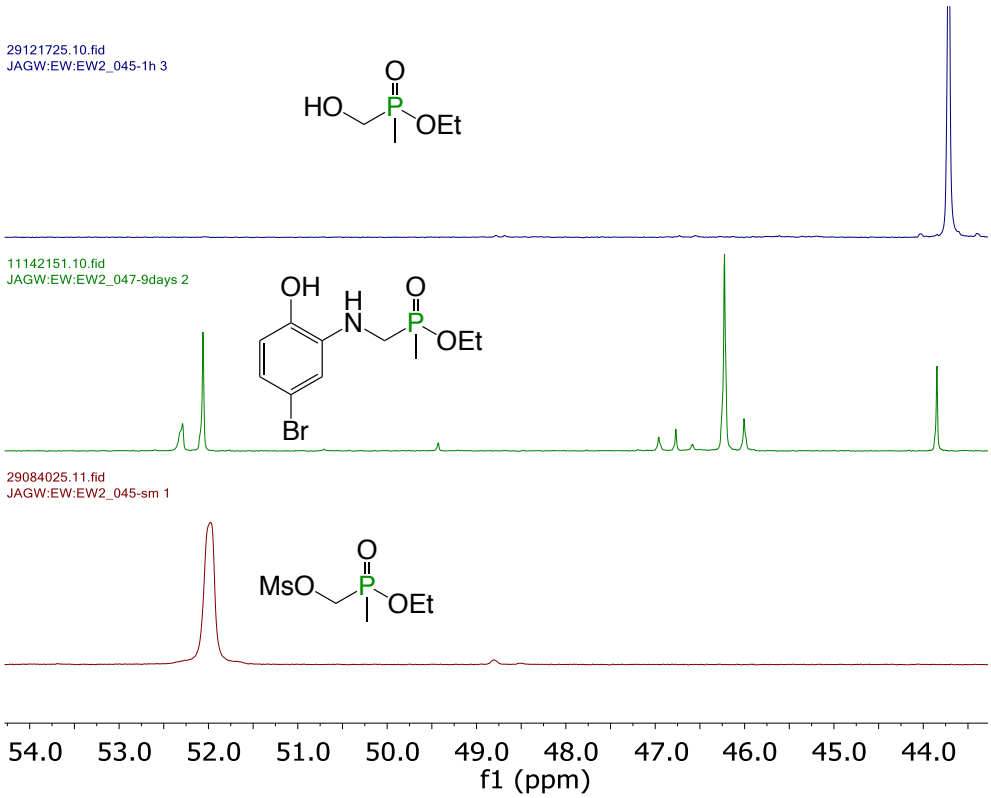

Figure 2.5 ^{31}P NMR spectra illustrating the attempted alkylation of 2-amino-4-bromophenol with the mesylate (**12**) ($CDCl_3$, 162 MHz, 298 K).

The Arbuzov reaction of diethyl methylphosphonite with paraformaldyde in THF was seen as an alternative method to alkylation for the introduction of phosphinate binding groups. Such an approach has been used successfully in

Durham, for the introduction of phosphinate groups onto cyclen (12-N_4) and 9-N_3 based macrocyclic ligands.[15] The reaction with 2-amino-4-bromophenol was unsuccessful, however, with only starting material present in the ESI-MS and ^{1}H NMR spectrum after heating at 85 ^{o}C overnight (**Scheme 2.7**).

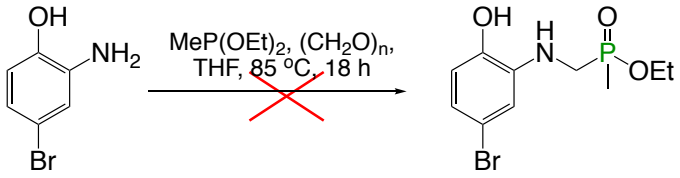

Scheme 2.7 Attempted Arbuzov reaction between methyl diethylphosphinite and 4-bromo-2-aminophenol.

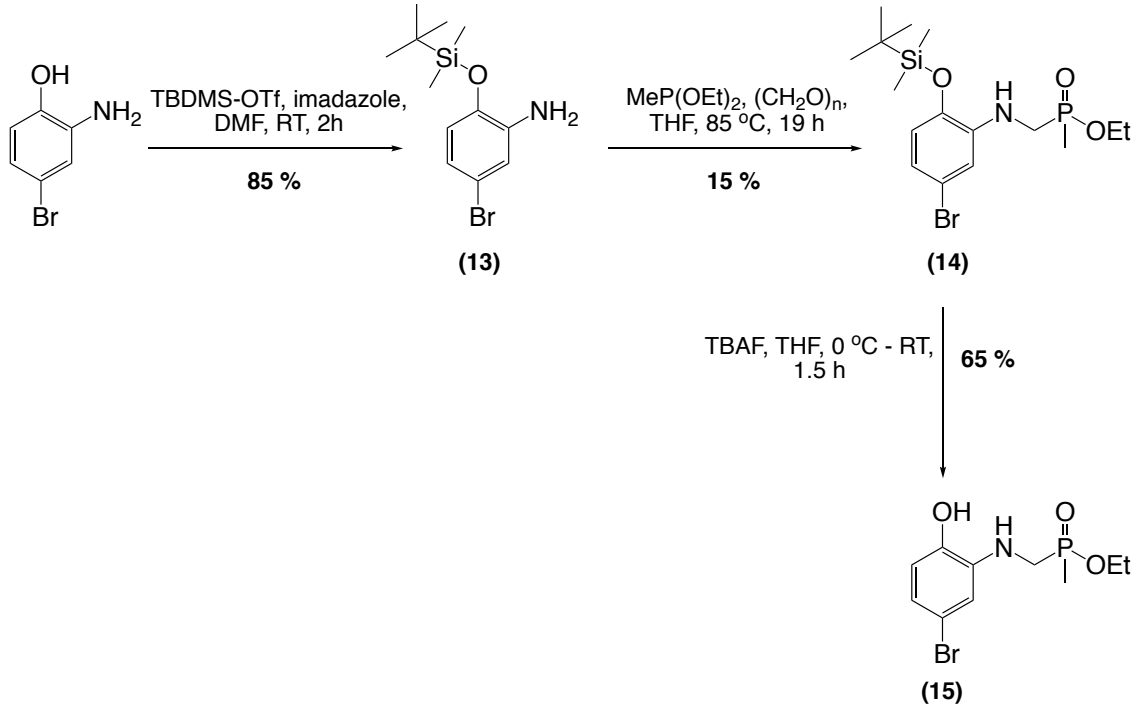

Scheme 2.8 The synthetic approach for the formation of intermediate, (**15**).

An alternative synthetic approach was designed, where the phenol substituent was first protected as a *tert*-butyldimethyl silyl ether (**Scheme 2.8**). Silyl protection was carried out under mild conditions in high yield. The resulting Arbuzov condensation was successful with (**13**), forming (**14**), albeit in low yield. These observed low yields could be ascribed to the presence of the sterically demanding *ortho*-substituted silyl ether. Silyl de-protection was achieved using

tetrabutylammonium fluoride (TBAF) in THF at room temperature, producing (**15**) in a moderate, but acceptable, yield after purification by column chromatography.

Alkylation of (**15**) resulted in the formation of a mixture of compounds, including O-alkylation, N-alkylation and cyclisation products (**Scheme 2.9**). It was found that these products could not be separated by conventional chromatography due to close, if not identical, R_f values in a range of commonly used solvent systems. Reverse phase HPLC was also attempted. The desired product (**L**^{3}) was, however, not isolated directly as co-elution with the cyclised product was observed.

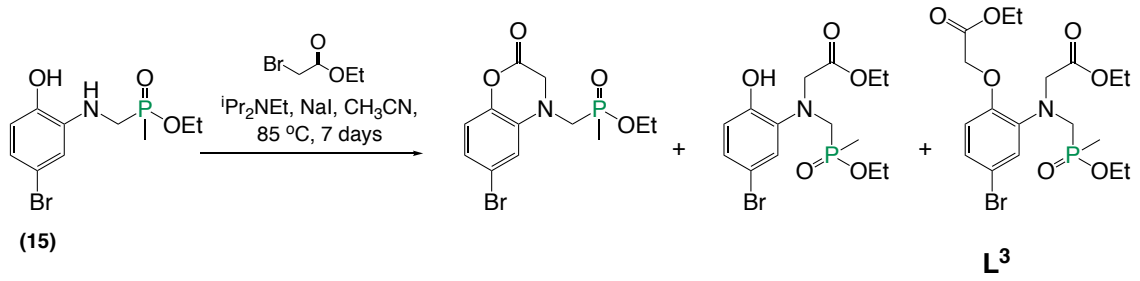

Scheme 2.9 The mixture of products formed after the alkylation of (**15**).

The introduction of phosphinate groups via N-alkylation is, therefore, not straightforward due to the problems encountered along the multistep synthetic pathway.

2.3.2 Synthesis of a [5, 5, 5] phosphinate ligand by O-alkylation, L^4

Due to the problems associated with introducing the phosphinate group via N-alkylation (**Section 2.3.1**), an alternative strategy was attempted, where the phosphinate group is introduced in the first step of the reaction sequence by O-alkylation. The greater nucleophilicity of aromatic amines over phenol groups meant that the amine must either be protected, or introduced at a later stage from other functional groups such as nitro substituents.

The synthesis of the ethyl ester of **L**^{4} was achieved from the O-alkylation of commercially available 2-nitrophenol using (**12**) as the mesylate-based alkylating agent (**Scheme 2.10**). Alkylation of 2-nitrophenol in acetonitrile with

(**12**) and potassium carbonate as the base formed (**16**) in moderate yield after purification by column chromatography. Reaction completion was determined from a colour change from bright orange to pale brown, highlighting the consumption of the 2-nitrophenoxide salt.

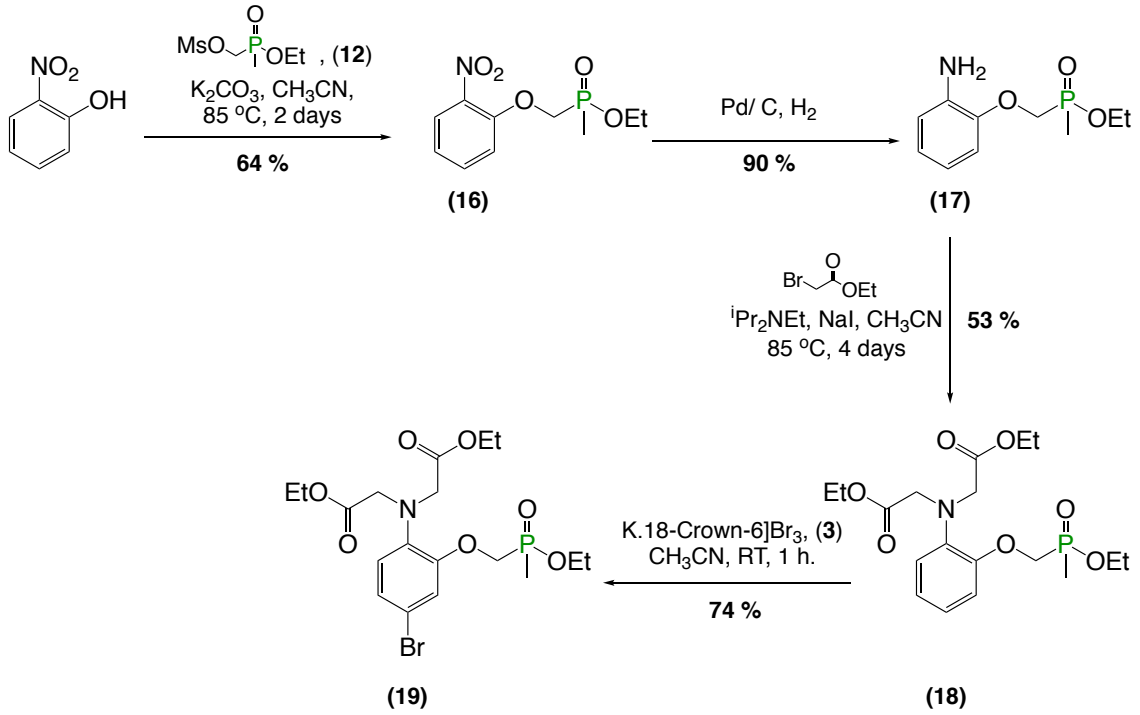

Scheme 2.10 The synthesis of the ethyl ester of $\mathbf{L^4}$, (**19**).

Reduction of the nitro group was accomplished via hydrogenation using hydrogen gas catalysed by palladium on carbon (Pd / C), forming the amine (**17**) in high yield. Alkylation of (**17**) was achieved under the same conditions used for 2-aminophenol and 2-amino-4-bromophenol with ethyl bromoacetate and Hünig's base. Reaction completion was determined by ESI-MS, when only the *N,N*-di-alkylated product could be detected after 4 days of heating at reflux. Treatment of (**18**) with [K.18-Crown-6]Br_3 (**3**), formed (**19**) in high yields after purification in a procedure identical to that reported previously (**Scheme 2.3**).

An alternative synthetic approach was attempted in order to see if O-alkylation of (**6**) could be achieved with the phosphinate alkylating agent (**12**). This approach would allow the formation of an alternative phosphinate-based ligand, an analogue of ($\mathbf{L^1}$-$\mathbf{L^4}$) where the bromine functionalisation is *para*- to the oxygen atom on the aromatic ring. Surprisingly, however, cyclisation was also

observed when the O-alkylation of (**6**) was attempted with (**12**) under the same conditions used successfully when either *tert*-butyl or ethyl bromoacetate were used as the alkylating agent (**Scheme 2.11**). The poorer electrophilicity of the phosphinate alkylating agent means that ring cyclisation is favoured over alkylation.

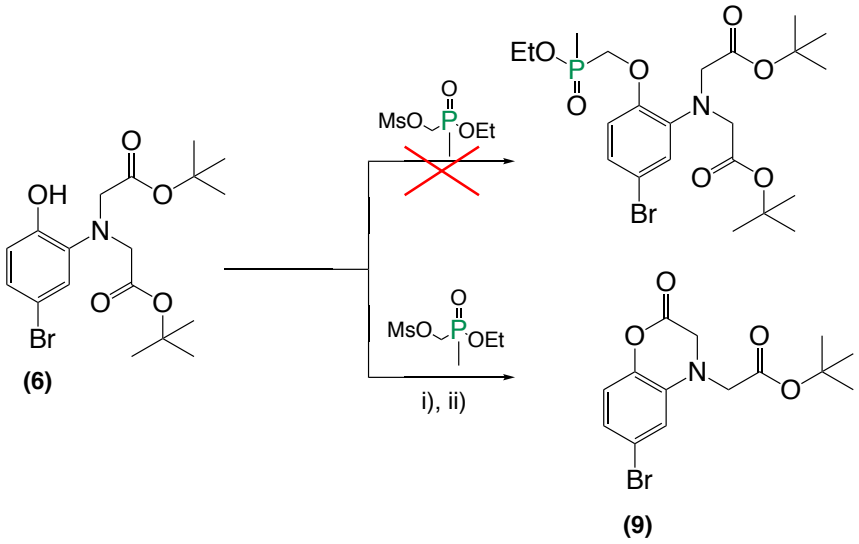

Scheme 2.11 The cyclisation of (**6**), upon attempted alkylation with (**12**). Conditions: i) K_2CO_3, CH_3CN, 85 ^oC and ii) Hünig's base, CH_3CN, 85 ^oC.

It was determined, therefore, that in the synthesis of phosphinate based ligands it is essential that the ethyl methylphosphinate group be introduced in the first step of the reaction sequence by O-alkylation. This eliminates the competitive kinetically favourable cyclisation reaction that has been observed consistently (**Scheme 2.5** and **2.9**).

It is also important to note that O-alkylation as the first step does not necessarily prevent cyclisation. Alkylation of 2-nitrophenol with *tert*-butyl bromoacetate forming (**20**), and subsequent hydrogenation, resulted in the spontaneous formation of (**21**). Cyclisation was seen to occur on standing at room temperature for a number of days, and was achieved in 1 h upon heating in acetonitrile at 85 ^oC (**Scheme 2.12**). Cyclisation didn't occur with the phosphinate compound (**17**) because such nucleophilic substitution reactions will not occur at a pentavalent phosphorus atom.

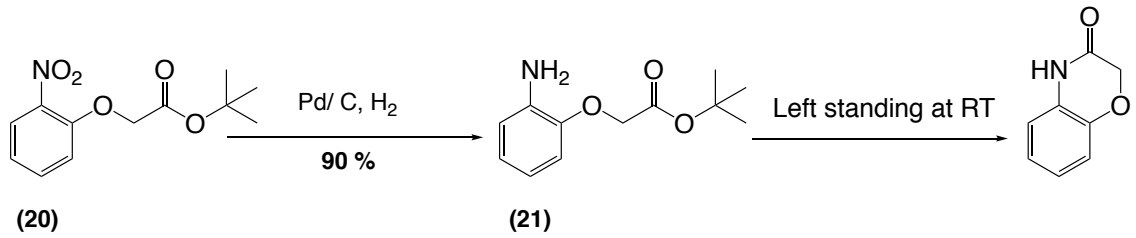

(20) **(21)**

Scheme 2.12 Showing spontaneous cyclisation of (**21**) at room temperature (RT = 298 K).

2.3.3 Synthesis of a [6, 5, 5] phosphinate ligand, L^5

Ligand L^5 differs significantly from the other ligands L^4 and L^5 bearing phosphinate binding groups discussed previously. Upon the binding of divalent cations such as Mg^{2+}, it is expected that a [6, 5, 5] chelate ring arrangement would form, in contrast to the [5, 5, 5] chelate rings observed in the APTRA ligand series[8-10] bearing both carboxylate and phosphinate groups (**Figure 2.6**). The number of binding groups is also varied between (L^1-L^4) (expected pentadentate binding of Mg^{2+}) and L^5 (expected tetradentate binding of Mg^{2+}). These differences in denticity and ring size formed could dramatically change the binding selectivity of Mg^{2+} over Ca^{2+} and Zn^{2+}.

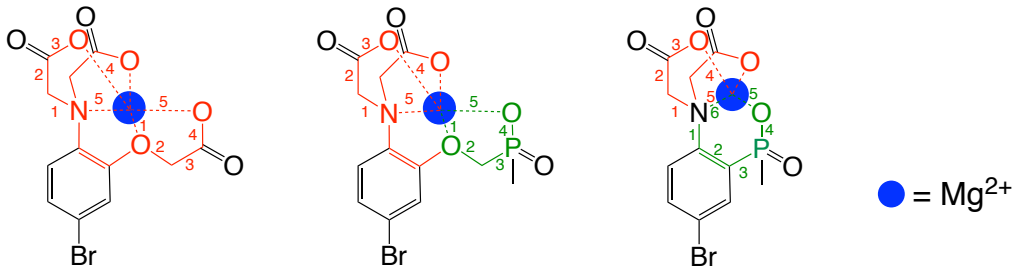

L^1 **L^4** **L^5**

[5, 5, 5] **[5, 5, 5]** **[6, 5, 5]**

Figure 2.6 The difference in the size of chelate ring formed on binding of Mg^{2+} to L^1, L^4 and L^5. Red highlights carboxylate ring, green highlights phosphinate ring.

The first step in the synthetic route of L^5 was the alkylation of commercially available 4-bromo-2-iodoaniline. It was found, however, that mono-alkylation occurred preferentially under a range of base and solvent combinations (**Scheme 2.13**, **Table 2.3**). Mono-alkylation using ethyl bromoacetate and

Hünig's base formed (**22**) in moderate yield after heating at reflux for 3 days (**Scheme 2.13** and **Scheme 2.14**). In each instance, the reaction was carried out with a significant excess of ethyl bromoacetate and Hünig's base, in order to drive the reaction towards completion. No trace of any *N,N*-di-alkylated product could be identified from ESI-MS and ^{1}H NMR analysis. The lack of reactivity observed could be due to the steric bulk of the *ortho*-iodo-substituent, preventing *N,N*-di-alkylation from taking place.

In order to successfully form the target pro-ligand $\mathbf{L^5}$ a number of alternative approaches were devised. It was hoped that *N,N*-di-alkylation could be carried out after alkylation of either: (**23**) (**Scheme 2.14**), or the phosphinate coupled product of 4-bromo-2-iodoaniline, ethyl (2-amino-5-bromo-phenyl) (methyl) phosphinate (**Scheme 2.13**).

Coupling of ethyl methylphosphinate (**10**) with the secondary amine (**22**) was achieved selectively in moderate yield, with triethylamine in toluene, using $[Pd(dppf)Cl_2]CH_2Cl_2$ as the catalyst. Alkylation of (**23**) was then undertaken using conditions identical to those used previously. It was thought that the introduction of an *ortho*-phosphinate group at the expense of a sterically bulky *ortho*-iodo-substituent would favour the second alkylation reaction to form the target proligand $\mathbf{L^5}$. A number of conditions were attempted, highlighted in **Table 2.3**, with a variety of reaction times and equivalents of the base and alkylating agent used. In each instance, however, only trace amounts of the *N,N*-di-alkylated product were detected in ESI-MS, none of which was isolated during various purification procedures.

The direct coupling of 4-bromo-2-iodoaniline with (**10**) was seen as the first step in another alterative synthetic pathway to the ethyl ester of $\mathbf{L^5}$ (**Scheme 2.13**). The reaction was, however, unsuccessful under the same conditions used for (**22**), with only starting material present after heating at reflux overnight. This made the alternative approach of phosphinate coupling before *N,N*-di-alkylation in the formation of the ethyl ester of $\mathbf{L^5}$ an unfeasible synthetic pathway (**Scheme 2.13**).

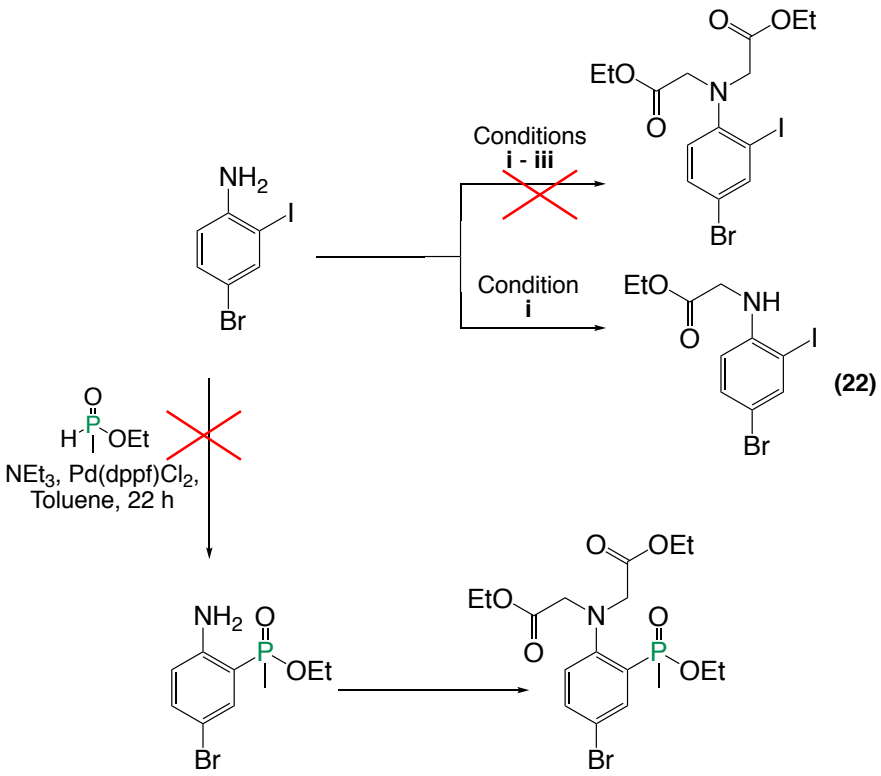

Scheme 2.13 Initial synthetic routes to the ethyl ester of $\mathbf{L}^5$. Conditions **i-iii** are highlighted in **Table 2.3**.

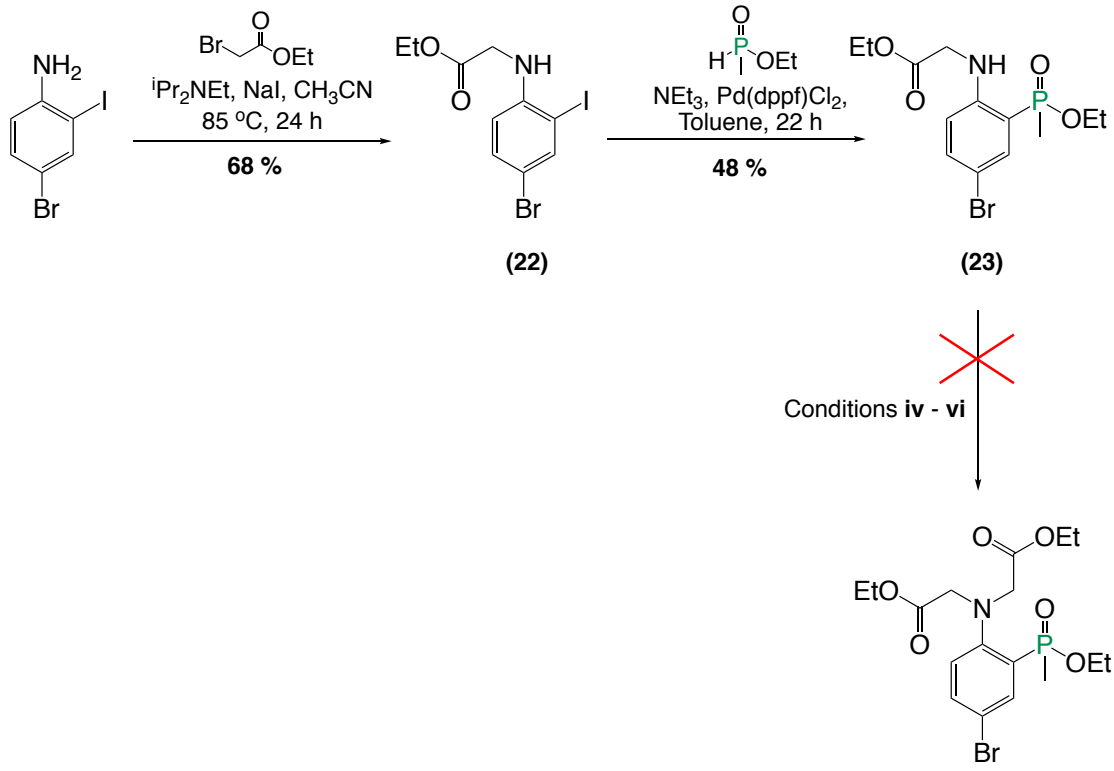

Scheme 2.14 The planned synthetic route to the ethyl ester of $\mathbf{L}^5$. Conditions **iv-vi** are highlighted in **Table 2.3**.

Table 2.3 Conditions **i-vi** used in the attempted synthesis of the ethyl ester of $\mathbf{L^5}$. Observations were made from both ESI-MS and ^{1}H NMR.

	Conditions	**Observations**
i	Ethyl bromoacetate, Hünig's base, NaI, CH_3CN, 3 days, 85 ^oC.	Complete conversion to (**20**) No starting material observed No *N,N*-di-alkylation observed.
ii	Ethyl bromoacetate, Cs_2CO_3, NaI, CH_3CN, 3 days, 85 ^oC.	Majority starting material Trace amounts of (**22**) < 5 % from crude NMR.
iii	Ethyl bromoacetate, NaH, NaI, DMF, 2 days, 60 ^oC.	Starting material, from ESI-MS.
iv	4 equiv. ethyl bromoacetate, Hünig's base, NaI, CH_3CN, 9 days, 85 ^oC.	Majority starting material Trace amounts of *N,N*-di-alkylated product – none isolated.
v	10 equiv. ethyl bromoacetate, Hünig's base, NaI, CH_3CN, 7 days, 85 ^oC.	Starting material
vi	Ethyl bromoacetate as the solvent, Hünig's base, 7 days, 85 ^oC.	Majority starting material Trace amounts of *N,N*-di-alkylated product – none isolated.

With all attempts to form $\mathbf{L^5}$ unsuccessful, the binding properties of tridentate (**23,** ethyl ester of $\mathbf{L^6}$) with Mg^{2+}, Ca^{2+} and Zn^{2+} will instead be reported in naphthalene-based systems. Upon ester hydrolysis (**23**) will form a [6, 5] ring chelate on coordination to divalent cations.

2.4 Conclusions of Synthetic Studies

A selection of ligands bearing carboxylate and phosphinate groups have been synthesised and characterised that form different chelate ring sizes on the binding of divalent cations, i.e. [5, 5, 5] vs. [6, 5].

Alkylation conditions involving the use of Hünig's base in acetonitrile were seen to be the most successful and were used throughout to introduce carboxylate binding groups. However, a large excess of the alkylating agent was required in most cases. Ligands $\mathbf{L^1}$ and $\mathbf{L^2}$ were synthesised as both their *tert*-butyl and ethyl esters from the commercially available 2-aminophenol and 2-amino-4-bromo-phenol respectively, in moderate overall yields (**Figure 2.7**).

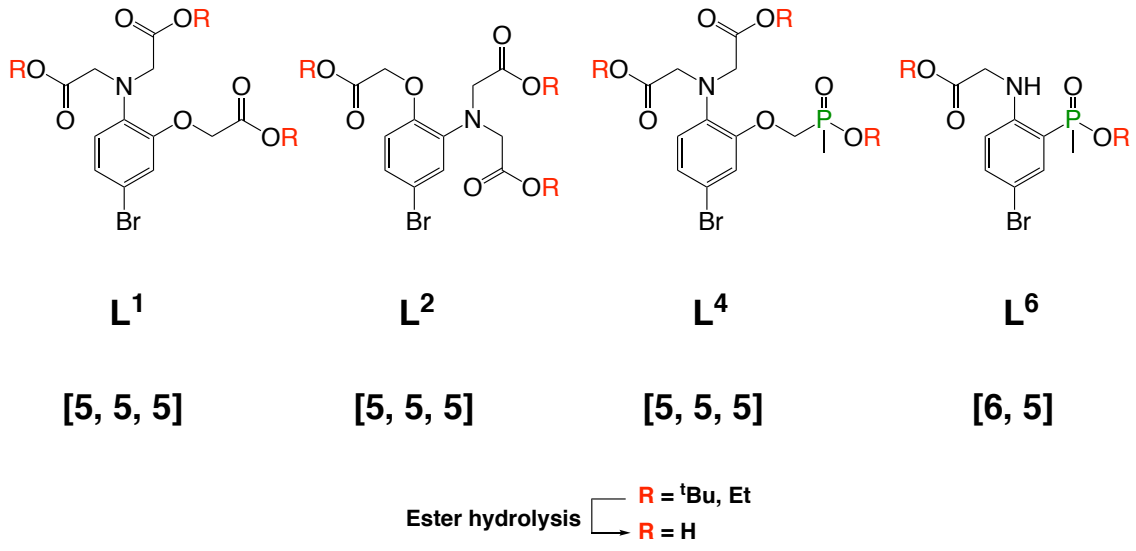

Figure 2.7 Functionalised ligands $\mathbf{L^1}$, $\mathbf{L^2}$, $\mathbf{L^4}$ and $\mathbf{L^6}$ synthesised during this chapter.

Novel phosphinate pro-ligands $\mathbf{L^4}$ and $\mathbf{L^6}$ were synthesised as their ethyl esters. The phosphinate group was introduced by one of two routes: by alkylation of 2-nitrophenol with (**10**) in the case of $\mathbf{L^3}$ and use of a palladium-catalysed cross-coupling reaction of (**22**) with (**10**) in the case of $\mathbf{L^6}$. The introduction of a phosphinate group by O-alkylation was found to prevent the competitive cyclisation reaction that occurred in the N-alkylation pathway or when O-alkylation was carried out after N-alkylation (**Scheme 2.9** and **Scheme 2.11** respectively).

A number of conditions (**iv–vi, Table 2.3**) were tried in an attempt to achieve *N,N*-di-alkylation of the ethyl ester of $\mathbf{L^6}$. In each of the conditions attempted, however, it was found that only trace amounts of the *N,N*-di-alkylated product were detected, none of which were isolated (**Scheme 2.14** and **Table 2.3**).

All pro-ligands $\mathbf{L^1}$, $\mathbf{L^2}$, $\mathbf{L^4}$ and $\mathbf{L^6}$ synthesised in this chapter have been functionalised with a bromine substituent on the aromatic ring. Functionalisation occurred either from commercially available starting materials or was introduced via a mild and effective bromination reaction, using the tribromide salt [K18-Crown-6]Br_3, (**3**).

In subsequent chapters, pro-ligands $\mathbf{L^1}$, $\mathbf{L^2}$, $\mathbf{L^4}$ and $\mathbf{L^6}$ will be incorporated into naphthalene-, lanthanide(III)- and ruthenium(II)-based luminescence systems to study the metal ion binding affinity and selectivity towards different divalent cations. Comparisons will be made between carboxylate and phosphinate binding groups to determine cation affinity and selectivity.

2.5 References

[1] A.E. Martell, *Adv. Chem. Ser.,* 1967, 62, 272-294.

[2] P. Atkins, T. Overton, J. Rourke, M. Weller and F. Armstrong, Inorganic Chemistry, Fifth Edition, 2010, Chapter 7, p. 218-219.

[3] R. D. Hancock, *J. Chem. Educ.,* 1992, **69**, 615-621.

[4] R. G. Pearson, *J. Am. Chem. Soc.*, 1963, **85**, 3533.

[5] R. Y. Tsien, *Biochemistry.*, 1980, **19**, 2396-2404.

[6] M. Brady, S. D. Piombo, C. Hu and D. Buccella., *Dalton Trans.*, 2016, **45**, 12458.

[7] T. Fujii, Y. Shindo, K. Hotta, D. Citterio, S. Nishiyama, K. Suzuki and K. Oka, *PLOS ONE.,* 2011, **6**, e23684.

[8] G. Grynkiewicz, M. Poenie and R. Y. Tsien, *Bio. Chem.,* 1985, **260**, 3440-3450.

[9] L. A. Levy, E. Murphy, B. Raju and R. E. London, *Biochemistry.*, 1988, **27**, 4041-4048.

[10] B. Raju, E. Murphy, L. A. Levy, R. D. Hall and R. E. London, *Am. J. Physical.,* 1989, **256**, 540-548.

[11] P. A. Otten, R. E. London, and L. A. Levy, *Bioconjugate Chem.,* 2001,**12**, 76-83.

[12] B. Metten, M. Smet, N. Boens and W. Dehaen, *Synthesis*, 2005, **11**, 1838-1844.

[13] R. Hata, H. Nonaka, Y. Takakusagi, I. Yoichi, K. Ichikawa and S, Sando, *Chem. Commun.*, 2015, **51**, 12290-12292.

[14] M. A. Zolfigol, G. Chehardoli, S. Salehzadeh, H. Adams and M. D. Ward, *Tetrahedron Lett.,* 2007, **48**, 7969-7973.

[15] E. Cole, R. C. B. Copley, J. A. K. Howard, D. Parker, G. Ferguson, J. F. Gallagher, B. Kaitner, A. Harrison and L. Royle, *J. Chem. Soc., Dalton Trans,* 1994, 1619-1629.

[16] J. Simecek, M. Schulz, J. Notni, J. Plutnar, V. Kubicek, J. Havlickova and P. Hermann, *Inorg. Chem.,* 2012, **51**, 577-590.

[17] R. Gallicchio, S. Giacomobono, A. Nardelli, T. Pellegrino, V. Simeon, D. Gattozzi, F. Maddalena, P. Mainenti and G. Storto, *J. Bone. Miner. Metab.*, 2014, **32**, 434-440.

[18] A. M. P. Romani, *Arch. Biochem. Biophys.*, 2011, **512**, 1-23.

3. APTRA vs. APDAP: A direct comparison

3.1 Introduction

The *o*-aminophenol-*N,N,O*-triacetic acid (APTRA) ligand developed by London has been used extensively in a range of metal ion binding applications.[1-4] It is known to bind 'free' Mg^{2+} in the low mM range, when incorporated into a wide range of fluorescence systems. Selectivity is an issue, however, with APTRA being more selective towards Ca^{2+} than Mg^{2+}. In order to get around the selectivity issues during cell studies, the cells are often pre-treated with highly selective Ca^{2+} sensors based on BAPTA, to eliminate any Ca^{2+} interference.[5]

The APTRA chelators were first reported nearly 40 years ago, yet there is still a remarkable lack of variety in ligand design for Mg^{2+} sensors in the literature. Bidentate β-keto acids have been found to have a higher selectivity towards Mg^{2+},[6, 7] but they can bind to both 'free' Mg^{2+} and $MgATP^{2-}$, limiting their use for *in vivo* applications.[8] It is critical, therefore, that a greater emphasis be put into the development of new ligand types for Mg^{2+}, in order to solve this selectivity conundrum.

This chapter explores the development of an alternative binding moiety for Mg^{2+}, namely *o*-aminophenol-*N,N*-diacetic acid phosphinate (APDAP). The APDAP ligand is structurally similar to APTRA with the introduction of a phosphinate group at the expense of a carboxylate binding group, maintaining a pentadentate denticity for divalent cations (**Figure 3.1**). It was hoped that this modification could improve the Mg^{2+} / Ca^{2+} selectivity, allowing the future possibility of determining Mg^{2+} concentrations in metal-rich cellular environments, such as the endo(sarco)plasmic reticulum. It is critical, however, to maintain the mM affinity that APTRA has for Mg^{2+}, with 'free' Mg^{2+} believed to be in the low mM range in the majority of cells (0.8 to 1.2 mM).[9]

The synthesis and characterisation of APDAP is reported here. Analysis of its pK_a and binding of Mg^{2+}, Ca^{2+} and Zn^{2+} via absorbance spectroscopy is also reported, with direct comparisons made to the absorbance binding studies undertaken on APTRA by Buccella *et al.*[10]

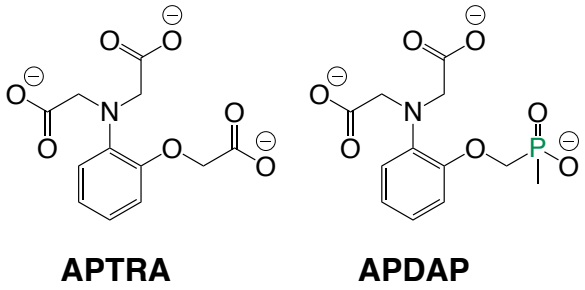

Figure 3.1 Pentadentate ligands APTRA and APDAP.

3.2 Synthesis and characterisation

The synthesis of APDAP (**24**), was achieved in a multi-step reaction sequence from commercially available 2-nitrophenol. The formation of (**18**) was reported in **Chapter 2** via a series of alkylation and hydrogenation reactions. Each step occurs in moderate to good yield, after purification.

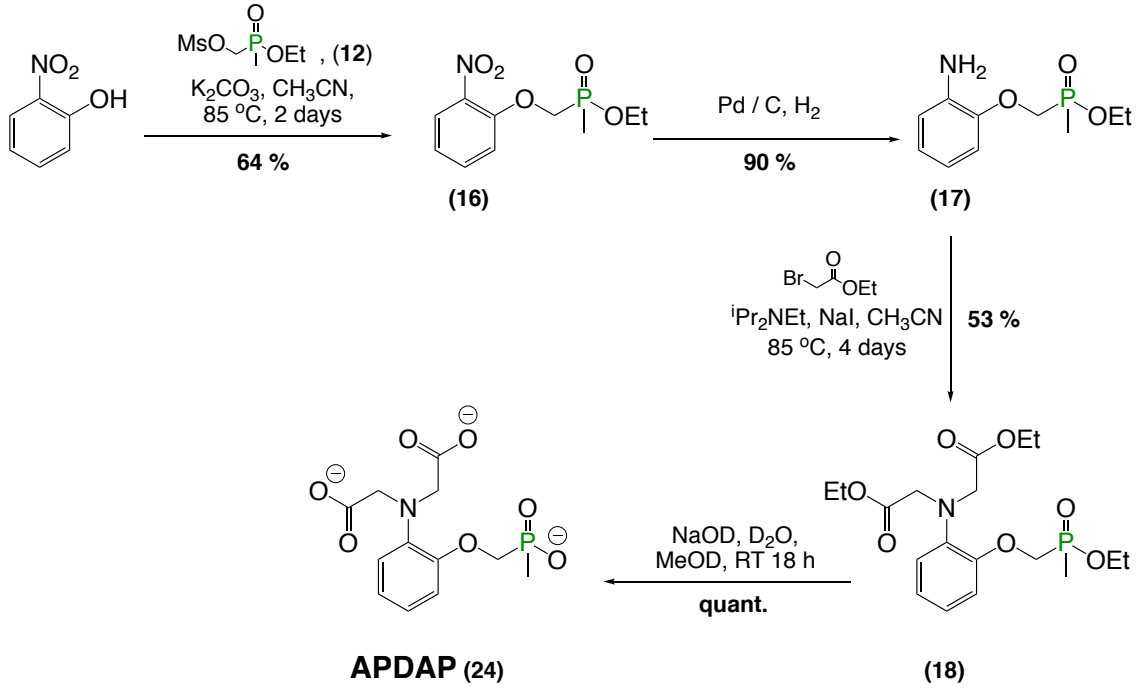

Scheme 3.1 The synthesis of **APDAP**, (**24**).

Ester hydrolysis of (**18**) was undertaken using sodium deuteroxide in D_2O and CD_3OD in quantitative yields. Deuterated solvents were used for the basic hydrolysis so that the course of the reaction could be monitored easily by ^{1}H NMR and ^{31}P NMR. A chemical shift change from 48.3 to 36.5 ppm in ^{31}P NMR

signalled that hydrolysis was complete. The purity of (**24**) was assessed by analytical HPLC, in an acetonitrile / ammonium bicarbonate buffered system.

3.3 APDAP pH studies

An investigation was undertaken to determine the effect of pH change on the absorbance spectrum of APDAP. Absorbance spectroscopy was used rather than fluorescence because APDAP shows only weak fluorescence at inconveniently high energy. An investigation via absorbance spectroscopy also allows a direct comparison to be made to APTRA absorbance studies in the literature.[10] APTRA analogues have been found previously to be rather unstable in solution due to successive decarboxylation and oxidation reactions.[10-11] These observations have resulted in the pK_a not being accurately determined in the majority of cases.[3, 5,6, 8, 10,12] Where pH studies have been made, a pK_a of 5.5 was determined using absorbance spectroscopy.[4]

In the case of APDAP, it was found that on protonation of the aniline nitrogen atom a decrease in the absorbance at 254 nm, 285 nm and an increase at 273 nm was observed over the pH range 4.5 to 8.5. A sigmoidal fit of the absorbance at 254 nm against the pH revealed a pK_a of 6.03(8) (**Figure 3.2**).

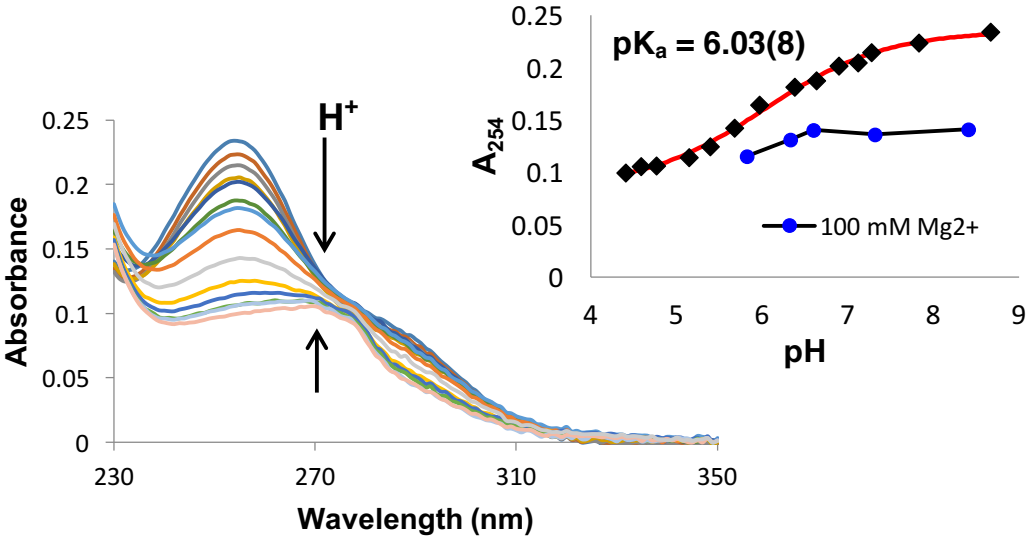

Figure 3.2 Absorbance pH titration of APDAP; the inset shows the sigmoidal fit of absorbance at 254 nm against pH with its calculated pK_a, and given with an error associated with the fitting. Blue shows the corresponding change in pH of APDAP after saturation with Mg^{2+} (100 mM) in the physiological range. Ligand concentration = 50 µM, in 100 mM KCl, 298 K.

Over the physiological pH range (pH 6.5 to 7.5), only small changes in the absorbance were observed, suggesting that the deprotonated carboxylate groups, the aniline nitrogen atom and the ether oxygen atom are each available for coordination to metal ions. Such an interpretation is supported by a number of pK_a studies for APTRA analogues in the literature.[1,6,10,12] It is important to note that it is essential that there be little / no absorbance change with pH in the physiological pH range so that any absorbance changes observed can be unequivocally ascribed to a binding event and not a pH fluctuation.

The metal-bound APDAP ligand is insensitive to changes in pH within the physiological range. Following the addition of 100 mM Mg^{2+} to a solution of APDAP, minimal absorbance changes were observed in the range of pH 6.5 to 7.5. The pH insensitivity in the Mg^{2+} 'bound' complex reported here, has been observed previously with carboxylate-based APTRA analogues of this type, allowing them to be used in a range of *in vivo* and *in cellulo* applications.[5,8]

3.4 Binding studies of APDAP with Mg^{2+}, Ca^{2+} and Zn^{2+}

The absorption spectral changes of APDAP following addition of divalent cations Mg^{2+}, Ca^{2+} and Zn^{2+} were investigated at 298 K in HEPES buffer (pH 7.21) (**Figure 3.3**). It was crucial that the system was buffered, in order to keep the pH constant within the physiological range. All reported errors for binding constants of Mg^{2+}, Ca^{2+} and Zn^{2+} are due to experimental variability, generated from the three repeat measurements and not an error associated with the fitting. Direct comparisons between the binding affinity of Mg^{2+}, Ca^{2+} and Zn^{2+} to APDAP and APTRA are highlighted in **Table 3.1**.

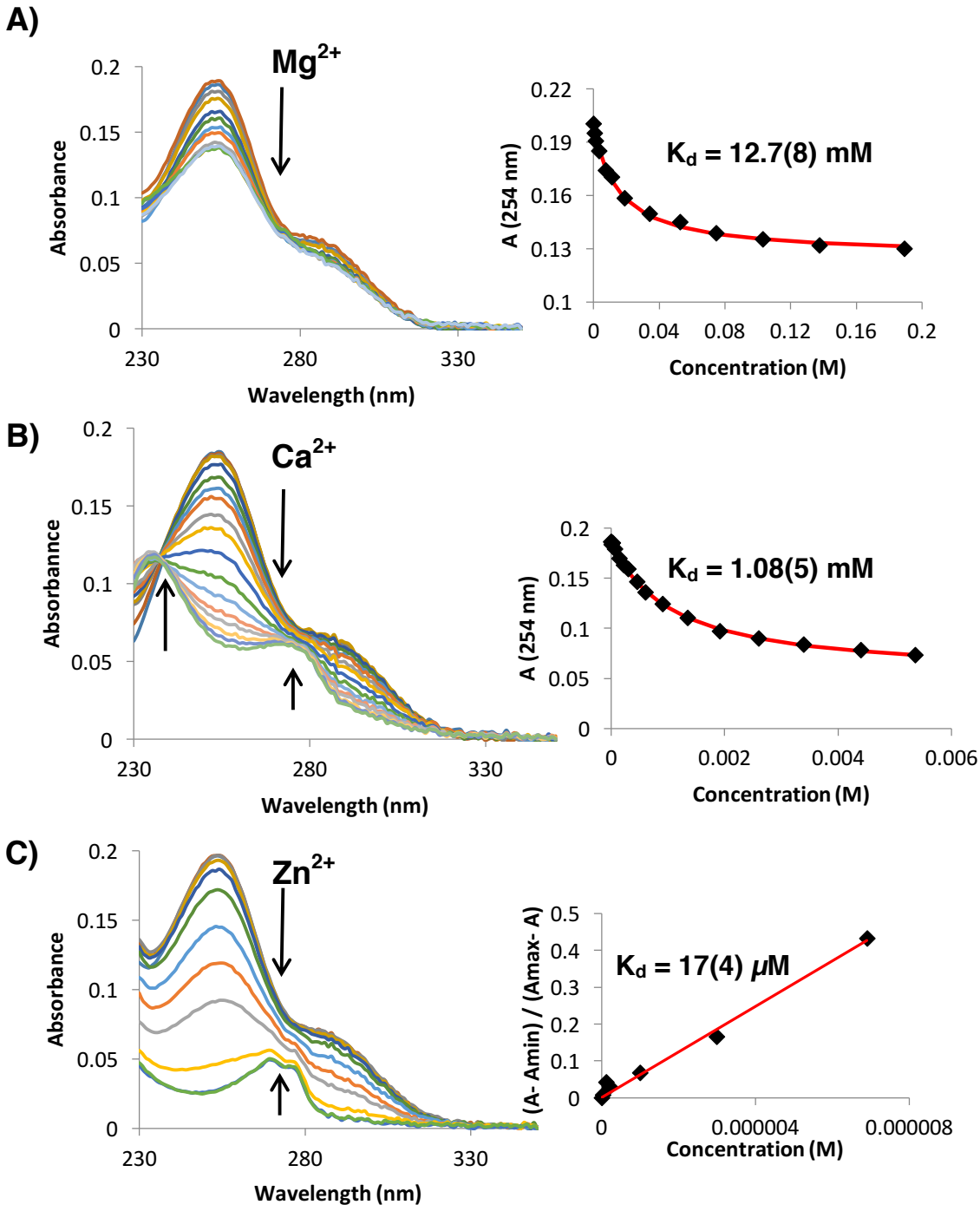

Figure 3.3 (Left) absorbance spectrum, (right) binding curve for the addition of **(A)** Mg^{2+}, **(B)** Ca^{2+} and **(C)** Zn^{2+} in aqueous solutions**.** Ligand concentration = 50 µM, in 50 mM HEPES, 100 mM KCl, pH 7.21. The reported binding constants are an average of three separate metal ion titrations, and the associated experimental error is given in parenthesis.

Table 3.1 The direct comparison of APTRA and APDAP via absorbance spectroscopy. [(a)] Measured by Parker and co-workers,[4] [(b)] measured by Buccella and co-workers.[10] The reported binding constants for APDAP are an average of three separate metal ion titrations, and the associated experimental error is given in parenthesis.

	pK_a	K (Mg^{2+}) (M^{-1})	K_d (Mg^{2+})	K (Ca^{2+}) (M^{-1})	K_d (Ca^{2+})	K (Zn^{2+}) (M^{-1})	K_d (Zn^{2+})
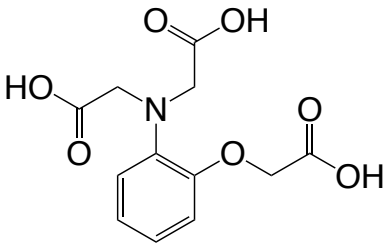 **APTRA**	5.5[a]	5.6(3) $x10^{2}$ [b]	1.79 mM[b]	1.02(7) $x10^{5}$ [b]	9.80 μM[b]	7(1) $x10^{7}$ [b]	14 nM[b]
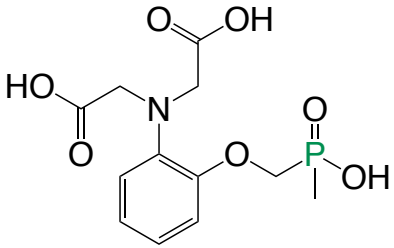 **APDAP**	6.03(8)	0.79(5) $x10^{2}$	12.7(8) mM	9.30(5) $x10^{2}$	1.08(5) mM	6(1) $x10^{4}$	17(3.5) μM

Addition of Mg^{2+} to a solution of APDAP resulted in a decrease in the observed absorbance at 254 nm and 285 nm. Fitting the absorbance at 254 nm against the concentration of $MgCl_2$ added to a 1:1 binding model, revealed a dissociation constant (K_d) of 12.7(8) mM. An approximate 7-fold weaker affinity of ADAP to Mg^{2+} was observed, therefore, when directly compared to APTRA[10] (**Table 3.1**). A different spectral response was found for Mg^{2+} binding compared to the changes accompanying protonation of the aniline nitrogen atom. This behaviour suggests that on the addition of Mg^{2+} to the APDAP chelate, the aniline nitrogen atom does not play a prominent role in binding, instead it is possible that APDAP may bind to Mg^{2+} in a tetradentate manner (**Figure 3.4**). The possible reduction in the number of coordinating groups to Mg^{2+}, could be a factor in the 7-fold reduction in the affinity of APDAP for Mg^{2+}, compared to APTRA.

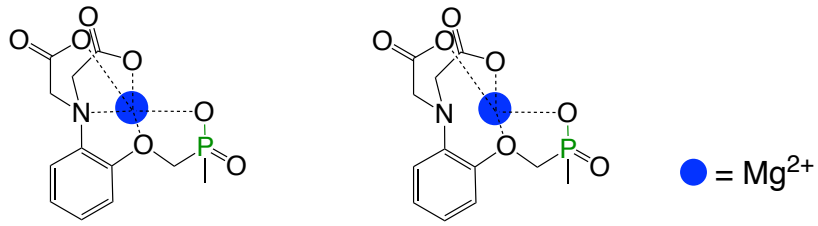

Figure 3.4 Different plausible coordination modes for APDAP to Mg^{2+}.

The addition of Ca^{2+} and Zn^{2+} to a solution of the APDAP chelator afforded a different response to that observed with Mg^{2+}, but a similar response to that seen on protonation of the aniline nitrogen atom under acidic conditions (**Figure 3.2**). A decrease in the absorbance at 254 nm and 285 nm was seen, coupled with an increase in the absorbance at 273 nm. Such behaviour suggests that the aniline nitrogen atom does participate in binding to both Ca^{2+} and Zn^{2+}. Dissociation constants of 1.08(5) mM and 17(4) μM were calculated respectively for Ca^{2+} and Zn^{2+}, from non-linear least squares iterative fitting to a 1:1 binding model (**Figure 3.3**, **Table 3.1**).

APTRA analogues are typically more selective towards Ca^{2+} than Mg^{2+}, with a μM vs. mM affinity commonly displayed. Such an affinity profile allows them to be used as low affinity Ca^{2+} probes in calcium-rich regions of the body.[13] The Mg^{2+} / Ca^{2+} selectivity is, however, seen to be significantly improved by

incorporating a phosphinate group in place of a carboxylate binding group maintaining a pentavalent denticity around the metal ion. A mM affinity for the binding of Mg^{2+} and Ca^{2+} to APDAP is reported, remarkably showing a 110-fold weaker affinity for the binding of Ca^{2+} compared to that observed for APTRA by Buccella *et al* [10] (**Table 3.1**). The mM selectivity to both Mg^{2+} and Ca^{2+} shown here hasn't previously been reported for a ligand of this denticity. It is, however, typical of the bidentate β-keto acids such as KMG-104[14] and KMG-301.[15]

3.5 DFT studies: APTRA vs. APDAP

3.5.1 X-ray crystal structures of APTRA with divalent metal ions

The *o*-aminophenol-*N,N,O*-triacetic acid binding framework has been previously shown to bind a wide variety of divalent cations. Hualin and Peiyi synthesised and characterised a range of APTRA complexes with first row transition metals including Mn^{2+}, Co^{2+}, Ni^{2+} and Zn^{2+}, where a single crystal was obtained for the complex containing Co^{2+}.[16] More recently, Buccella and co-workers have characterised the solid state structures of APTRA with Mg^{2+}, Ca^{2+} and Zn^{2+}.[10] It was found that the APTRA complexes containing Mg^{2+} and Zn^{2+} complemented the observation first made by Hualin and Peiyi in the Co^{2+} complex, where the metal complex of APTRA crystallises as $[M(H_2O)_6][M(APTRA)]_2$ with a distorted octahedral geometry around the metal ion.[10,16] All of the donor atoms in the pentadentate chelate are bound to the divalent metal ion, with the sixth and final coordination site of the metal ion occupied by a bridging carboxylate of a neighbouring complex, forming long chains of $[M(APTRA)]^-$ in the solid state (**Figure 3.5**).[10,16]

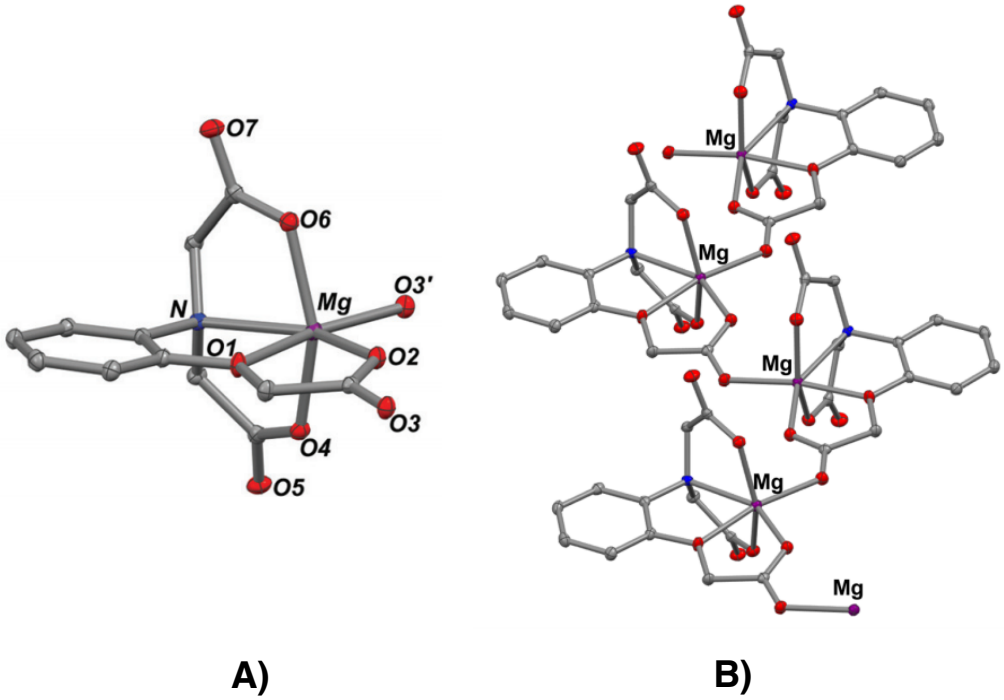

Figure 3.5 The crystal structure of (**A**) $[Mg(APTRA)L]^-$ and (**B**) long chains of $[Mg(APTRA)L]^-$ in the solid state with bridging carboxylates (L) of neighbouring complexes as reported by Buccella *et al.*[10] An identical crystal structure was reported in the analogous Zn^{2+} complex, $[Zn(APTRA)L]^-$.

Complexation of APTRA with Ca^{2+} formed a dimeric species with the formula $[Ca(OH_2)_3]_2\{[APTRA)Ca(OH_2)_2](\mu\text{-}H_2O)_2\}Cl_2$, and showed major structural differences in the solid state to the speciation observed with Mg^{2+}, Zn^{2+} and Co^{2+} (**Figure 3.6**).[10] The dimeric species formed is made up of two APTRA ligands that are bridged by two water molecules and two $Ca(OH_2)_3$ ions.

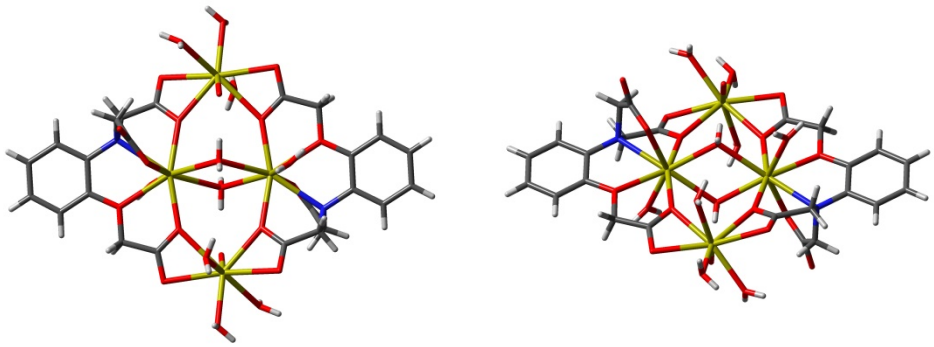

Figure 3.6 The crystal structure of $[Ca_4(APTRA)_2(H_2O)_{10}]^{2+}$ as reported by Buccella *et al.*[10]

It is interesting to note that unlike $[M(H_2O)_6][M(APTRA)]_2$ (complexes formed following addition of Mg^{2+}, Zn^{2+} and Co^{2+}), each Ca^{2+} ion is bound to two APTRA ligands, and in total the two APTRA ligands are bound to four Ca^{2+} ions in the solid state. The larger Ca^{2+} ions (radius = 114 pm) each maintain a coordination number of eight, while the smaller Mg^{2+}, Zn^{2+} and Co^{2+} ions favour a coordination number of six, in an octahedral geometry.

3.5.2 DFT studies: The addition of divalent metal ions to APTRA and APDAP

It has been shown in **Section 3.4** that from absorbance binding studies of APDAP with Mg^{2+}, Ca^{2+} and Zn^{2+}, an enhancement of the Mg^{2+} / Ca^{2+} selectivity is reported, with a 110-fold weaker affinity for the binding of Ca^{2+} compared to that observed for APTRA by Buccella.[10]

In order to gain a greater insight into the significantly weaker affinity for Ca^{2+} observed for the phosphinate chelate APDAP, a series of DFT calculations were carried out. The primary objective of the investigation was to calculate the binding energies and the bond distances / bite angles following complexation of Mg^{2+}, Ca^{2+} and Zn^{2+} to APTRA and APDAP. It was hoped that these calculations could provide some insight into the enhanced Mg^{2+} selectivity reported for APDAP.

In the crystal structure characterised by Buccella *et al*. (**Figure 3.5**), APTRA complexes containing Mg^{2+} and Zn^{2+} ions crystallised in long chains of $[M(APTRA)]^-$, with a carboxylate ligand occupying the sixth coordination site. In an attempt to replicate experimental conditions in aqueous solutions, the DFT simulations were instead run primarily with a water molecule occupying the sixth coordination site of the metal ion.

Simulated DFT structures of APTRA and APDAP bound to Mg^{2+}, Ca^{2+} and Zn^{2+} in a distorted octahedral geometry are shown in **Figure 3.7**.

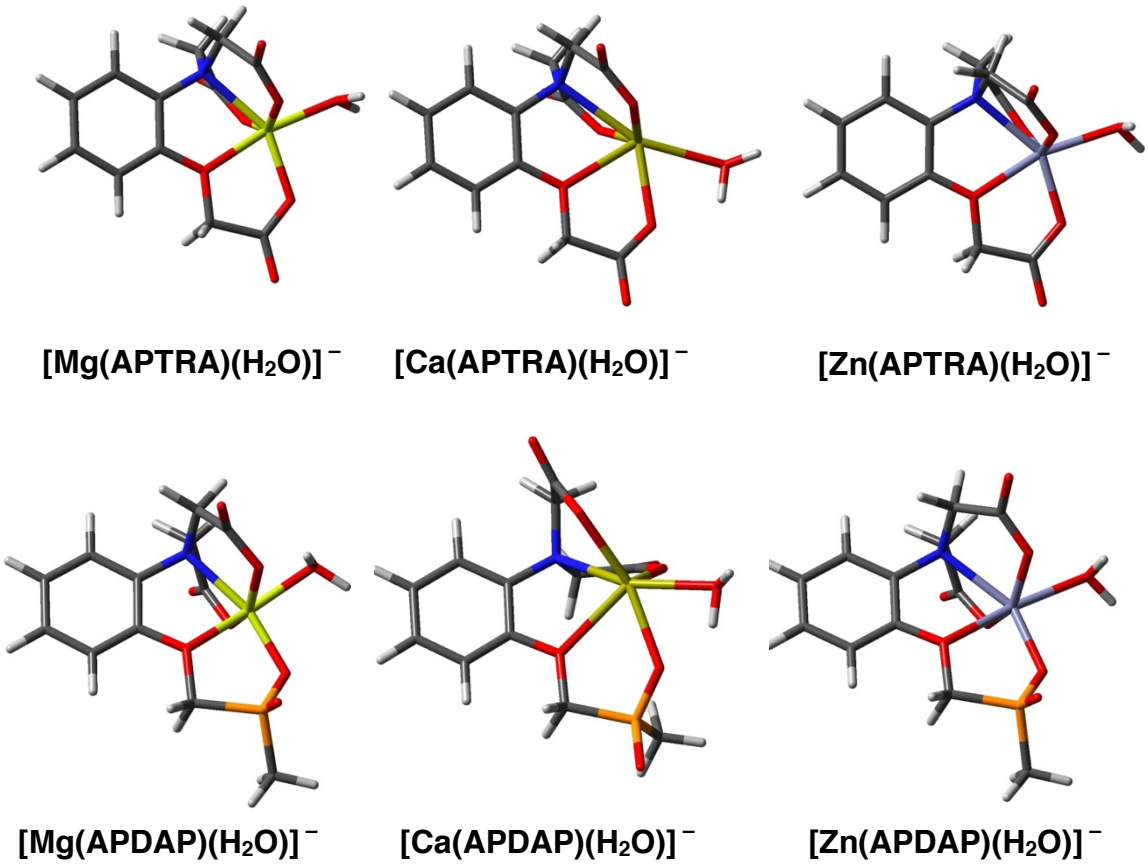

Figure 3.7 The simulated structures of APTRA and APDAP coordinated to Mg^{2+}, Ca^{2+} and Zn^{2+}. A metal coordination number of six has been assumed for the coordination of each metal ion. Functional / basis set / solvent (B3LYP / 6-311++G(d,p) / H_2O).

For the binding of each divalent metal ion a coordination number of six was assumed, although for Ca^{2+} a larger coordination number of eight was expected in solution because of its larger ionic radius, and the 8-coordinate complex formed in the solid state.[10] The binding energies found for the binding of Ca^{2+}, therefore, have a significant error associated with the calculation, as it is possible that multiple $[Ca(APTRA)(H_2O)_n]^{-}$ (where n = 1, 2 or 3) anions are present in aqueous solution. Depending on the coordination and hydration number of Ca^{2+} in the DFT simulation, the binding energies will change considerably. Results obtained, therefore, provided little information into the rationale behind the reduced Ca^{2+} binding affinity observed for APDAP.

The C–C, C–O, P–C and P–O bond lengths in APTRA and APDAP were calculated from the simulated structures in **Figure 3.7**, to provide a greater understanding into the experimental binding affinities observed for Mg^{2+} and Ca^{2+}. Bond lengths of the M–O and M–N binding groups in both $[M(APTRA)(H_2O)]^-$ and $[M(APDAP)(H_2O)]^-$ (where M = Mg^{2+} and Ca^{2+}) have also been determined to calculate the bite angles around the metal ions.

It is apparent from **Table 3.2**, that C–C, C–O, P–C and P–O bond lengths are almost identical in APTRA and APDAP respectively for the binding of Mg^{2+} and Ca^{2+}. There is, however, a noticeable difference in the relative C–C, C–O in APTRA and P–C and P–O bond lengths in APDAP, where longer P–C and P–O bonds are reported over their carboxylate analogues.

Table 3.2 The C–C, C–O, P–C and P–O bond distances / Å in APTRA and APDAP when bound to Mg^{2+} and Ca^{2+}. Functional / basis set / solvent (B3LYP / 6-311++G(d,p) / H_2O).

Bond distances / Å	**$[M(APTRA)(H_2O)]^-$**		**$[M(APDAP)(H_2O)]^-$**	
	M = Mg^{2+}	**M = Ca^{2+}**	**M = Mg^{2+}**	**M = Ca^{2+}**
C–C	1.539	1.538	-	-
C–O	1.275	1.271	-	-
P–C	-	-	1.868	1.858
P–O	-	-	1.551	1.547

Due to the complexity associated with the multiple possible coordination numbers of Ca^{2+} in solution ($[M(APTRA)(H_2O)_n]^-$), a DFT study into the metal-donor group bond distances and bite angles in APTRA and APDAP was investigated with Mg^{2+} and Zn^{2+} only. These divalent metal ions have a very similar ionic radius, and both form 6-coordinate complexes in solution.

A comparison between the calculated bond lengths for APTRA has been made with those determined experimentally, taken from the X-ray crystal structure reported by Buccella.[10] No such comparisons to experimental bond lengths were made with APDAP, as no conditions to isolate a single crystal of $[Mg(APDAP)L]^-$, $[Ca(APDAP)L]^-$ or $[Zn(APDAP)L]^-$ have been established.

The metal-donor group bond distances for APTRA and APDAP and the bite angle around the Mg^{2+} and Zn^{2+} metal ions are highlighted in **Table 3.3**, **Table 3.4** and **Table 3.5**. Similar metal-donor group bond distances are displayed

in APTRA for the binding of both Mg^{2+} and Zn^{2+}, and are comparable to the experimental values measured from the X-ray crystal structure of the $[M(APTRA)(L)]^-$ complexes (**Table 3.3**).

The phosphinate-based chelate APDAP, however, displayed significant differences in the calculated bond distances for the binding of Mg^{2+} and Zn^{2+} to APTRA. In general, metal-donor group bond lengths were shorter in the $[Mg(APDAP)L]^-$ complex, compared to its APTRA analogue. It is apparent from **Table 3.4**, that the M–O(CH_2) bond length in $[Mg(APDAP)L]^-$ was noticeably shorter than the other three complexes studied, containing both Mg^{2+} and Zn^{2+}. For example, a 0.262 Å shorter bond length was seen relative to the zinc complex $[Zn(APDAP)L]^-$. It is interesting to note that much less bond length variation was displayed between $[Zn(APTRA)L]^-$ and $[Zn(APDAP)L]^-$, and was comparable to the values calculated for $[Mg(APTRA)L]^-$ (**Table 3.3** and **Table 3.4**).

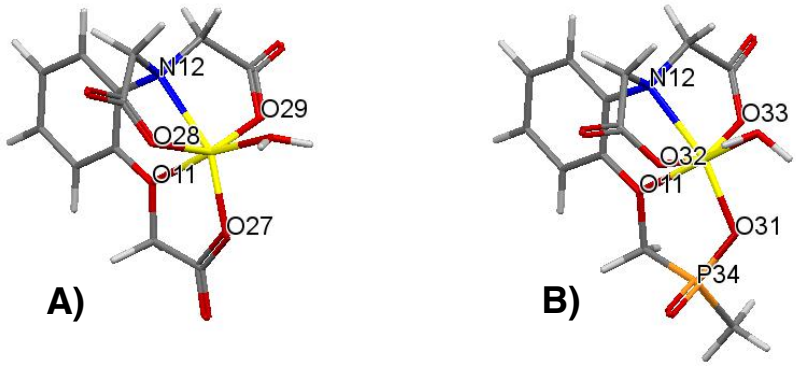

Figure 3.8 The simulated structures of **(A)** $[Mg(APTRA)(H_2O)]^-$ and **(B)** $[Mg(APDAP)(H_2O)]^-$.

Table 3.3 Comparison of the calculated and experimental bond distances in APTRA after coordination to Mg^{2+} and Zn^{2+}. (B3LYP / 6-311++G(d,p) / H_2O). Calculated bond distances are obtained from crystallographic data.[10] Calc. L = H_2O, Expt. L = carboxylate from an adjacent $[M(APTRA)]^-$ complex.

M–L bond	$[Mg(APTRA)L]^-$ / Å		$[Zn(APTRA)L]^-$ / Å	
	Calc	Expt	Calc	Expt
M–N12	2.336	2.307	2.382	2.248
M–O11	2.161	2.140	2.251	2.198
M–O27	2.037	2.042	2.037	2.052
M–O28	2.033	2.038	2.019	2.044
M–O29	2.028	2.013	2.013	2.069
M–O(L)	2.135	2.045	2.258	2.042

Table 3.4 The calculated bond distances in APDAP after coordination to Mg^{2+} and Zn^{2+}. (B3LYP / 6-311++G(d,p) / H_2O). L = H_2O. No experimental bond distances were measured.

M–L bond	$[Mg(APDAP)L]^-$ / Å		$[Zn(APDAP)L]^-$ / Å	
	Calc	Expt	Calc	Expt
M–N12	2.233	-	2.366	-
M–O11	2.088	-	2.350	-
M–O31	1.966	-	1.991	-
M–O32	2.056	-	2.022	-
M–O33	1.971	-	2.020	-
M–O(L)	2.093	-	2.302	-

Table 3.5 Comparison of the bite angles between the donor groups of APTRA and APDAP coordinated to Mg^{2+} and Zn^{2+}. (B3LYP / 6-311++G(d,p) / H_2O). L = H_2O.

Complex	Bite angles / °			
	O11–Mg–N12	O^-–Mg–N12	O^-–Mg–N12	O11–Mg–O^- [a]
$[Mg(APTRA)L]^-$	73.94	77.31	77.12	75.18
$[Zn(APTRA)L]^-$	72.11	78.11	78.22	74.63
$[Mg(APDAP)L]^-$	78.39	79.83	80.07	83.89
$[Zn(APDAP)L]^-$	71.19	78.85	77.97	78.56

[a] O^- = phosphinate oxygen for APDAP, O-carboxylate for APTRA.

It is evident from **Table 3.5** that the bite angles around the Mg^{2+} ion in $[Mg(APDAP)L]^-$ are larger than those calculated in both $[Mg(APTRA)L]^-$ and $[Zn(APDAP)L]^-$. Similar to the metal-donor group bond lengths seen for $[Zn(APDAP)L]^-$, the calculated bite angles are also comparable to those observed for the Mg^{2+} and Zn^{2+} complexes of APTRA.

For the binding of Mg^{2+}, the longer P–C and P–O bond lengths in APDAP, give rise to a larger chelate ring size, with less acute bite angles around the Mg^{2+} ion (**Table 3.2** and **Table 3.5**). The largest difference was observed with the $(CH_2)O–Mg–O$ angle of the phosphinate ligating group, where a 9^o less acute bite angle was seen relative to the carboxylate binding group in APTRA (**Table 3.5** and **Table 3.6**).

3.5.3 APDAP vs. APTRA: Explaining the enhanced Mg^{2+} / Ca^{2+} selectivity

Although no data was collected from DFT studies for the Ca^{2+} complex of APDAP ($[Ca(APDAP)L_n]^-$), a number of important conclusions can be drawn from the information obtained for the Mg^{2+} and Zn^{2+} complexes. It has been shown in **Section 3.5.2** that the phosphinate-based APDAP chelate possesses much longer P–C and P–O bonds, generating a less acute bite angles around Mg^{2+} than that observed for APTRA (**Table 3.2**). Consistent with this observation, shorter $M–O(CH_2)$, $M–O(PO(CH_3)CH_2O)$ and M–N bond lengths were also found in $[Mg(APDAP)L]^-$ with the phosphinate chelate being more 6-membered in character than the smaller bite angles seen in the APTRA series.

According to the chelate effect first introduced in **Section 2.1**, larger metal ions of a higher coordination number have a more pronounced reduction in complex stability with an increased chelate ring size.[18,19] Larger cations such as Ca^{2+}, therefore, preferentially favour the formation of 5-membered ring chelates over 6-membered, with an ideal bite angle of 69^o.[18,19] Smaller cations such as Mg^{2+} and Zn^{2+}, have a lower coordination number and form more stable 6-membered chelates.[18,19] It is possible, therefore, to potentially tune the metal ion selectivity by changing the ring chelate size around a metal ion.[18,19]

A systematic comparison between the bite angle in carboxylate and phosphinate binding groups in APTRA and APDAP respectively is shown in **Figure 3.9**. A typical aliphatic 5-membered ring (ethylenediamine, EN)[18] and a 6-membered chelate (trimethylenediamine, TN) formed on the binding to divalent metal ions has been included in **Figure 3.9** for comparison.[18]

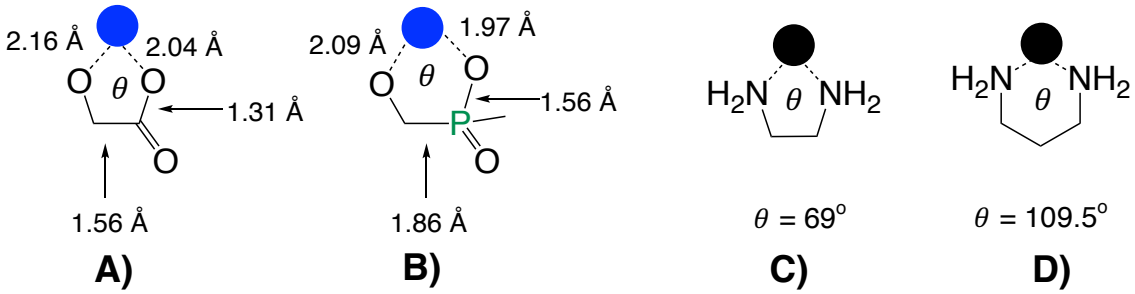

Figure 3.9 Calculated $(CH_2)O–Mg–O$ bite angles in (**A**) $[Mg(APTRA)L]^-$ and (**B**) $[Mg(APDAP)L]^-$. Literature examples of (**C**) 5-membered ethylene diamine (EN) and (**D**) 6-membered trimethylenediamine (TN) on the binding of divalent metal ions, provided for a comparison.[18] Blue is a Mg^{2+} ion, black represents a theoretical divalent metal ion.

Table 3.6 The $(CH_2)O–Mg–O$ bite angles in $[Mg(APTRA)L]^-$ and $[Mg(APDAP)L]^-$.

Complex	**$(CH_2)O–Mg–O$ bite angles, θ / °**
$[Mg(APTRA)L]^-$ (A)	75.18
$[Mg(APDAP)L]^-$ (B)	83.89

The increase in the $(CH_2)O–Mg–O$ bite angle and the reduced M–N and M–O bond lengths observed in $[Mg(APDAP)L]^-$, suggests that the phosphinate-based APDAP ligand possesses features similar to that observed with a 6-membered ring chelate. In 6-memebered ring chelates, such as TN (**Figure 3.9**), an ideal bite angle of 109.5° is typically observed, significantly larger than those reported for 5-membered ring chelates (**Figure 3.9** and **Table 3.6**).[18,19] The larger ring chelate formed in $[Mg(APDAP)L]^-$, therefore, will tend to thermodynamically favour the binding of the smaller Mg^{2+} cation over Ca^{2+}. Such behaviour is identical to that observed by Martell and Hancock in a detailed investigation into the binding of metal ions to a range of both 5- and 6-membered ring chelates.[18,19]

Similar work involving the binding of metal cations to phosphinate ligating groups has been carried out previously in Durham. The introduction of phosphinate groups onto both 9-N_3 and 12-N_4 macrocyclic ligands has been reported to modify ion selectivity, identical to that observed for APDAP in this work. Parker and co-workers synthesised a range of carboxylate- and phosphinate-based macrocyclic ligands such as 1,4,7-triazacyclononane-1,4,7-triyltrimethylelenetris-(phenylphosphinate), to bind to a range of divalent and trivalent metal ions, including Cu^{2+}, Ga^{3+} and Fe^{3+}.[17] Similarly to the calculated bond lengths observed for $[Mg(APDAP)L]^{-}$, longer P–C and P–O bonds were reported in the macrocyclic phosphinate series over their carboxylate analogues. A less acute bite angle around the metal ion was seen in the phosphinate series, that inherently favoured the binding of smaller metal ions.[17]

3.6 Conclusions for the direct comparison of APTRA and APDAP

A new pentadentate binding moiety for divalent cations, namely *o*-aminophenol-*N,N*-diacetic acid phosphinate (APDAP) has been synthesised in a four step reaction sequence from 2-nitrophenol in good yield. The APDAP chelate is a phosphinate analogue of APTRA, with the incorporation of a phosphinate binding group at the expense of a carboxylate ligating group to maintain a pentadentate denticity (**Figure 3.10**).

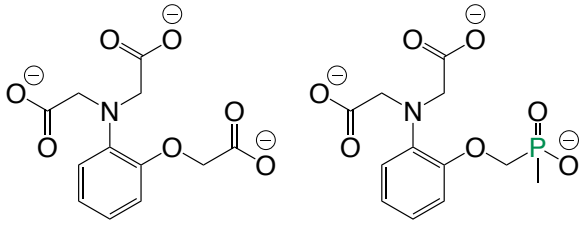

Figure 3.10 Pentadentate ligands APTRA and APDAP.

The APDAP chelate revealed a pK_a of 6, slightly higher than the value of 5.5 previously reported for APTRA via absorbance spectroscopy.[10] Absorbance binding studies were carried out following addition of Mg^{2+}, Ca^{2+} and Zn^{2+}, where an enhanced selectivity for the binding of Mg^{2+} compared to APTRA was observed. Although APDAP displayed a 7-fold weaker affinity towards Mg^{2+}, a

dramatically reduced affinity was reported following addition of Ca^{2+} and Zn^{2+}. For the binding of Ca^{2+} ions for example, a 110-fold weaker binding affinity was observed, and a dissociation constant of 1.08(5) mM was calculated from a 1:1 binding model. K_d values in this range for the binding of Ca^{2+} have never been seen before for ligands of this denticity, with a mid-μM affinities typically observed within the APTRA series of indicators.[1-6,10,12]

In order to gain greater insight into the binding of Mg^{2+}, Ca^{2+} and Zn^{2+} to APDAP a detailed DFT investigation was undertaken. All simulations were run with each of the oxygen and nitrogen donor groups coordinated to the metal ion, with a water molecule occupying the sixth and final coordination site in an attempt to replicate experimental solution conditions. A number of binding energies, bond lengths and bite angles were calculated for both APTRA and APDAP. The viability of the calculations was tested by comparing the data to experimental results obtained from the crystal structure of $[Mg(APTRA)L]^-$ (where M = Mg^{2+}, Ca^{2+} and Zn^{2+}).

From the computational DFT study it was found that the APDAP chelate possesses longer P–C and P–O bonds compared to the carboxylate analogue APTRA. The metal-donor group bond lengths and bite angles around the metal ion were calculated with both Mg^{2+} and Zn^{2+}, the similar ionic radius and coordination number of these ions eliminates complications resulting from the multiple hydration numbers possible for $[Ca(APTRA)(H_2O)_n]^-$ (where n = 1, 2 or 3) in solution. It was found that in the case of $[Mg(APDAP)L]^-$ the $(CH_2)O$–Mg–O bond lengths were much shorter than their APTRA analogues with a 9° more obtuse bite angle. For $[Zn(APDAP)L]^-$, however, all bond lengths and bite angles calculated were broadly similar to those measured with APTRA.

The larger Ca^{2+} ion thermodynamically favours the formation of 5-membered chelate rings. The increase in the bite angle observed for Mg^{2+} and the reduction in the M–O and M–N bond lengths, allows the APDAP chelate ring to possess more 6-membered ring chelate character around Mg^{2+} ions. Such behaviour provides a possible explanation into the dramatically reduced affinity observed for the binding of Ca^{2+} to APDAP. The larger ring size with the

phosphinate APDAP chelate formed inherently favours the binding of smaller cations, such as Mg^{2+} over Ca^{2+}.

3.7 References

[1] L. A. Levy, E. Murphy, B. Raju and R. E. London, *Biochemistry.*, 1988, **27**, 4041-4048

[2] R. E London, *Annu. Rev. Physiol.*, 1991, **53**, 241- 56.

[3] P.A. Otten, R. E. London and L. A. Levy, *Bioconjugate Chem.*, 2001, **12**, 76- 83.

[4] O. Reany, T. Gunnlaugsson and D. Parker, *J. Chem. Soc., Perkin Trans.* 2000, **2**, 1819-1831.

[5] Q. Lin, J. J Gruskos and D. Buccella, *Org. Biomol. Chem.*, 2016, **14**, 11381.

[6] P. A. Otten, R. E. London and L. A. Levy, *Bioconjugate Chem.*, 2001, **12**, 203-212.

[7] Y. Suzuki, H. Komatsu, T. Ikeda, N. Saito, S. Araki, D. Citterio, H. Hissamoto, Y. Kitamuru, T. Kubota, J. Nakagawa, K. Oka and K. Suzuki, *Anal. Chem.*, 2002, **74**, 1423-1428.

[8] S. C. Schwartz, B. Pinto- Pacheco, J- P. Pitteloud and D. Buccella, *Inorg. Chem.*, 2014, **53**, 3204- 3209.

[9] A. M. P. Romani, *Arch. Biochem. Biophys.*, 2011, **512**, 1-23.

[10] M. Brady, S. D. Piombo, C. Hu and D. Buccella, *Dalton Trans.*, 2016, **45**, 12458- 12464

[11] M. Booy and T. W. Swaddle, *Can. J. Chem.*, 1977, **55**, 1762.

[12] Q. Lin, J. J. Gruskos and D. Buccella, *Org. Biomol. Chem.*, 2016, **14**, 11381.

[13] B. Raju, E. Murphy, L. A. Levy, R. D. Hall and R. E. London, *Am. J. Physiol.*, 1989, **256**, 540-548.

[14] H. Komatsu., N. Iwasawa., D. Citterio., Y. Suzuki., T. Kubota., K. Tokuno., Y. Kitamura., K. Oka., K. Suzuki, *J. Am. Chem. Soc.,* 2004, **126**, 16353-16360.

[15] T. Fujii., Y. Shindo., K. Hotta., D. Citterio., S. Nishiyama., K. Suzuki., K. Oka, *PLoS One.,* 2011, **6**, e23684.

[16] Z. Hualin and L. I. Peiyi, *Polyhedron.*, 1990, **9**, 2873-2878.

[17] E. Cole, R. C. B. Copley, J. A. K. Howard, D. Parker, G. Ferguson, J. F. Gallagher, B. Kaitner, A. Harrison and L. Royle, *J. Chem. Soc., Dalton Trans,* 1994, 1619-1629.

[18] R. D. Hancock, *J. Chem. Educ.*, 1992, **69**, 615-621.

[19] R. D. Hancock and A. E. Martell, *Chem. Rev.*, 1989, **89**, 1875-1914.

4. Ligands containing naphthalene as the fluorophore

4.1 Introduction

Levy *et al*. have previously demonstrated that the incorporation of the APTRA binding moiety into 1-naphthalene and 2-naphthalene systems generates indicators that display a ratiometric response towards Mg^{2+} and Ca^{2+}.[1] Ratiometric indicators are highly advantageous in sensing applications. A wavelength shift on the binding of metal ions allows the concentration to be measured at two specific wavelengths. Such behaviour allows ratiometric methods of analysis to be used, meaning that the binding measurements of Mg^{2+} and other cations are unaffected by the concentration of the indicator, cell loading or photochemical bleaching during *in vivo* studies.[1] The bi-aryl naphthalene derivatives developed by Levy *et al*. are shown in **Figure 4.1**.

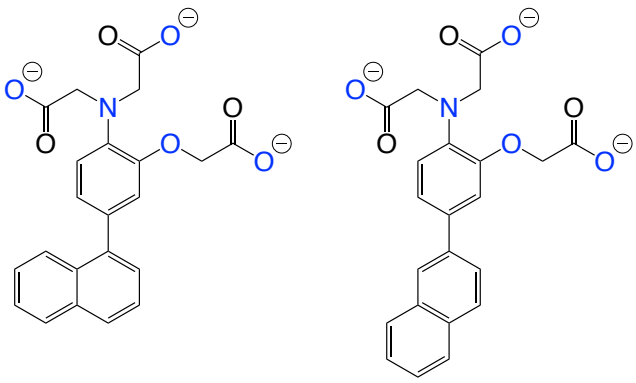

(A) **(B)**

Figure 4.1 Naphthalene-based indicators developed by Levy *et al*. from **(A)** 1-naphthalene and **(B)** 2-naphthalene derivatives.[1]

Building on the success of this work carried out in 2001, pro-ligands $\mathbf{L^1}$, $\mathbf{L^2}$, $\mathbf{L^4}$ and $\mathbf{L^6}$ have been incorporated into 1-naphthalene based systems, and are denoted as the naphthalene derivatives $\mathbf{NapL^1}$, $\mathbf{NapL^2}$, $\mathbf{NapL^4}$ and $\mathbf{NapL^6}$ (**Figure 4.2**). The 1-naphthalene systems were preferred because of the greater wavelength shift upon saturation with Mg^{2+} in the excitation spectrum (30 nm shift for the 1-naphyl vs. 23 nm shift for the 2-naphthyl derivatives).[1]

Instead of the bi-aryl ligand utilised in the work undertaken by Levy *et al.*, a naphthalene-1-alkynylaryl system has been developed with an alkyne link between the APTRA binding moiety and the naphthalene reporter group. This approach allows the possibility to use the ligands in the naphthalene series as fluorophores to analyse the behaviour of the new binding moieties of **L**^{4} and **L**^{6} containing phosphinate groups. It also provides the opportunity for **NapL**^{1}, **NapL**^{2}, **NapL**^{4} and **NapL**^{6} to act as a model for related lanthanide-based systems (**Chapter 5**) as pyridylalkynylaryl-based compounds are commonly used as chromophores in 12-N_4 macrocyclic ligands to sensitise europium-based emission.

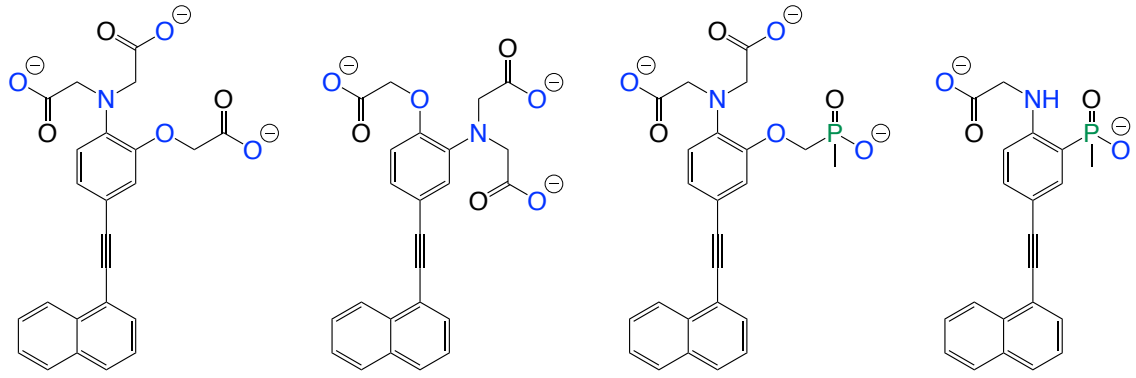

NapL^{1} **NapL**^{2} **NapL**^{4} **NapL**^{6}

Figure 4.2 Target naphthalene-based ligands **NapL**^{1}, **NapL**^{2}, **NapL**^{4} and **NapL**^{6}.

The synthesis and characterisation of the ligands is reported here. The analysis of pK_a and the binding properties of **NapL**^{1}, **NapL**^{2}, **NapL**^{4} and **NapL**^{6} via fluorescence spectroscopy is also discussed. Direct comparisons across the naphthalene series have been made, to determine how the binding affinity and selectivity is affected by the position of nitrogen and oxygen atoms on the APTRA binding moiety relative to the aromatic reporter group. Direct comparisons between the APTRA (**NapL**^{1}, **NapL**^{2}) and the newly synthesised APDAP (**NapL**^{4}) binding moieties are made. The effect of different chelate ring sizes formed on binding of Mg^{2+}, Ca^{2+} and Zn^{2+}, typically [5, 5, 5] vs. [6, 5], is also assessed.

4.2 Synthesis and characterisation

The synthesis of the naphthalene-based ligands **NapL^1**, **NapL^2**, **NapL^4** and **NapL^6** begins with the introduction of an alkyne group via a Sonogashira reaction of (triisopropylsilyl)acetylene (TIPS-acetylene) with the ethyl esters of **L^1**, **L^2**, **L^4** and **L^6** in THF (**Scheme 4.1**). It was found that relatively long reaction times were required, together with the addition of a large excess of TIPS-acetylene (5-6 equivalents). Shorter reaction times and fewer equivalents of TIPS-acetylene resulted in incomplete conversion. Such a behaviour presented problems during purification, as similar R_f values were observed for the starting material and product, making purification via conventional chromatography rather difficult to achieve. Typically, $Pd(PPh_3)_2Cl_2$ is used as the catalyst in Sonogashira cross-coupling reactions. However, only starting material was observed by both ESI-MS and ^{1}H NMR after heating at reflux in THF for 3 days when this catalyst was used. The $Pd(dppf)Cl_2$ catalyst was found to be the most suitable, forming (**25**)-(**28**) in high yields after purification by column chromatography.

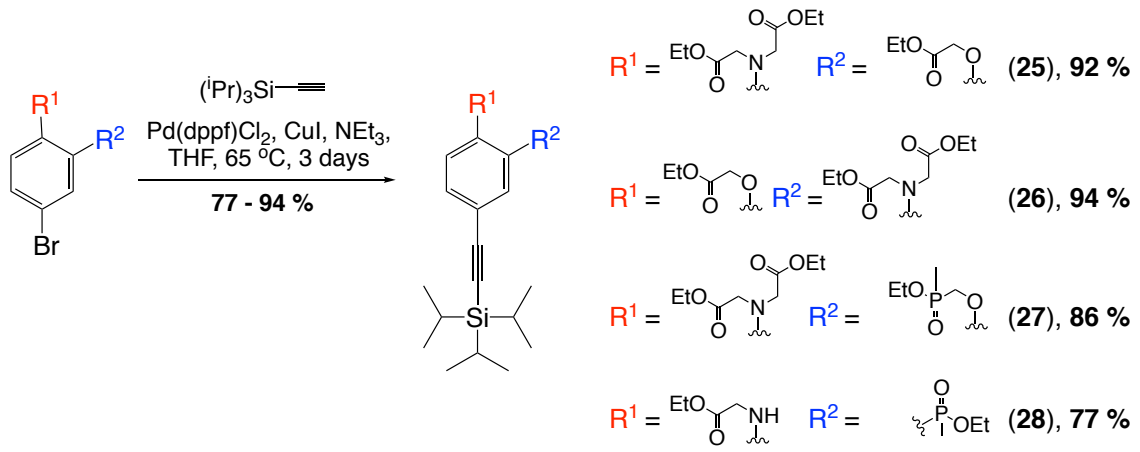

Scheme 4.1 Sonogashira cross-coupling reactions of ethyl esters of **L^1**, **L^2**, **L^4** and **L^6** with TIPS-acetylene.

Alkyne de-protection was attempted under a number of conditions to form the unprotected alkyne (**Scheme 4.2**). Carbon-silicon bond cleavage using triethylamine trihydrofluoride (NEt_3.3HF) has been used previously to de-protect trimethylsilyl (TMS) alkynes in high yields.[2] The reaction, however, was unsuccessful in this instance, with no evidence of any reaction by ESI-MS after 4 days heating at 35 °C. It is possible that the increased steric hindrance provided

by the TIPS group may inhibit the attack of fluoride at the silicon centre. The use of tetrabutylammonium fluoride (TBAF) in THF at room temperature was used as an alternative de-protection method which led to the formation of (**30**) in moderate yield, after purification by column chromatography (**Scheme 4.2**).

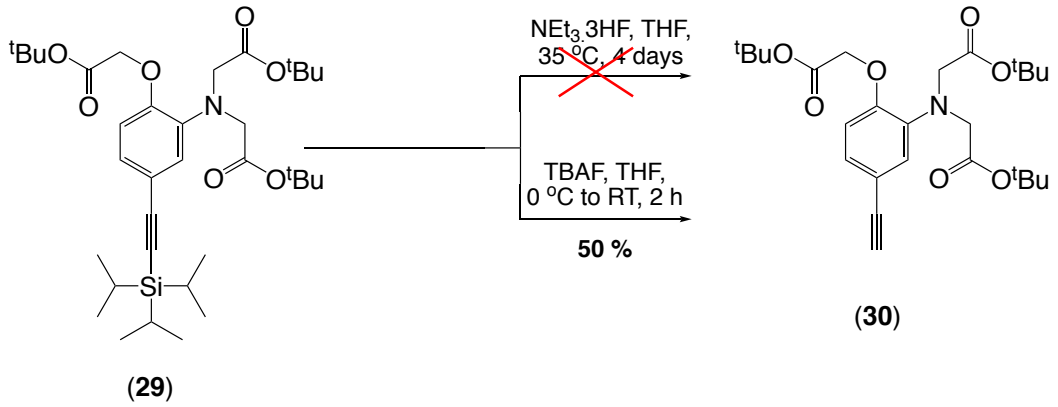

(**29**) (**30**)

Scheme 4.2 Attempted alkyne de-protection of (**29**) with $NEt_3.3HF$[2] or TBAF in THF.

In an effort to increase the overall yield of the Sonogashira cross-coupling reaction, a one pot de-protection and cross-coupling reaction with 1-bromonaphthalene was undertaken. Initially $Pd(PPh_3)_4$ was used as the catalyst. However, this led to the formation of triphenylphosphine oxide as a by-product which was difficult to remove by conventional column chromatography. $Pd(dppf)Cl_2$ was used as an alternative catalyst with copper iodide forming (**31**)-(**34**) in low yields after purification by column chromatography. It was essential that silyl protected alkynes (**25**)-(**28**) were added in a 1:1 stoichiometry with 1-bromonaphthalene. Similar R_f values in common solvent systems between the de-protected alkyne and the cross-coupled product resulted in purification problems, even when only a slight excess was used.

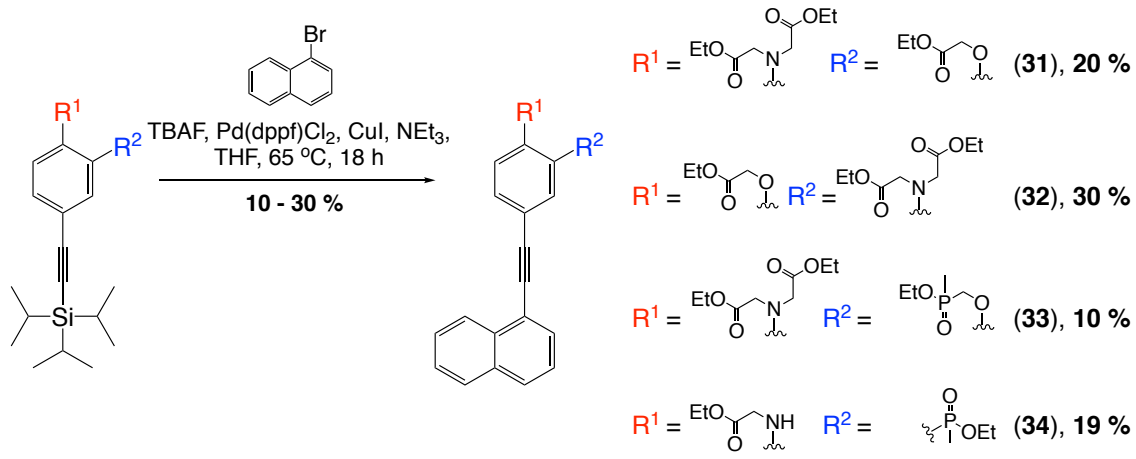

Scheme 4.3 One pot de-protection reaction of silyl acetylenes and Sonogashira cross-coupling reaction with 1-bromonaphthalene.

The 'one pot' method was low yielding, especially for the ligands bearing phosphinate groups (**33**) and (**34**).

Ethyl ester hydrolysis of (**31**)-(**34**) was undertaken in basic conditions, using sodium deuteroxide and deuterated solvents to allow the the hydrolysis reaction to be monitored easily by ^{1}H NMR (**Scheme 4.4**). Each hydrolysis reaction proceeded smoothly, forming **NapL^{1}** (**35**), **NapL^{2}** (**36**), **NapL^{4}** (**37**) and **NapL^{6}** (**38**) in quantitative yields. Product purity was determined by ESI-MS, accurate mass analysis and analytical HPLC.

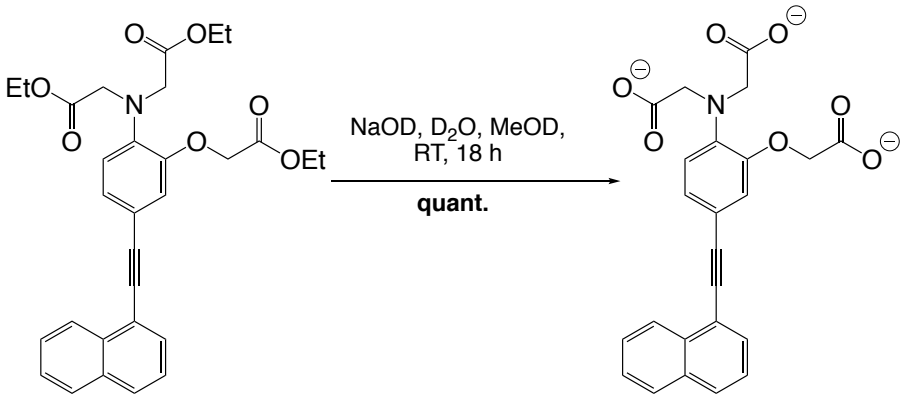

(**31**) **NapL^{1}, (35)**

Scheme 4.4 Ethyl ester hydrolysis of (**31**) to form **NapL^{1}** (**35**). The same procedure was repeated for (**32**), (**33**) and (**34**) to form **NapL^{2}** (**36**), **NapL^{4}** (**37**) and **NapL^{6}** (**38**) respectively.

4.3 Photophysical studies of NapL^1, NapL^2, NapL^4 and NapL^6

The photophysical properties of **NapL^1**, **NapL^2**, **NapL^4** and **NapL^6** were examined in aqueous solutions at 298 K. pH titrations were carried out at a constant ionic strength in 100 mM KCl. Metal binding titrations with Mg^{2+}, Ca^{2+} and Zn^{2+} were carried out in 50 mM HEPES buffer and 100 mM KCl at a constant pH of 7.21 to simulate physiological conditions.

The absorption spectra for **NapL^1**, **NapL^2**, **NapL^4** and **NapL^6** in water are shown in **Figure 4.3**, and the absorption maximum for each naphthalene derivative is listed in **Table 4.1**. Molar extinction coefficients were calculated from a linear plot of the absorbance maximum at four different concentrations according to the Beer-Lambert law (**Equation 3.1**).

$$A = \varepsilon cl \qquad \textbf{Eq.3.1}$$

where: A is the absorbance, ε is the molar extinction coefficient, c is the concentration and l is the path length of the cell (1 cm).

The values of the calculated molar extinction coefficients and quantum yields are listed in **Table 4.1**, and as expected, are all comparable due to the fact that only small structural modifications have been made to the naphthalene derivatives in each instance.

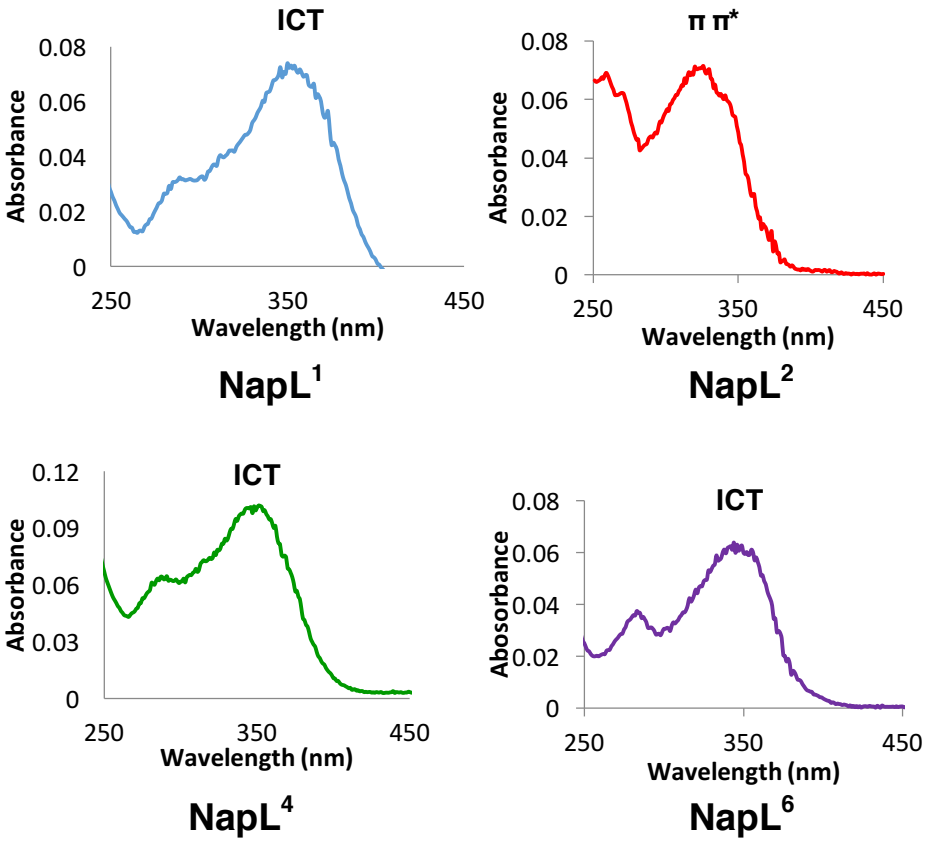

Figure 4.3 Absorbance spectra of **NapL**[1], **NapL**[2], **NapL**[4] and **NapL**[6] in H_2O, 298 K.

Table 4.1 The absorption λ_{max} and calculated molar extinction coefficients (ε) for **NapL**[1], **NapL**[2], **NapL**[4] and **NapL**[6] in H_2O, 298 K. The molar extinction coefficients (ε) were determined from the Beer-Lambert Law, A = εcl. Quantum yields (Φ) $\pm$ 20 % measured in H_2O. [a]Quinine sulphate (in 0.5 M H_2SO_4) and [b]POPOP were used as the fluorescence standards.

Ligand	Absorption λ_{max} / nm	ε x10^3 / M^{-1}cm^{-1}	Φ_{H_2O} / %
NapL[1]	354	14.1(3)	0.3[a]
NapL[2]	318	13.8(6)	1.3[b]
NapL[4]	350	10.7(2)	0.7[a]
NapL[6]	341	12.9(4)	0.8[a]

The excitation and emission spectra of the four naphthalene-1-alkynylaryl derivatives were recorded in water at 298 K; the normalised emission and excitation spectra are shown in **Figure 4.4**. The excitation and emission maxima

are listed in **Table 4.2**, with a comparison to the wavelength maximum exhibited by the commercially available Mag-Fura-2.[3]

It is clear from the analysis of the absorption, excitation and emission profiles of **NapL^1**, **NapL^2**, **NapL^4** and **NapL^6** that the position of the aniline nitrogen atom on the aromatic system has a notable effect on the observed wavelength maximum in each instance. The derivatives **NapL^1**, **NapL^4** and **NapL^6** each have an aniline nitrogen *para* to the fluorophore, displaying comparable maximum wavelengths in their absorption, excitation and emission spectra. Ligand **NapL^2**, however, exhibits different photophysical properties, with the aniline nitrogen placed *meta* to the naphthalene fluorophore, displaying higher absorbance, excitation and emission energies.

The higher emission energy observed when the aniline nitrogen is *meta* gives rise to a significantly smaller Stokes' shift of 54 nm between the excitation and emission spectra for **NapL^2**. When the aniline nitrogen is *para* to the naphthalene fluorophore in the case of **NapL^1**, **NapL^4** and **NapL^6**, however, a 204 nm, 200 nm and 166 nm Stokes' shift was seen respectively (**Figure 4.4**).

Large Stokes' shifts are indicative of organic fluorophores that contain an intramolecular charge transfer (ICT) transition. The donation of electron density in the aromatic system from the lone pair of the aniline nitrogen stabilises the excited state, resulting in a bathochromic shift of the absorbance, excitation and emission energy maxima towards the red region of the spectrum in **NapL^1**, **NapL^4** and **NapL^6**. No such charge transfer process is conceivable with **NapL^2** with lower wavelength maxima reported in the absorbance, excitation and emission spectra.

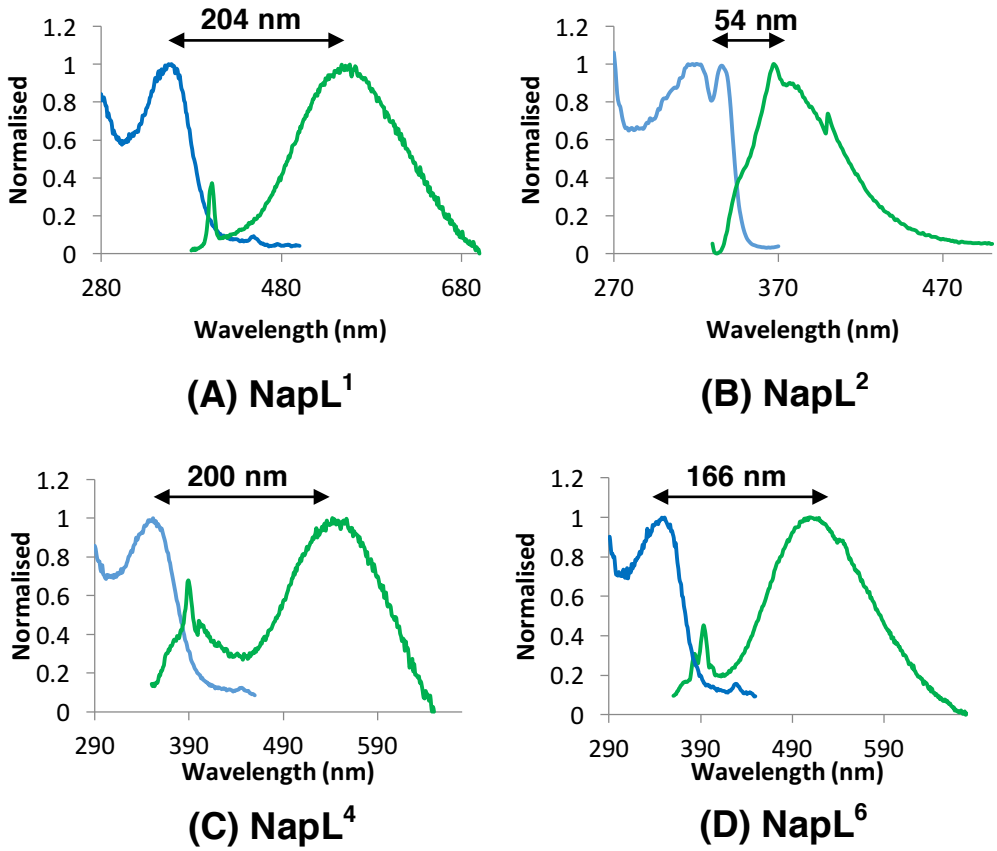

Figure 4.4 Excitation and emission spectra of **(A) NapL[1]** (λ_{ex} = 354 nm, λ_{em} = 530 nm), **(B) NapL[2]** (λ_{ex} = 354 nm, λ_{em} = 370 nm), **(C) NapL[4]** (λ_{ex} = 350 nm, λ_{em} = 530 nm) and **(D) NapL[6]** (λ_{ex} = 347 nm, λ_{em} = 501 nm). Excitation is shown in blue; emission is shown in green, and the corresponding Stokes' shifts are indicated. Ligand concentration 5 μM in 50 mM HEPES, 100 mM KCl, pH = 7.21, 298 K.

Table 4.2 Excitation and emission λ_{max} comparison between **NapL[1]**, **NapL[2]**, **NapL[4]**, **NapL[6]** and Mag-Fura-2 in in 50 mM HEPES, 100 mM KCl, pH = 7.21, 298 K. λ_{ex} and λ_{em} wavelengths for each derivative are displayed in **Figure 4.4**.

Ligand	Excitation λ_{max} (nm)	Emission λ_{max} (nm)
NapL[1]	358	562
NapL[2]	318	372
NapL[4]	350	550
NapL[6]	341	507
Mag-Fura-2[3]	370[3]	510[3]

Typically, Stokes' shifts in comparable systems are below 200 nm. Mag-Fura-2 for example, has a Stokes' shift of 140 nm,[3] while the

1-arylnaphthalene APTRA derivative, developed by London, shows a Stokes' shift of 174 nm.[1] The larger Stokes' shift reported here is probably associated with the increased conjugation provided by the alkyne, compared to the single carbon-carbon bond between the APTRA binding moiety and the 1-naphthalene fluorophore. The increased planarity of the aromatic framework provided in the pyridylalkynylaryl system, also reduces the energy lost by non-radiative decay pathways, causing the wavelength maximum to increase. Such large Stokes' shifts are a highly desirable feature of fluorescent sensors, reducing the interference between absorption and emission processes in photophysical studies.

4.4 pH Studies of NapL^1, NapL^2, NapL^4 and NapL^6

For the vast majority of APTRA analogues in the literature, the pK_a is often not fully determined, as it is thought that APTRA binding moieties are unstable at a low pH and on prolonged standing in aqueous solution.[4-6] An investigation into the response of **NapL^1**, **NapL^2**, **NapL^4** and **NapL^6** with pH in absorption and fluorescence spectroscopy is reported here. All titrations were carried out at a constant ionic strength in 100 mM KCl at 298 K.

4.4.1 Absorbance pH studies of NapL^1, NapL^2, NapL^4 and NapL^6

Normalised absorbance spectra of the ligands in basic and acidic solutions are shown in **Figure 4.5**. In basic solutions, **NapL^1**, **NapL^2**, **NapL^4** and **NapL^6** have an absorption maximum of 351 nm, 318 nm, 350 nm and 345 nm respectively. On protonation of the aniline nitrogen at low pH, a reduction in the absorbance and a blue shift is noted with **NapL^1**, **NapL^4** and **NapL^6**, with an increase in absorbance observed for **NapL^2**.

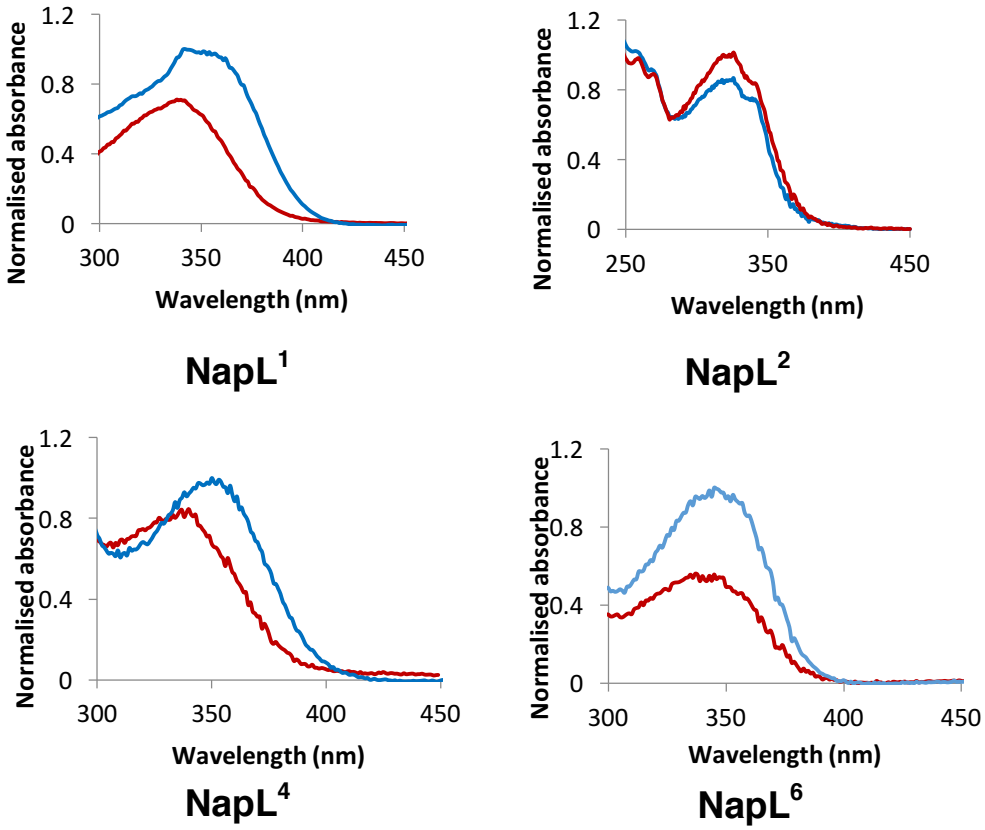

Figure 4.5 Absorbance spectrum of **NapL**[1], **NapL**[2], **NapL**[4] and **NapL**[6] in basic and acidic solutions. Ligand concentration = 10 μM in 100 mM KCl, 298 K.

4.4.2 Fluorescence pH studies of NapL[1], NapL[2], NapL[4] and NapL[6]

The effect of pH on the excitation spectrum of carboxylate-based **NapL**[1] and **NapL**[2] is shown in **Figure 4.6**. pK_a values of 6.2 and 5.7 were determined respectively.

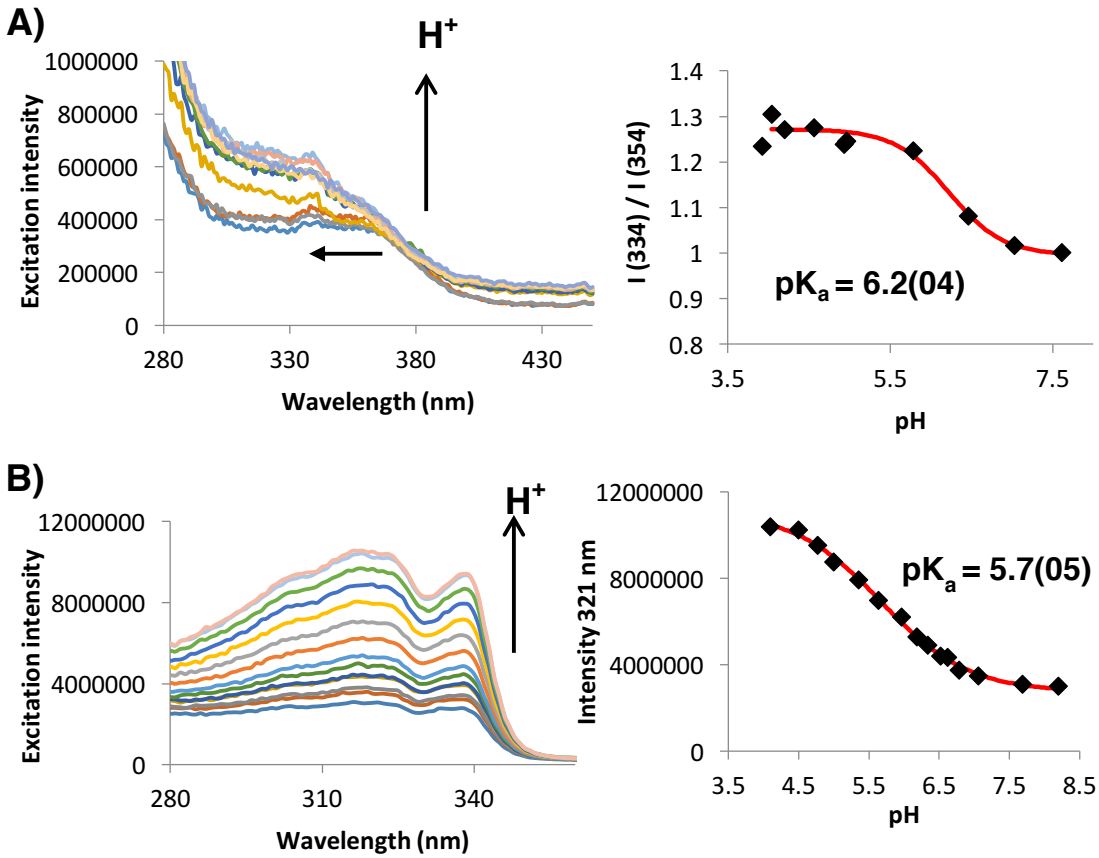

Figure 4.6 (Left) the effect of the pH on the excitation spectrum; (right) the sigmoidal fit of (top) the excitation ratio and (bottom) the excitation intensity with pH of **(A) NapL^1** (λ_{em} = 530 nm) and **(B) NapL^2** (λ_{em} = 370 nm). Ligand concentration = 10 μM in 100 mM KCl, 298 K. Calculated pK_a values are given with an error associated with the fitting.

It is apparent from analysis of **Figure 4.6** that ligand **NapL^1** exhibits a ratiometric response to pH in excitation spectroscopy. A 20 nm hypsochromic shift towards the blue is noted in the excitation spectrum from 354 nm to 334 nm, following aniline nitrogen protonation (pH 8.2 to 4.0). This ratiometric pH response is consistent with the elimination of intramolecular charge transfer within the naphthalene ligand. Protonation stabilises the excited state, as the conjugation involving the aniline nitrogen lone pair is lost. Thus, a pronounced wavelength shift occurs towards the blue region of the spectrum, in both the excitation and absorbance spectra (**Figure 4.5** and **Figure 4.6**). No pronounced changes were observed in the fluorescence emission spectrum of **NapL^1** with pH, however, following excitation at 351 nm.

Ligand **NapL^2**, in contrast, displayed a 'turn-on' response, following reduction of pH from 9.5 to 4.0, with no shift in the excitation or emission

wavelengths on protonation. A 3.5-fold 'turn-on' ratio was observed in both the fluorescence excitation and emission spectra. Such a 'turn-on' effect in solutions at reduced pH can be ascribed to the elimination of photo-induced electron transfer (PET) quenching of the excited state from the aniline lone pair of electrons, that occurs in basic solutions.

Phosphinate-based **NapL^4** and **NapL^6** have pK_a's of 5.2 and 5.1 respectively, comparable to those determined for **NapL^1** and **NapL^2**. The effect of the pH on the excitation spectrum of **NapL^4** and the emission spectrum of **NapL^6** is shown in **Figure 4.7**. An almost identical ratiometric excitation response observed for **NapL^1** was found for the phosphinate derivative, **NapL^4**, with a 28 nm hypsochromic shift observed over the pH range 7.6 to 3.9.

Ligand **NapL^6**, in contrast to **NapL^1**, **NapL^2** and **NapL^4**, showed no pronounced pH sensitivity in the excitation spectrum. On excitation at 342 nm, however, a 2-fold reduction in the emission intensity was observed in acidic solutions. A pK_a of 5.1 was calculated from fluorescence emission spectroscopy, comparable to the pK_a values determined from excitation spectroscopy for **NapL^1**, **NapL^2** and **NapL^4** (**Figure 4.7**).

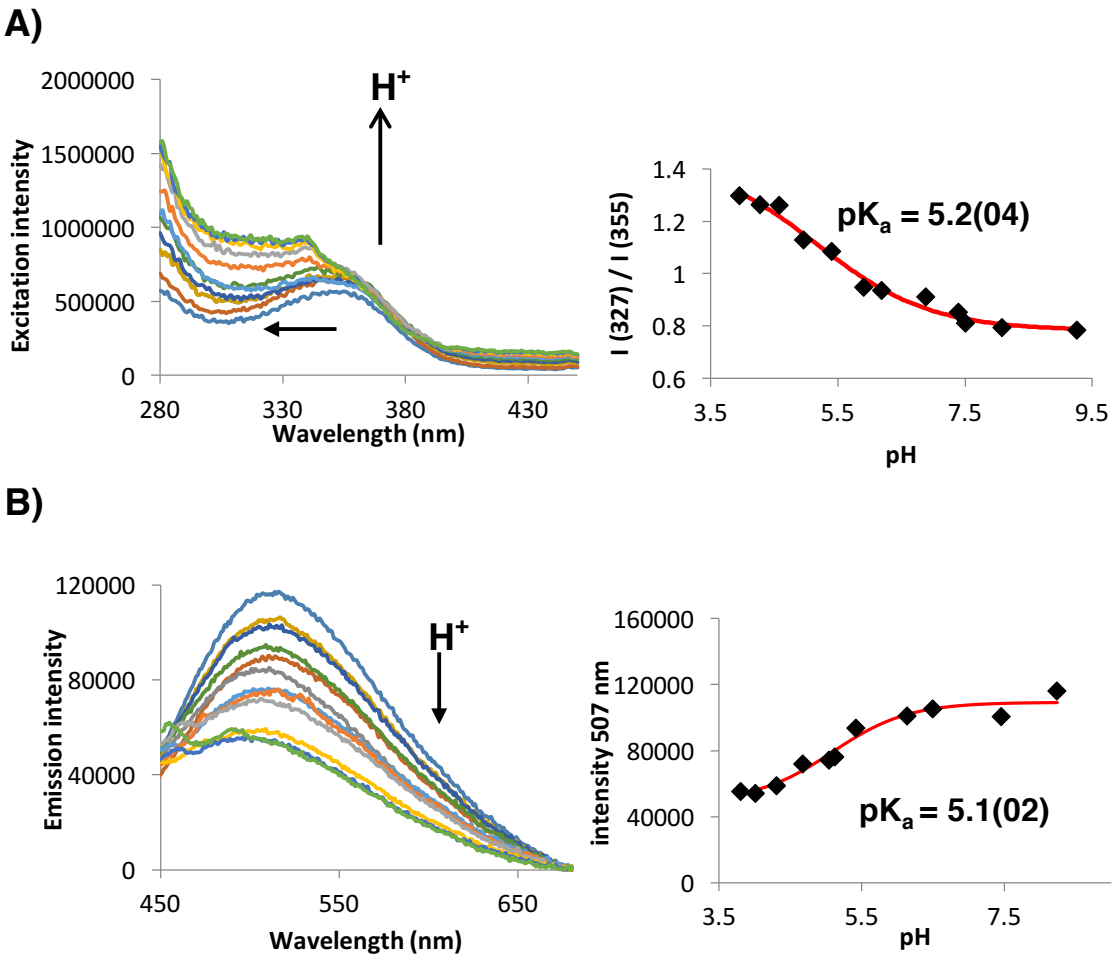

Figure 4.7 (Left) the effect of the pH on the excitation (top) and emission spectrum (bottom); (right) the sigmoidal fit of the intensity with pH of (**A**) **NapL^4** (λ_{em} = 530 nm) and (**B**) **NapL^6** (λ_{ex} = 342 nm). Ligand concentration 10 μM in 100 mM KCl, 298 K. Calculated pK_a values are given with an error associated with the fitting in parenthesis.

The presence of the aniline nitrogen either *para* or *meta* to the naphthalene fluorophore was seen to have little effect on the observed pK_a values across the series. Naphthalene derivatives **NapL^1**, **NapL^2**, **NapL^4** and **NapL^6**, each display pK_a values in the range 5.1 to 6.2, comparable to APTRA based sensors in the literature. Mag-Fura-2, for example, has a pK_a of 5.0 determined from fluorescence excitation spectroscopy.[3]

It is also important to note that from the analysis of **Figure 4.6** and **Figure 4.7**, naphthalene analogues **NapL^1**, **NapL^2**, **NapL^4** and **NapL^6** are all insensitive to pH changes in the physiological range pH 6.5 to 7.5. Insignificant changes in the fluorescence emission and excitation spectra were observed

within this region, making them suitable probes to sense the change in metal ion concentrations *in vivo* or *in cellulo.* Such pH insensitivity over the physiological range is a characteristic feature of the Fura-2 family of indicators, including Mag-Fura-2, where it is known that at physiological pH the aniline nitrogen and carboxylate groups are all deprotonated and available for the binding of divalent metal cations.[3,7,8]

4.5 Binding studies of carboxylate-based NapL^1 and NapL^2

The binding of carboxylate-based APTRA analogues **NapL^1** and **NapL^2** to Mg^{2+}, Ca^{2+} and Zn^{2+} is reported here. It is expected that a [5, 5, 5] set of ring chelates will form in each instance on metal binding. Comparisons will be made between **NapL^1** and **NapL^2** to determine how the position of the aniline nitrogen atom on the APTRA binding moiety affects the selectivity and affinity for Mg^{2+}, Ca^{2+} and Zn^{2+}.

4.5.1 Absorbance binding studies of NapL^1 and NapL^2

The absorption spectra of **NapL^1** and **NapL^2** were recorded in 50 mM HEPES, 100 mM KCl at a pH maintained at 7.21. An absorbance maximum of 354 nm and 326 nm in the 'metal-free' state was reported for **NapL^1** and **NapL^2** respectively (**Figure 4.8**, **Table 4.4**).

A 28 nm hypsochromic shift to lower wavelengths was observed following binding of Mg^{2+}, Ca^{2+} and Zn^{2+} to **NapL^1** with a maximum of 326 nm in the metal-bound state and an isosbestic point present at 330 nm. Ligand **NapL^2**, however, displayed significant differences to **NapL^1,** with no blue shift observed in the absorption spectrum on metal binding. A small increase in the absorbance intensity was, however, observed at 326 nm (**Figure 4.8, Table 4.3**).

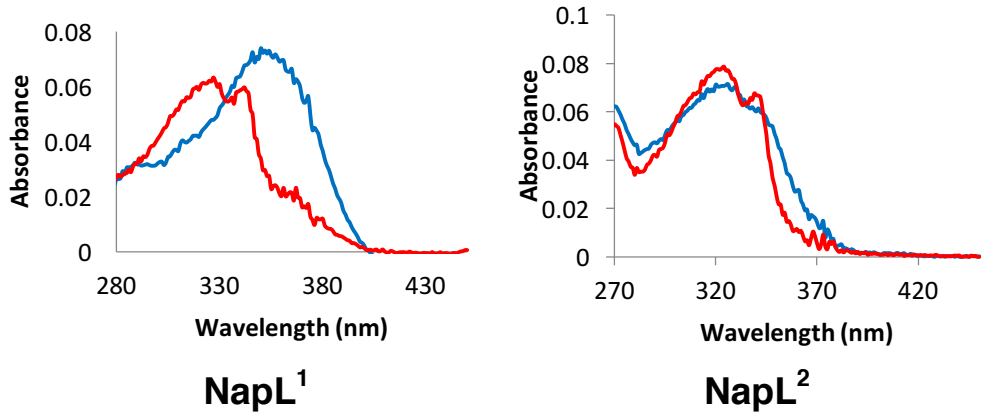

Figure 4.8 The absorption spectrum of **NapL**^{1} and **NapL**^{2} in the 'free' and 'metal-bound' state after the addition of 40 mM Mg^{2+} in aqueous solutions. The same spectral response is observed after the addition of Ca^{2+} and Zn^{2+} for both **NapL**^{1} and **NapL**^{2} in 50 mM HEPES, 100 mM KCl, pH = 7.21, 298 K

Table 4.3 The absorption maximum for the 'free' ligand and the 'metal-bound' state after the addition of 40 mM Mg^{2+} to **NapL**^{1} and **NapL**^{2} in 50 mM HEPES, 100 mM KCl, pH = 7.21, 298 K.

Ligand	Absorption λ_{max} (nm)
NapL^{1}	354, 326
NapL^{2}	326, 326

4.5.2 Excitation and emission binding studies of NapL^{1}

Excitation and emission studies following the addition of Mg^{2+}, Ca^{2+} and Zn^{2+} to **NapL**^{1} and **NapL**^{2} were carried out at 298 K in HEPES buffer at a constant pH of 7.21. All reported errors for the calculated dissociation constants (K_d) are due to an experimental variability.

In the metal-free state, **NapL**^{1} exhibits an excitation maximum at 358 nm. On the addition of Mg^{2+}, Ca^{2+} and Zn^{2+}, a pronounced wavelength shift of 38 nm towards the blue was observed (**Figure 4.9**). The wavelength shift observed on metal binding is similar to that observed on protonation of the aniline nitrogen atom at a reduced pH (**Section 4.4.2**). Such behaviour implies that the aniline nitrogen atom is taking part in binding to Mg^{2+}, Ca^{2+} and Zn^{2+}.

Ligand **NapL[1]** has the potential to be used as an excitation-based ratiometric sensor, with two distinct bands present in the excitation spectra in the 'free' and 'bound' states.

The excitation-based ratiometric behaviour seen here has been reported previously in a number of different cation sensors for Mg^{2+} and Ca^{2+},[1,3,9,10] including Mag-Fura-2 where a 35 nm shift towards the blue was observed in the metal-bound state.[3] Ratiometric behaviour for sensors of this type was first highlighted by Tsien and co-workers in the development of the parent probe Fura-2, for Ca^{2+} sensing.[7]

The wavelength shift observed in the absorbance and excitation spectrum for cation sensors of this type can be attributed to the change in character of the excited state. In the 'metal-free' form the excited state is based on intramolecular charge transfer from the lone pair of electrons on the aniline nitrogen atom to the aromatic fluorophore. On protonation and metal ion binding, the conjugation between the lone pair and the aromatic fluorophore is lost, disrupting the charge transfer process in the 'metal-bound' species.

TD-DFT models have been utilised to study the effect of Mg^{2+} binding on the excited state of Mag-Fura-2. It was found that after complexation with Mg^{2+} ions, no charge transfer occurred, with the excited state possessing localised $\pi\pi^*$ character.[8] The perturbation of the ICT state on metal binding, therefore, results in the hypsochromic shift observed in both the absorbance and excitation spectrum.

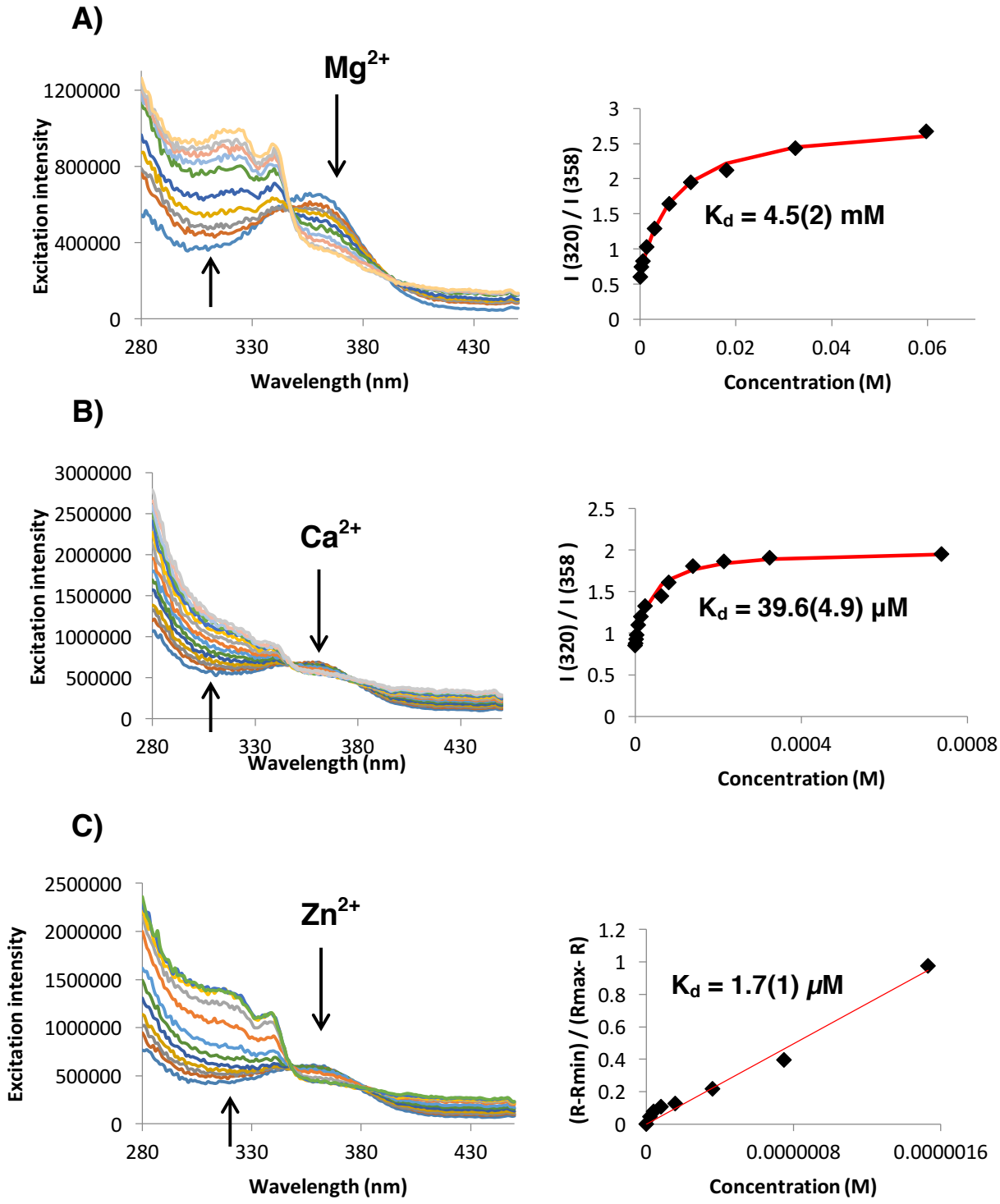

Figure 4.9 (Left) excitation spectrum; (right) fitting of excitation intensity against the added concentration of **(A)** Mg^{2+}, **(B)** Ca^{2+} and **(C)** Zn^{2+} in a 1:1 binding model. **NapL^1** concentration = 5 µM, in 50 mM HEPES, 100 mM KCl, pH 7.21, 298 K. λ_{em} = 530 nm. The reported binding constants are an average of two separate metal ion titrations, and are given with the experimental error in parenthesis.

Dissociation constants have been calculated from excitation spectra, using the ratio of the metal-free (350 nm) and metal-bound (320 nm) species in each instance. Data was fitted to a 1:1 binding model against the concentration of added Mg^{2+}, Ca^{2+} and Zn^{2+}. A 1:1 ligand:metal stoichiometry for the addition of metal ions has been assumed, based on the 1:1 binding present in multiple APTRA analogues in the literature.[1,3,9,10] Dissociation constants of 4.5 mM, 39.6 μM and 1.7 μM were obtained for Mg^{2+}, Ca^{2+} and Zn^{2+} respectively (**Figure 4.9**).

The emission spectrum of **NapL^1** has two maxima at 372 nm and 537 nm, observed following excitation at the isosbestic point in the absorbance spectrum (λ_{ex} = 330 nm, **Figure 4.10**) in both the metal-free and bound states. Upon binding of Mg^{2+} a 5-fold and 2-fold increase in the intensity was seen at 372 nm and 537 nm respectively. Addition of Ca^{2+}, on the other hand, led to a 5-fold increase in the emission intensity at 372 nm, and a smaller decrease in the intensity at 537 nm (See **Appendix, Figure A.1**). The ligand **NapL^1**, therefore, also has the potential to be used as an emission-based ratiometric indicator, as a different 'turn-on' emission spectral response is seen at both 372 nm and 537 nm.

Excitation at the absorbance maximum of **NapL^1** (λ_{ex} = 354 nm), resulted in a 3-fold decrease or 'turn-off' in the total emission intensity at 562 nm, and a small blue shift of 40 nm (**Figure 4.10**).

Comparable dissociation constants for the binding of Mg^{2+}, Ca^{2+} and Zn^{2+} were determined from fluorescence emission spectral changes, to those determined using excitation spectroscopy from **Figure 4.9**. The dissociation constants calculated for the binding of Mg^{2+} via emission spectroscopy are highlighted in **Figure 4.10** (λ_{ex} = 330 nm and λ_{ex} = 354 nm). Dissociation constants fell in the low mM range. Excitation at the isosbestic point of 330 nm, allowed the K_d values to be calculated from the ratio of the emission intensity at 372 nm and 537 nm reducing potential interference from environmental effects. The dissociation constants determined for the binding of Ca^{2+} and Zn^{2+} via changes observed in emission spectroscopy are very similar to those calculated

in **Figure 4.9,** and close to within the experimental error (See **Appendix Figure A.1** and **Figure A.2**).

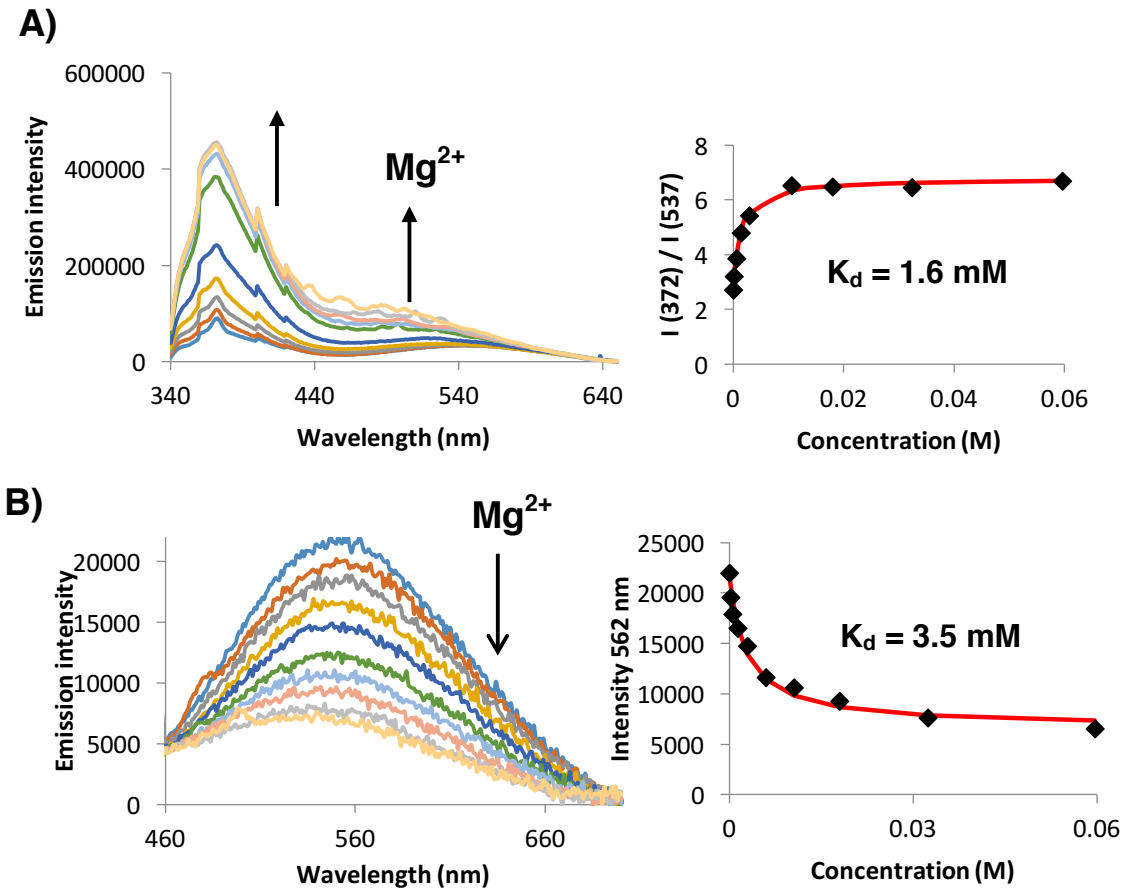

Figure 4.10 (Left) emission spectrum of **NapL^1**; (right) fitting of emission intensity against the added concentration with excitation at **(A)** λ_{ex} = 330 nm and **(B)** λ_{ex} = 354 nm after the addition of Mg^{2+}. Ligand concentration = 5 μM, in 50 mM HEPES, 100 mM KCl, pH 7.21.

4.5.3 Excitation and emission binding studies of NapL^2

In contrast to the excitation- and emission-based ratiometric behaviour reported for **NapL^1**, the behaviour of **NapL^2** was non-ratiometric, following addition of Mg^{2+}, Ca^{2+} and Zn^{2+}. No blue shift was observed in the absorbance, excitation or emission spectra, on binding of divalent cations. The wavelength maximum in the 'metal-free' and 'bound' states was 318 nm and 372 nm in the excitation and emission spectrum respectively (**Figure 4.11**).

Unlike **NapL^1**, the excited state of **NapL^2** is thought to possess localised $\pi\pi^*$ character, in both the 'metal-free' and the 'metal-bound' states. No significant

amounts of intramolecular charge transfer occurs in the 'metal-free' state of **NapL^2**, because no conjugation of the *meta* aniline nitrogen lone pair of electrons into the naphthalene fluorophore is conceivable. The absence of any charge transfer processes in the 'un-bound' state of **NapL^2**, means that no wavelength shift occurs on the binding of divalent metal ions.

The ligand **NapL^2** can be considered as a 'turn on' sensor, with a 3.2-, 6- and 9-fold increase in the excitation and emission intensity respectively, following addition of Mg^{2+}, Ca^{2+} and Zn^{2+} (**Figure 4.11**). The emission and excitation profiles after the addition of divalent cations are comparable to those found earlier following protonation of the aniline nitrogen, where a 3.5-fold 'turn-on' response was observed in acidic solution (see **Section 4.4.2**). This behaviour suggests that as with **NapL^1**, the aniline nitrogen takes part in binding to Mg^{2+}, Ca^{2+} and Zn^{2+}. The 'turn-on' nature of **NapL^2** on protonation and metal ion binding, can be attributed to the suppression of photo-induced electron transfer (PET) quenching of the ligand excited state caused by the aniline nitrogen lone pair of electrons in basic and 'metal-free' solutions.

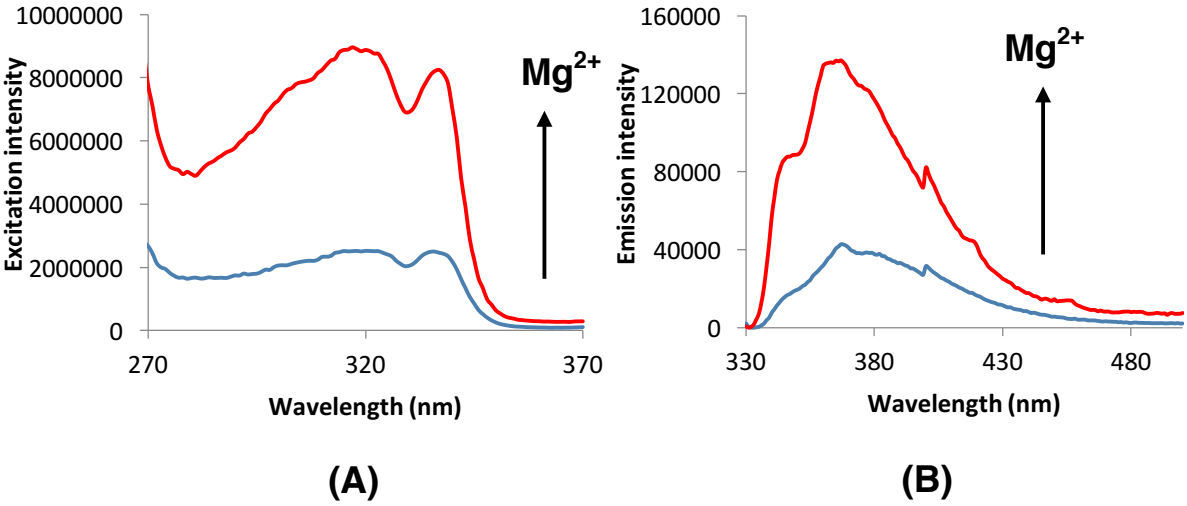

Figure 4.11 The increase in the fluorescence **(A)** excitation and **(B)** emission intensity on the addition of 35 mM Mg^{2+}. A 3.5- and 9-fold 'turn-on' in the excitation and emission intensity was observed on the addition of Ca^{2+} and Zn^{2+} respectively. Ligand concentration = 10 μM, in 50 mM HEPES, 100 mM KCl, pH 7.21. λ_{ex} = 326 nm, λ_{em} = 377 nm.

Fluorescence excitation titrations following addition of Mg^{2+}, Ca^{2+} and Zn^{2+} to **NapL^2** are shown in **Figure 4.12**, along with their calculated dissociation constants (K_d), determined for a 1:1 ligand to metal binding stoichiometry.

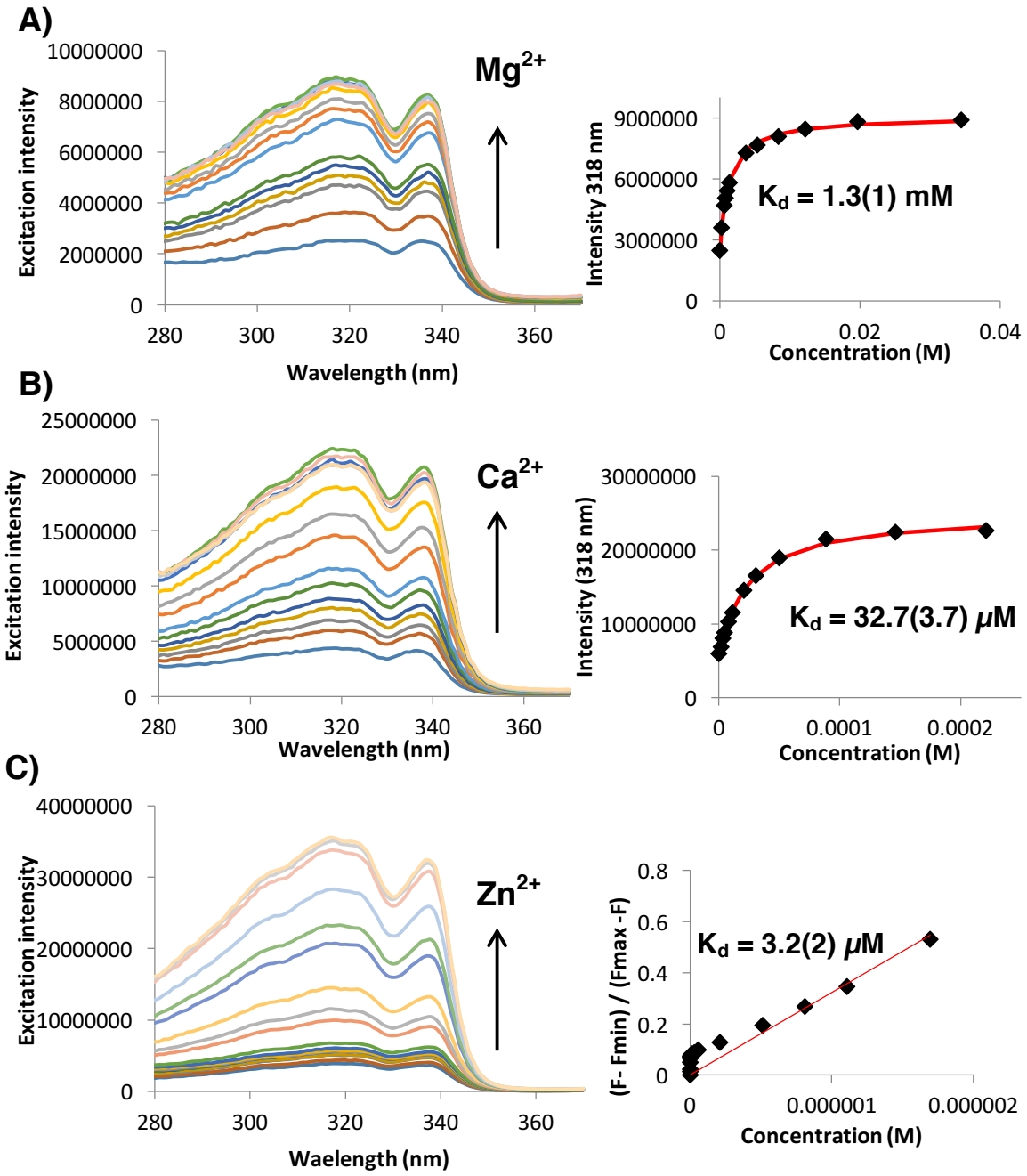

Figure 4.12 (Left) excitation spectrum; (right) fitting of excitation intensity against the added concentration of **(A)** Mg^{2+}, **(B)** Ca^{2+} and **(C)** Zn^{2+} in a 1:1 binding model. **NapL^2** ligand concentration = 10 μM, in 50 mM HEPES, 100 mM KCl, pH 7.21, 298 K, λ_{em} = 377 nm. The reported dissociation constants are an average of two separate metal ion titrations, and are given with the experimental error in parenthesis.

The dissociation constants for the 1:1 stoichiometry between metal ion and indicator were calculated by iteratively fitting the change in the excitation

maximum with the concentration of added Mg^{2+}, Ca^{2+} and Zn^{2+}. Dissociation constants of 1.3 mM, 32.7 μM and 3.2 μM were determined respectively.

Comparable dissociation constants, within the experimental error, to those calculated in **Figure 4.12** were found for the binding of Mg^{2+}, Ca^{2+} and Zn^{2+} to **NapL^2** via fluorescence emission spectroscopy (See **Appendix Figure A.3**, **Figure A.4** and **Figure A.5** respectively).

4.5.4 Summary: Comparison of of the metal ion binding affinities and selectivities of NapL^1 and NapL^2

Changing the position of the nitrogen and oxygen atoms on the APTRA binding framework was found not to dramatically affect the pK_a of the four naphthalene derivatives (**Section 4.4**). The reported affinity and selectivity for Mg^{2+}, Ca^{2+} and Zn^{2+} is also comparable, whether the aniline nitrogen atom is *para* or *meta* to the naphthalene fluorophore. A summary of the excitation and emission maxima and the calculated association constants for **NapL^1** and **NapL^2** compared to commercially available Mag-Fura-2 is highlighted in **Table 4.4**.

Both **NapL^1** and **NapL^2** have dissociation constants in the low mM range for the addition of Mg^{2+}. These values align with the concentrations of 'free' Mg^{2+} in mammalian cells (0.8-1.5 mM)[11] and the affinity of commercially available sensors such as Mag-Fura-2, where an association constant of 1.8 mM has been determined previously (**Table 4.4**).[3]

In accordance with many APTRA analogues reported in the literature, **NapL^1** and **NapL^2** have dissociation constants for Ca^{2+} in the mid μM range. Dissociation constants of 39.6 μM and 32.7 μM were calculated for **NapL^1** and **NapL^2** respectively. In comparison, the aryl-naphthalene derivatives developed by London *et al.* gave a dissociation constant of 17 μM,[1] while Mag-Fura-2 gave rise to a dissociation constant of 25 μM.[3] The Ca^{2+} / Mg^{2+} selectivity of **NapL^1** and **NapL^2** is not a surprise, and is an ever present problem associated with the APTRA series of fluorescent indicators. The higher affinity reported for Ca^{2+} over Mg^{2+} allows sensors **NapL^1** and **NapL^2**, along with many APTRA analogues

before them, to have the potential to also be used as low affinity Ca^{2+} sensors in calcium-rich regions of the body.

The dissociation constants for Zn^{2+} binding with **NapL^1** and **NapL^2** are in the low μM range, and values of 1.7 μM and 3.2 were observed respectively (**Table 4.4**). This is a significantly lower affinity than the values observed for many APTRA analogues reported in the literature, where a nM affinity was typically observed. A 20 nM dissociation constant for Mag-Fura-2 has been previously observed, for example.[12]

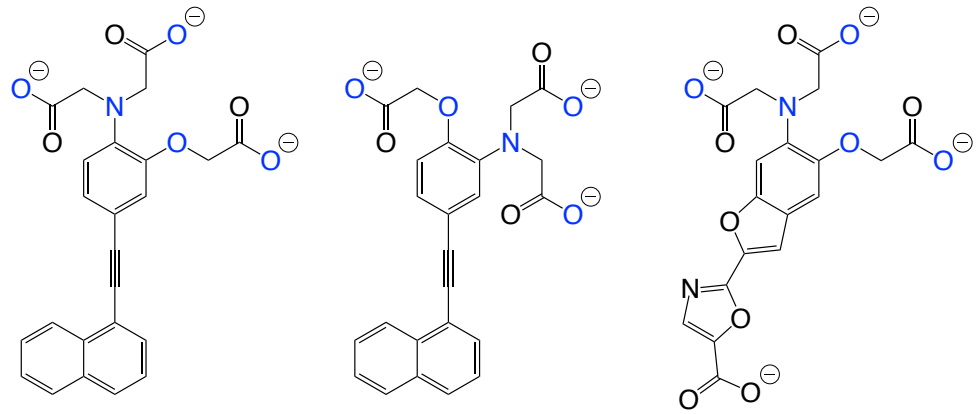

NapL^1 **NapL^2** **Mag-Fura-2**

Figure 4.13 The structures of **NapL^1**, **NapL^2** and Mag-Fura-2.[3]

Table 4.4 The direct comparison of the excitation maximum, emission maximum and dissociation constants for the binding of Mg^{2+}, Ca^{2+} and Zn^{2+} to **NapL^1**, **NapL^2** and commercially available Mag-Fura-2[3] in aqueous solutions. Mg^{2+} saturated wavelengths are highlighted in red.

Ligand	Excitation λ_{max} (nm)	Emission λ_{max} (nm)	K_d (Mg^{2+})	K_d (Ca^{2+})	K_d (Zn^{2+})
NapL^1	358, 320	562, 522	4.5(2) mM	39.6(4.9) μM	1.7(1) μM
NapL^2	318, 318	372, 372	1.3(1) mM	32.7(3.7) μM	3.2(2) μM
Mag-Fura-2[3]	370, 335[3]	510, 510[3]	1.9 mM[3]	25 μM[3]	20 nm[12]

The position of the aniline nitrogen on the APTRA binding moiety relative to the position of the fluorophore does, however, have a notable effect on the excitation and emission profiles in the 'free' and 'metal-bound' states of **NapL^1** and **NapL^2**. Ligand **NapL^1** is a ratiometric sensor in both excitation and emission, allowing dissociation constants to be calculated from two independent wavelengths. Such ratiometric behaviour has been seen in numerous APTRA analogues, and is due to the perturbation of the internal charge transfer from the aniline nitrogen to the aromatic fluorophore on metal ion binding.

The **NapL^2** ligand, is, however, non-ratiometric. Instead a 'turn-on' response is observed in both the excitation and emission spectra following protonation or binding to Mg^{2+}, Ca^{2+} and Zn^{2+}.

4.6 Binding studies of the phosphinate ligands NapL^4 and NapL^6

The binding of the phosphinate-based APTRA analogues **NapL^4** and **NapL^6** to Mg^{2+}, Ca^{2+} and Zn^{2+} is reported here. Ligand **NapL^4** contains the APDAP binding moiety previously discussed in **Chapter 3** where a single phosphinate group is added at the expense of a carboxylate binding group. Ligand **NapL^6**, unlike **NapL^1**, **NapL^2** and **NapL^4**, is tridentate, with one carboxylate, one phosphinate and the aniline nitrogen atom available to bind to a metal ion at physiological pH. It is expected that **NapL^6** will form a [6, 5] chelate ring arrangement on metal binding.

Comparisons will be made with the carboxylate-based APTRA analogues **NapL^1** and **NapL^2** (**Section 4.5**) to assess the effect of introducing a phosphinate group at the expense of a carboxylate group on metal ion binding affinity and selectivity for Mg^{2+}, Ca^{2+} and Zn^{2+}.

4.6.1 Absorbance binding studies of NapL^4 and NapL^6

The phosphinate analogue, **NapL^4**, was found to have a maximum absorption wavelength of 350 nm in the metal-free state. Unlike the carboxylate-based ligand **NapL^1**, **NapL^4** showed no blue shift or isosbestic point on the addition of Mg^{2+}. A blue shift was, however, observed in the absorption spectrum

on the addition of Ca^{2+} and Zn^{2+} with an absorbance maximum at 314 nm in the metal-bound state and an isosbestic point at 330 nm (**Figure 4.14, Table 4.5**).

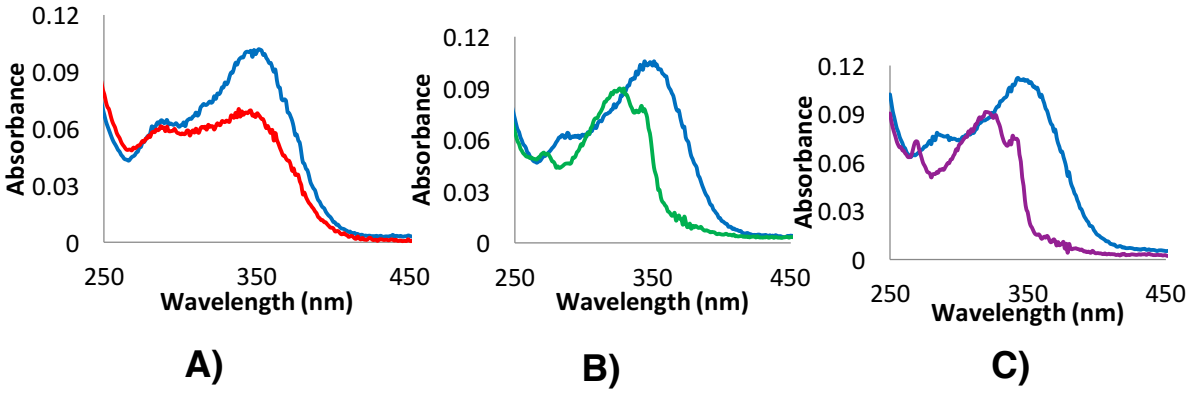

Figure 4.14 Absorbance spectrum of **NapL^4** following addition of **(A)** Mg^{2+} (8 mM) **(B)** Ca^{2+} (4 mM) and **(C)** Zn^{2+} (20 μM). Ligand concentration = 10 μM in 50 mM HEPES, 100 mM KCl, pH = 7.21, 298 K.

The absorbance spectrum of **NapL^6**, in contrast, showed small changes following the addition of 150 mM Mg^{2+}, 2.4 mM Ca^{2+} and 55.6 μM Zn^{2+}. A wavelength maximum of 346 nm was measured in the absorbance spectrum both before and after the addition of divalent metal ions (**Figure 4.15, Table 4.5**).

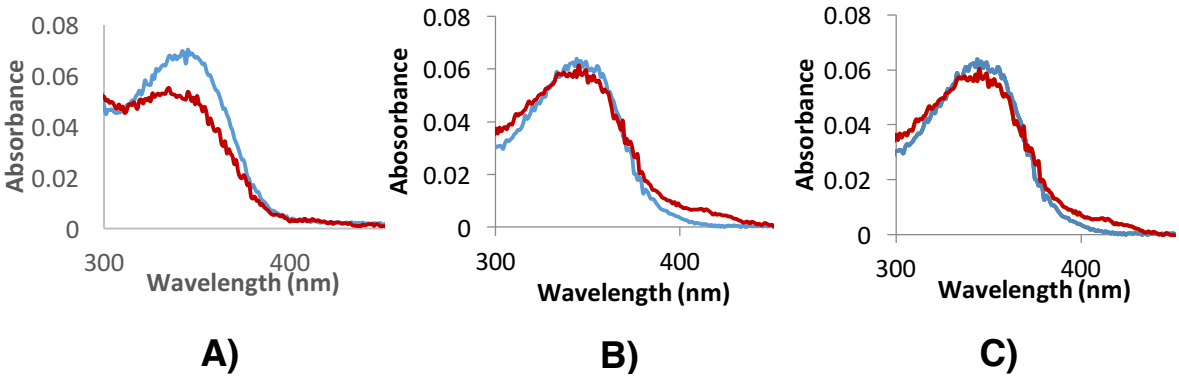

Figure 4.15 Absorbance spectrum of **NapL^6** for the addition of **(A)** Mg^{2+} (160 mM), **(B)** Ca^{2+} (2.4 mM) and **(C)** Zn^{2+} (56 μM). Ligand concentration = 5 μM in 50 mM HEPES, 100 mM KCl, pH = 7.21, 298 K.

Table 4.5 The absorption maximum for the 'free' ligand and the metal-bound state after the addition of Mg^{2+}, Ca^{2+} and Zn^{2+} to **NapL^4** and **NapL^6** in aqueous solutions.

Ligand	**Absorbance λ_{max} (nm)**			
	'free'	**Mg^{2+}**	**Ca^{2+}**	**Zn^{2+}**
NapL^4	350	350	314	314
NapL^6	346	346	346	346

4.6.2 Fluorescence binding studies of phosphinate-based NapL^4

The binding of the phosphinate-based APTRA analogues **NapL^4** and **NapL^6** to Mg^{2+}, Ca^{2+} and Zn^{2+} was investigated in aqueous solution by fluorescence emission and excitation spectroscopy.

Unlike **NapL^1**, the APDAP phosphinate analogue **NapL^4** showed no significant ratiometric behaviour in its absorption (**Figure 4.13**) or excitation spectra following the addition of Mg^{2+}. A small shift of 10 nm to lower wavelength was observed between the 'metal-free' and the 'metal-bound' states (**Figure 4.16**).

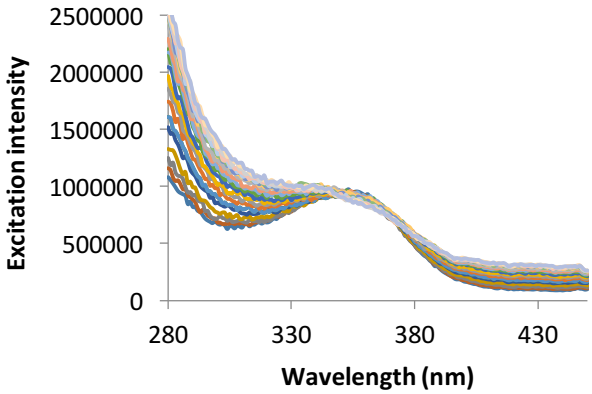

Figure 4.16 The excitation spectrum of **NapL^4** following addition of Mg^{2+}. In 50 mM HEPES, 100 mM KCl, pH = 7.21, 298 K.

A different response was, therefore, observed for the addition of Mg^{2+} compared to the excitation-based pH response of **NapL^4**. At low pH, a 28 nm wavelength shift to lower wavelengths was reported (**Section 4.4.2**, **Figure 4.7**), suggesting that the aniline nitrogen of **NapL^4** does not take part in binding to Mg^{2+}. Indeed, no ratiometric behaviour was observed in the excitation spectrum on saturation with Mg^{2+}.

The small changes observed in excitation intensity on addition of Mg^{2+} meant it was not feasible to generate dissociation constants via this method. Instead, dissociation constants were determined from variations in the fluorescence emission spectra, following excitation at 350 nm. An emission maximum at 545 nm was found in the 'metal-free' state, with an 18 nm shift to lower wavelengths on saturation with Mg^{2+} (**Figure 4.17**).

The emission spectrum of **NapL^4** for addition of Mg^{2+}, and the excitation spectrum of **NapL^4** for addition of Ca^{2+} and Zn^{2+}, are presented in **Figure 4.17**. Dissociation constants of 0.5 mM, 0.4 mM and 3.3 μM were obtained respectively, assuming a 1:1 stoichiometry between Mg^{2+}, Ca^{2+} and Zn^{2+} ions.

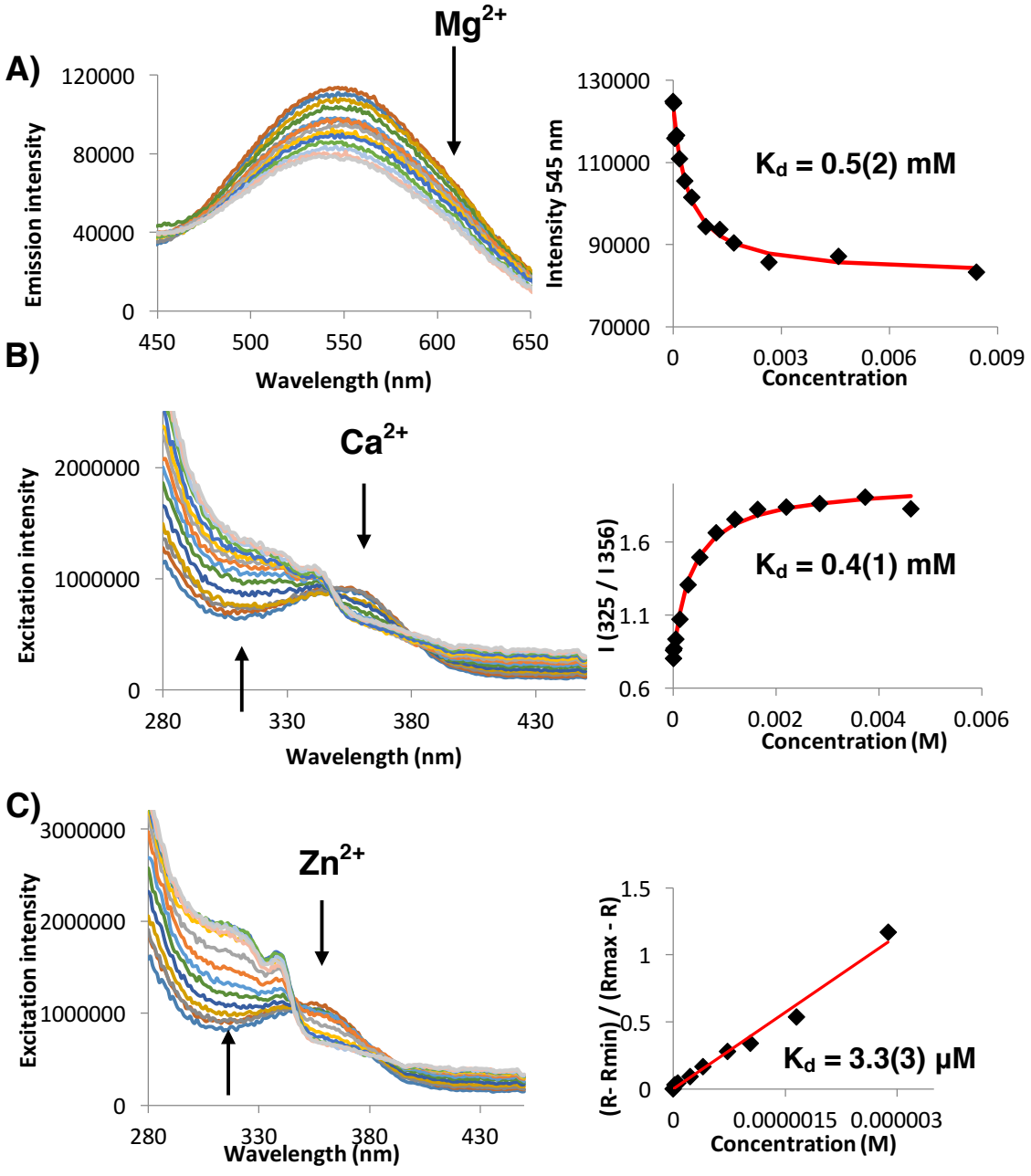

Figure 4.17 (Left) emission / excitation spectra; (right) fitting of excitation intensity against the added concentration of **(A)** Mg^{2+}, **(B)** Ca^{2+} and **(C)** Zn^{2+} to a 1:1 binding model. **NapL^4** ligand concentration = 10 µM, in 50 mM HEPES, 100 mM KCl, pH 7.21, 298 K, λ_{ex} = 350 nm, λ_{em} = 530 nm. The reported dissociation constants are an average of two separate metal ion titrations, and are given with the experimental error in parenthesis.

It is evident from analysis of K_d data shown in **Figure 4.17** that the addition of Ca^{2+} and Zn^{2+} to **NapL^4** resulted in the same excitation-based ratiometric response observed on the protonation of **NapL^4**. A 31 nm hypsochromic shift was observed following addition of both Ca^{2+} and Zn^{2+}. A similar response was observed with the binding of Mg^{2+}, Ca^{2+} and Zn^{2+} to the carboxylate analogue **NapL^1**, suggesting that the aniline nitrogen atom of **NapL^4** takes part in binding to both Ca^{2+} and Zn^{2+}. On binding, the intramolecular charge transfer process from the aniline nitrogen atom to the naphthalene fluorophore is disrupted, with the excited state possessing localised π π* character in the 'bound' state.[8]

The emission spectral response of **NapL^4** following addition of Ca^{2+} and Zn^{2+} was studied, with excitation at 330 nm and 350 nm. Excitation at the isosbestic point in the absorbance spectra (λ_{ex} = 330 nm) resulted in two emission maxima at 372 nm and 544 nm (**Figure 4.18**), as observed for **NapL^1**. Upon the addition of Ca^{2+}, inconsistent changes in the emission intensity at both 372 nm and 544 nm meant that a dissociation constant could not be calculated. Ligand **NapL^4**, however, did possess an emission-based ratiometric behaviour for the addition of Zn^{2+}, producing a comparable dissociation constant within the experimental error from that measured from excitation spectroscopy (See **Appendix, Figure A.6**).

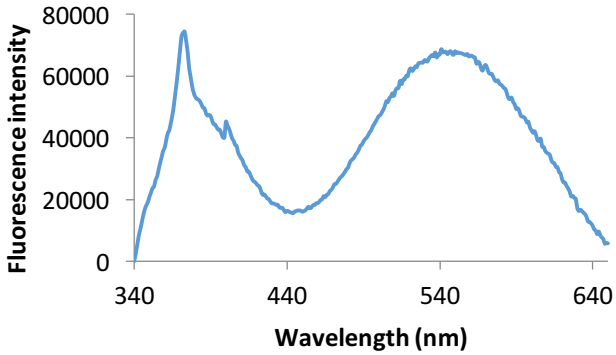

Figure 4.18 The emission spectrum of **NapL^4**, in its 'metal-unbound' state. Ligand concentration = 10 μM in 50 mM HEPES, 100 mM KCl, pH = 7.21, 298 K.

Excitation at the absorbance maximum of **NapL^4** (λ_{em} = 350 nm), resulted in a 3-fold reduction of the total emission intensity at 544 nm (**Figure 4.19**). Comparable dissociation constants were calculated from the decrease in fluorescence emission at 544 nm that lie within the error of the K_d measured for the binding of Ca^{2+} by excitation spectroscopy.

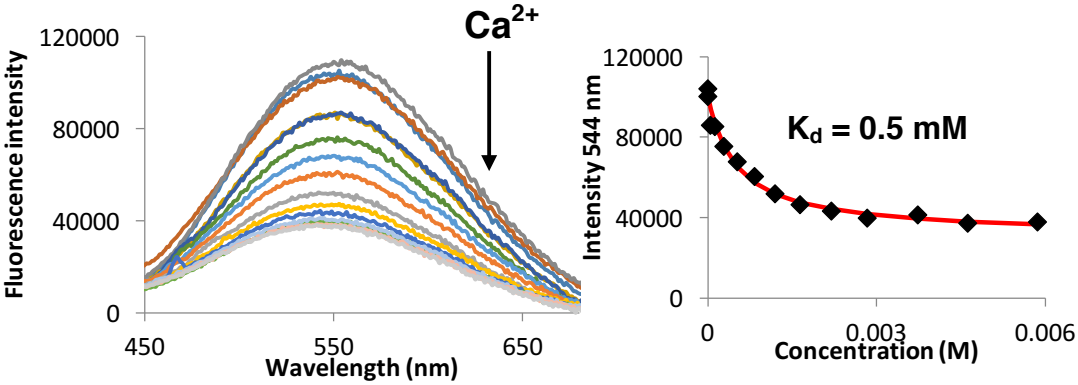

Figure 4.19 (Left) emission spectrum of **NapL^4**; (right) fitting of emission intensity against the added concentration with excitation at λ_{ex} = 350 nm following addition of Ca^{2+}. Ligand concentration = 10 μM, in 50 mM HEPES, 100 mM KCl, pH 7.21, 298 K.

4.6.3 Summary: Comparison of of the metal ion binding affinities and selectivities of NapL^1 and NapL^4

Ligands **NapL^1** and **NapL^4** have significant differences in their spectral response, affinity and selectivity to Mg^{2+}, Ca^{2+} and Zn^{2+}.

The carboxylate-based ligand, **NapL^1**, can be incorporated into the Fura-2 family of indicators. Metal ion sensors of this type, including Mag-Fura-2, are known to undergo intramolecular charge transfer processes, typically, showing ratiometric behaviour on protonation and on addition of Mg^{2+}, Ca^{2+} and Zn^{2+}.[1,3,8,8,11] The protonation or metal ion binding of the aniline nitrogen, disrupts this charge transfer donation of the nitrogen lone pair, resulting in pronounced wavelength shifts both the absorbance and excitation spectra.[8]

Ligand **NapL^4**, however, showed no significant intensity change or hypsochromic shift on the binding of Mg^{2+}, indicating that the aniline nitrogen does not take part in binding to Mg^{2+}, with the intramolecular charge transfer process from the aniline nitrogen atom to the fluorophore still present in the

'metal-bound' state. Near identical behaviour was observed for the binding of Mg^{2+} to APDAP, (**Section 3.4**, **Figure 3.4**), where it was also thought that the aniline nitrogen atom, likewise, takes no part in binding to Mg^{2+}. It is therefore, both interesting and surprising to note that **NapL^4** has a lower dissociation constant and, therefore, a higher affinity for Mg^{2+}, compared to that reported for **NapL^1** and **NapL^2** (4.5 mM vs. 0.5 mM, **Table 4.6**).

In contrast, the binding of **NapL^4** with Ca^{2+} and Zn^{2+} resulted in emission and excitation-based ratiometric behaviour, comparable to that found with **NapL^1** and the pH response of **NapL^4**. Such behaviour demonstrates that the aniline nitrogen of **NapL^4** takes part in binding to Ca^{2+} and Zn^{2+}, eliminating the charge transfer process to the naphthalene fluorophore. Comparable affinity for Zn^{2+}, K_d = 1.7 μM, 3.2 μM and 3.3 μM was evident for **NapL^1**, **NapL^2** and **NapL^4** respectively. The presence of a phosphinate group, instead of a carboxylate binding group, therefore, has no dramatic effect on Zn^{2+} binding affinity, with each dissociation constant remaining in the low μM range.

The phosphinate-based APDAP chelate shows much higher Mg^{2+} / Ca^{2+} binding selectivity than the carboxylate analogue APTRA, with a 110-fold weaker binding affinity towards Ca^{2+}. Ligand **NapL^4**, predictably, follows the same trend, with a 10-fold reduced affinity for Ca^{2+}, and a K_d value in the low mM range compared to the μM range observed for **NapL^1** and **NapL^2**. Dissociation constants of 0.4 mM and 39.6 μM were calculated for **NapL^4** and **NapL^1** respectively (**Table 4.5**).

In **Section 3.5**, a detailed DFT investigation was carried out in an attempt to gain an improved understanding towards the increased Mg^{2+} selectivity observed for the APDAP chelate. It was found from a DFT computational study that longer P–O, and P–C bonds were present in the phosphinate chelate resulting in less acute bite angles around Mg^{2+} in $[Mg(APDAP)(H_2O)]^-$. Significantly shorter M–O and M–N bond lengths were measured in the Mg^{2+} complex, with the phosphinate chelate possessing features more characteristic of a 6-membered ring chelate than its carboxylate analogue. An enhanced selectivity for Mg^{2+} was also observed when the APDAP chelate was incorporated

into a naphthalene fluorophore. Although the P–O, P–C, M–N and M–O bond lengths were not calculated in **NapL^4**, it is expected that they are longer than the C–O, C–C bond lengths in **NapL^1**, contributing to the 10-fold reduced affinity reported for Ca^{2+}. It is thought, therefore, that the increased binding selectivity observed for **NapL^4** with Mg^{2+}, is due to binding of the larger Ca^{2+} being more thermodynamically unfavourable in the less acute APDAP ring chelate.

The excitation and emission maxima of **NapL^1**, **NapL^2** and **NapL^4**, and the measured dissociation constants for the addition of Mg^{2+}, Ca^{2+} and Zn^{2+} are highlighted in **Table 4.6**, with a comparison to Mag-Fura-2.[3]

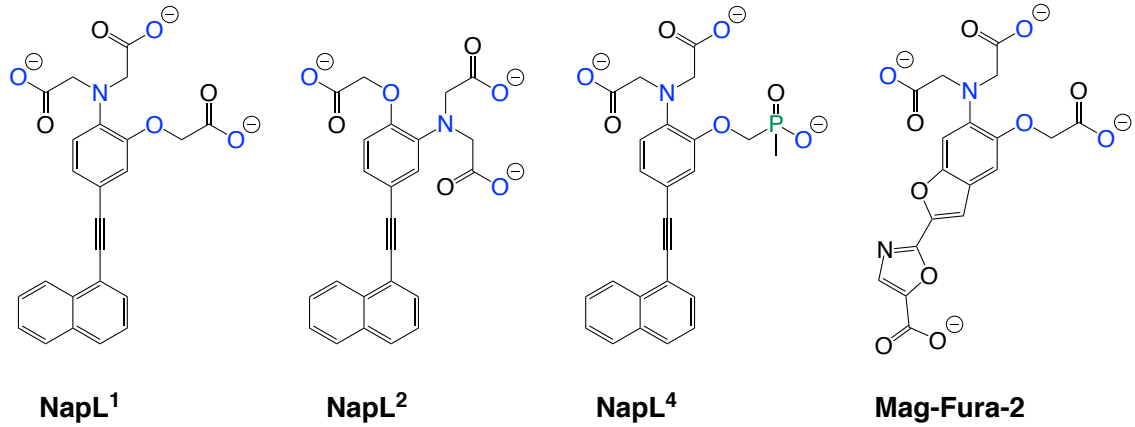

Figure 4.20 The structures of **NapL^1**, **NapL^2**, **NapL^4** and Mag-Fura-2.[3]

Table 4.6 The direct comparison of the excitation maximum, emission maximum and association constants following addition of Mg^{2+}, Ca^{2+} and Zn^{2+} to **NapL^1**, **NapL^2**, **NapL^4** and commercially available Mag-Fura-2[5] in aqueous solutions. Mg^{2+} saturated wavelengths are highlighted in red. The reported dissociation constants are an average of two separate metal ion titrations, given with an associated experimental error in parenthesis.

Ligand	Excitation λ_{max} (nm)	Emission λ_{max} (nm)	K_d (Mg^{2+})	K_d (Ca^{2+})	K_d (Zn^{2+})
NapL^1	358, 320	562, 522	4.5(2) mM	39.6(4.9) μM	1.7(1) μM
NapL^2	318, 318	372, 372	1.3(1) mM	32.7(3.7) μM	3.2(2) μM
NapL^4	350, 344	550, 547	0.5(2) mM	0.4(1) mM	3.3(3) μM
Mag-Fura-2[3]	370, 335[3]	510, 510[3]	1.9 mM[3]	25 μM[3]	20 nm[12]

The low mM affinity reported for the binding of Ca^{2+} is significant, eliminating the major drawback of the APTRA indicators, in that they are significantly more selective for Ca^{2+} over Mg^{2+}. The reduction in affinity observed for Ca^{2+} with **NapL^4**, and the APDAP binding moiety in particular, could allow 'free' Mg^{2+} concentrations to be investigated in Ca^{2+} rich regions of the body including the end(sarco)plasmic reticulum.

4.6.3 Fluorescence binding studies of the phosphinate-based ligand, NapL^6

The problems associated with the synthesis of the ethyl ester of **L^5** outlined in **Chapter 2**, meant that the binding affinity and selectivity for the tridentate ligand **L^6** was studied instead, as the naphthalene-1-alkynlaryl derivative, **NapL^6**.

Following addition of Mg^{2+} (150 mM), Ca^{2+} (2.4 mM) or Zn^{2+} (55.6 μM) only small changes were observed in the absorbance (**Figure 4.15**), emission and excitation spectra of **NapL^6** with no shift in the observed wavelength on metal binding. Such behaviour suggests that there is only weak binding between **NapL^6** and Mg^{2+}, Ca^{2+} and Zn^{2+}. The addition of of Mg^{2+}, for example, resulted in a 1.6-fold reduction in emission intensity at 599 nm (**Figure 4.21**). A dissociation constant of 16.5 mM was calculated for the binding of Mg^{2+}, but had a 40 % error associated with the fitting due to the small emission changes observed after each measurement.

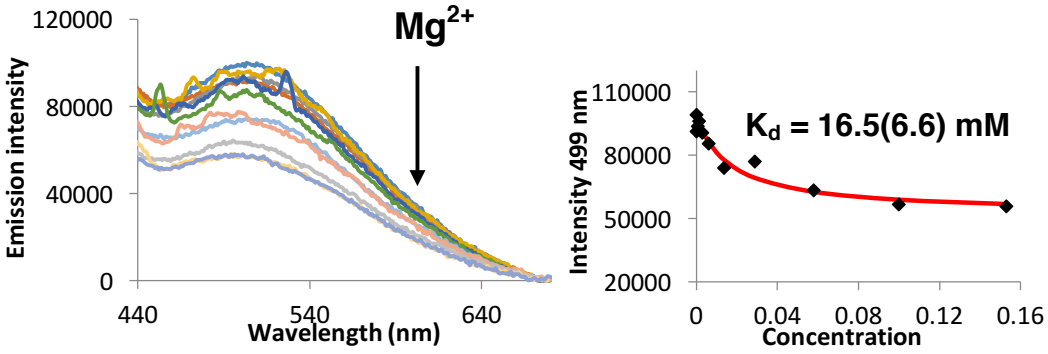

Figure 4.21 (Left) emission spectrum of **NapL^4**; (right) fitting of the emission intensity against the added concentration of Mg^{2+} to a 1:1 binding model. **NapL^6** concentration = 5 µM in 50 mM HEPES, 100 mM KCl, pH 7.21, 298 K, λ_{ex} = 347 nm.

The addition of Ca^{2+} (2.4 mM) and Zn^{2+} (55.6 μM) also resulted in negligible change in absorbance, emission and excitation spectra (**Figure 4.22**). Due to the small changes observed on the addition of Ca^{2+} and Zn^{2+}, no accurate fluorescence titrations were undertaken with these metal ions.

NapL^6 is a tridentate ligand, compared to the five potential donor groups in pentadentate **NapL^1**, **NapL^2** and **NapL^4**. In coordination chemistry, ligands with a higher denticity are favoured for strong binding to larger metal ions. Ca^{2+} ions for example, typically favour the formation of complexes with larger coordination numbers than Mg^{2+} and Zn^{2+} due to their larger ionic radius. The octadentate ligand BAPTA, developed by Tsien, is a perfect example of this theory, forming 8-coordinate complexes with Ca^{2+}.[13]

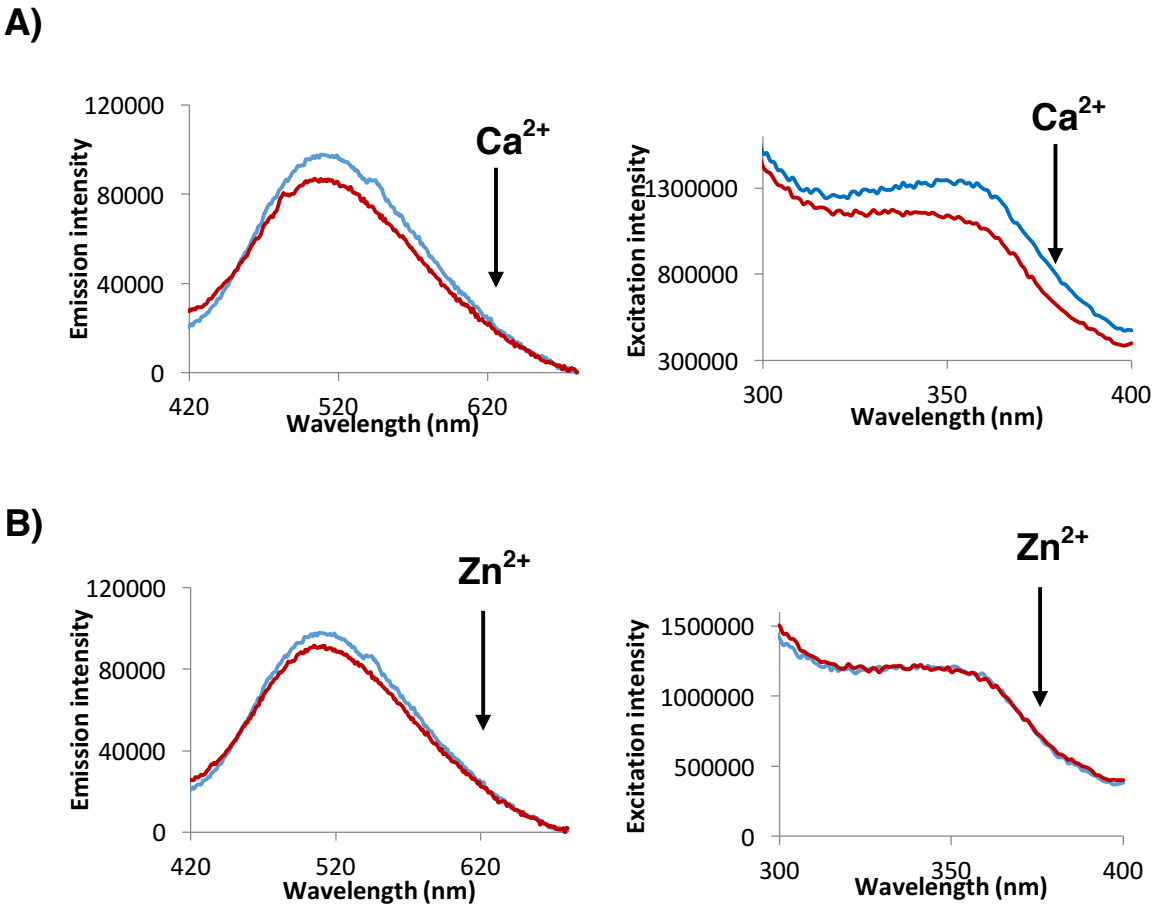

Figure 4.22 (Left) emission spectrum (λ_{ex} = 347 nm); (right) excitation (λ_{em} = 501 nm) spectrum following addition of **(A)** Ca^{2+} (2.4 mM) and **(B)** Zn^{2+} (55.6 μM) in aqueous solutions. Ligand concentration = 5 µM, in 50 mM HEPES, 100 mM KCl, pH 7.21.

The low denticity of **NapL^6**, accounts for the weakness of its binding to Mg^{2+}, Ca^{2+} and Zn^{2+}. The addition of further carboxylate groups into the structure to improve the binding affinity for divalent metal ions was found to be experimentally difficult, and wasn't achieved under the conditions attempted in **Chapter 2**.

4.7 Applications of NapL^4: Measuring Mg^{2+} concentrations in serum

It is thought that 'free' Mg^{2+} concentrations are maintained within the narrow range of 0.7-1.1 mM in the blood plasma, comparable to the concentration of 'free' Mg^{2+} within the majority of mammalian cells.[14] Maintaining a constant level of 'free' or ionised Mg^{2+} in serum is vital for human health, with Mg^{2+} imbalances resulting in the onset of hypermagnesemia and hypomagnesaemia. These electrolytic disturbances in the blood have been linked to a number of diseases, such as hypertension,[15] Alzheimer's, Parkinson's disease, diabetes and chronic kidney disease.[16]

Concentrations of 'free' Mg^{2+} in human serum are often not determined in clinical medicine due to the lack of selective techniques to detect 'free' Mg^{2+} ions. Commercially available Mag-Fura-2 has been used to determine the concentration of 'free' Mg^{2+} in cells where the 'free' Ca^{2+} concentration is 100 nm.[17] The concentration of 'free' Ca^{2+} in serum is, however, significantly higher with concentrations of 1.1 mM commonly observed in healthy humans.[18] APTRA indicators are, therefore, unsuitable for this role due to their μM binding affinity to Ca^{2+}. The development of a technique to measure the concentration of 'free' Mg^{2+} levels in the blood is of a critical importance in order to diagnose and to prevent the onset of a number of these diseases.

There is a real lack of Mg^{2+} fluorescent probes to detect 'free' Mg^{2+} concentrations in human serum. Ion sensitive electrodes have been used to determine the concentration of free Mg^{2+} within the serum.[19-20] They have significant disadvantages, however, in that they are commonly not selective towards the detection of Mg^{2+}, but are also able to monitor 'free' Ca^{2+} and Na^+ ions in solution.[19] More recently, DNAzyme-based electrochemical biosensors

have also been used to investigate the concentration of Mg^{2+} in serum, displaying a high selectivity for Mg^{2+} over Ca^{2+} and Zn^{2+}.[21]

Ligand **NapL^4** possesses many characteristics that make it suitable to detect 'free' Mg^{2+} in human serum. It has no pH interference in the physiological range and a low mM binding affinity for Ca^{2+} (K_d = 0.4 mM), compared to the μM affinity displayed by the APTRA fluorescence sensors. Excitation of **NapL^4** at 350 nm in newborn-calf serum (NCS) resulted in only background fluorescence from the proteins in serum being observed. (**Figure 4.23**). The binding studies of **NapL^4** with Mg^{2+} were instead carried out in a buffered 'serum mimic' containing 50 mM HEPES and concentrations of Na^+, K^+, Ca^{2+} and Mg^{2+} in accordance with the mean values found in human serum shown in **Table 4.8.**

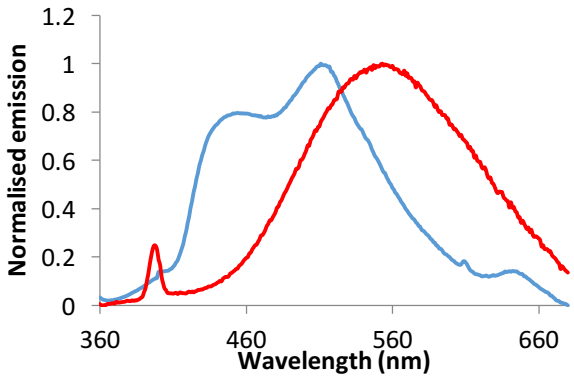

Figure 4.23 The normalised emission of **NapL^4** in 50 mM HEPES, 100 mM KCl, pH 7.21, 298 K shown in red, and **NapL^4** in newborn calf serum (NCS) at 298 K shown in blue.

Table 4.8 Representative concentrations of selected cations in serum for healthy patients.[18]

Ion	Mean concentration in serum (mM)
H^+	5×10^{-5}
Li^+	< 0.01
Na^+	140
K^+	4
Mg^{2+}	0.6
Ca^{2+}	1.1

Absorption and emission studies following the addition of Mg^{2+} to **NapL^4** were carried out in the 'serum mimic'. Studies both with and without 0.6 mM Mg^{2+} were acquired to determine how the affinity and the measured dissociation constants were affected.

It is apparent from the analysis of the absorbance spectra in **Figure 4.24** that partial saturation of **NapL^4** was observed in the 'serum mimic' with a hypsochromic shift displayed and an isosbestic point at 330 nm. Such a wavelength shift is characteristic of Ca^{2+} binding and has been observed previously for **NapL^4** in **Section 4.6.2**. The 1.1 mM concentrations of Ca^{2+} present in the buffered solution did not completely saturate **NapL^4**. On the addition of a further 1.0 mM Mg^{2+}, saturation was achieved, with a further reduction in the absorbance at 324 nm observed.

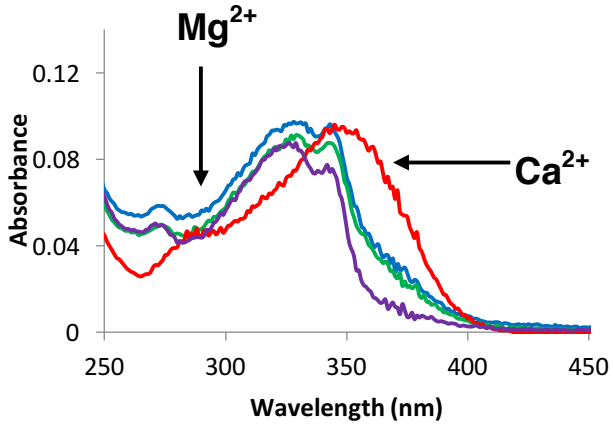

Figure 4.24 Absorbance spectra of **NapL^4** in the 'unbound' state shown in red. Partial saturation with 1.1 mM Ca^{2+} and 1.1 mM Ca^{2+}, 0.6 mM Mg^{2+} from the 'serum mimic'. Complete saturation was observed following addition of a further 1 mM Mg^{2+}, 298 K.

The emission spectra of **NapL^4** in the buffered 'serum mimic', both with and without 0.6 mM Mg^{2+}, are shown in **Figure 4.25**. Ligand **NapL^4**, displays a wavelength maximum at 545 nm following excitation at the absorbance maximum in the 'unbound state' of **NapL^4** (λ_{ex} = 350 nm). Upon the binding of Mg^{2+}, a non-ratiometric behaviour was reported, with a 1.6- and 1.5-fold decrease in fluorescence emission intensity at 545 nm in **Figure 4.25 A)** and **B)** respectively.

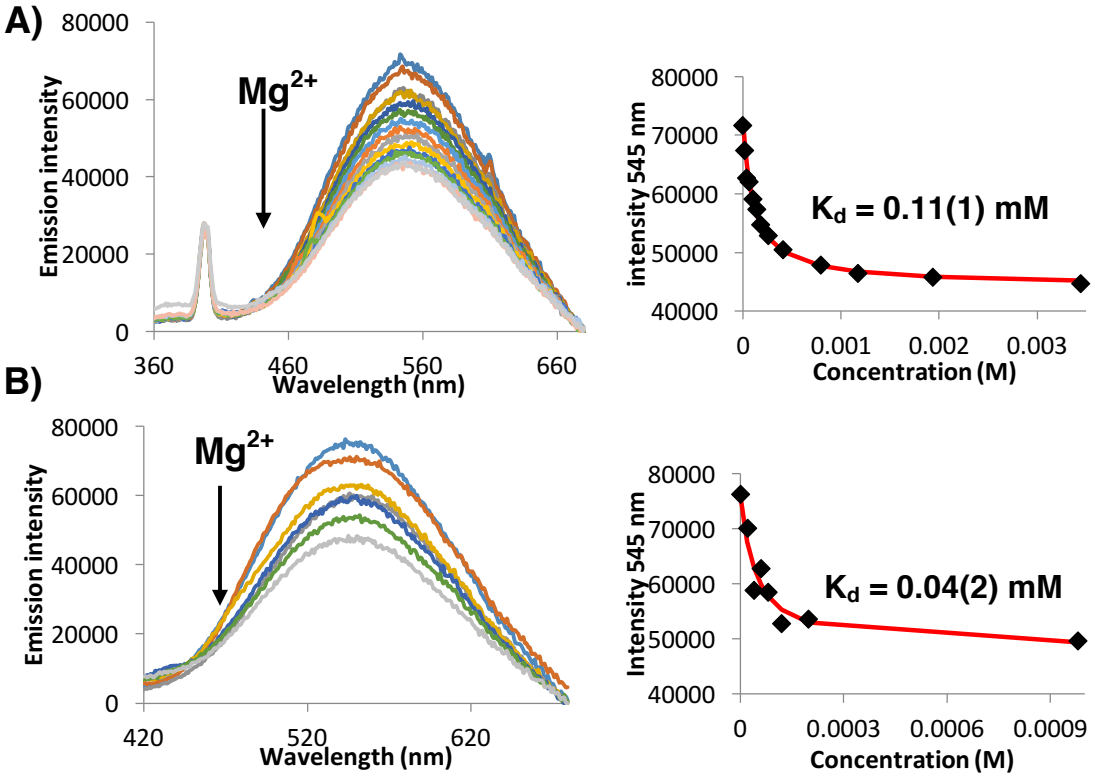

Figure 4.25 (Left) emission spectrum; (right) fitting of the emission intensity against the added concentration of Mg^{2+}. Titration in 'serum mimic' **(A)** with and **(B)** without the presence of 0.6 mM $MgCl_2$ typically found in human serum. **NapL^4** ligand concentration = 10 μM, in 50 mM HEPES, 140 mM NaCl, 4 mM KCl, and 1.1 mM $CaCl_2$, pH 7.21, λ_{ex} = 350 nm, 298 K.

Dissociation constants of 0.04 mM and 0.11 mM were calculated respectively for the 1:1 binding between Mg^{2+} and **NapL^4** in the 'serum mimic' with and without the presence of 0.6 mM Mg^{2+}. As expected, the dissociation constants measured were lower than the 0.5 mM reported for the binding of Mg^{2+} in 50 mM HEPES at 298 K, as **NapL^4** is, initially, in its unbound state. The addition of 0.6 mM Mg^{2+} to the 'serum mimic' reduced the observed K_d value further, as a larger fraction of **NapL^4** was in its metal-bound state before commencing the Mg^{2+} titration.

It is unlikely, however, that **NapL^4** will be suitable for the detection of Mg^{2+} in human serum. From the analysis of **Figure 4.25** it is evident that **NapL^4** displays an approximately 10-fold stronger affinity towards Mg^{2+} than the concentration of 'free' Mg^{2+} present in human serum (0.7-1.1 mM).[14]

4.8 Conclusions for the Naphthalene series

Four naphthalene-1-alkynylaryl ligands, denoted **NapL^1**, **NapL^2**, **NapL^4** and **NapL^6**, were synthesised from their respective ligating units, **L^1**, **L^2**, **L^4** and **L^6** via multiple carbon-carbon cross-coupling reactions (**Figure 4.26**). Photophysical studies revealed that the position of the aniline nitrogen atom (either *para* or *meta* to the fluorophore) had a significant effect on the absorbance, emission and excitation profiles. As expected **NapL^1**, **NapL^4** and **NapL^6** have pronounced Stokes' shifts of 166-204 nm, which are larger than those observed for fluorescent APTRA indicators in the literature such as Mag-Fura-2.[3]

From fluorescent emission and excitation studies, ligands **NapL^1**, **NapL^2**, **NapL^4** and **NapL^6** were found to be insensitive to pH in the physiological range (6.5-7.5). All pK_a values calculated are in the range 5.2-6.2, comparable to the pK_a of commercially available Mag-Fura-2.[3]

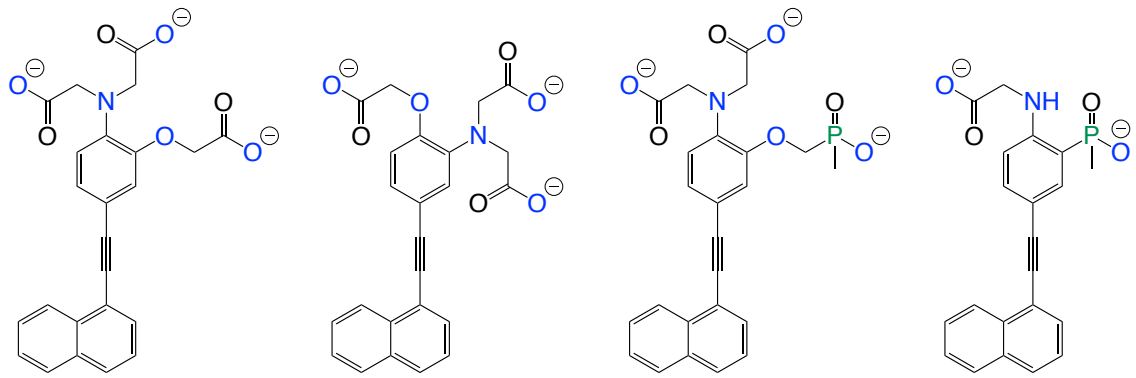

Figure 4.26 Structures of naphthalene based ligands **NapL^1**, **NapL^2**, **NapL^4** and **NapL^6**.

Fluorescence emission and excitation binding studies were conducted with Mg^{2+}, Ca^{2+} and Zn^{2+} in 50 mM HEPES and 100 mM KCl at a constant pH of 7.21. In the case of **NapL^1** and **NapL^2**, it was found that changing the position of the aniline nitrogen atom on the aromatic system produced comparable affinities for divalent metal cations. A typical Mg^{2+} / Ca^{2+} selectivity for **NapL^1** and **NapL^2** was observed supporting literature precedent in the APTRA series. The position of the aniline nitrogen atom did, however, determine whether a ratiometric or non-ratiometric response towards the binding of Mg^{2+}, Ca^{2+} and Zn^{2+} was observed.

The introduction of a phosphinate group at the expense of a carboxylate binding group was found to increase the affinity for Mg^{2+} and reduce the affinity for Ca^{2+}, compared to **NapL^{1}** and **NapL^{2}**. Phosphinate-based **NapL^{4}** was found to be significantly more selective for the binding of Mg^{2+}, displaying a 10–fold weaker affinity for Ca^{2+} than that reported for carboxylate-based **NapL^{1}** and **NapL^{2}**. DFT studies in **Chapter 3** on the APDAP binding group showed a less acute bite angle around the Mg^{2+}, with smaller M–N and M–O reported. Such behaviour suggests that it is more thermodynamically favourable for the binding of the smaller Mg^{2+} ion over the larger Ca^{2+} ion in the APDAP chelate.

The reduced affinity found for the binding of Ca^{2+} to **NapL^{4}** (K_d = 0.4 mM) allowed an investigation into the binding of 'free' Mg^{2+} in serum to be explored. Analysis was carried out in a buffered 'serum mimic' containing representative concentrations of Na^{+}, K^{+}, Ca^{2+} and Mg^{2+}. K_d values of 0.04 mM and 0.11 mM, in the presence and absence respectively of 0.6 mM Mg^{2+}, were reported in the competitive media.

Tridentate ligand **NapL^{6}** was found to have a low affinity for Mg^{2+} (K_d = 16.5 mM), with a significant 40 % error in the fitting because of the small fluorescence changes observed after each addition of Mg^{2+}. No fluorescence emission or excitation studies for the addition of Ca^{2+} and Zn^{2+} were carried out with **NapL^{6}** because of the small changes observed even after the addition of 2.4 mM Ca^{2+} and 55.6 μM Zn^{2+}. The tridentate binding moiety displayed by **L^{6}** is, therefore, unsuitable to detect 'free' Mg^{2+}, Ca^{2+}, Zn^{2+}. It has been demonstrated from **NapL^{1}**, **NapL^{4}** and **NapL^{6}** that a larger denticity (pentadentate) on metal ion binding is preferred.

Table 4.9 A summary of the calculated pK_a and dissociation constants of **NapL[1]**, **NapL[2]**, **NapL[4]** and **NapL[6]** via fluorescence excitation spectroscopy, All pK_a values are given along with an error associated with the fitting. The reported binding constants following addition of Mg^{2+}, Ca^{2+} and Zn^{2+} to **NapL[1]**, **NapL[2]** and **NapL[4]** are an average of 2-3 separate metal ion binding titrations, and are given with the experimental error in parenthesis. Mg^{2+} saturated wavelengths are highlighted in red.

	Absorption λ_{max} (nm)	**ε / 10^3 ($M^{-1}cm^{-1}$)**	**Excitation λ_{max} (nm)**	**Emission λ_{max} (nm)** λ_{ex} = 354 nm	**pK_a**	**Log K (Mg^{2+})**	**K_d (Mg^{2+})**	**Log K (Ca^{2+})**	**K_d (Ca^{2+})**	**Log K (Zn^{2+})**	**K_d (Zn^{2+})**
NapL[1]	354 326	14.1(3)	358 320	562 522	6.2(04)	2.4(2)	4.5(2) mM	4.4(05)	39.6(4.9) µM	5.8(02)	1.7(1) µM
NapL[2]	326 326	13.8(6)	318 318	372 372	5.7(05)	2.9(1)	1.3(8) mM	4.5(05)	32.7(3.7) µM	5.5(02)	3.2(2) µM
NapL[4]	350 350	10.7(2)	350 336	550 547	5.2(04)	3.3(2)	0.5(2) mM	3.3(03)	0.4(1) mM	5.5(1)	3.3(3) µM
NapL[6]	347 347	12.2(4)	341 341	507 507	5.1(02)	1.8	16.5 mM	-	-	-	-
Mag-Fura-2[3]	369	-	370	511	-	-	1.9 mM	-	25 µM	-	20 nm[12]

4.9 References

[1] P.A. Otten, R. E. London and L. A. Levy, *Bioconjug. Chem.*, 2001, **12**, 76- 83.

[2] M. Starck, R. Pal and D. Parker, *Chem. Eur. J.*, 2016, **22**, 570- 580.

[3] B. Raju, E. Murphy, L. A. Levy, R. D. Hall and R. E. London, *Am. J. Physiol.*, 1989, **256**, 540-548.

[4] M. Brady, S. D. Piombo, C. Hu and D. Buccella, *Dalton Trans.*, 2016, **45**, 12458.

[5] A. E. Martell, R. J. Motekaitis, A. R. Fried, J. S. Wilson and D. T. MacMillan*, Can. J. Chem.*, 1975, **53**, 3771-3476.

[6] Q. Lin, J. J. Gruskos and D. Buccella, *Org. Biomol. Chem.*, 2016, **14**, 11381.

[7] G. Grynkiewicz, M. Poenie and R. Y. Tsien, *J. Biol. Chem.*, 1985, **260**, 3440-3450.

[8] G. Zhang, D. Jacquemin and D. Buccella, *J. Phys. Chem. B.*, 2017, **121**, 696-705.

[9] M. S. Afzal, J-P. Pitteloud and D. Buccella, *Chem. Commun.*, 2014, **50**, 11358.

[10] G. Zhang, J. J. Gruskos, M. S. Afzal and D. Buccella, *Chem. Sci.*, 2015, **6**, 6841

[11] A. M. P. Romani, *Arch. Biochem. Biophys.*, 2011, **512**, 1-23.

[12] T. J. B. Simons, *J. BioChem. Biophys. Methods.*, 1993, **27**, 25-37.

[13] R. Y. Tsien, *Biochemistry.*, 1980, **19**. 2396-2404.

[14] J. H. F. Baaij, J. G. J. Hoenderop and R. J. M. Bindels, *Physiol Rev.*, 2015, **95**, 1-46

[15] L. M. Resnick, *Am. J. Hypertens.*, 1993, **6**, 123S-132S.

[16] A. Tin and M. E. Grams, *Kidney Int.*, 2015, 820-827.

[17] J. Yin, Y. Hu and J. Yoon, *Chem. Soc. Rev.*, 2015, **44**, 4619-4644.

[18] D. Parker in 'Crown Compounds Toward Future Applications', ed. S. J. Cooper, VCH, 1992, Chapter 4, pp. 51-69.

[19] H. Ising, F. Bertschat, T. Günther, E. Jeremias and A. Jeremias, Eu. *J. Clin. Chem. Clin. Biochem.*, 1995, **33**, 365-371.

[20] M. Maj-Zurawska and A. Lewenstam, *Anal. Chim. Acta.*, 1990, **236**, 331-335.

[21] X. Gao, H. Huang, S. Niu, H. Ye, Z. Lin, B. Qiu and G. Chen, *Anal. Methods.*, 2012, **4**, 94.

5. The APTRA binding group in metal-based systems

5. Part 1: Lanthanide(III)-based systems

5.1 Introduction

Lanthanide complexes offer a number of fundamental advantages over other luminescent systems such as the naphthalene-based systems discussed in **Chapter 4**. They have sharp emission bands that are characteristic of each lanthanide, and their emission spectra are to a first approximation independent of the coordination environment. They possess large pseudo-Stokes' shifts between the absorbance and emission of light. The Laporte and spin-forbidden nature of the f-f transitions of many of the lanthanide(III) ions result in a long lifetime of the excited state (μs – ms), allowing time-gated experiments to be carried out in biological media. The application of a short delay between excitation and observation of lanthanide emission eliminates all background (or auto) fluorescence, allowing the emission of the lanthanide complex to be observed selectively.[1,2]

One significant drawback of lanthanide complexes, however, is their inability to be excited directly, due to their low molar extinction coefficients (typically < 3 mol^{-1} dm^3 cm^{-1}).[3] To overcome this issue, an aromatic chromophore or 'antenna' is commonly used to 'sensitise' the lanthanide emission, by absorbing light and transferring it to the excited state of the lanthanide ion. This is commonly called the 'antenna effect', and is depicted by a Jablonski diagram (**Figure 5.1**).

The choice of chromophore is an important factor to consider when designing highly emissive lanthanide complexes for biological applications. The energy gap between the T_1 excited state of the chromophore and the Ln^{3+} excited states (Eu^{3+} $^5D_0$ = 17,200 cm^{-1}, Tb^{3+} $^5D_4$ = 20,400 cm^{-1})[1] must be sufficiently large for energy transfer to occur. Back energy transfer may occur at room temperature if this energy gap is less than 1800 cm^{-1}, resulting in complexes with reduced lifetimes and quantum yields under ambient conditions.[4]

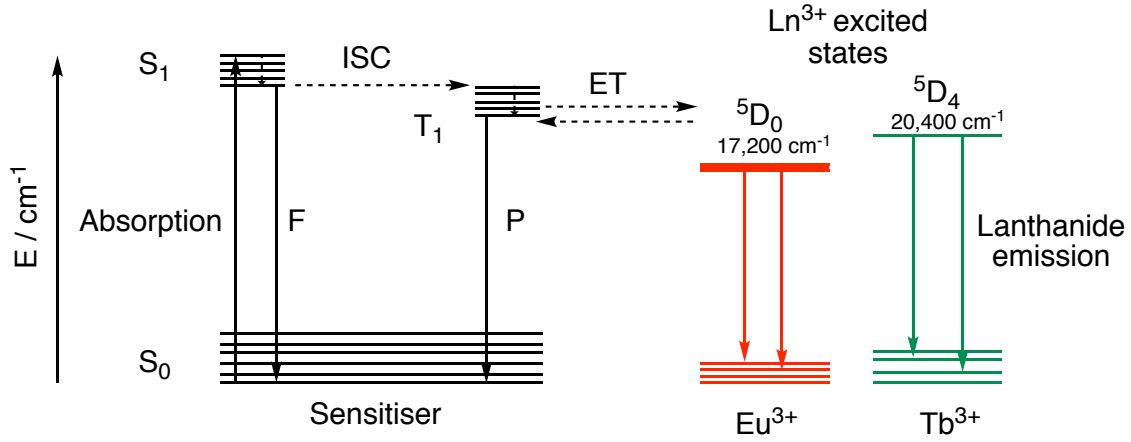

Figure 5.1 Jablonski diagram not to scale, showing the typical pathway for sensitised emission of Eu^{3+} and Tb^{3+} complexes via the antenna effect. Where F = sensitiser fluorescence, P = sensitiser phosphorescence, ISC = inter system crossing and ET = energy transfer.

Lanthanide ions are hard metal ions, and are predominantly encapsulated within thermodynamically and kinetically stable 9-N_3 and 12-N_4 macrocycle ligands, such as 1,4,7,10-tetraazacyclododecane-1,4,7,10-tetraacetic acid (DOTA). A coordination number of 8 or 9 is preferred to oxygen and nitrogen donors, forming complexes of high stability and preventing the premature release of the toxic lanthanide ion.

A vast array of lanthanide complexes have been used to study the affinity and selectivity of different cations (K^+, Mg^{2+}, Ca^{2+}, Zn^{2+}) and anions (HS^-). In each example, the chromophore commonly also acts as the selective metal ion binding domain. Upon binding of the ion in question, a luminescence change occurs (either ‘turn on’ or ‘turn off’) which can then be plotted against the concentration of the guest added. Examples of a range of lanthanide-based cation sensors from the literature are shown in **Figure 5.2**.

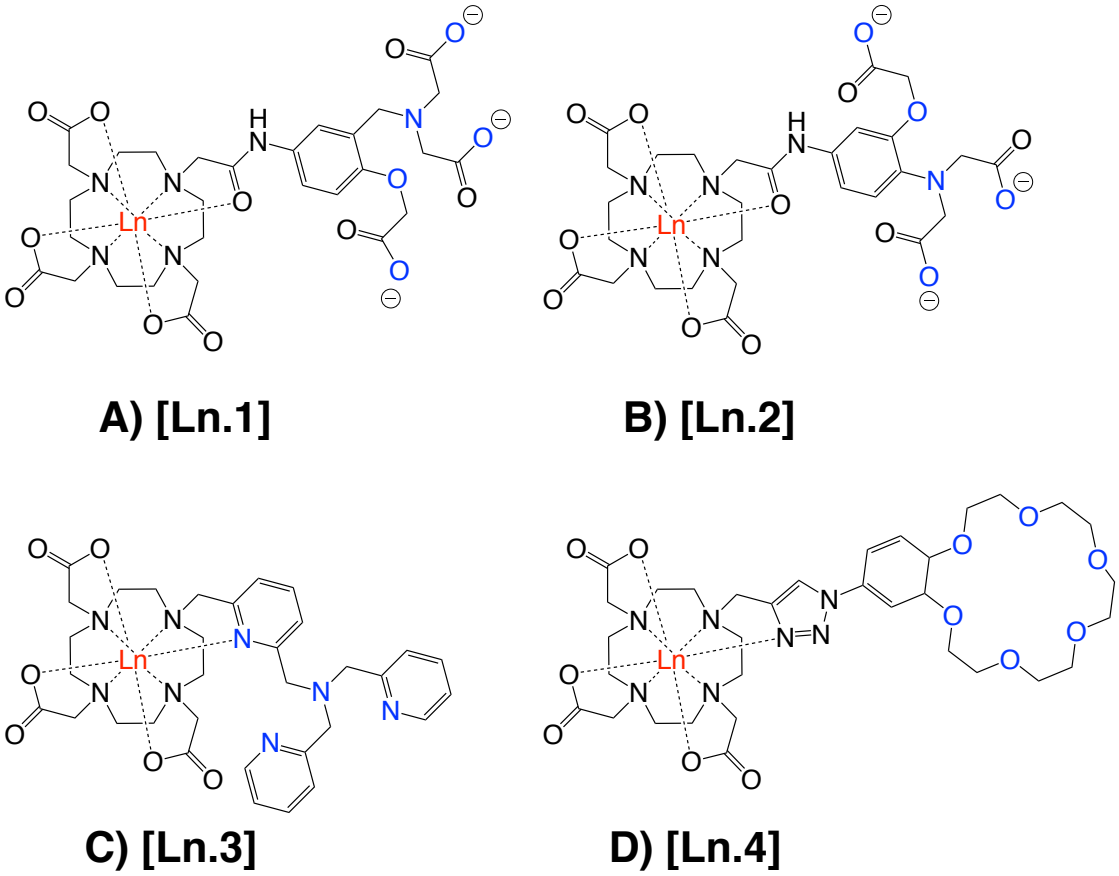

Figure 5.2 Lanthanide-based metal ion sensors (**A**) **[Ln.1]** for Zn^{2+} (μM affinity) in extracellular fluid,[5] (**B**) **[Ln.2]** APTRA-based sensor for Mg^{2+} (mM affinity), Ca^{2+} (μM affinity) and Zn^{2+} (μM) [6], (**C**) **[Ln.3]** for Zn^{2+},[7] and (**D**) **[Ln.4]** for K^{+} ions (μM).[8] Binding groups are highlighted in blue.

In 2000 Parker and co-workers developed a number of Tb^{3+} based lanthanide probes for divalent cations. These include **[Ln.1]** which was found to have a relatively high affinity for Zn^{2+}, with a binding constant of 0.6 μM in a simulated extracellular background.[5] The isomer, **[Ln.2]**, is an APTRA-based probe, with low mM affinity for Mg^{2+} and μM affinity for Ca^{2+} and Zn^{2+} ions.[6]

Later, Pope *et al*. reported a highly emissive europium-based probe, **[Ln.3]**, for the detection of Zn^{2+} in competitive ionic media containing biological concentrations of Mg^{2+}, Ca^{2+}, Na^{+} and K^{+}.[7] Upon the addition of one equivalent of Zn^{2+} an increase in the number of inner sphere water molecules was observed, from 0 to 2. Such behaviour indicates that the pyridine donor in the tris(2-pyridylmethyl)amine (TPA) binding moiety is no longer bound to the europium centre. The change in coordination environment of Eu^{3+} on Zn^{2+} binding

changes the lifetime of the complex, as the coordination environment around the europium centre is altered. The sensor can, therefore, be used to study the binding of Zn^{2+} via both intensity and lifetime studies.[7]

In the final example, in 2016, Sørensen and co-workers reported an 18-crown-6 based sensor with a triazole link between the lanthanide complex and the chromophore for the sensing of K^+ (**[Ln.4]**).[8] No response was observed towards K^+ in water with either the Eu^{3+} or Tb^{3+} complex, but a log K of 5.3(02) was observed for the Eu^{3+} complex in methanol, consistent with the affinity of 18-benzocrown-6.[8]

Taking this background literature into account, the aim of the work described in this chapter was to synthesise a range of lanthanide complexes in order to study the binding of Mg^{2+}, Ca^{2+} and Zn^{2+} (**Figure 5.3**). APTRA based pro-ligands $\mathbf{L^1}$ and $\mathbf{L^2}$ (synthesised previously in **Chapter 2**) were the ligands of choice and were incorporated into both pyridylalkynylaryl and pyridylaryl chromophores. Each complex synthesised is an analogue of a DOTA ligand based on a 12-N_4 macrocycle, containing one chromophore to sensitise the lanthanide emission, and three pendent carboxylate groups to ensure that stable 8- to 9-coordinate complexes are formed. The chromophore employed also acts as the binding moiety for divalent cations. A luminescence intensity change (either 'turn on' or 'turn off') with **[Ln.L^1]**, **[Ln.L^2]** and [**Ln.bL^2]** is expected, following the binding of Mg^{2+}, Ca^{2+} and Zn^{2+}.

Direct comparisons are made between **[Ln.L^1]**, **[Ln.L^2]** and **[Ln.bL^2]**, to determine whether the position of the nitrogen and oxygen atoms on the aromatic chromophore affects the affinity and selectivity towards Mg^{2+} and which chromophore – either a pyridylalkynylaryl or a pyridylaryl – is favoured for high Mg^{2+} affinity and selectivity. Target lanthanide complexes are highlighted in **Figure 5.3**.

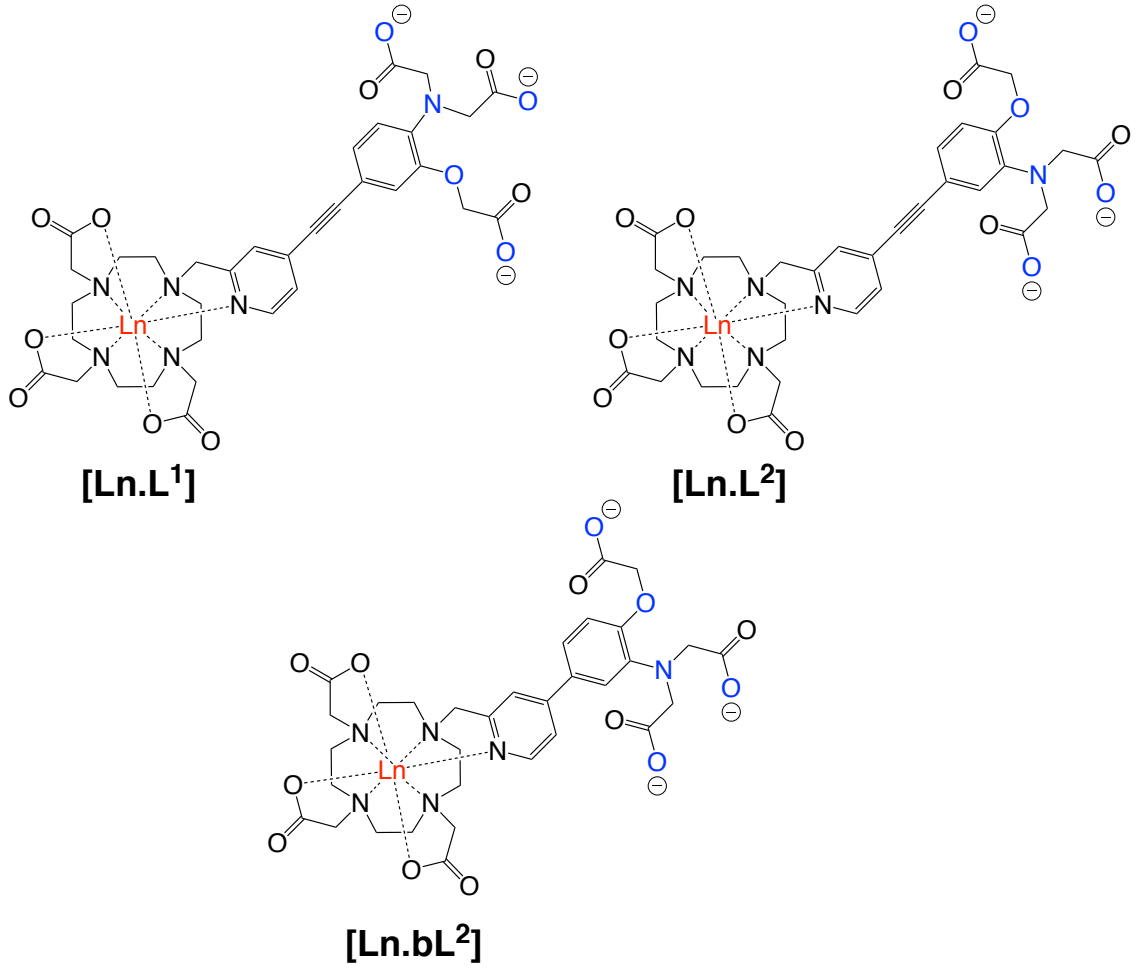

Figure 5.3 Target lanthanide complexes **[Ln.L^1]**, **[Ln.L^2]** and **[Ln.bL^2]**. Expected binding groups to divalent metal ions are highlighted in blue.

5.2 Synthesis and characterisation

The ethyl- and *tert*-butyl esters of 1,4,7,10-tetraazacyclododecane-1,4,7-triacetic acid (DO3A), were prepared by literature procedures, forming (**39**)[9] and (**40**)[10] in moderate yields after purification (**Scheme 5.1**). The triester (**39**) was used for pyridylalkynylaryl-based chromophores and was hydrolysed under basic conditions to avoid competitive acid-promoted hydration of the alkyne. The *tert*-butyl ester (**40**), however, was used with the pyridylaryl chromophore, where no such problems can arise under acidic hydrolysis conditions.

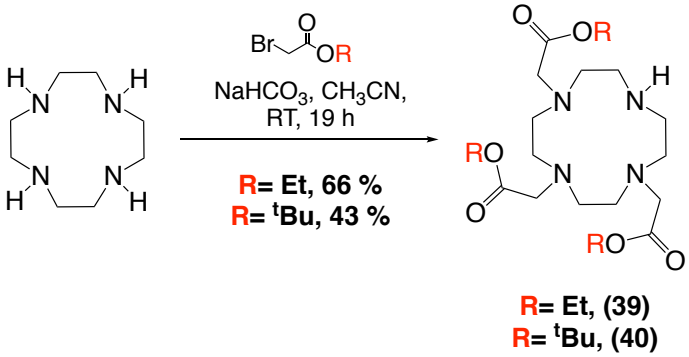

Scheme 5.1 Synthesis of the ethyl- and *tert*-butyl esters of DO3A.[9,10]

The pyridine fragment of the chromophore 4-bromo-2-(hydroxymethyl)pyridine (**42**) was synthesised from commercially available 4-bromo-2-methylpyridine, using a procedure adapted from Canty and co-workers (**Scheme 5.2**).[11] Functionalising the 4-position of the pyridine with a bromine atom allows the binding moiety to be introduced to the chromophore, via palladium-catalysed cross-coupling reactions. The first step in the synthesis of (**42**) involved the formation of the pyridine N-oxide (**41**) from 4-bromo-2-methylpyridine and m-CPBA. Moderate yields of the N-oxide were achieved, after purification by alumina column chromatography.

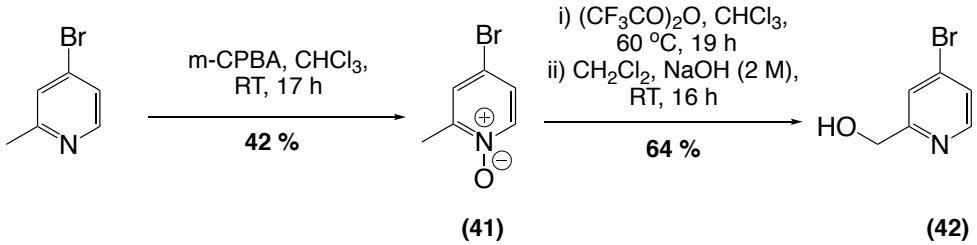

Scheme 5.2 The synthesis of 4-bromo-2-(hydroxymethyl)pyridine, (**42**).[11]

On treatment of the N-oxide, (**41**), with trifluoroacetic anhydride in chloroform, a trifluoroacetate ester intermediate is formed via a [3, 3] sigmatopic rearrangement reaction.[12] Ester hydrolysis to the desired alcohol was undertaken in a biphasic mixture with sodium hydroxide (2 M) in dichloromethane, forming (**42**) in good yield after purification by column chromatography.

5.2.1 Synthesis of [Ln.L^1] and [Ln.L^2]

The complexes [**Ln.L^1**] and [**Ln.L^2**] were synthesised using identical procedures in a multi-step reaction sequence from their TIPS protected alkyne. Compounds (**25**) and (**26**) have previously been shown to form in high yields via Sonogashira cross-coupling reactions of TIPS-acetylene with the ethyl esters of **L^1** and **L^2** (**Scheme 4.1**). As reported in **Chapter 4**, the most effective Sonogashira cross-coupling reactions with aryl bromides were achieved in a one pot reaction involving de-protection of the silyl alkyne and cross-coupling of the aryl bromide. It was found that using Pd(dppf)Cl_2 and copper iodide as the catalysts, the compounds (**43**) and (**47**) were obtained in moderate yields (**Scheme 5.3**). Purification was achieved, in each instance, via silica gel column chromatography.

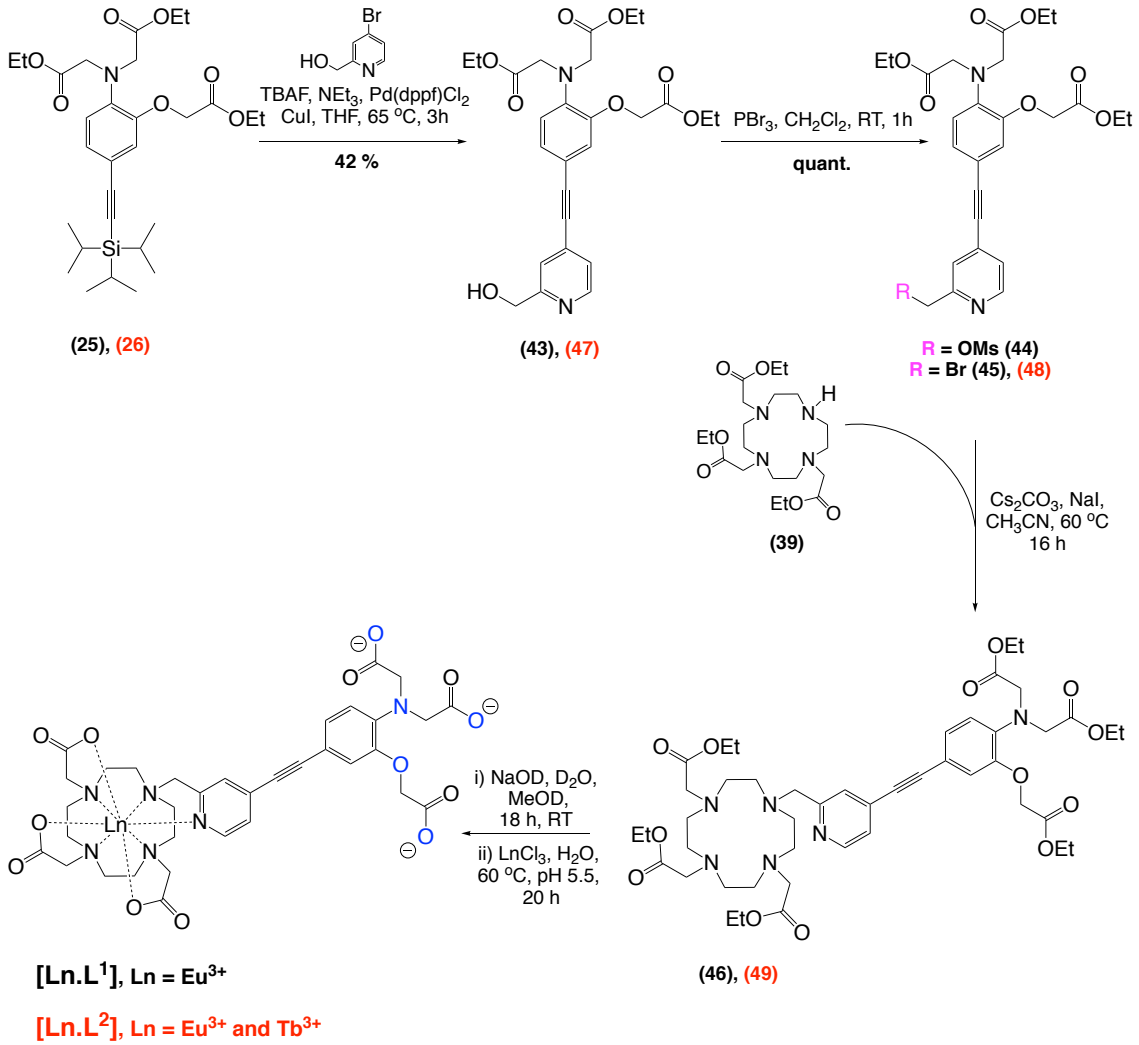

Scheme 5.3 The synthesis of **[Ln.L^1]**. An identical procedure was used for the synthesis of **[Ln.L^2]**. The numbering of analogous intermediates for the synthesis of **[Ln.L^2]** is given in red.

Before alkylating onto macrocycles can be accomplished, the chromophore is commonly converted into its mesylate, acting as the leaving group in nucleophilic substitution reactions. Mesylate (**44**), however, was found to be rather unstable, and no alkylation was observed when the reaction was attempted with both potassium carbonate and caesium carbonate in anhydrous acetonitrile.

An alternative approach was, therefore, used where the alcohol functionality in (**43**) and (**47**) was converted to a bromide by reacting with phosphorus tribromide (PBr_3) in dichloromethane at room temperature. In most

instances the bromides (**45**) and (**48**) were not isolated but used immediately to alkylate (**39**) or (**40**) directly in 1:1 stoichiometry.

Alkylation of the macrocycle (**39**) with (**45**) or (**48**) was achieved in anhydrous acetonitrile at 60 ^{o}C with caesium carbonate as the base. Purification by column chromatography on silica formed (**46**) and (**49**), before universal ester hydrolysis was undertaken under basic conditions at room temperature. After hydrolysis, lanthanide complexation was carried out by treatment with their respective chloride salts ($LnCl_3.6\ H_2O$), in water at pH 5.5 and heating at 60 ^{o}C. Reaction progress was monitored by ESI-MS, showing the characteristic isotope patterns of the lanthanide in question. The pH of the solution was then raised to pH 8-10, allowing any unreacted Ln^{3+} to precipitate out as $Ln(OH)_3$, which was then removed via syringe filtration.

Purification of **[Ln.L^1]** and **[Ln.L^2]** was performed using semi-preparative reverse phase HPLC with an acetonitrile and ammonium carbonate buffered system. Complex purity was assessed by ESI-MS, and by HPLC analysis.

5.2.2 Synthesis of [Ln.bL^2]

The bi-aryl complex **[Ln.bL^2]** was synthesised in a multi-step reaction sequence from the *tert*-butyl ester of **L^2**, (**7**). The synthesis of the boronate ester (**50**) was achieved via the Miyaura borylation reaction, a versatile method for the coupling of aryl halides and triflates with diboronate esters such as bis(pinacolato)diboron (B_2pin_2).[13-15] The Miyaura borylation reaction was carried out with (**7**) in a microwave reactor using a procedure adapted from Dehaen and co-workers.[13] The boronate (**50**) was formed quickly within 2 h and is isolated in moderate yield, after purification by silica gel column chromatography. With the boronate in place, the next step was a palladium-catalysed Suzuki cross-coupling reaction of (**50**) and 4-bromo-2-(hydroxymethyl)pyridine, (**26**). The alcohol (**51**) was formed in moderate yield, in a mixture of dimethoxyethane (DME) and water at 85 ^{o}C (**Scheme 5.4**).

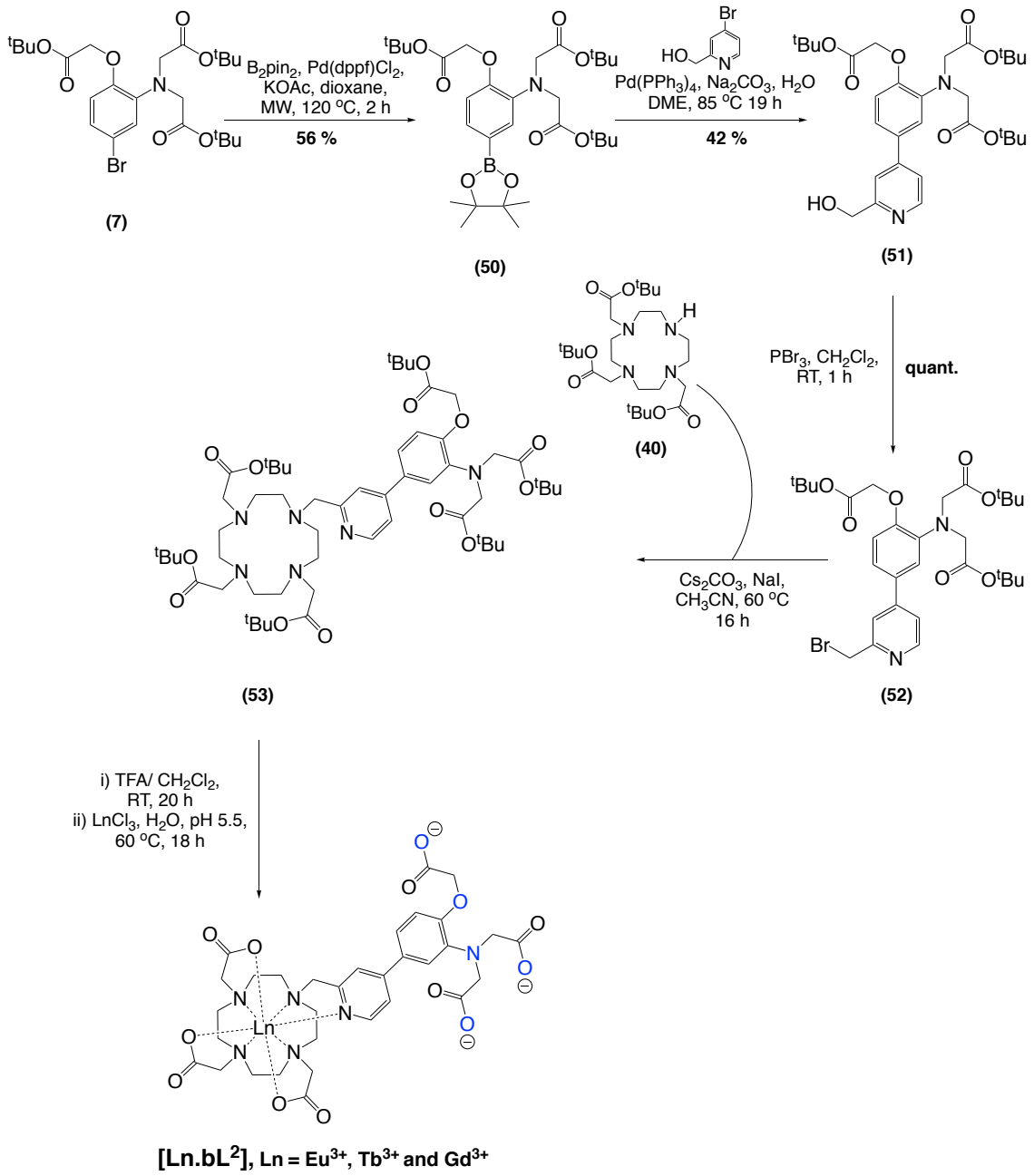

Scheme 5.4 The synthesis of **[Ln.bL^2]**.

Treatment of the alcohol (**51**) with phosphorus tribromide (PBr_3) in dichloromethane at room temperature formed the benzylic bromide (**52**). The procedure is identical to that utilised in the synthesis of (**45**) and (**48**). The benzylic bromides were used directly, without being purified or fully characterised. Alkylation of DO3A-*tert*-butyl ester (**40**) with (**52**) was followed by universal *tert*-butyl ester hydrolysis under acidic conditions, using a 1:1 ratio of trifluoroacetic acid (TFA) and dichloromethane. Lanthanide complexation to form **[Ln.bL^2]** was carried out using the same conditions as those used for the

synthesis of **[Ln.L^1]** and **[Ln.L^2]** (**Scheme 5.3**). Purification of **[Ln.bL^2]** was achieved by semi-preparative reverse phase HPLC, with the purity of **[Ln.bL^2]** determined by analytical HPLC and ESI-MS.

5.3 Photophysical properties of [Ln.L^1], [Ln.L^2] and [Ln.bL^2]

5.3.1 The pyridylalkynylaryl chromophore, [Ln.L^1] and [Ln.L^2]

The absorbance spectrum of **[Eu.L^1]** is presented in **Figure 5.4**, with three absorbance maxima at 270 nm, 318 nm and 380 nm. The transitions at 270 nm and 318 nm are characteristic of a localised π π* excited state. The broad structureless transition at 380 nm, however, is assigned to an ICT transition associated with electron donation from the *para* aniline nitrogen atom relative to the aromatic chromophore.

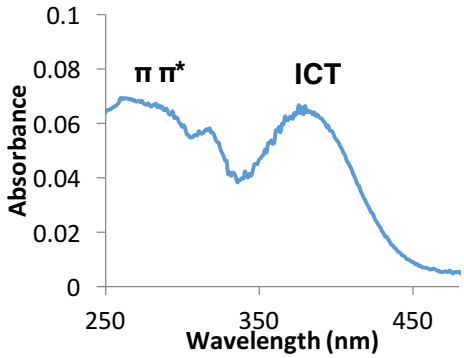

Figure 5.4 Absorbance spectrum of **[Eu.L^2]**. Complex concentration = 5 μM in water, 298 K.

Excitation at 380 nm gave rise to very weak Eu^{3+} emission at room temperature in both acidic and basic solutions, eliminating the possibility of quenching arising from photo-induced electron transfer (PET). At 77 K, however, highly structured and characteristic Eu^{3+} emission was observed with characteristic emission bands present, associated with the $\Delta J = 0$ to $\Delta J = 4$ transitions (**Figure 5.5**). Such behaviour suggests that at room temperature the ICT excited state is too low in energy for an efficient energy transfer to the $^5D_0$ excited state of Eu^{3+}. Charge transfer (CT) transitions are thermally activated, with the loss of energy due to back energy transfer from the $^5D_0$ excited state suppressed at low temperatures.[16,17] Lowering the temperature reduces the rate

of the back energy transfer reaction, allowing efficient sensitisation of Eu^{3+} to occur at 77 K.

The localised π π* transition at 318 nm, however, was found to be sufficiently high in energy to sensitise Eu^{3+} emission. Upon excitation at 318 nm under ambient conditions no ligand phosphorescence was observed in the emission spectrum, only Eu^{3+} emission bands (**Figure 5.6**).

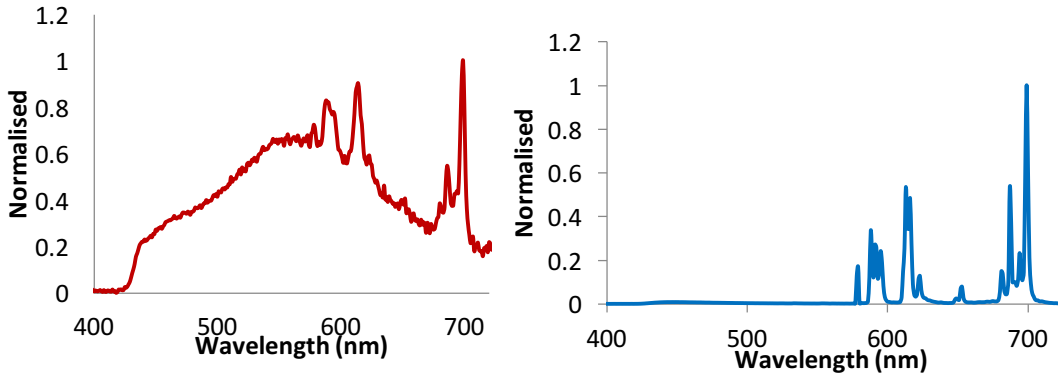

Figure 5.5 (Left) normalised emission spectrum of **[Eu.L^1]** at 298 K in water; (right) emission at 77 K in an ethanol glass. λ_{ex} = 380 nm.

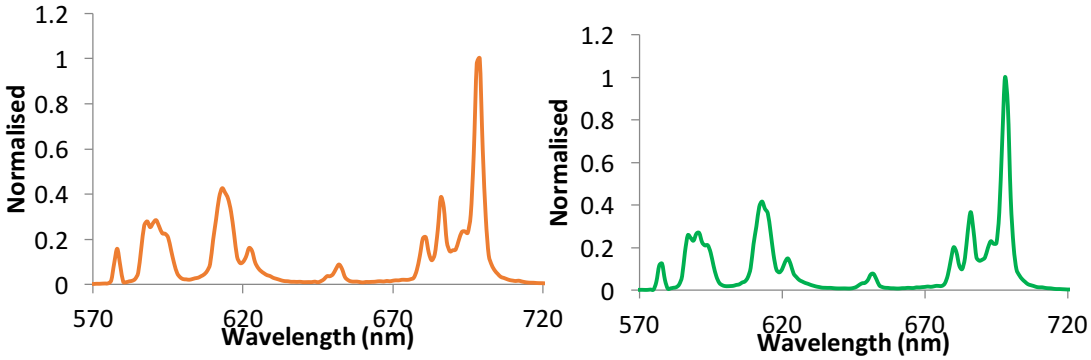

Figure 5.6 Normalised emission spectra of **[Eu.L^1]** and **[Eu.L^2]** in water, λ_{ex} = 318 nm at 298 K.

The absorbance spectrum of **[Eu.L^2]**, in comparison, shows a broad shoulder at 360 nm and a structured wavelength maximum at 318 nm, due to a localised π π* transfer transition within the chromophore (**Figure 5.7**). A broad shoulder is present in the absorbance spectrum with a maximum of 368 nm, and is assigned to an ICT transition. The ICT transition observed for **[Eu.L^2]** is less

pronounced than that of **[Eu.L^1]**, due to the poorer electron donation ability of the phenolic oxygen atom.

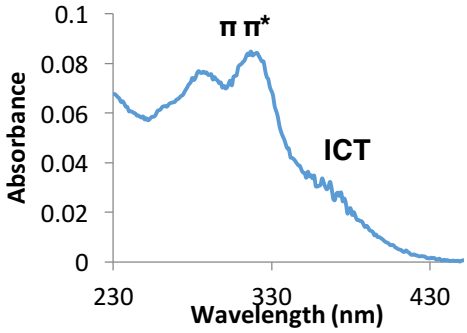

Figure 5.7 Absorbance spectrum of **[Eu.L^2]**. Complex concentration = 5 μM in water, 298 K.

The emission spectrum of **[Eu.L^2]** was recorded after excitation at 318 nm (**Figure 5.6**). An identical emission spectral response to that of **[Eu.L^1]** was observed, with a ratio of 0.4 between the 'hypersensitive' $\Delta J = 2$ and $\Delta J = 4$ emission bands. Excitation at the localised π π* transition of the pyridylalkynylaryl chromophore, however, was found not to sensitise Tb^{3+} emission efficiently at room temperature, even in deoxygenated solutions (See **Appendix**, **Figure A.8**). The weak terbium-emission observed for **[Tb.L^2]**, has been seen previously in the literature with chromophores bearing electron donating substituents.[18,19] The $^5D_4$ excited state of Tb^{3+} (20,400 cm^{-1}) is higher in energy than the $^5D_0$ of Eu^{3+} (17,200 cm^{-1}), and closer in energy to the excited state of the chromophore. A thermally activated back energy transfer process is, therefore, possible at room temperature. The rate of back energy transfer is much slower at low temperatures (77 K), allowing the chromophore to sensitise terbium-centred emission more efficiently (See **Appendix**, **Figure A.9**).

The weak terbium-centred emission observed with **[Tb.L^2]**, at room temperature, led to the pK_a and the binding studies of Mg^{2+}, Ca^{2+} and Zn^{2+} being carried out only with the europium-based analogue **[Eu.L^2]**.

The photophysical properties of **[Eu.L^1]**, **[Eu.L^2]** and **[Tb.L^2]** are compared in **Table 5.1**. Luminescence lifetime measurements in both H_2O and D_2O at room

temperature revealed hydration numbers of one (q = 1) for both **[Eu.L^1]** and **[Eu.L^2]**, with a total lanthanide coordination number of nine (**Equation 5.1**).[20]

$$q_{Eu} = 1.2\left(k_{H_2O} - k_{D_2O} - 0.25 - 0.075n\right) \quad \textbf{Eq. 5.1}$$

As expected, the lifetime of the Eu^{3+} excited state of both **[Eu.L^1]** and **[Eu.L^2]** is shorter in H_2O, because of a more favourable non-radiative O-H vibrational pathway to quench europium emission. No luminescence lifetimes were measured for **[Tb.L^2]**, owing to the very weak Tb^{3+} emission at room temperature. It was assumed that the hydration number, like for **[Eu.L^2]**, was one (q = 1).

Table 5.1 Photophysical data of **[Eu.L^1]**, **[Eu.L^2]** and **[Tb.L^2]** in H_2O, 298 K. For luminescence lifetime measurements of **[Eu.L^1]** and **[Eu.L^2]**, λ_{ex} = 315 nm, λ_{em} = 613 nm, 298 K. Quantum yields (Φ) $\pm$ 20 % measured using a $[Ru(bpy)_3]^{2+}$ standard in H_2O. [a] Not measured because of the weak emission observed at room temperature.

Complex	λ_{ex} (nm)	ε / 10^3 ($M^{-1}cm^{-1}$)	τ_{H_2O} (ms)	τ_{D_2O} (ms)	q	Φ_{H_2O} / %
[Eu.L^1]	315	11.5(2)	0.61	1.87	1.0	13
[Eu.L^2]	315	18.4(4)	0.61	1.89	1.0	11
[Tb.L^2]	314	17.9(2)	[a]	[a]	[a]	[a]

The pyridylalkynylaryl chromophore exhibits solvatochromism in both lanthanide complexes **[Eu.L^1]** and **[Eu.L^2]**. In less polar solvents such as methanol, ethanol and *tert*-butanol, a small bathochromic shift is observed of the localised π π* maximum with the disappearance of the broad structureless transition assigned to an ICT state at 368 nm. A linear increase in the total emission intensity was reported for **[Eu.L^1]** with a decrease in solvent polarity. No apparent correlation with solvent polarity was seen, however, with **[Eu.L^2]** where the aniline nitrogen is *meta* to the chromophore (**Figure 5.8**). Lanthanide complexes containing similar push-pull electron rich chromophores are well known to exhibit solvatochromic behaviour.[19] It has been shown previously that complexes bearing aniline nitrogen atoms *para* to the chromophore also display a linear dependence to solvent polarity.[21] An increase in the total emission

intensity was observed in less polar solvents, and can be attributed to the ICT state becoming increasingly destabilised as the solvent polarity is reduced.[21]

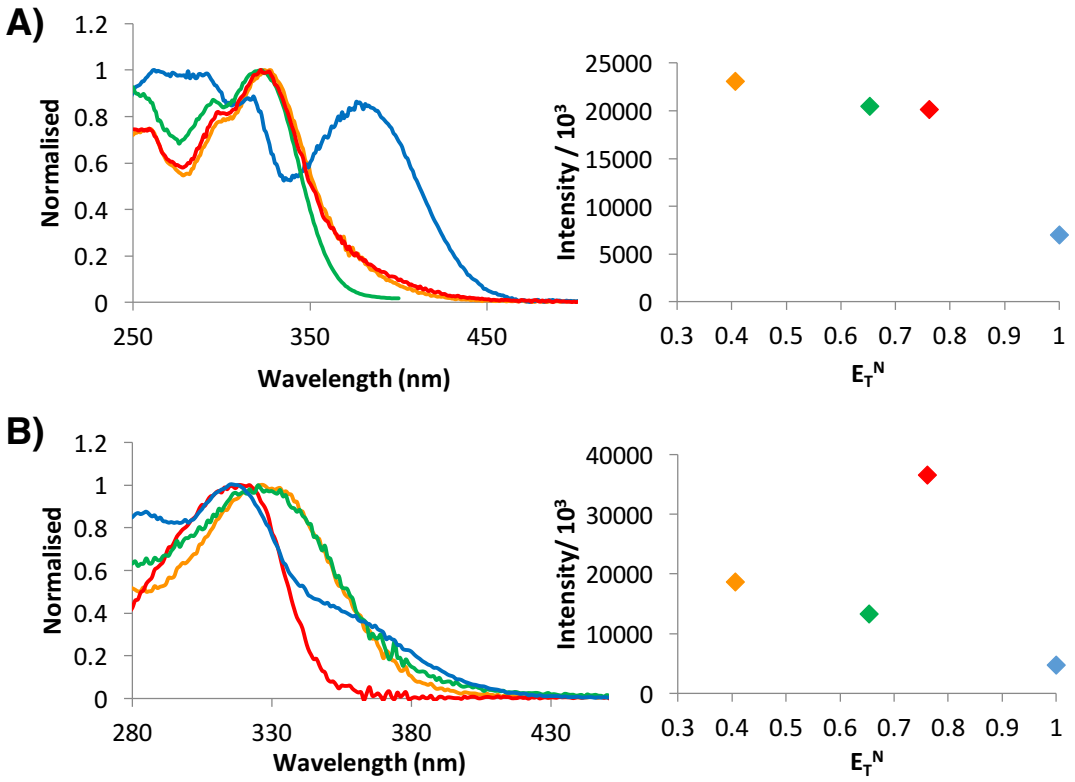

Figure 5.8 (Right) Normalised absorbance spectra of (**A**) **[Eu.L^1]** and (**B**) **[Eu.L^2]** in water, methanol, *tert*-butanol and ethanol at 298 K. (Left) the relationship of the integrated emission intensity against the Reichardt's normalised solvent polarity (E_T^N).[22]

5.3.2 The pyridylaryl chromophore, [Ln.bL^2]

The absorbance spectrum of **[Tb.bL^2]** is shown in **Figure 5.9**. The presence of a pyridylaryl chromophore instead of a pyridylalkynylaryl chromophore (as seen with **[Eu.L^1]** and **[Eu.L^2]**), shifts the absorbance maximum towards the blue. The effect is similar to that observed in the naphthalene series in **Chapter 4**, and can be attributed to the reduction in the conjugation length, and the loss of planarity in the bi-aryl system, allowing aryl-aryl carbon-carbon bond rotation to occur. An absorbance wavelength maximum of 280 nm was seen in aqueous solutions, arising from to a localised $\pi\,\pi^*$ excited state transition in the chromophore (**Figure 5.9**). A broad shoulder was seen at lower energy with a

maximum of 348 nm and could arise from intramolecular charge transfer (ICT) within the bi-aryl chromophore.

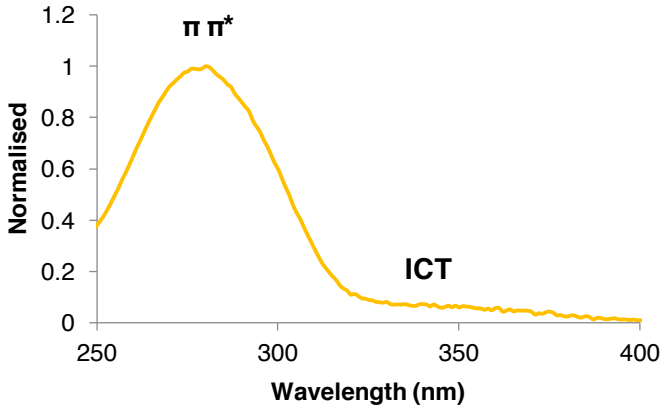

Figure 5.9 Absorbance spectrum of **[Tb.bL^2]** in water at 298 K.

The triplet excited state of the chromophore was too high in energy to efficiently sensitise europium-centred emission, with the loss of energy due to non-radiative vibrational quenching pathways. A significant amount of ligand phosphorescence was also seen at ambient temperatures (**Figure 5.10**). There was, however, efficient energy transfer to the higher lying $^5D_4$ excited state of Tb^{3+}, resulting in the characteristic terbium-centred emission with the ΔJ = -2 to ΔJ = 1 emission bands observed at room temperature (**Figure 5.10**).

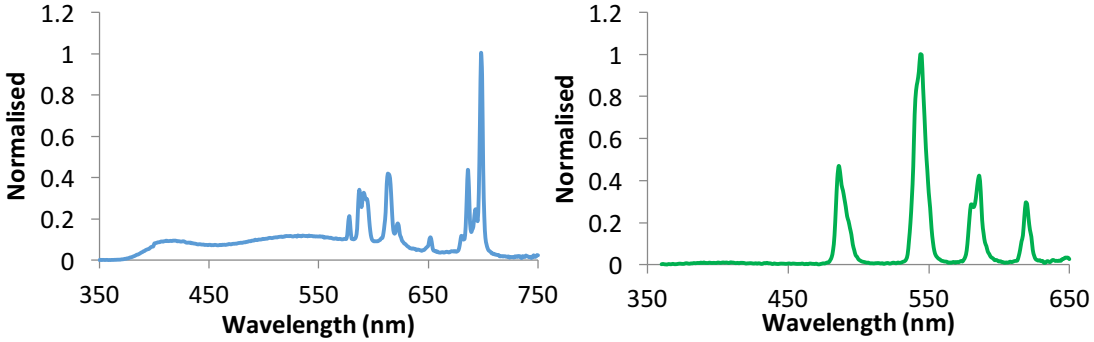

Figure 5.10 Normalised emission spectra of (left) **[Eu.bL^2]** and (right); **[Tb.bL^2]** in water, λ_{ex} = 280 nm at 298 K.

Table 5.2 Photophysical data for **[Eu.bL^2]** and **[Tb.bL^2]**. Lifetimes for **[Tb.bL^2]** were measured under both aerated (**A**) and deoxygenated (**D**) conditions (λ_{ex} = 280 nm, λ_{em} = 544 nm for **[Tb.bL^2]** and λ_{ex} = 280 nm, λ_{em} = 613 nm for **[Eu.bL^2]**). The hydration number (q) was determined under deoxygentated conditions. Quantum yields (Φ) $\pm$ 20 % were measured in aerated and deoxygenated samples in H_2O and ethanol using a quinine sulphate standard in 0.5 M H_2SO_4. [a] Data not collected.

Complex	λ_{ex} (nm)	ε / 10^3 ($M^{-1}cm^{-1}$)	τ_{H_2O} (ms)		τ_{D_2O} (ms)		$\tau_{glycerol}$ (ms)		Φ_{H_2O} / %		Φ_{EtOH} / %		q
			A	D	A	D	A	D	A	D	A	D	
[Eu.bL^2]	280	[a]	0.50	0.56	1.70	1.82	0.77	[a]	[a]	[a]	[a]	[a]	[a]
[Tb.bL^2]	280	6.0	0.42	1.52	0.72	2.30	1.13	[a]	3.4	5.4	1.5	3.1	0.9

The photophysical properties of **[Eu.bL^2]** and **[Tb.bL^2]** are reported in **Table 5.2**. Luminescence lifetime measurements and quantum yields (Φ) of **[Tb.bL^2]** were determined in both aerated and deoxygenated samples at room temperature. Significantly shorter lifetimes were recorded at ambient temperatures for the bi-aryl **[Eu.bL^2]** and **[Tb.bL^2]** complexes, compared to **[Eu.L^1]** and **[Eu.L^2]**, comprised of a pyridylalkynylaryl chromophore. At room temperature a large error of 13 % was associated with the excited state lifetimes of **[Tb.bL^2]** in D_2O, calculated from the standard deviation of four separate measurements. This behaviour led to discrepancies in the calculated hydration number (q) according to **Equation 5.2**.

Due to the uncertainty in the measurements under aerated conditions, possibly due to the presence of back energy transfer, the hydration number was instead determined from deoxygenated samples of bi-aryl **[Tb.bL^2]** where quenching from triplet oxygen is eliminated (**Table 5.2** and **Equation 5.2**).[20] A hydration number of one (q = 1) was determined from deoxygenated solution, with an overall lanthanide coordination number of nine (**Table 5.2**).

$$q_{Tb} = 5.0\,(k_{H_2O} - k_{D_2O} - 0.06 - 0.010n) \quad \textbf{Eq. 5.2}$$

The bi-aryl complex **[Tb.bL^2]**, displayed a brighter emission intensity and a much longer excited state lifetime in deoxygenated samples in both H_2O and D_2O. A 1.6-fold increase in the total luminescence emission intensity was observed with a 3.6- and 3.2-fold increase in the excited state lifetime in H_2O and D_2O respectively. Such behaviour is characteristic of the reduction of quenching of the triplet excited state of the chromophore by $^3O_2$, and suggests that back energy transfer from the $^5D_4$ excited state of Tb^{3+} to the triplet excited state of the chromophore is taking place at room temperature. The bi-aryl complex **[Tb.bL^2]**, therefore, could be used as an emission- and lifetime-based pO_2 sensor.

Lifetimes of this order of magnitude are uncommon for Tb^{3+} complexes. In the majority of lanthanide-based systems, the higher energy of the $^5D_4$ excited state of Tb^{3+}, and the poorer overlap with O-H and O-D vibrational oscillators, results in a longer lifetime than their europium-based analogues.[23] Surprising,

and uncharacteristically short Tb^{3+} excited state lifetimes have been seen in comparable bi-aryl systems containing pyridylaryl chromophores with electron-donating substituents, including multiple reports by Maury and co-workers.[24,25]

Increasing the viscosity of the solution was found to increase the lifetime of the excited state in both **[Eu.bL^2]** and **[Tb.bL^2]**, where a 1.5- and 2.7-fold increase was observed in glycerol compared to water respectively. This behaviour was first observed by Maury and co-workers, and a number of millisecond-scale viscosity probes containing bi-aryl chromophores have been very recently developed.[24,25] All terbium complexes studied by Maury displayed low millisecond lifetimes in methanol, with a 4-fold increase in the excited state lifetime seen in glycerol (0.24 to 0.89 ms).[25] Maury and co-workers attributed this observation to the perturbation of carbon-carbon rotation of the bi-aryl chromophore in more viscous solutions, reducing the energy lost by non-radiative relaxation pathways. Unlike **[Eu.bL^2]**, however, europium complexes studied by Maury were found to be insensitive to changes in viscosity. It was suggested that back energy transfer from the $^5D_4$ state was essential to viscosity sensitivity.[24,25] An energy gap of less than 1800 cm^{-1} is typically required for back energy transfer to occur, and is much more commonly observed with Tb^{3+} as the $^5D_4$ state is higher in energy than the $^5D_0$ of Eu^{3+}.[4,19]

In order to further understand the short lifetimes observed for **[Tb.bL^2]** and the effect of solution viscosity proposed by Maury, a study into the solvent effect on the excited state lifetime was carried out, under both oxygenated and deoxygenated conditions, with solvents of varying viscosity and polarity.

The absorbance spectra of **[Tb.bL^2]** in a range of solvents is shown in **Figure 5.11**. It is clear that in less polar alcoholic solvents, for example, methanol, isopropanol and *tert*-butanol, a bathochromic shift in the absorbance wavelength was observed. A 5 nm shift of the wavelength maximum (π π^*) was seen in methanol and a 10 nm red shift in isopropanol, ethanol and *tert*-butanol (**Figure 5.11**). The solvatochromic behaviour and the general decrease in lifetime observed in more polar solvents implies that the triplet excited state is stabilised by dipolar interactions, and is lower in energy.[4,26] Ethanol was seen to be an

exception of this rule with a lifetime of 0.23 ms reported in aerated conditions, significantly lower than the 0.43 ms observed for water.

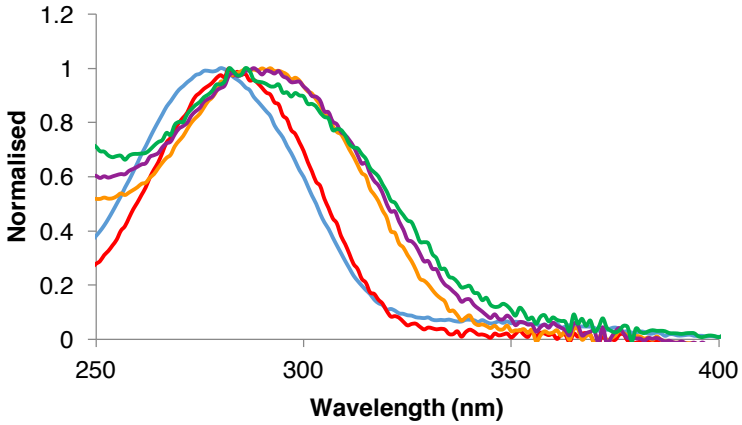

Figure 5.11 Normalised absorbance spectra of **[Tb.bL^2]** in water, methanol, ethanol, isopropanol and *tert*-butanol at 298 K.

Table 5.3 Excited state lifetimes of **[Tb.bL^2]** in a range of solvents with varying viscosity and polarity (determined from the Reichardt's normalised solvent polarity parameter (E_T^N))[22] at 298 K. Where (**A**) is in aerated and (**D**) is in deoxygenated solutions (λ_{ex} = 280 nm, λ_{em} = 544 nm). [a] No excited state lifetime was measured.

Solvent	Viscosity (cP) at 298 K	Lifetime (ms)		E_T^N [22]
		A	D	
H_2O	0.89	0.43	1.52	1.000
Methanol	0.54	0.59	1.87	0.765
Ethanol	1.02	0.23	1.70	0.655
***t*-Butanol**	4.31	0.85	1.51	0.602
***i*-Propanol**	2.04	0.67	1.33	0.552
Glycerol	934	1.13	[a]	-

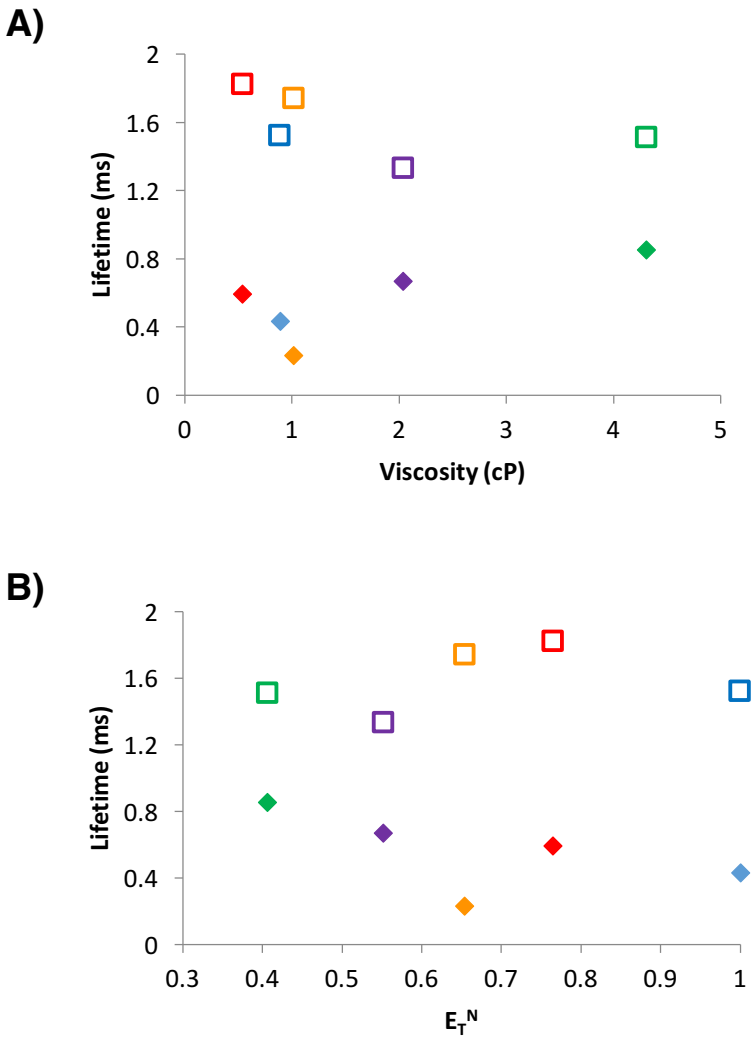

Figure 5.12 The excited state lifetime of **[Tb.bL^2]** relative to (**A**) the solvent viscosity and (**B**) the Reichardt's normalised solvent polarity parameter (E_T^N)[22] of water, methanol, ethanol, isopropanol and *tert*-butanol. Square highlights deoxygenated and diamond shows aerated conditions at 298 K.

It is evident from the analysis of **Table 5.3** and **Figure 5.12**, that there is no significant correlation observed between the excited state lifetime of **[Tb.bL^2]** with viscosity or solvent polarity, in both aerated and deoxygenated solutions (**Figure 5.12**). A similar response to solvent polarity was observed for **[Eu.L^2]** in **Section 5.3.1** where the aniline nitrogen is *meta* to the chromophore.

Significantly longer lifetimes and larger quantum yields were seen in deoxygenated conditions of all solvents studied, due to the elimination of the competitive quenching of the T_1 state of the chromophore by triplet oxygen. Such behaviour all but confirms the presence of back energy transfer from the $^5D_4$ state

of Tb^{3+} to the excited state of the chromophore. The energy of the ligand triplet excited state was estimated by studying the phosphorescence spectrum of **[Gd.bL^2]** at 77 K in an ethanol glass. The energy of the 0-0 component of the π π* transition was estimated to be 22,250 cm^{-1}, which is sufficiently high to permit efficient energy transfer to Tb^{3+} in **[Tb.bL^2]** (See **Appendix Figure A.10**). A broad ICT excited state was also observed centred around 25,000 cm^{-1} but extending beyond 22,000 cm^{-1}, suggesting that the system may be prone to thermally activated back-energy transfer from Tb^{3+} (energy of $^5D_4$ = 20,500 cm^{-1}) to repopulate the ICT excited state (or indeed even the ^{3}π–π*).

The presence of back energy transfer was also reported in the bi-aryl systems studied by Maury, and it was deemed essential for viscosity sensitivity.[24,25] Luminescence lifetimes were measured in methanol / glycerol in varying proportions, with solutions displaying a range of viscosities.[24,25] A linear increase in the lifetime was reported in solutions of an increased viscosity. No such linearity for viscosity is seen here in the case of **[Tb.bL^2]**, suggesting that the mechanism for the reduction in the excited state lifetime is not due to non-radiative vibrational relaxation via aryl-aryl rotation. Solvent viscosity will remain unchanged in both aerated and deoxygenated environments, so aryl-aryl rotation of the chromophore is unlikely be the reason for the reduced lifetime seen.

It is thought that instead of a viscosity sensitivity, what is observed in bi-aryl complexes of this nature is a balance between the competing Tb^{3+} emission and quenching of the triplet excited state by dissolved oxygen. Schumpe and co-workers investigated the solubility of oxygen in aqueous solutions, and found that as the mole fraction of glycerol increased there was a large linear decrease in oxygen solubility.[48] It is likely, therefore, that an identical effect led to a linear increase in lifetime with viscosity presented in the work by Maury.[24,25] Instead of an increased excited state lifetime due to restricted rotation, the lifetime is increasing because of a decreased oxygen solubility in solution as the mole fraction of glycerol is increased. Such behaviour reduces the amount of triplet oxygen quenching of the triplet excited state of the chromophore and increase the luminescence lifetime.

5.4. pK_a studies of [Eu.L^1], [Eu.L^2] and [Tb.bL^2]

A study into the effect of the pH on the absorbance and emission spectra of complexes containing a pyridylalkynylaryl chromophore in the case of **[Eu.L^1]** and **[Eu.L^2]**, and a pyridylaryl-based system **[Tb.bL^2]** was carried out. As for the naphthalene series of ligands in **Chapter 4**, pH titrations were run at 298 K at a constant ionic strength in 100 mM KCl. The structures of **[Eu.L^1]**, **[Eu.L^2]** and **[Tb.bL^2]** are shown in **Figure 5.13** for reference.

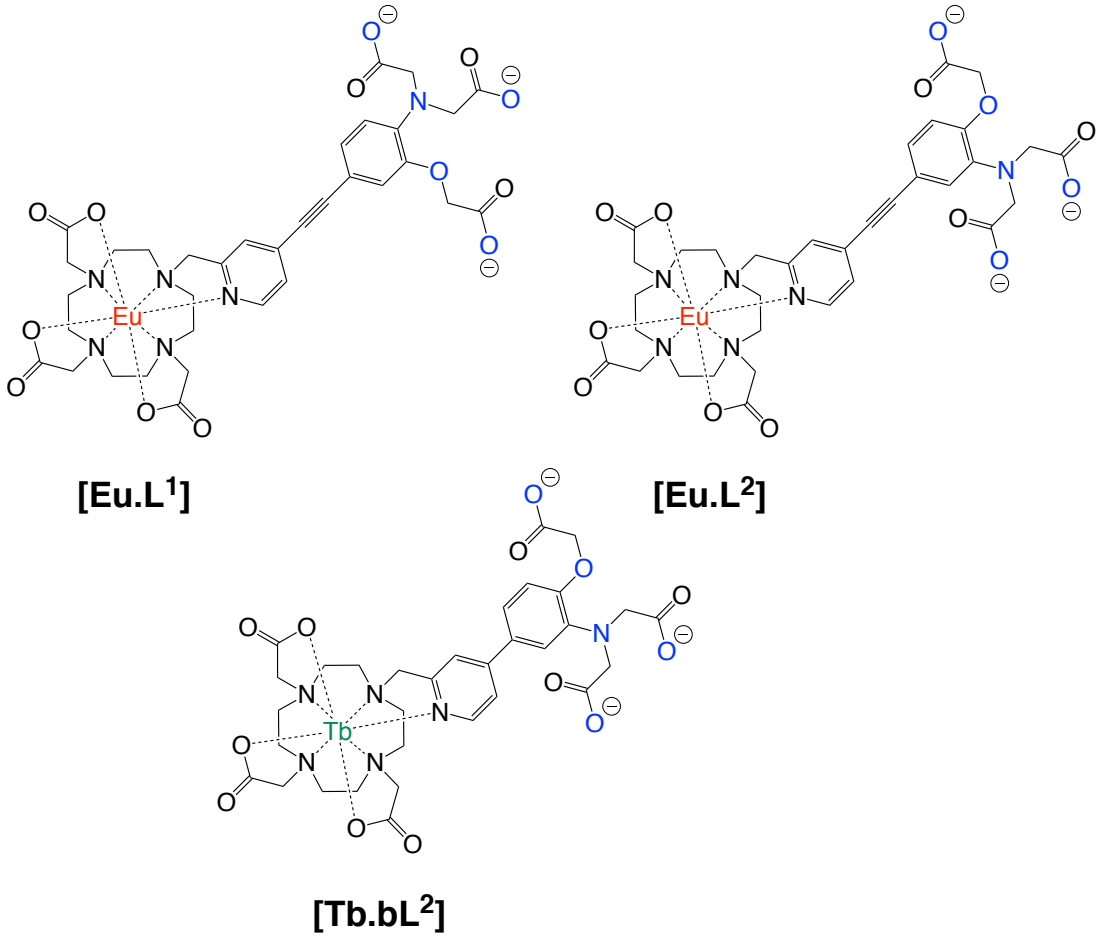

Figure 5.13 The structures of complexes **[Eu.L^1]**, **[Eu.L^2]** and **[Tb.bL^2]**.

5.4.1 Absorbance pK_a studies of [Eu.L^1], [Eu.L^2] and [Tb.bL^2]

In basic solution, the absorbance spectrum of **[Eu.L^1]** displays three maxima at 270 nm, 315 nm and 378 nm, in a profile identical to that shown in **Figure 5.4**. The change in the absorbance intensity at 316 nm and 378 nm was

investigated from pH 7.7 to 3.3. Following addition of acid and the reduction of the pH, a 15 nm hypsochromic shift of the ICT band from 378 nm to 363 nm was observed (**Figure 5.14**). The blue shift is attributed to protonation of the aniline nitrogen atom under acidic conditions. No pronounced changes in the absorbance intensities were reported at 270 nm or 315 nm in solutions of a reduced pH. An isosbestic point is present in the absorbance spectrum at 370 nm (**Figure 5.14**).

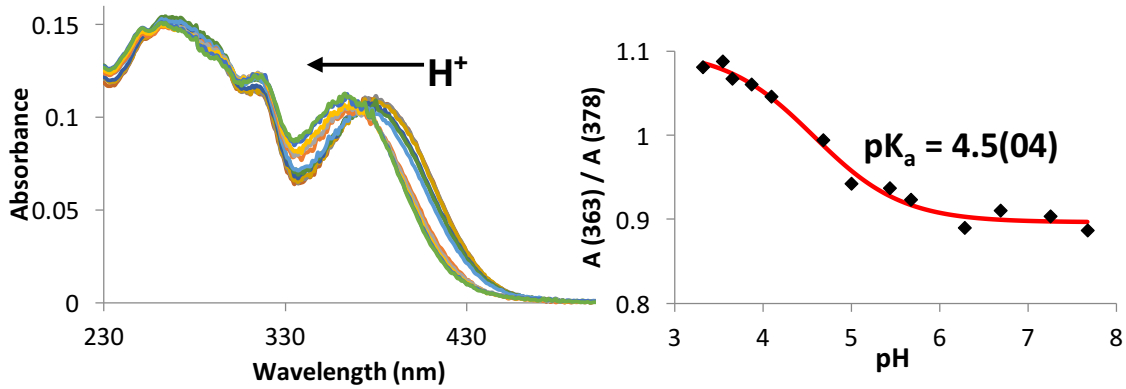

Figure 5.14 (Left) Absorbance spectrum; (right) sigmoidal fit of the absorbance ratio at 363 nm and 378 nm against the pH. **[Eu.L^1]** concentration = 10 μM in 100 mM KCl, 298 K.

The observed blue shift allows the pK_a to be determined from a ratio of the wavelength maxima in both acidic and basic solutions. A pK_a of 4.5 was calculated, slightly lower than that of APTRA, where a value of 5.5 has been revealed previously from absorbance spectroscopy experiments.[6] The lower pK_a of **[Eu.L^1]** compared to APTRA arises because the *para* nitrogen lone pair of electrons is conjugated within the aromatic chromophore, and is less readily available for protonation under acidic conditions.

Absorbance spectra for **[Eu.L^2]** and **[Tb.bL^2]** are shown in **Figure 5.15**. It is evident that the change in pH from basic to acidic conditions had no significant effect on the spectral form in absorption. No change in the absorbance intensity was reported at the wavelength maximum, and no hypsochromic shift occurred at low pH, e.g. with **[Eu.L^2]**. Absorbance spectroscopy is, therefore, unsuitable to monitor *meta* aniline nitrogen protonation with **[Eu.L^2]** and **[Tb.bL^2]**, due to the absence of a pronounced ICT state.

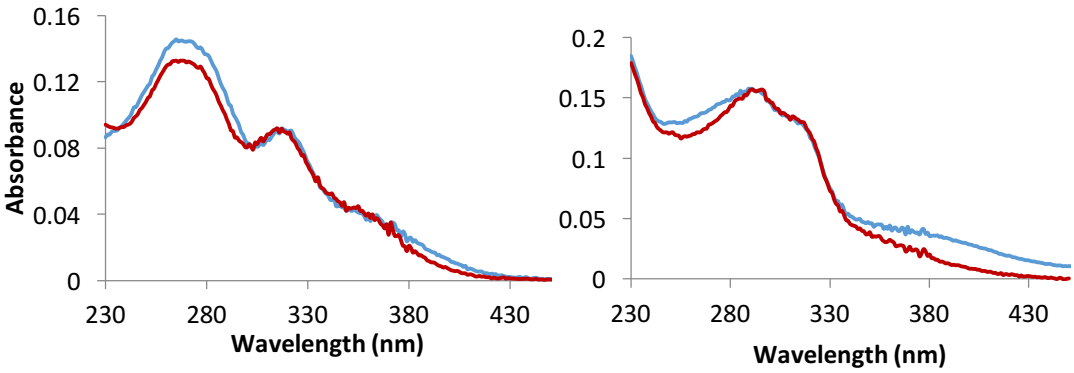

Figure 5.15 Absorbance spectrum of **[Eu.L^2]** and **[Ln.bL^2]** in basic and acidic solutions at constant ionic strength of 100 mM KCl, 298 K.

5.4.2 Fluorescence emission pK$_a$ studies of [Eu.L^1], [Eu.L^2] and [Tb.bL^2]

Fluorescence emission spectra of **[Eu.L^1]**, **[Eu.L^2]** and **[Tb.bL^2]** were recorded with excitation at the localised π π* excited state in each case. It is apparent from the emission spectra shown in **Figure 5.16**, and the fluorescence excitation spectrum (See **Appendix Figure A.11** and **Figure A.13**), that no pH sensitivity is observed over the pH range 4-8 for **[Eu.L^1]** and **[Tb.bL^2]**. No pK$_a$ values can, therefore, be obtained for these two complexes by fluorescence spectroscopic methods.

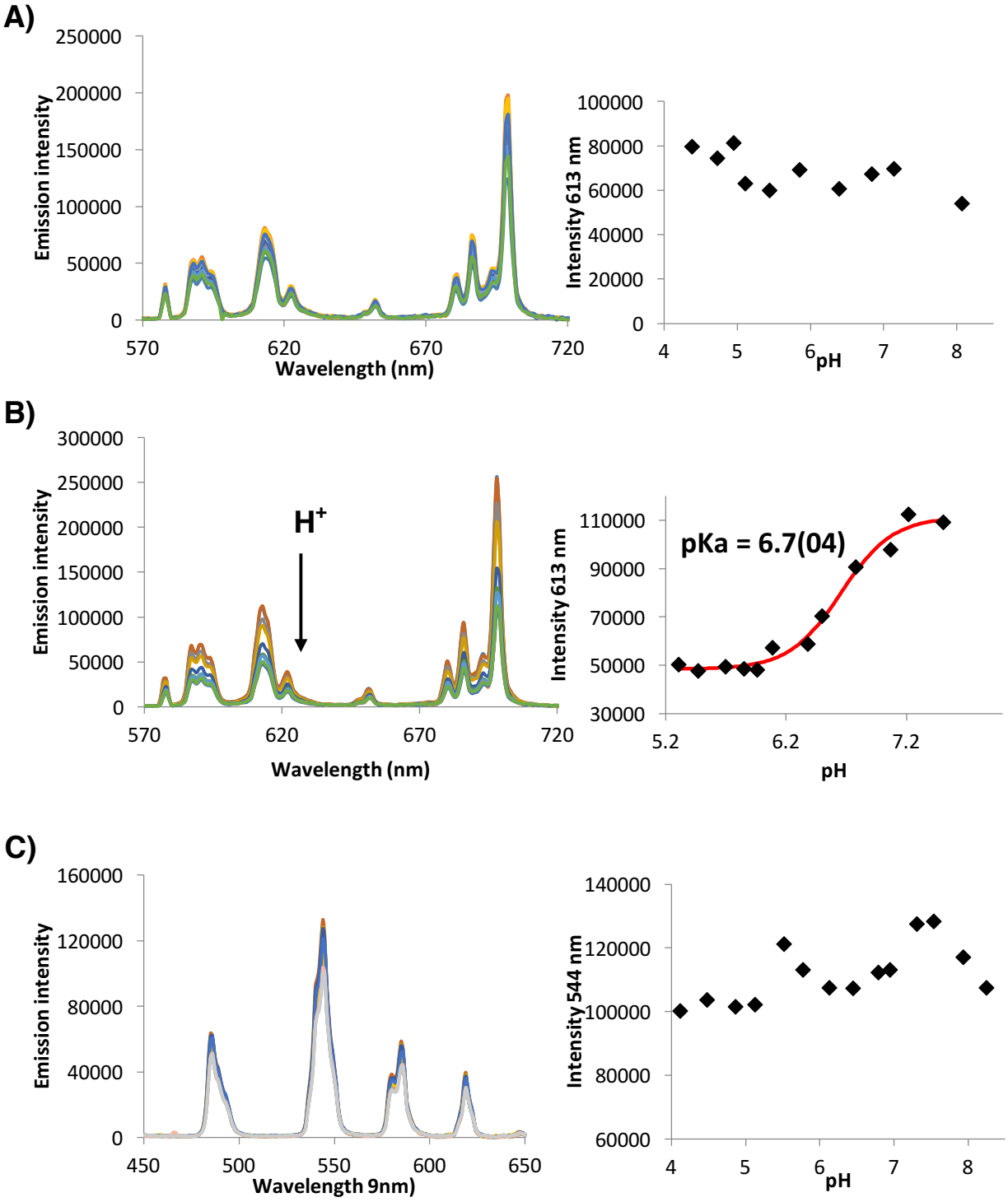

Figure 5.16 (Left) emission spectra; (right) sigmoidal fitting of the emission intensity against the pH of **(A) [Eu.L^1]** (λ_{ex} = 315 nm), **(B) [Eu.L^2]** (λ_{ex} = 315 nm) and **(C) [Tb.bL^2]** (λ_{ex} = 280 nm) in 100 mM KCl, 298 K.

In contrast, **[Eu.L^2]** displayed a fluorescence emission and excitation response to pH in the range 7.5—5.3. A 2.2-fold 'turn-off' in the total emission intensity following protonation of the aniline nitrogen was seen. A pK_a of 6.7 was

calculated from both fluorescence emission and excitation spectroscopy from a non-linear least squares iterative analysis (See **Appendix** for the pH dependence of the excitation spectrum, **Figure A.12**).

It is clear from **Figure 5.16** that **[Eu.L^1]** and **[Tb.bL^2]** are insensitive to pH changes in the physiological range, making then suitable probes to detect Mg^{2+} *in vivo*. The complex **[Eu.L^2]**, displayed a more pronounced luminescence change in the physiological range, where a 1.2-fold reduction in its emission intensity from pH 7.5 to 6.8 was observed. The Mg^{2+} complex of **[Eu.L^2]** (saturated with 50 mM Mg^{2+}), however, is insensitive to pH within the pH range 6 to 8.2. Such behaviour indicates that following the addition of 50 mM Mg^{2+}, the aniline nitrogen becomes bound to Mg^{2+}, and is no longer available for protonation at reduced pH (**Figure 5.17**).

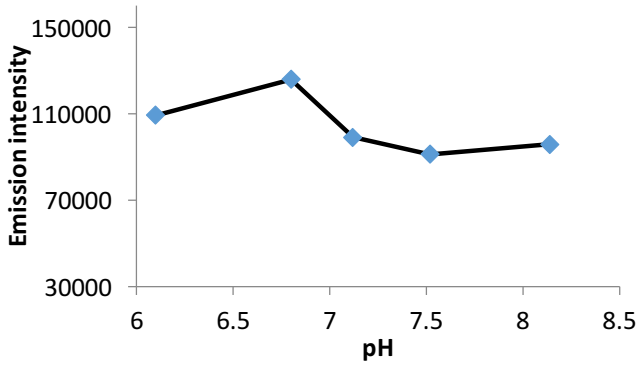

Figure 5.17 Emission spectrum of **[Eu.L^2]** from pH 6 to 8.2 after saturating with Mg^{2+} (50 mM), (λ_{ex} = 315 nm). **[Eu.L^2]** concentration = 5 μM in 100 mM KCl, 298 K.

5.5 Binding studies of [Eu.L^1] and [Eu.L^2]

The absorbance, emission and excitation binding studies of **[Eu.L^1]** and **[Eu.L^2]** with Mg^{2+}, Ca^{2+} and Zn^{2+} in a buffered solution of 50 mM HEPES, 100 mM KCl at 298 K (pH 7.21) are reported here. Such studies probe how the affinity and selectivity of the APTRA binding moiety is affected once incorporated into both pyridylalkynylaryl- and pyridylaryl-based chromophores involved in coordination to lanthanide(III) ions. Direct comparisons will be made with **NapL^1** and **NapL^2** in the model naphthalene series, discussed in detail in **Chapter 4**. Similarly, to the analysis of **NapL^1** and **NapL^2**, it will be determined what effect, if any, the position of the aniline nitrogen has on the affinity and selectivity for Mg^{2+}, Ca^{2+} and Zn^{2+}.

5.5.1 Absorbance binding studies of [Eu.L^1] and [Eu.L^2]

In the 'metal-free' state **[Eu.L^1]** has two wavelength maxima in the absorbance spectrum at 315 nm and 380 nm. After subsequent additions of Mg^{2+}, Ca^{2+} and Zn^{2+}, an increase in the absorbance at 315 nm, and a decrease in the absorbance intensity at 380 nm was observed, with no shift in either of the wavelength maxima. Following addition of Mg^{2+}, Ca^{2+} and Zn^{2+}, an isosbestic point is present in the absorption spectra, at 345 nm for Mg^{2+} and 339 nm for Ca^{2+} and Zn^{2+} (**Figure 5.18**).

It is apparent from analysis of **Figure 5.18**, that following addition of Ca^{2+} and Zn^{2+} to **[Eu.L^1]**, the ICT state at 380 nm is perturbed, with the complete loss of the ICT transition in the absorbance spectrum on metal ion binding saturation. On binding of Mg^{2+}, however, a different spectral response was seen, with a 1.6-fold decrease in the absorbance of the ICT state at 380 nm. Such a spectral response indicates that the aniline nitrogen atom *para* to the chromophore in **[Eu.L^1]** plays a more prominent role in binding to Ca^{2+} and Zn^{2+}, compared to Mg^{2+}.

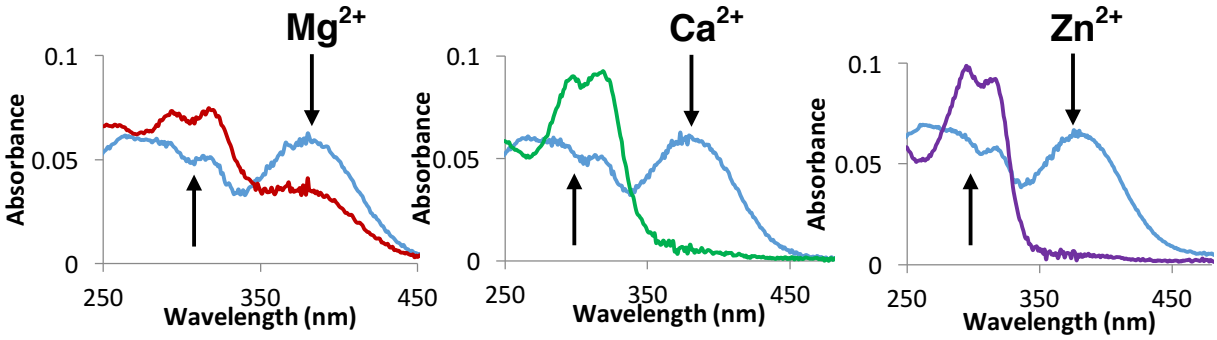

Figure 5.18 Absorbance spectrum of **[Eu.L^1]** for the addition of **(A)** Mg^{2+} (150 mM), **(B)** Ca^{2+} (15 mM) and **(C)** Zn^{2+} (35 μM). **[Eu.L^1]** concentration = 5 μM in 50 mM HEPES, 100 mM KCl, pH 7.21, 298 K.

The absorbance spectrum of **[Eu.L^2]**, in comparison, displays a wavelength maximum at 315 nm in HEPES buffered solution (pH 7.21), in both the metal-free and 'bound' states. An increase in the absorbance intensity was observed at 315 nm on the binding of divalent metal ions, with a 1.1-, 1.3- and

1.5-fold increase seen following the addition of Mg^{2+}, Ca^{2+} and Zn^{2+} respectively. No shift in the wavelength maximum occurred on metal ion binding. The disappearance of the broad shoulder present at 368 nm in the metal-unbound state of **[Eu.L^2]**, gave rise to an isosbestic point at 343 nm following the binding of divalent metal ions (**Figure 5.19**).

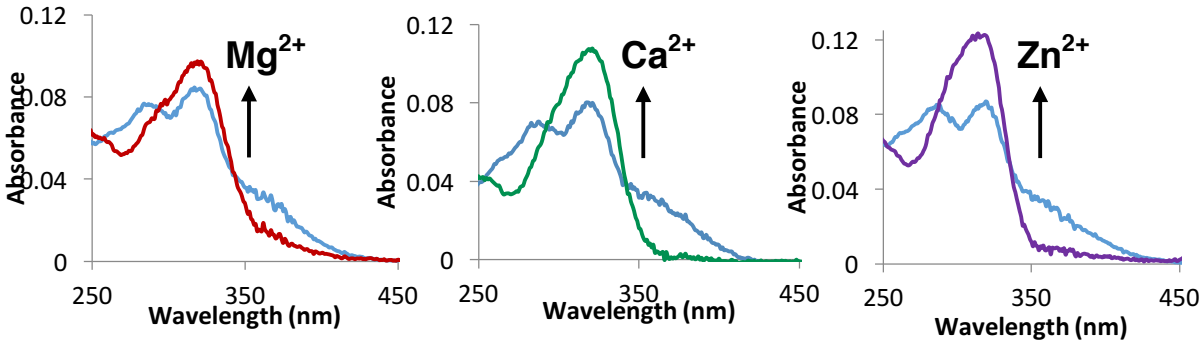

Figure 5.19 Absorbance spectrum of **[Eu.L^2]** for the addition of **(A)** Mg^{2+} (20 mM), **(B)** Ca^{2+} (3.5 mM) and **(C)** Zn^{2+} (11 μM). **[Eu.L^2]** concentration = 5 μM in 50 mM HEPES, 100 mM KCl, pH 7.21, 298 K

5.5.2 Luminescence binding studies of [Eu.L^1] and [Eu.L^2]

Luminescence emission binding studies of **[Eu.L^1]** and **[Eu.L^2]** with Mg^{2+}, Ca^{2+} and Zn^{2+} were carried out with excitation at the isosbestic point (339 nm or 343 nm). Following the addition of aliquots of Mg^{2+}, Ca^{2+} and Zn^{2+}, the change in the emission intensity of the 'hypersensitive' $\Delta J = 2$ and $\Delta J = 4$ transitions was monitored. Dissociation constants were calculated by iteratively fitting the change in the emission intensity at 613 nm of the 'hypersensitive' $\Delta J = 2$ transition, against the concentration of added divalent metal ions to a 1:1 binding model.

The luminescence emission spectra following the addition of Mg^{2+}, Ca^{2+} and Zn^{2+} to **[Eu.L^1]** are shown in **Figure 5.20**. After the addition of Mg^{2+} and Ca^{2+} to **[Eu.L^1]** a decrease in the Eu^{3+} total emission intensity was observed. A 1.5-fold and 1.8-fold reduction was reported at both 613 nm ($\Delta J = 2$) and 699 nm ($\Delta J = 4$). The addition of Zn^{2+}, however, resulted in a 1.8-fold 'turn-on' in the fluorescence emission intensity. Dissociation constants of 7.5 mM, 0.9 mM

and 1.8 μM were calculated respectively using this data, following the addition of Mg^{2+}, Ca^{2+} and Zn^{2+} (**Figure 5.20)**.

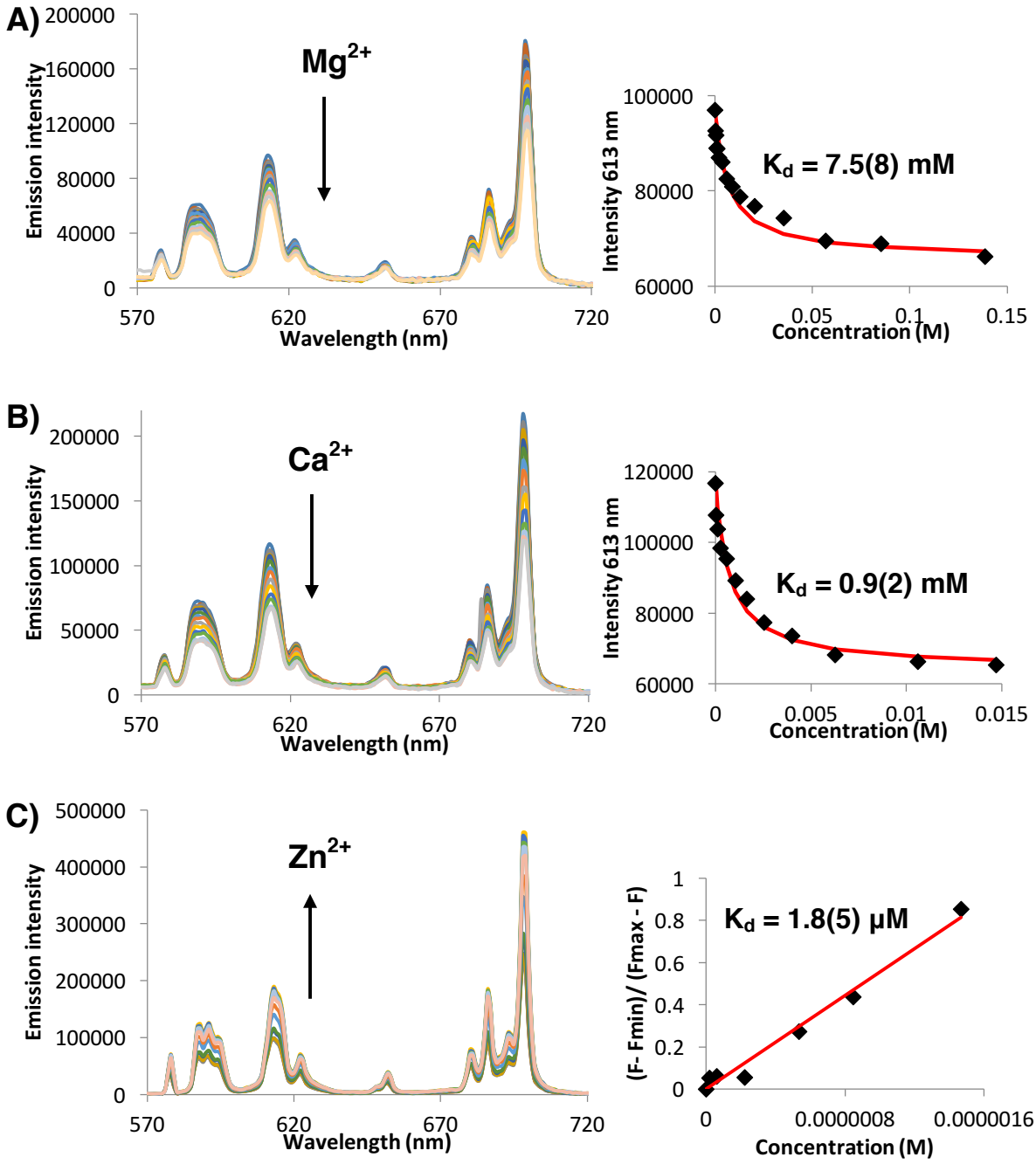

Figure 5.20 (Left) emission spectra; (right) fitting of the emission intensity against the added concentration of **(A)** Mg^{2+}, **(B)** Ca^{2+} and **(C)** Zn^{2+} to a 1:1 binding model. **[Eu.L^1]** complex concentration = 5 μM in 50 mM HEPES, 100 mM KCl, pH 7.21, 298 K, λ_{ex} = 339 nm. The reported dissociation constants are an average of two separate metal ion titrations, and are given with the experimental error in parenthesis.

The excitation spectrum of **[Eu.L^1]** has two maxima at 287 nm and 314 nm. The maximum observed at 380 nm in the absorbance spectrum associated with

conjugation of the *para* aniline nitrogen lone pair is not present in the excitation spectrum. As for to **NapL^1** (**Chapter 4**), an excitation-based ratiometric response was observed following the addition of Mg^{2+}, Ca^{2+} and Zn^{2+} to **[Eu.L^1]**. No significant wavelength shifts of either of the peak maxima at 287 nm and 314 nm in the excitation spectrum were reported. The fluorescence intensities at 287 nm and 314 nm, however, decreased at different rates after the addition of divalent metal ions, allowing dissociation constants to be calculated from a ratio of the two peaks.

The excitation spectrum for the binding of Mg^{2+} to **[Eu.L^1]** is shown in **Figure 5.21**. Fluorescence excitation spectra for the addition of Ca^{2+} and Zn^{2+} showed a similar response to that of Mg^{2+}. Their calculated dissociation constants are shown in the **Appendix** for reference (**Figure A.14** and **Figure A.15**). Comparable K_d values, within the experimental error to those observed from emission spectroscopy (**Figure 5.20**), were calculated from the variation of the fluorescence excitation spectra, following addition of Mg^{2+} (**Figure 5.21**), Ca^{2+} and Zn^{2+} (See **Appendix**, **Figure A.14** and **Figure A.15**).

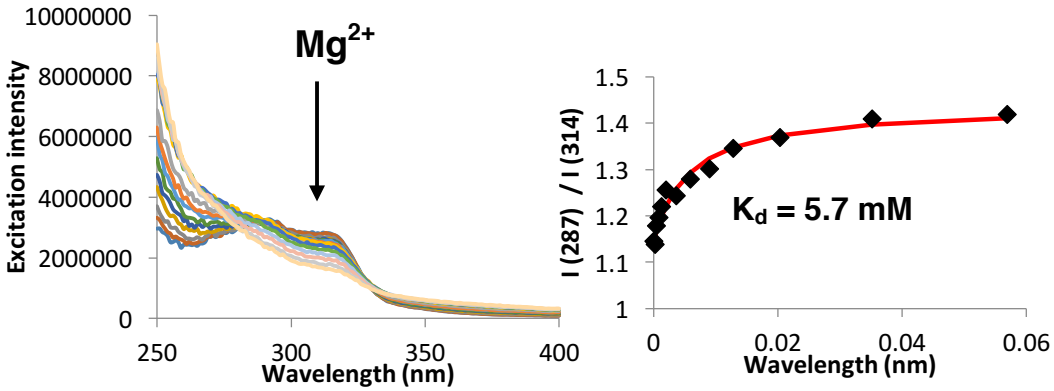

Figure 5.21 (Left) excitation spectrum; (right) fitting of the ratio of excitation intensity at 287 nm and 314 nm against the added concentration of Mg^{2+} to a 1:1 binding model. **[Eu.L^1]** concentration = 5 μM in 50 mM HEPES, 100 mM KCl, pH 7.21, 298 K, λ_{em} = 613 nm.

In contrast to the emission spectral response observed for **[Eu.L^1]**, the addition of Mg^{2+}, Ca^{2+} and Zn^{2+} to **[Eu.L^2]**, resulted in a 1.4-, 2.5-, 6-fold fluorescence enhancement at 613 nm (**Figure 5.22**). Dissociation constants of

3.7 mM, 0.9 mM and 1.9 μM were calculated, for Mg^{2+}, Ca^{2+} and Zn^{2+} respectively (**Figure 5.22**).

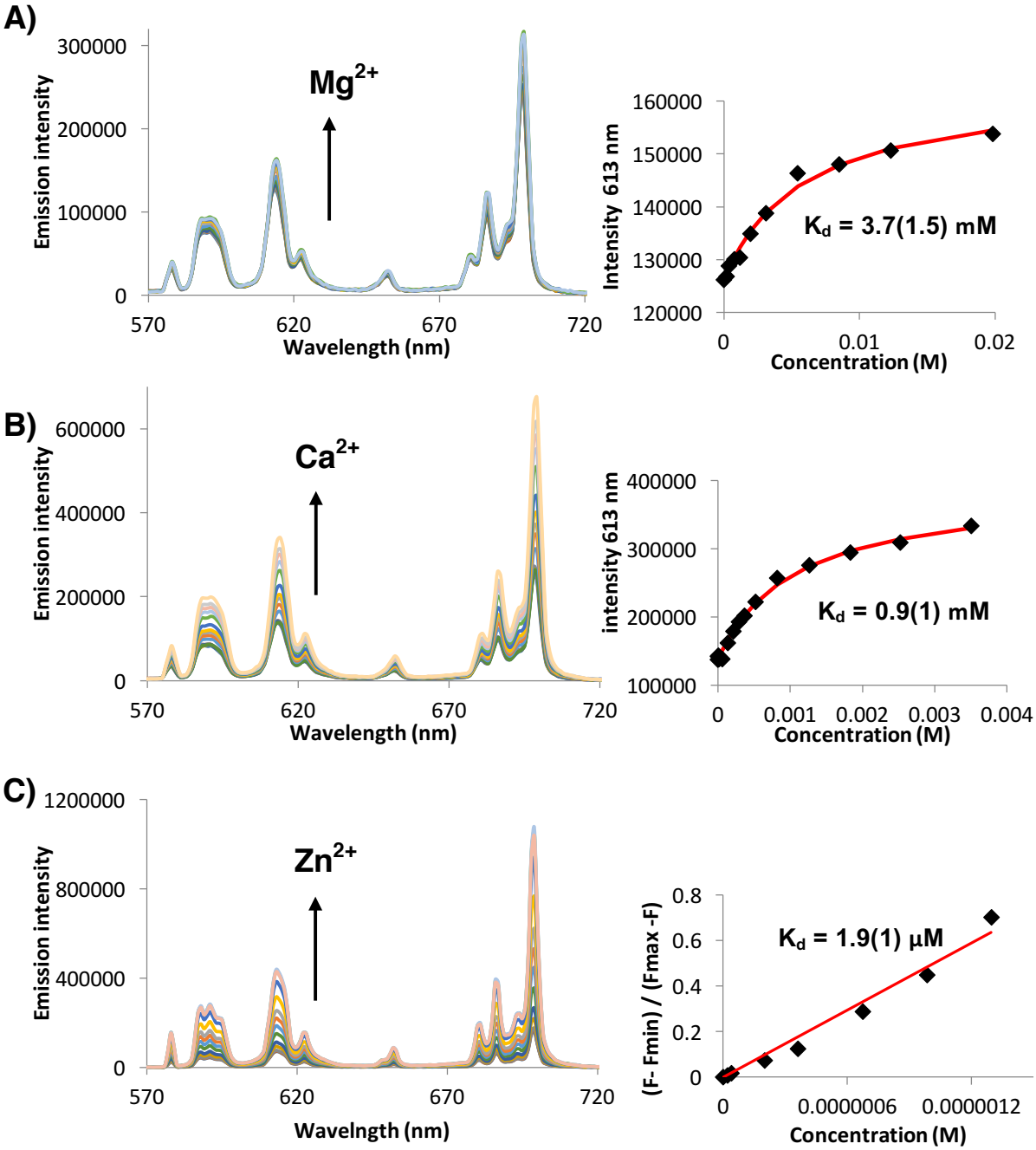

Figure 5.22 (Left) emission spectra; (right) fitting of the emission intensity against the added concentration of **(A)** Mg^{2+}, **(B)** Ca^{2+} and **(C)** Zn^{2+} to a 1:1 binding model. **[Eu.L^2]** complex concentration = 5 μM in 50 mM HEPES, 100 mM KCl, pH 7.21, 298 K, λ_{ex} = 343 nm. The reported dissociation constants are an average of two separate metal ion titrations, and are given with the experimental error in parenthesis.

The excitation spectrum of **[Eu.L^2]** displayed a peak maximum at 310 nm in aqueous buffered solution. Unlike **[Eu.L^1]**, a non-ratiometric excitation response was observed following the addition of Mg^{2+} (**Figure 5.23**), Ca^{2+} and Zn^{2+} (See **Appendix Figure A.16** and **Figure A.17**). A non-ratiometric excitation-based response was also observed for the model naphthalene ligand **NapL^2**, and was attributed to the loss of intramolecular charge transfer from the aniline nitrogen atom.

A K_d value of 9.0 mM was calculated from the fluorescence excitation spectrum for the binding of Mg^{2+} to **[Eu.L^2]**. A significant error of 48 % was associated with the fitting, due to the small changes in the excitation intensity after each addition of Mg^{2+}. At the wavelength maximum of 310 nm, only a 1.1-fold increase in the excitation intensity was observed on saturation with Mg^{2+} (35 mM). A dissociation constant of 9.0 mM is outside the experimental error determined by emission spectroscopy in **Figure 5.22**, but the affinity for Mg^{2+} is close to the required low mM range.

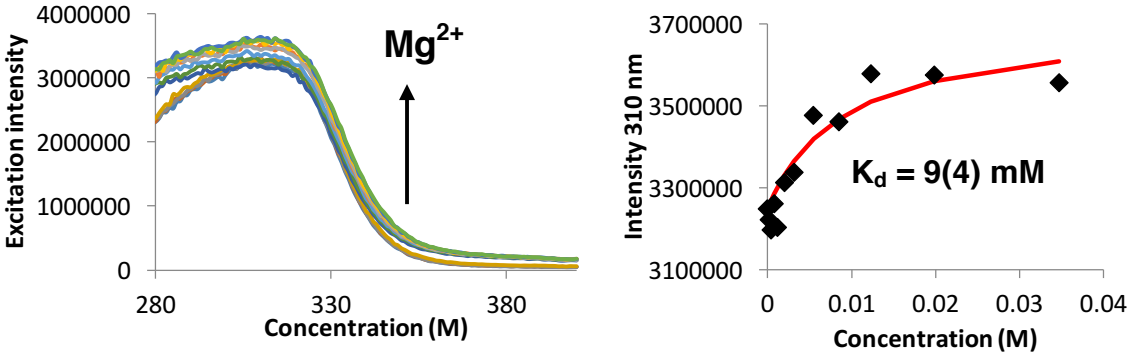

Figure 5.23 (Left) excitation spectrum of **[Eu.L^2]**; (right) fitting of the excitation ratio at 310 nm against the added concentration of Mg^{2+} (λ_{em} = 613 nm). **[Eu.L^2]** concentration = 5 µM in 50 mM HEPES, 100 mM KCl, pH 7.21, 298 K.

Unlike Mg^{2+}, the excitation-based dissociation constants recorded for the binding of Ca^{2+} and Zn^{2+} were measured with higher accuracy and within the experimental error to those determined via emission spectroscopy (**Figure 5.22**). A 1.5- and 5.5-fold increase in the excitation maxima were observed, for Ca^{2+} and Zn^{2+} respectively. Dissociation constants of 1.1 mM and 2.3 μM were

calculated from the excitation spectral variation (See **Appendix**, **Figure A.16** and **Figure A.17**).

The enhancement effect observed in both emission and excitation spectra for the addition of Mg^{2+}, Ca^{2+} and Zn^{2+}, can be attributed to the elimination of photo-induced electron transfer (PET) present in the 'metal-free' state. Upon metal binding to the *meta* aniline nitrogen, the quenching pathway of the Eu^{3+} excited state is perturbed. An identical effect was observed for the addition to divalent cations to analogue **NapL^2** in **Chapter 4**.

5.5.3 The effect of Mg^{2+} binding on the coordination environment of [Eu.L^1] and [Eu.L^2]

It is apparent from the emission spectra shown in **Figure 5.20** and **Figure 5.22**, that the coordination environment of Eu^{3+} in both **[Eu.L^1]** and **[Eu.L^1]** is unaffected by the binding of Mg^{2+}. A total emission change is reported, either a reduction for **[Eu.L^1]** or an increase following addition of Mg^{2+} to **[Eu.L^2]**. No significant change was observed in the ratio of the 'hypersensitive' $\Delta J = 2$ and $\Delta J = 4$ emission bands (**Figure 5.24**).

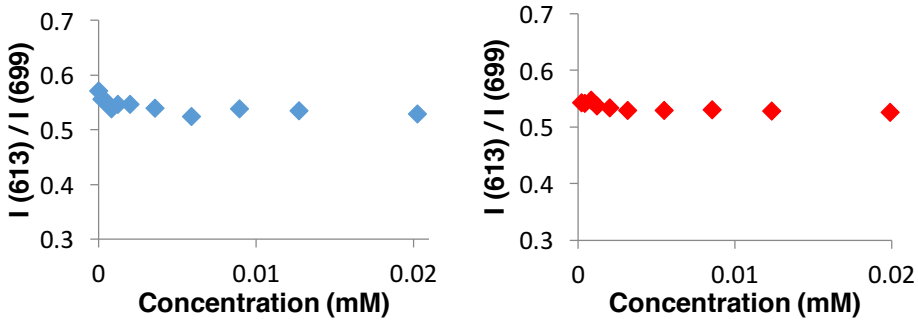

Figure 5.24 The ratio of the hypersensitive $\Delta J = 2$ (613 nm) and $\Delta J = 4$ (699 nm) bands for **[Eu.L^1]** and **[Eu.L^2]** (50 mM HEPES, 100 mM KCl, pH 7.21, λ_{ex} = 315 nm) following addition of Mg^{2+} (40 mM).

Table 5.4 The luminescence lifetimes of **[Eu.L^1]** and **[Eu.L^2]** in HEPES (50 mM, 100 mM KCl, pH 7.21) in both H_2O and D_2O (λ_{ex} = 315 nm, λ_{em} = 613 nm). Red highlights the lifetimes after the addition of Mg^{2+} (40 mM).

Complex	$\tau_{HEPES+H_2O}$ (ms)	$\tau_{HEPES+D_2O}$ (ms)	*q*
EuL^1	0.60	1.69	1
	0.59	1.61	1
EuL^2	0.65	1.85	1
	0.59	1.70	1

Luminescence lifetime measurements of **[Eu.L^1]** and **[EuL^2]** were measured in 50 mM HEPES, 100 mM KCl at a constant pH of 7.21, in the absence or presence of Mg^{2+} (40 mM) (**Table 5.4**).The negligible changes in the luminescence lifetimes observed before and after the addition of Mg^{2+} also indicate that the coordination environment of the Eu^{3+} centre remains unchanged on metal ion binding. A hydration number of one (q = 1), and a total stable coordination number of nine is maintained throughout for each complex.

5.5.4 Summary: Comparison of the binding affinities and selectivities of [Eu.L^1] and [Eu.L^2] with their naphthalene analogues

Charge neutral lanthanide complexes **[Eu.L^1]** and **[Eu.L^2]** displayed low mM affinities for both Mg^{2+} and Ca^{2+}, and low μM affinities for Zn^{2+}. It is clear that the position of the nitrogen atom, either *para* or *meta*, relative to the aromatic chromophore had no significant effect on the affinity or selectivity towards the different metal ions studied. Following addition of Mg^{2+}, for example, K_d values of 7.5 mM and 3.7 mM for **[Eu.L^1]** and **[Eu.L^2]** were calculated respectively. The slightly higher affinity of **[Eu.L^2]** for Mg^{2+}, is likely be due to the *meta* aniline nitrogen atom playing a more prominent role in binding to Mg^{2+}. It is thought from absorbance measurements, and the presence of the ICT state at 380 nm on Mg^{2+} saturation, that in the case of **[Eu.L^1]** the aniline nitrogen atom does not play a prominent role in binding to Mg^{2+}(**Figure 5.18**). For **[Eu.L^2]**, however, the pH insensitivity shown in the physiological range of the Mg^{2+} 'bound' complex

indicates that when the aniline nitrogen is *meta* to the chromophore, it does participate in binding to Mg^{2+} (**Figure 5.15**). The aniline nitrogen atom, when both *para* and *meta*, is thought to take part in binding to both Ca^{2+} and Zn^{2+} in **[Eu.L^1]** and **[Eu.L^2]**. Comparable dissociation constants are reported from both fluorescence emission and excitation spectroscopy.

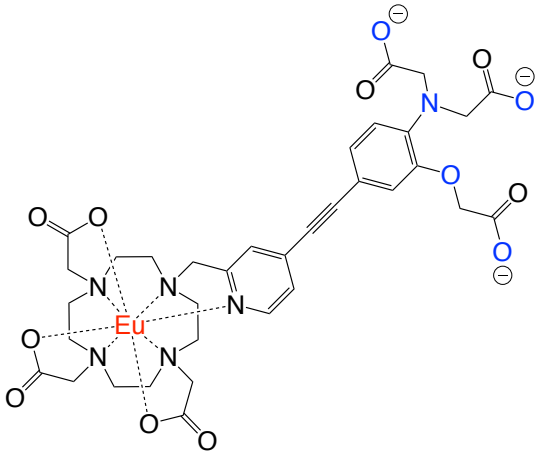

[Eu.L^1]

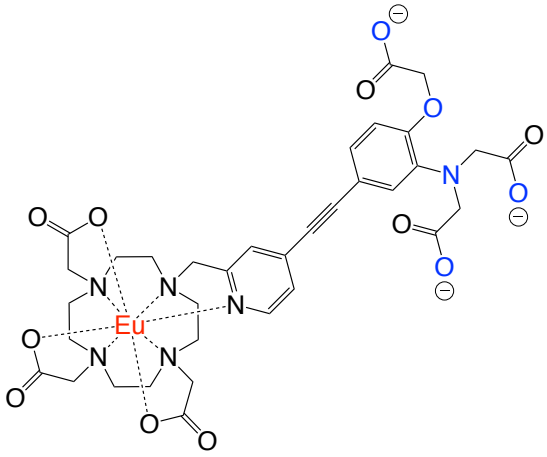

[Eu.L^2]

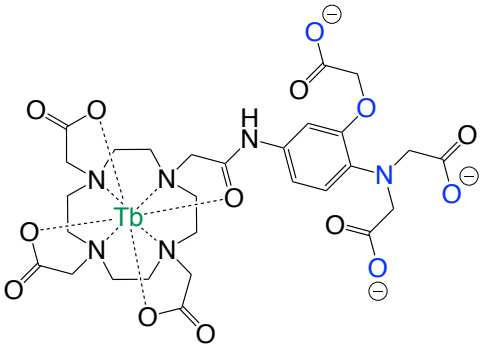

[Tb.2]

Figure 5.25 The structures of **[Eu.L^1]**, **[Eu.L^2]** and **[Tb.2]** (Parker *et al.*).[6]

Table 5.5 The direct comparison of the dissociation constants for the binding of Mg^{2+}, Ca^{2+} and Zn^{2+} to **[Eu.L^1]**, **[Eu.L^2]** and **[Tb.2]** (Parker *et al.*) in aqueous solutions at 298 K. All dissociation constants have been determined by luminescence emission spectra.

Complex	K_d (Mg^{2+})	K_d (Ca^{2+})	K_d (Zn^{2+})
[Eu.L^1]	7.5(8) mM	0.9(2) mM	1.8(5) μM
[Eu.L^2]	3.7(1.5) mM	0.9(1) mM	1.9(1) μM
[Tb.2][6]	0.8 mM[6]	53.7 μM[6]	10.5 μM[6]

The pentadentate APTRA binding moiety has been incorporated into lanthanide systems previously in Durham.[5,6] Complex **[Ln.2]** shown in **Figure 5.2** and **Figure 5.25**, was synthesised by Parker *et al.*, and was designed to sense Zn^{2+} in a competitive ionic media.[5,6] As with **[Eu.L^1]** and **[Eu.L^2]**, low mM affinities were displayed for the binding of Mg^{2+} (log K = 3.17, K_d = 0.8 mM) and a low μM affinity was seen for Zn^{2+} (log K = 5.93, K_d = 1.2 μM). Typical μM affinities for the binding of Ca^{2+} (log K = 4.27, K_d = 53.7 μM) were also reported,[5,6] consistent with the behaviour of the APTRA-based indicator Mag-Fura-2.[27]

It is apparent from the analysis of **Figure 5.20** and **Figure 5.22** that both **[Eu.L^1]** and **[Eu.L^2]** display a much lower affinity for Ca^{2+} than their naphthalene analogues **NapL^1**, **NapL^2** and the lanthanide-based APTRA complex **[Tb.2]**.[6] For example, the europium complexes **[Eu.L^1]** and **[Eu.L^2]**, have a 23- and 28-fold weaker affinity towards Ca^{2+} compared to **NapL^1** and **NapL^2**, and a 17-fold lower affinity than **[Tb.2]**.[6] A direct comparison of the K_d values for binding of Mg^{2+}, Ca^{2+} and Zn^{2+} to **[Eu.L^1]**, **[Eu.L^2]** and **[Tb.2]** is highlighted in **Table 5.5**.

The significant improvement in the Mg^{2+} / Ca^{2+} selectivity displayed is extremely rare, and has never been observed previously for ligands and complexes of this type. In each instance, carboxylate-based APTRA indicators in the literature typically display a μM affinity towards Ca^{2+}.[5,6,28] The lower affinity observed for Ca^{2+} binding could be, due in part, to the highly electron-rich push-pull system associated with pyridylalkynylaryl chromophores. In the case of **[Eu.L^1]**, for example, the aniline nitrogen lone pair is highly conjugated with the aromatic chromophore and, therefore, is less available for donation.

The enhanced Mg^{2+} / Ca^{2+} selectivity of **[Eu.L^1]** and **[Eu.L^2]**, reported here, could allow them to be used to study 'free' Mg^{2+} concentrations, even in calcium-rich regions of the body. In the endo(sarco)plasmic reticulum and in serum elevated Ca^{2+} concentrations occur which are far above basal mammalian cell levels. Mg^{2+} homeostasis has, therefore, not been previously studied in these regions using any luminescent probe.

5.6 Binding studies of bi-aryl [Tb.bL^2]

The absorbance, emission and excitation binding studies of a terbium-based complex, **[Tb.bL^2]**, containing a bi-aryl pyridylaryl chromophore are reported in aqueous solution. Binding studies were carried out with **[Tb.bL^2]** rather than **[Eu.bL^2]**, due to the more efficient energy transfer arising from the triplet excited state of the chromophore to the $^5D_4$ excited state of Tb^{3+}. Comparisons will be made to **[Eu.L^1]**, and particularly **[Eu.L^2]**, which also possesses a *meta* aniline nitrogen atom on the APTRA binding moiety. It was decided that binding studies would be carried out with the bi-aryl system containing a *meta* aniline nitrogen, as **[Eu.L^2]** displayed a higher affinity for Mg^{2+}, compared to that observed with **[Eu.L^1]**, while maintaining almost identical affinities for Ca^{2+} and Zn^{2+}.

The study set out to examine how the use of a bi-aryl pyridylaryl chromophore, affects the affinity and selectivity towards Mg^{2+}, Ca^{2+} and Zn^{2+}, and which chromophore is preferred for the maximum Mg^{2+} affinity and best Mg^{2+} / Ca^{2+} selectivity.

5.6.1 Absorbance binding studies of [Tb.bL^2]

The absorbance spectrum of **[Tb.bL^2]** displayed a peak maximum at 280 nm, an identical response to that shown in **Figure 5.9**. Following the addition of Mg^{2+}, Ca^{2+} or Zn^{2+}, an increase in the absorbance intensity at 280 nm was observed, with no shift in the wavelength maximum. The absorbance spectra for **[Tb.bL^2]** before and after addition of Mg^{2+}, Ca^{2+} and Zn^{2+} are shown in **Figure 5.26.**

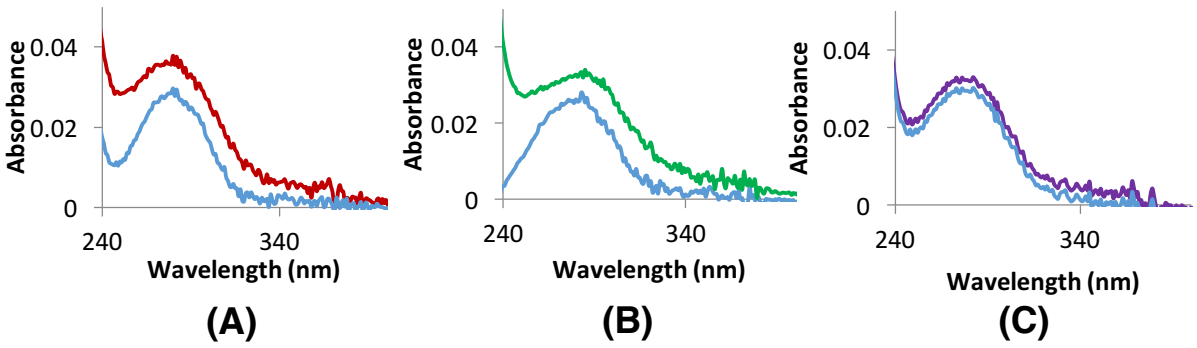

Figure 5.26 Absorbance spectrum of **[Tb.bL^2]** following addition of **(A)** Mg^{2+} (200 mM), **(B)** Ca^{2+} (4.5 mM) and **(C)** Zn^{2+} (9.5 μM). **[Tb.bL^2]** concentration = 5 μM in 50 mM HEPES, 100 mM KCl, pH 7.21, 298 K

5.6.2 Luminescence binding studies of [Tb.bL^2]

Titrations of **[Tb.bL^2]** with Mg^{2+}, Ca^{2+} and Zn^{2+} were carried out in buffered solution at a constant pH with excitation at 280 nm, the wavelength maximum from the absorbance spectrum.

The terbium-centred emission spectra following addition of Mg^{2+}, Ca^{2+} and Zn^{2+} to **[Tb.bL^2]** are shown in **Figure 5.27**, displaying typical Tb^{3+} emission bands $\Delta J = 2$ to $\Delta J = -1$. After addition of Mg^{2+} and Ca^{2+} a 2.6- and 2.5-fold reduction in emission intensity at 544 nm was found. The addition of Zn^{2+}, however, resulted in a 1.8-fold increase in emission intensity. The emission response observed here is identical to that observed following the addition of Mg^{2+}, Ca^{2+} and Zn^{2+} to **[Eu.L^1]** (**Figure 5.20**). Dissociation constants of 16.9 mM, 0.8 mM and 0.5 μM were calculated respectively for the binding of Mg^{2+}, Ca^{2+} and Zn^{2+} (**Figure 5.27**).

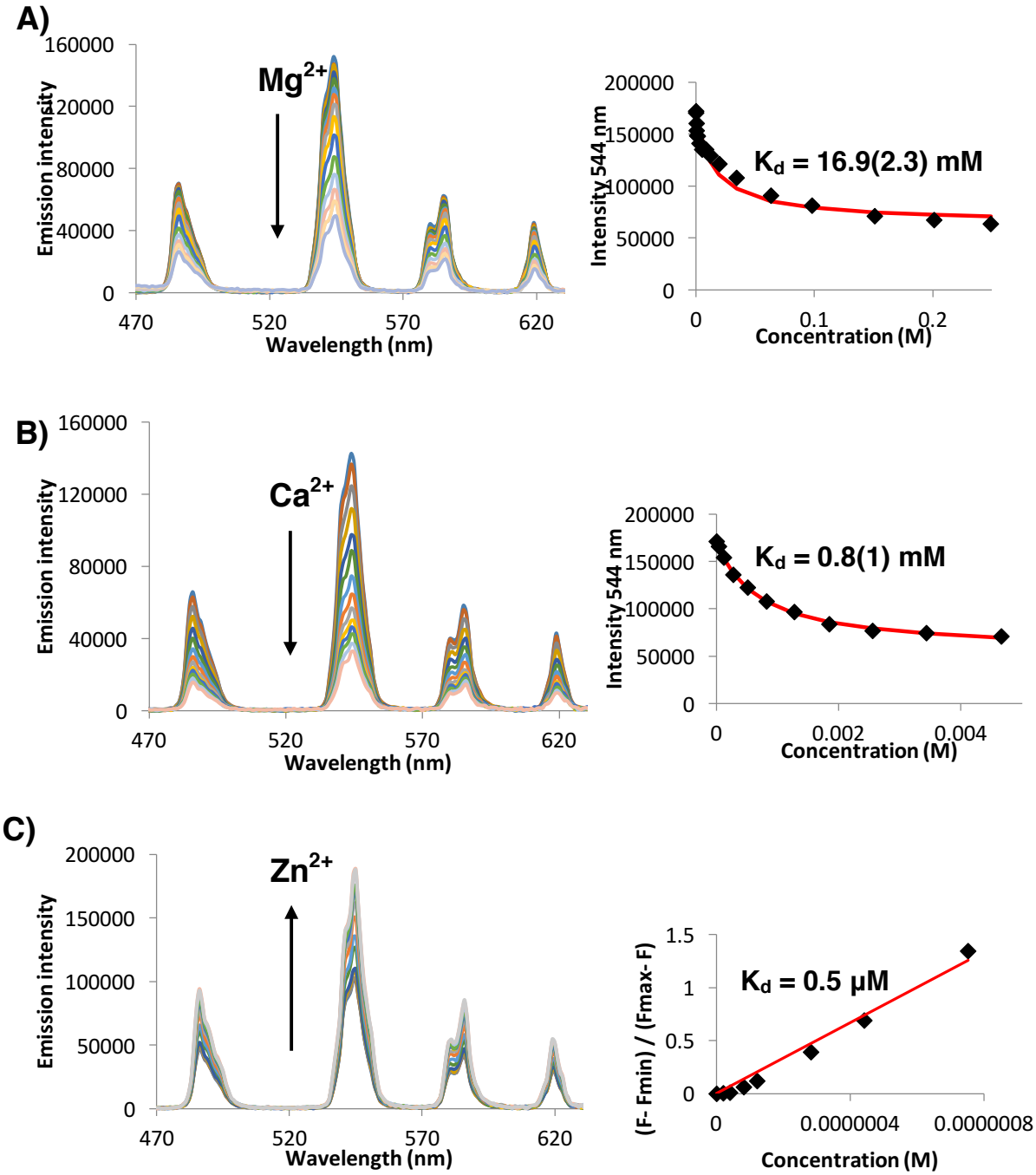

Figure 5.27 (Left) excitation spectrum of **[Tb.bL^2]**; (right) fitting of the excitation ratio at 544 nm against the added concentration of **(A)** Mg^{2+}, **(B)** Ca^{2+} and **(C)** Zn^{2+} to a 1:1 binding model. **[Tb.bL^2]** concentration = 5 µM in 50 mM HEPES, 100 mM KCl, pH 7.21, λ_{ex} = 280 nm 298 K.

The bi-aryl complex **[Tb.bL^2]**, displayed a ratiometric emissive response following addition of Mg^{2+} (**Figure 5.28**) and Zn^{2+} (**Appendix A.18**), but a non-ratiometric response for the addition of Ca^{2+} (**Appendix A.19**). Such behaviour is surprising, and was not seen with **[Eu.L^1]** and **[Eu.L^1]**, containing a

pyridylalkynylaryl chromophore. Following the addition of Mg^{2+} and Zn^{2+} to **[Tb.bL^2]**, comparable K_d values of 17.7 mM and 1 μM were calculated from the ratio of the ΔJ = 2 (486 nm) and ΔJ = 1 (544 nm) emission band intensities of **[Tb.bL^2]** (**Figure 5.28**).

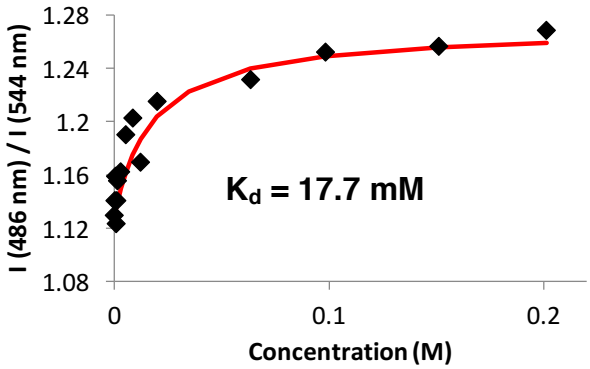

Figure 5.28 The ratiometric response of **[Tb.bL^2]** following addition of Mg^{2+}. The dissociation constant was calculated from the intensity ratio of the ΔJ = 2 (486 nm) and ΔJ = 1 (544 nm) emission bands. **[Tb.bL^2]** concentration = 5 μM in 50 mM HEPES, 100 mM KCl, pH 7.21, λ_{ex} = 280 nm, 298 K.

The excitation spectrum of **[Tb.bL^2]** displays a peak maximum at 280 nm in both metal-free and 'bound' states (**Figure 5.29**), matching that observed in the absorbance spectrum. Following addition of Mg^{2+}, a 2.4-fold reduction in the excitation intensity at 280 nm was observed. The fluorescence excitation spectra for the addition of Ca^{2+} and Zn^{2+} are shown in the appendix for reference, similarly showing no shift in the wavelength maxima on binding (**Figure A.20** and **Figure A.21**). Comparable K_d values within experimental error, were measured for the binding of Mg^{2+} (**Figure 5.29**), Ca^{2+} (**Figure A.20**) and Zn^{2+} (**Figure A.21**) via fluorescence excitation spectroscopy.

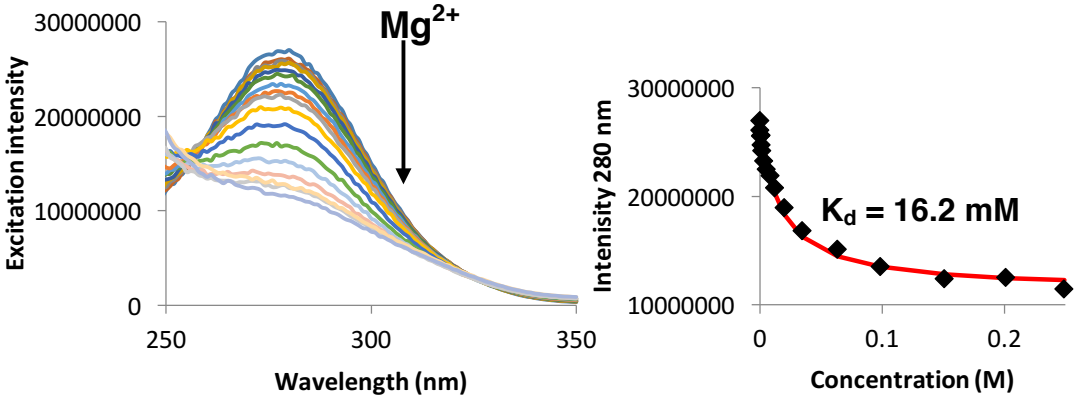

Figure 5.29 (Left) excitation spectrum of **[Tb.bL^2]**; (right) fitting of the excitation ratio at 280 nm against the added concentration of Mg^{2+} (λ_{em} = 544 nm). **[Tb.bL^2]** concentration = 5 µM in 50 mM HEPES, 100 mM KCl, pH 7.21, 298 K.

5.6.3 The effect of Mg^{2+} binding on the excited state lifetime of [Eu.bL^2] and [Tb.bL^2]

Luminescence lifetime measurements of **[Eu.L^1]** and **[EuL^2]**, containing a pyridylalkynylaryl chromophore, were found to be invariant with addition of Mg^{2+}. Such behaviour indicates that the coordination environment of Eu^{3+} remains unchanged on Mg^{2+} binding. In the case of the bi-aryl complex **[Tb.bL^2]**, however, a linear dependence between the luminescence lifetime of the $^5D_4$ state of Tb^{3+}, and increasing concentrations of Mg^{2+} was found (**Figure 5.30**, R^2 = 0.985). Following the addition, and complete saturation of **[Tb.bL^2]** with 200 mM Mg^{2+}, a 1.4-fold increase in the lifetime of the Tb^{3+} excited state was calculated (**Figure 5.30**, **Table 5.6**).

Maury and co-workers have been carrying out extensive work into terbium-based bi-aryl systems containing electron donating substituents, with apparent applications as viscosity probes.[25] In a similar study to that reported by Maury, it was found that both **[Eu.bL^2]** and **[Tb.bL^2]** are sensitive to changes in viscosity, but significant longer lifetimes were also observed in less polar solvents and in deoxygenated solutions. Such behaviour suggests that the excited state lifetime is not dependent on vibrational quenching from aryl-aryl rotations, but instead from oxygen quenching of the triplet excited state of the chromophore (**Section 5.3.2**).

The bi-aryl complex **[Tb.bL^2]** showed a linear response in excited state lifetime following addition of Mg^{2+} (200 mM) in aqueous solution (**Figure 5.30** and **Table 5.6**). It is tempting to speculate, therefore, that the binding of Mg^{2+} to **[Tb.bL^2]**, causes a destabilising effect on the triplet excited state and reduces the amount of back energy transfer and triplet oxygen quenching resulting in a longer excited state lifetime. Europium-based complex **[Eu.bL^2]**, in contrast showed no significant change in the excited state lifetime following the addition of Mg^{2+} (200 mM). A change of 0.50 ms to 0.43 ms was observed, and arguably lies within the error associated with the luminescence lifetime measurement.

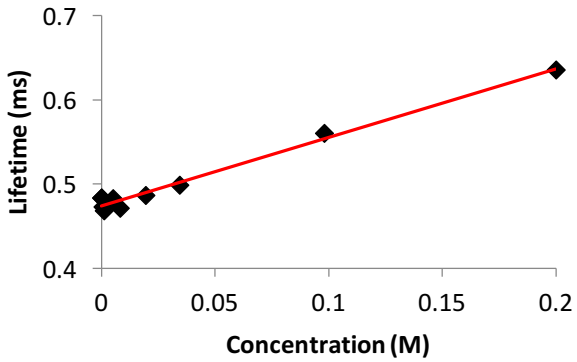

Figure 5.30 The linear dependence of the excited state lifetime of **[Tb.bL^2]** following addition of Mg^{2+}. **[Tb.bL^2]** concentration = 5 μM in 50 mM HEPES, 100 mM KCl, pH = 7.21,λ_{ex} = 280 nm, λ_{em} = 544 nm at 298 K. (R^2 = 0.985).

Table 5.6 The effect on the excited state lifetime of **[Tb.bL^2]** and **[Eu.bL^2]** following addition of 200 mM Mg^{2+}.

Complex	τ_{HEPES} **(ms)**	$\tau_{HEPES+Mg^{2+}}$ **(ms)**
[Tb.bL^2]	0.48	0.64
[Eu.bL^2]	0.50	0.43

The increase in the luminescence lifetime of the $^5D_4$ state following addition of Mg^{2+} is surprising, however, as it is apparent from **Figure 5.27** that the total luminescence intensity of **[Tb.bL^2]** decreased on Mg^{2+} binding. A decrease in the total luminescence intensity suggests that a quenching of the

excited state is taking place, and is usually coupled with a decrease in the lifetime rather than the increase observed.

5.6.4 Summary: Pyridylalkynylaryl vs. pyridylaryl chromophores

The complex **[Tb.bL^2]** displays a number of fundamental disadvantages over the use of complexes containing pyridylalkynylaryl chromophores, including **[Eu.L^1]** and **[Eu.L^2]**. Although a similar low mM and low μM affinity is observed for the binding of Ca^{2+} and Zn^{2+}, a weaker binding is reported for Mg^{2+}. K_d values of 3.7 mM and 16.9 mM were observed for **[Eu.L^2]** and **[Tb.bL^2]** respectively. The affinity for Mg^{2+} is, therefore, approximately 10-times weaker than that required to follow changes in the concentration of 'free' Mg^{2+} in the majority of mammalian cells.

However, **[Tb.bL^2]** displayed a ratiometric emission response, following addition of Mg^{2+} and Zn^{2+}. Comparable K_d values were calculated to those reported from excitation at the absorbance wavelength maximum.

Complexes containing both a pyridylalkynylaryl (**[Eu.L^1]** and **[Eu.L^2]**) and a pyridylaryl chromophore (**[Tb.bL^1]**) were found to have a low mM affinity for Ca^{2+}. The significantly lower affinity for Ca^{2+} observed, compared to traditional APTRA indicators, shows that the effect can't solely be down to the electron-rich push-pull system present in pyridylalkynylaryl chromophores, and must be caused by a combination of effects.

The excited state lifetime of complexes bearing a bi-aryl chromophore were found to be significantly lower than their pyridylalkynylaryl counterparts, and showed no linearity with a viscosity or solvent polarity. A linear response of lifetime and concentration with [Mg^{2+}] was found. Both **[Eu.L^1]** and **[Eu.L^2]**, however, had emission lifetimes that were independent of added Mg^{2+}.

The high energy excitation required for the less conjugated pyridylaryl complex **[Tb.bL^2]**, is another important disadvantage and limits its possible biological applications in its current state. Its use *in vivo* and *in cellulo* is restricted, as confocal microscopy experiments for visualisation in cells typically require

excitation at 355 nm or longer.[19,29] At this excitation wavelength, however, no Tb^{3+} emission would be observed with **[Tb.bL^2]**, as a higher energy excitation is required.

The structure of **[Tb.bL^2]** could be modified in order to shift the absorbance wavelength to lower energies and improve its performance for real biological applications. The addition of electron donating substituents, such as methoxy groups *ortho* to the chromophore, would shift the wavelength maximum towards the red. The use of different electron-donating groups has been previously used to great effect in Durham with pyridylalkynylaryl chromophores, to synthesise complexes with a wide range of wavelength maxima in the absorbance spectrum.[19]

5.7 Applications of [Eu.L^2]: Assessing 'free' Mg^{2+} in newborn calf serum

Lanthanide complexes have been used for sensing of several bioactive species in biological fluids.[23,30,31] Europium- and terbium-based complexes containing an azaxanthone sensitiser have been used, for example, as probes for bicarbonate anions in human serum.[23] To date, however, no lanthanide-based complexes have been used to monitor 'free' Mg^{2+} in human serum because of the Mg^{2+} / Ca^{2+} selectivity conundrum displayed by the majority of Mg^{2+} binding groups.

Measuring selectively the 'free' concentration of Mg^{2+} within human serum is of major interest. It is of critical importance that a greater understanding of the cause of Mg^{2+} imbalances within the serum is developed, for future disease prevention. In **Chapter 4** fluorescence emission binding studies of APDAP analogue **NapL^4** with Mg^{2+} were carried out in a 'serum mimic'. It was shown that a binding constant of 0.04 mM was calculated, making it unsuitable for the detection of 'free' Mg^{2+} in human serum as 'free' Mg^{2+} is present in the range of 0.7-1.1 mM.[32]

The use of an APTRA-based lanthanide luminescent probe was considered, to study the binding of Mg^{2+} in newborn calf serum (NCS). Europium-based complexes **[Eu.L^1]** and **[Eu.L^2]** displayed encouraging results in metal ion

binding titrations, with a low mM affinity seen following addition of both Mg^{2+} and Ca^{2+} (**Section 5.5**). It was hoped that the 1.8-fold weaker affinity towards Ca^{2+} observed for **[Eu.L^1]** and **[Eu.L^2]** over **NapL^4**, could allow them to be more suitable for the sensing of 'free' Mg^{2+} in human serum. Complex **[Eu.L^2]** was chosen over **[Eu.L^1]** for the Mg^{2+} titration in NCS, because of two main factors: first, **[Eu.L^2]** displayed a higher affinity for Mg^{2+} (K_d = 3.7 mM vs. 7.5 mM), and second the 'turn-on' emission response that occurred following addition of Mg^{2+}.

The emission spectra of **[Eu.L^2]** in NCS are shown in **Figure 5.31**, with excitation at both the absorbance wavelength maximum in the 'unbound state' (315 nm), and at the isosbestic point (343 nm) in HEPES buffer. The complex **[Eu.L^2]** was sufficiently bright at both of these excitation wavelengths, such that no time gated emission was required. A greater emission intensity, however, was observed following excitation at 315 nm, with a reduction in the interference from background fluorescence in the NCS.

The total emission intensity observed for **[Eu.L^2]** in NCS was significantly lower than that displayed in HEPES buffer solution, with a significantly reduced luminescence lifetime of 0.31 ms. Such behaviour can be attributed to the quenching effect of proteins such as bovine serum albumin (BSA) present in NCS. A titration of **[Eu.L^2]** with BSA showed that following addition of BSA (110 μM), a 1.9-fold reduction in the total emission intensity of **[Eu.L^2]** was observed (See **Appendix**, **Figure A.22**). The excited state lifetime of **[Eu.L^2]**, however, was unaffected by the addition of BSA with only a negligible change observed throughout the titration, that fell within the error associated with the measurement (See **Appendix**, **Figure A.23**). It is evident, therefore, that proteins other than BSA in NCS may also be causing a quenching of the $^5D_0$ Eu^{3+} excited state of **[Eu.L^2]**, or that other electron-rich species in the serum may quench the intermediate ligand excited state.

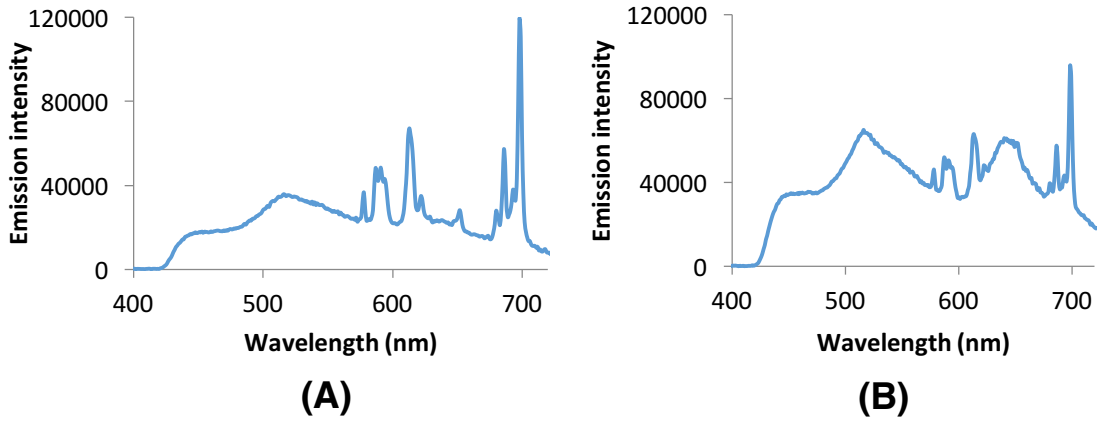

Figure 5.31 The emission spectrum of **[Eu.L^2]** in NCS (from ICP-OES concentrations of K^+, Ca^{2+} and Mg^{2+} are 3.9 mM, 2.6 mM and 0.8 mM respectively). λ_{ex} **(A)** = 315 nm and **(B)** 346 nm, 298 K. **[Eu.L^2]** concentration = 5 μM.

The evolution of the emission spectrum upon addition of Mg^{2+} in NCS is shown in **Figure 5.32**. Following addition of 100 mM Mg^{2+} a 1.3-fold decrease in emission intensity at 613 nm was observed following excitation at 315 nm (**Figure 5.32**). In a non-competitive ionic medium, a 1.4-fold increase in emission was earlier found after such an addition of Mg^{2+}. The decrease in the total emission observed can be attributed to the partial saturation of **[Eu.L^2]** in NCS owing to the presence of low mM concentrations of Mg^{2+}, and in particular Ca^{2+}. A larger modulation was seen with Ca^{2+} binding, the addition of further concentrations of Mg^{2+} to the partially saturated **[Eu.L^2]**, therefore, resulted in a decrease in the total emission intensity.

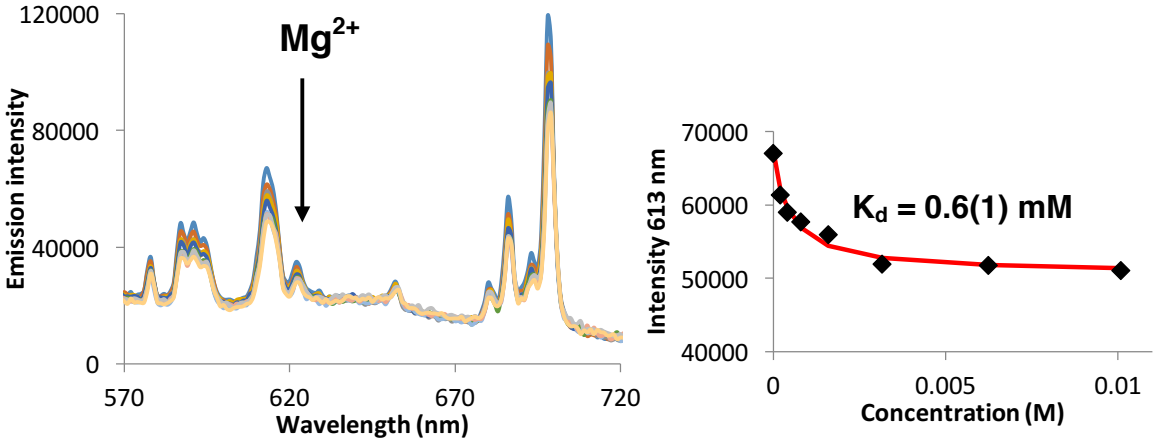

Figure 5.32 (Left) The emission spectrum of **[Eu.L^2]** in NCS following the addition of Mg^{2+}. (Right) the fitting of the emission intensity against the concentration of Mg^{2+} added to a 1:1 binding model. **[Eu.L^2]** concentration = 5 μM, λ_{ex} = 315 nm, 298 K.

A binding constant of 0.6 mM was calculated from the variation of the emission intensity at 613 nm with added Mg^{2+} (**Figure 5.32**). The excited state lifetime on saturation with Mg^{2+} was almost identical to that observed without any added Mg^{2+}, values of 0.30 ms and 0.31 ms were measured respectively. Such behaviour is comparable to that seen with the Mg^{2+} titration of **[Eu.L^2]** in 50 mM HEPES at pH 7.21, where no change in the luminescence lifetime was observed following addition of 40 mM Mg^{2+} (**Table 5.4**).

A comparable dissociation constant of 0.7 mM was recorded after excitation at 343 nm. The error associated with the fitting was higher, however, due to the smaller intensity changes observed on binding Mg^{2+}. A 10% decrease in emission intensity at 613 nm was observed at saturation with Mg^{2+}, with a 50 % error in the fitting recorded (See **Appendix**, **Figure A.24**).

The K_d values for Mg^{2+} binding determined from both of these spectral emission studies are comparable to the 'free' Mg^{2+} concentration in human serum (0.7-1.1 mM in healthy humans).[32] The APTRA-based complex **[Eu.L^2]**, therefore, could have the ability to detect 'free' Mg^{2+} concentrations in human serum.

5. Part 2: Ruthenium(II)-based systems

5.8 Introduction

Over the last 30-40 years, $[Ru(bpy)_3]^{2+}$ has become one of the most recognised and extensively studied metal complexes.[33-35] Its high chemical stability, reversible redox potentials and long excited state lifetime (μs) have allowed $[Ru(bpy)_3]^{2+}$ and its derivatives to be used in a range of applications, including solid-state light emitting devices.[36] Unlike the Laporte forbidden f-f transitions that are characteristic of the lanthanide series, the observed deep red emission of $[Ru(bpy)_3]^{2+}$ emulates from a metal-to-ligand charge-transfer state of triplet character, giving rise to longer lived phosphorescent emission. From density functional theory (DFT) calculations electrochemical and Raman studies, it has previously been shown that the LUMO is predominantly localised on the bipyridine (bpy) ligands.[37] The introduction of electron donating and electron withdrawing substituents can, therefore, be used in colour tuning applications by affecting the separation of the HOMO-LUMO energy gap.[38]

An array of $[Ru(bpy)_3]^{2+}$ derivatives have been investigated for a range of sensing applications. For example, Sauvage[39] and Thomas,[40,41] amongst others, have published numerous papers based on Ru^{2+} polypyridyl complexes that bind reversibly to DNA.[39-41] Complexes including $[Ru(bpy)_2(dppz)]^{2+}$ (**[Ru.4]**) are not significantly emissive in water, but luminescence is greatly enhanced upon intercalation into DNA.[39,41]

Ruthenium-based complexes have also been explored as selective cation sensors. Structurally, many are analogues of $[Ru(bpy)_3]^{2+}$ containing two bipyridine ligands with the third N^N ligand incorporating the cation binding moiety. Complexes have been synthesised containing predominantly macrocycles, such as benzo-15-crown-5 for the binding of Na^+ (**[Ru.1]** and **[Ru.2]**)[36] and 1,4-diaza-7,10,13-trithia-cyclopentadecane for the selective binding of Hg^{2+} (**[Ru.3]**)[42] (**Figure 5.33**). Solubility is often a problem. The vast majority of Ru^{2+} based complexes synthesised to bind metal ions are not water soluble,

with luminescence measurements instead having to be undertaken in organic solvents, such as acetonitrile and methanol.[36,42]

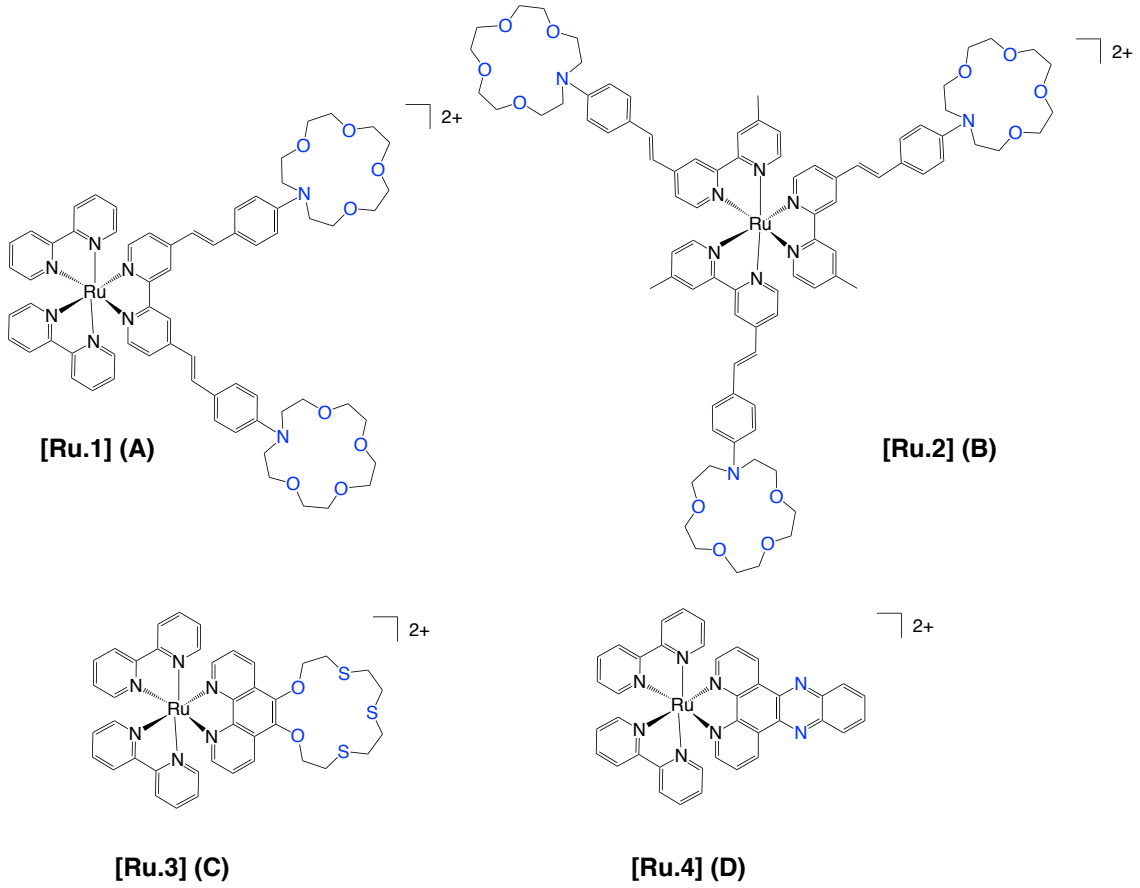

Figure 5.33 Ru^{2+} based cation sensors from the literature for Na^{+} **(A)** and **(B)**,[36] Hg^{2+} **(C)** [42] and **(D)** $[Ru(bpy)_2(dppz)]^{2+}$, a DNA intercalation complex developed by Sauvage *et al.*[39]

The aim of the work described in this section was to synthesise a Ru^{2+} based probe to study the binding of Mg^{2+}, Ca^{2+} and Zn^{2+}. Structurally, the complex contains two bipyridine ligands and a third bipyridine functionalised with an APTRA binding group to study the binding of divalent cations. Original targets are shown in **Figure 5.34**.

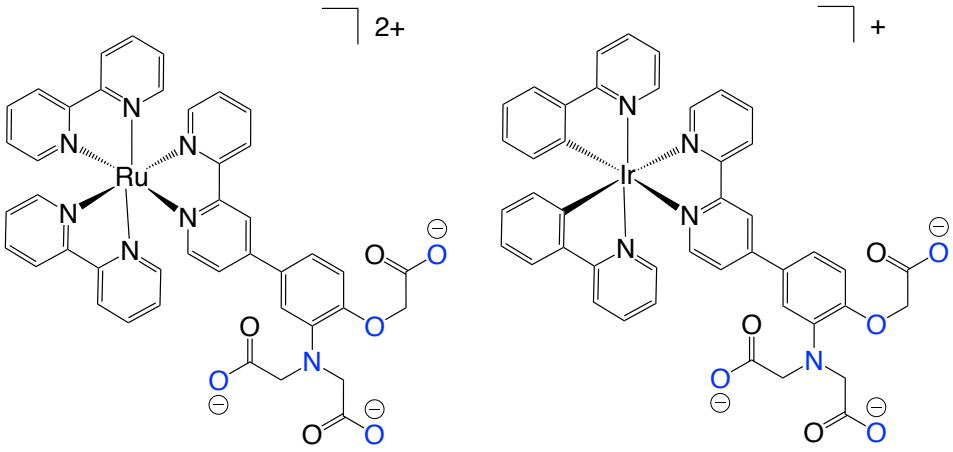

Figure 5.34 Target Ru^{2+} and Ir^{3+} complexes, **[Ru.bL^2]$^{2+}$** and **[Ir.bL^2]$^+$**, with PF_6^- counter ions.

Initially Ir^{3+} systems based on the well-known $[Ir(ppy)_2(bpy)]^+$ core were also considered as possible sensing probes. It was found, however, that the complexes functionalised with the desired metal binding unit were insoluble in water or even in 50 % water / 50 % methanol, limiting their ability to act as Mg^{2+} sensors in biological media. It was therefore decided that binding properties of the more water soluble **[Ru.bL^2]** series would be analysed. The binding affinity and selectivity for Mg^{2+}, Ca^{2+} and Zn^{2+} will be directly compared with that displayed by the bi-aryl Tb^{3+} system **[Tb.bL^2]**.

5.9 Synthesis and characterisation

4-Bromo-2,2'-bipyridine [**bpy-Br**], (**57**) was obtained in a four-step procedure from bipyridine, in a method adapted from Wenkert and Woodward (**Scheme 5.5**).[43] The mono-N-oxide, (**54**), was prepared from bipyridine and m-CPBA, before nitrating with concentrated sulphuric acid and potassium nitrate to form (**55**) in moderate yield. A subsequent nucleophilic displacement reaction following addition of acetyl bromide and removal of the N-oxide with PBr_3 at room temperature afforded (**57**) in excellent overall yield.

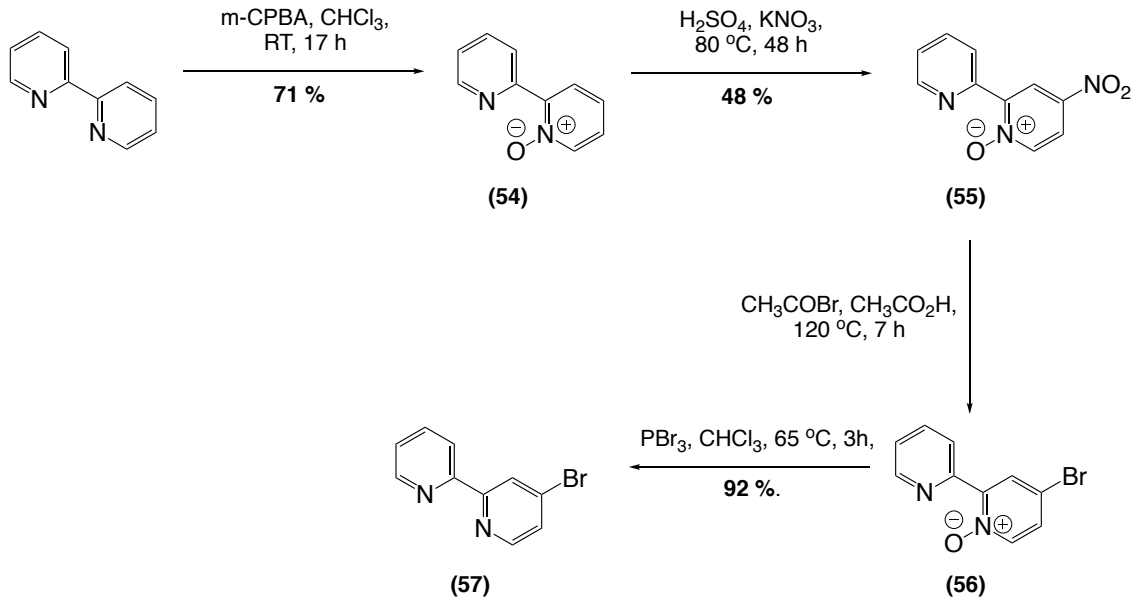

Scheme 5.5 The synthesis of 4- bromo-2,2'-bipyridine [bpy-Br], **(57)** from bipyridine.[43]

$[Ru(bpy)_2(bpy\text{-}Br)]^{2+}$, (**58**) was synthesised from *cis*-bis(2,2'-bipyridine) dichlororuthenium(II) hydrate in methanol, using silver nitrate as the chloride scavenger (**Scheme 5.6**). Suzuki cross-coupling methodology was used to couple (**58**) with (**50**) in DMSO, using $Pd(PPh_3)_4$ as the catalyst and sodium carbonate as the base. This method for cross-coupling onto bromo-substituted Ir^{3+} and Ru^{2+} complexes has been utilised in Durham to form a range of complex multimetallic systems.[44] The tris *tert*-butyl ester (**59**) was isolated as its PF_6 salt, by adding the DMSO reaction solution to a saturated aqueous solution of KPF_6. Purification was achieved by recrystallisation from a mixture of methanol and diethyl ether. *tert*-Butyl ester hydrolysis of (**59**) was carried out using trifluoroacetic acid in dichloromethane (1:1) to yield **[Ru.bL^2]** (**Scheme 5.6**).

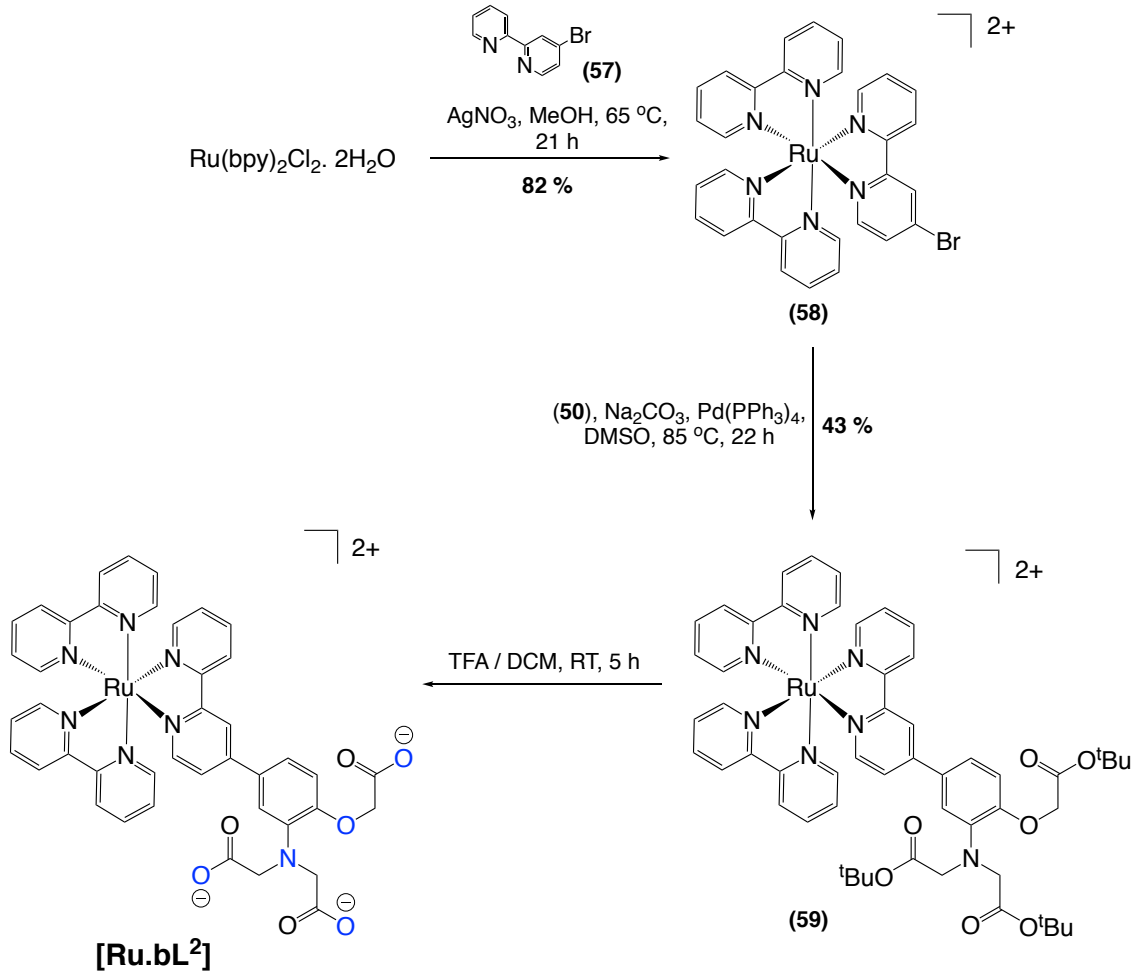

Scheme 5.6 The synthesis of **[Ru.bL^2]$^{2+}$**, isolated as its PF_6 salt.

5.10 Photophysical properties of [Ru.bL^2]$^{2+}$

The absorbance spectrum of **[Ru.bL^2]$^{2+}$** in aqueous solution at 298 K is shown in **Figure 5.35**. It displays a broad band at 457 nm which is attributed to a d to π* metal-to-ligand charge transfer (^{1}MLCT) transition. The sharp intense band at 288 nm is assigned to a π π* ligand centred (LC) transition of the bipyridine ligand.[35,45] Its nature was first confirmed by Lytle and Hercules in 1969, from absorbance measurements on protonated bipyridine.[45] The spectrum is almost identical to that of $[Ru(bpy)_3]^{2+}$.[35] The introduction of an APTRA binding group onto one bipyridine ligand, therefore, does not have a significant effect on the spectrum other than a small 7 nm red shift in the MLCT maximum.

The photophysical properties of **[Ru.bL^2]$^{2+}$** are shown in **Table 5.7**, together with those of $[Ru(bpy)_3]^{2+}$ for comparison.

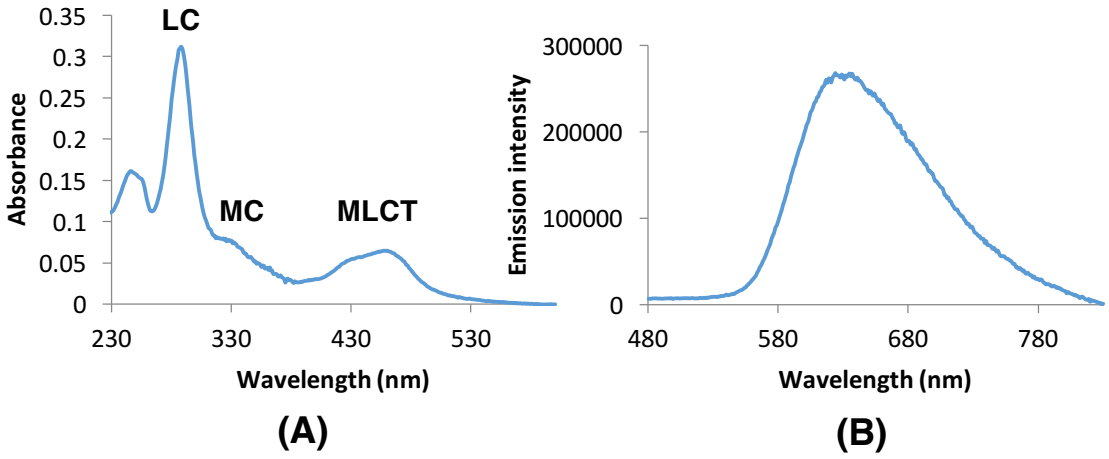

Figure 5.35 (A) The absorbance spectrum and **(B)** the emission spectrum of **[Ru.bL^2]$^{2+}$** in H_2O, 298 K, concentration = 15 μM, λ_{ex} = 457 nm.

Table 5.7 The photophysical properties of **[Ru.bL^2]$^{2+}$** and $[Ru(bpy)_3]^{2+}$ at 298 K. Properties of **[Ru.bL^2]$^{2+}$** were recorded in H_2O (< 1% DMSO). The MLCT wavelength maximum for **[Ru(bpy)$_3$]$^{2+}$** was measured in acetonitrile at 298 K.[35 a] Quantum yields (Φ) $\pm$ 20 % measured with a $[Ru(bpy)_3]^{2+}$ standard in H_2O.

Complex	λ_{MLCT} (nm)	ε / 10^3 ($M^{-1}cm^{-1}$)	Φ_{H_2O} / %
[Ru.bL^2]$^{2+}$	457	3.8(2)	7.0[a]
[Ru(bpy)$_3$]$^{2+}$ [30]	450	14.6[30]	2.8[30]

The emission spectrum of **[Ru.bL^2]$^{2+}$** was recorded in aqueous solution at 298 K, upon excitation at 457 nm (**Figure 5.35**). A broad and structureless emission spectrum is displayed, with a peak maximum of 629 nm, and a large shift of 172 nm between the ^{1}MLCT transition in the absorbance spectrum, and the ^{3}MLCT emission maximum. The spectral response reported here is comparable with $[Ru(bpy)_3]^{2+}$ based complexes in the literature, where a wavelength maximum within the range of 610-620 nm is typically seen.[35,38,46]

5.11 pK_a studies of $[Ru.bL^2]^{2+}$

5.11.1 Absorbance pK_a studies

The absorbance spectra of **$[Ru.bL^2]^{2+}$** in acidic and basic solutions are shown in **Figure 5.36**, displaying peak maxima at 288 nm and 457 nm in 100 mM KCl. In both acidic conditions the spectrum is identical to that observed in **Figure 5.35**. It is apparent from the analysis of **Figure 5.36**, that there is no change in peak intensities of the LC, MC or MLCT bands, with no shift in the wavelength maxima observed over the pH range of 4 to 10. No pK_a value for **$[Ru.bL^2]^{2+}$** could, therefore, be determined from absorbance spectroscopy.

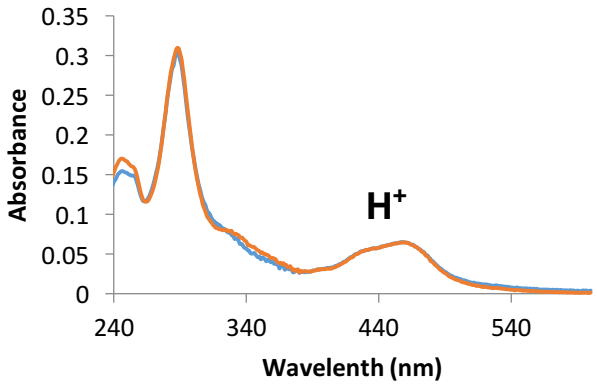

Figure 5.36 Absorbance spectrum of **$[Ru.bL^2]^{2+}$** in acidic (pH 4.8) and basic (pH 9.7) solutions. **$[Ru.bL^2]^{2+}$** concentration = 30 μM in 100 mM KCl, 298 K.

5.11.2 Emission pK_a studies

The variation of the emission spectrum with pH was monitored following excitation at 457 nm. In both acidic and basic solutions, an identically broad emission spectrum to that seen in **Figure 5.35** was displayed. A small 1.1-fold increase in the emission intensity was observed in acidic solution (**Figure 5.37**).

The emission intensity is insensitive to pH in the range 7-10, with a sharp increase in the emission intensity observed at around pH 7 from which a pK_a value of 6.9 was determined.

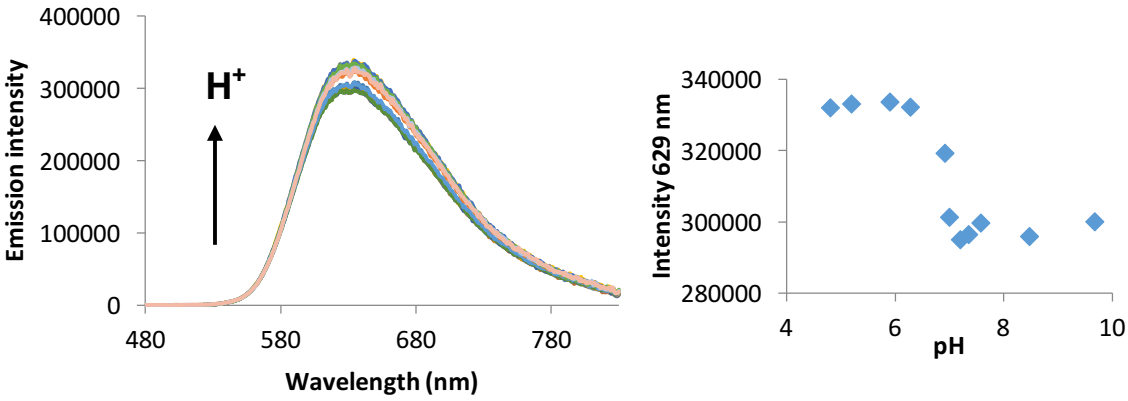

Figure 5.37 (Left) emission spectrum of **[Ru.bL^2]$^{2+}$** from pH from pH 9.7 to 5.8. (Right) the change in the emission intensity at 457 nm with pH. **[Ru.bL^2]$^{2+}$** concentration = 30 μM in 100 mM KCl, 100 mM KCl, 298 K.

5.12 Binding studies of [Ru.bL^2]$^{2+}$

The evolution of the absorbance, emission and excitation spectra of **[Ru.bL^2]$^{2+}$** upon binding with Mg^{2+}, Ca^{2+} and Zn^{2+} in aqueous solutions is reported here. Comparisons of the affinities and selectivities of biologically relevant divalent cations will be made to APTRA-based lanthanide complexes **[Eu.L^1]**, **[Eu.L^2]** and in particular **[Tb.bL^2]**, which contains a similar bi-aryl chromophore.

5.12.1 Absorbance binding studies with Mg^{2+}, Ca^{2+} and Zn^{2+}

It is evident from **Figure 5.38** that, following addition of Mg^{2+}, Ca^{2+}, Zn^{2+} to **[Ru.bL^2]$^{2+}$**, no change in the wavelength maxima was observed at the LC, MC and MLCT transitions in the absorbance spectra. The wavelength maximum of **[Ru.bL^2]$^{2+}$** is comparable to other ruthenium-based bi-aryl complexes including $[Ru(bpy)_2(phbpy)]^{2+}$ (phbpy = 4,4'-biphenyl-2,2'-bipyridine), where a wavelength maximum of 627 nm and an aerated quantum yield of 1.5 % was observed.[47]

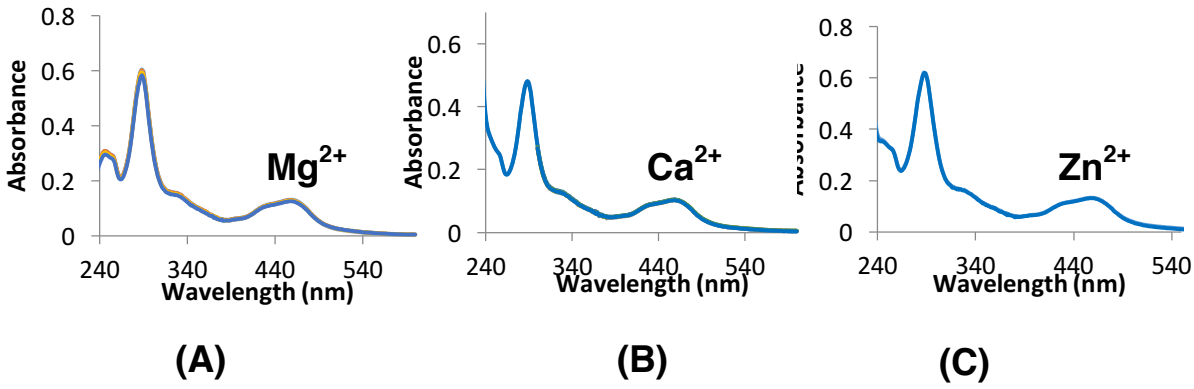

Figure 5.38 Absorbance spectra of **[Ru.bL^2]$^{2+}$** following the addition of **(A)** Mg^{2+} (60 mM), **(B)** Ca^{2+} (3.5 mM) and **(C)** Zn^{2+} (1.4 μM). **[Ru.bL^2]$^{2+}$** concentration = 30 μM in 50 mM HEPES, 100 mM KCl, pH 7.21, 298 K.

5.12.2 Emission binding studies with Mg^{2+}, Ca^{2+} and Zn^{2+}

Emission binding studies of **[Ru.bL^2]$^{2+}$** with divalent metal ions were carried out with excitation at the ^{1}MLCT state at 457 nm. A non-ratiometric emission- and excitation-based response was seen following the addition of the selected metal ions (**Figure 5.39**). In both the emission and excitation spectra of **[Ru.bL^2]$^{2+}$**, only small spectral intensity changes were observed. For example, a 1.3-, 1.3- and 1.2-fold decrease in the emission intensity was observed at 629 nm, following the addition of Mg^{2+}, Ca^{2+} and Zn^{2+} respectively. No wavelength shift of the emission or excitation peak maximum was observed upon binding saturation with any of the divalent metal ions tested.

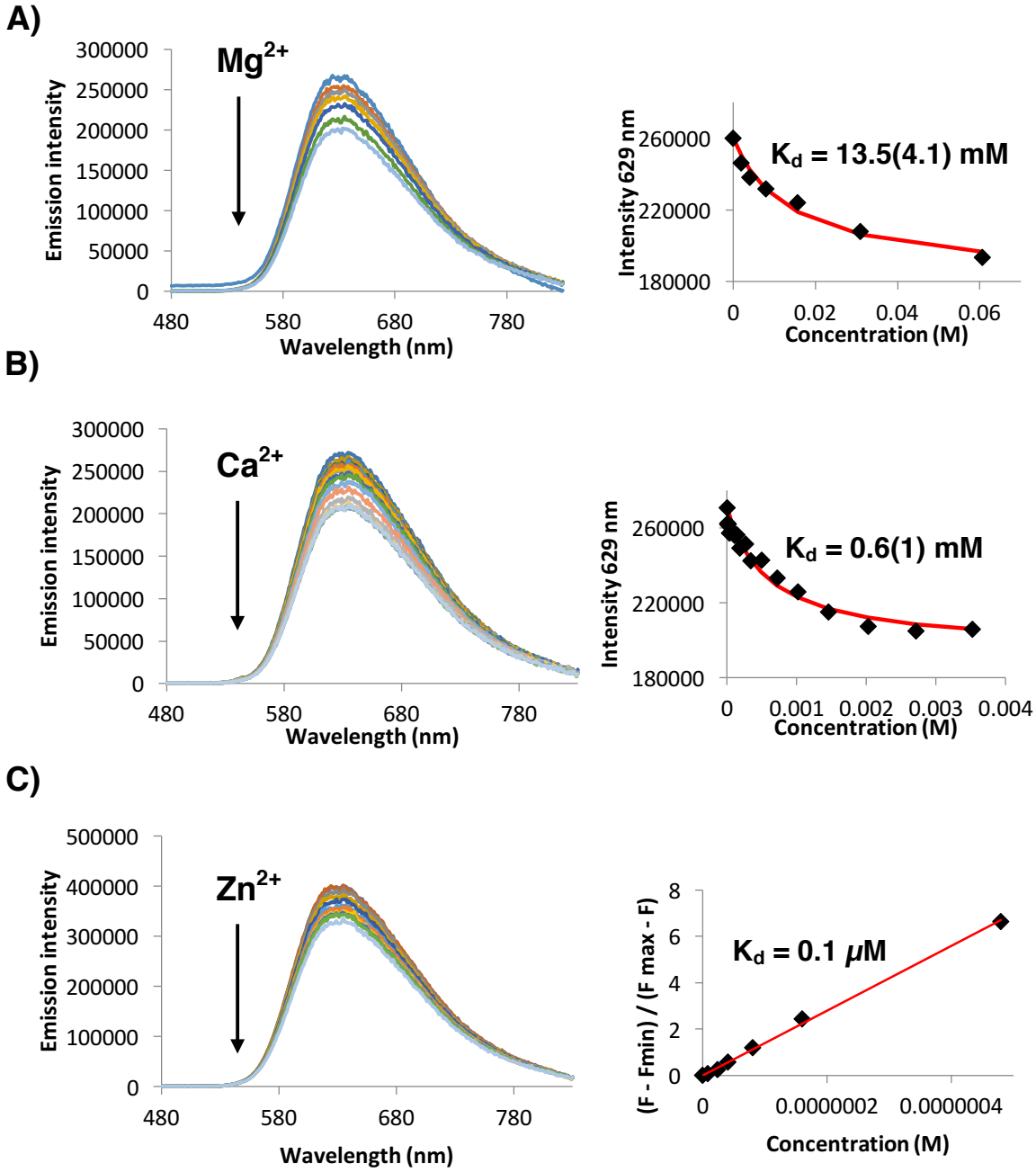

Figure 5.39 (Left) emission spectra; (right) fitting of the emission intensity against the added concentration of **(A)** Mg^{2+} (60 mM), **(B)** Ca^{2+} (3.5 mM) and **(C)** Zn^{2+} (1.4 μM) to a 1:1 binding model. **[Ru.bL^2]$^{2+}$** concentration = 30 μM in 50 mM HEPES, 100 mM KCl, pH 7.21, 298 K. Dissociations constants are provided with an error associated with the fitting.

Dissociation constants were calculated by iteratively fitting the change in the emission intensity at 629 nm against the concentration of the added divalent metal ions to a 1:1 binding model. K_d values of 13.5 mM, 0.57 mM and 0.10 μM were calculated, following the addition of Mg^{2+}, Ca^{2+} and Zn^{2+} respectively. The dissociation constants highlighted here for Mg^{2+} and Ca^{2+} are comparable to

those seen with **[Tb.bL^2]** (16.9 mM for Mg^{2+}, and 0.8 mM for Ca^{2+}), containing a bi-aryl chromophore. Complex **[Ru.bL^2]$^{2+}$**, however, was found to have a higher affinity for Zn^{2+}, with a dissociation constant of 0.1 μM determined. The Mg^{2+} affinity for bi-aryl complexes in the case of **[Tb.bL^2]** and **[Ru.bL^2]** was found to be significantly lower than that observed for **[Eu.L^1]** and **[Eu.L^2]**, containing a pyridylalkynylaryl chromophore.

In contrast to the effect observed here for **[Ru.bL^2]$^{2+}$** following the addition of divalent metal ions, a number of examples of complexes based on $[Ru(bpy)_3]^{2+}$ display emission-based hypsochromic shifts of their wavelength maximum on metal ion binding. The crown ether based **[Ru.1]**, for example, shown in **Figure 5.33**, was developed by Beer and co-workers, and exhibited a 16 nm and 3 nm shift towards the blue following the addition of Na^+ and Mg^{2+} respectively.[36] The emission wavelength maximum of complex **[Ru.2]** displayed a 14 nm blue shift following addition of Na^+, with a 2 nm hypsochromic shift observed on binding of Mg^{2+}. The vinyl-link in the bipyridine ligand was found to be essential for the spectral behaviour observed, with no wavelength shifts observed in the absence of the vinyl group.

5.13 Conclusions of this chapter

The synthesis and photophysical studies of three lanthanide complexes **[Ln.L^1]**, **[Ln.L^2]** and **[Ln.bL^2]** and one ruthenium complex **[Ru.bL^2]$^{2+}$** bearing APTRA binding groups have been reported. Carboxylate-based pro-ligands **L^1** and **L^2** were incorporated into both a pyridylalkynylaryl- or pyridylaryl-based chromophore for the sensitisation of lanthanide complexes, and a bipyridine ligand for coordination to Ru^{2+}. Complexes **[Eu.L^1]**, **[Eu.L^2]** and **[Tb.bL^2]** possess a hydration number of one (q = 1) in a stable 9-coordinate lanthanide complex.

The pH response and binding behaviour with Mg^{2+}, Ca^{2+} and Zn^{2+} were studied using emission spectroscopy. Complexes containing a pyridylalkynylaryl chromophore **[Eu.L^1]** and **[Eu.L^2]**, displayed a non-ratiometric response following addition of divalent metal cations, with no effect on the excited state lifetime observed. The bi-aryl complex **[Tb.bL^2]**, in contrast, showed a ratiometric

response following the addition of Mg^{2+} and Zn^{2+}, with an increase in the excited state lifetime only for Mg^{2+} binding, tentatively attributed to the reduction in back energy transfer and reduced oxygen quenching of the triplet excited state of the chromophore.

The complexes **[Eu.L^1]**, **[Eu.L^2]**, **[Tb.bL^2]** and **[Ru.bL^2]$^{2+}$** were found to have a significantly lower affinity towards Ca^{2+}, than the typical mid μM affinity observed in the naphthalene series (**Chapter 4**), and related literature-based APTRA indicators.[27,28] A low mM affinity for Ca^{2+} was found throughout this work, with K_d values in the range of 0.6-0.9 mM. For example, it was determined that **[Eu.L^2]** had a 28-fold lower affinity for Ca^{2+} than **NapL^2**, and a 17-fold weaker binding compared to **[Tb.2]** developed by *Parker et al*.[5,6] (**Table 5.6**).

Complexes containing a pyridylalkynylaryl chromophore were found to be the most selective for the binding of Mg^{2+}. Both **[Tb.bL^2]** and **[Ru.bL^2]$^{2+}$** displayed a 2-5-fold lower affinity towards Mg^{2+} compared to **[Eu.L^1]** and **[Eu.L^2]**, while showing comparable affinities for Ca^{2+} and Zn^{2+}.

The reduced affinity observed for Ca^{2+} in non-competitive media, allowed Mg^{2+} binding to be investigated in newborn calf serum (NCS). The study carried out with **[Eu.L^2]** is the first reported APTRA-based complex developed that can sense Mg^{2+} in serum. Encouraging results in NCS were obtained, following the addition of Mg^{2+}. A 'turn-off' response was seen in the emission spectrum, associated with a binding constant of 0.6 mM. This K_d value is comparable to the 'free' Mg^{2+} concentration in human serum.[32]

The pK_a and dissociation constants of **[Eu.L^1]**, **[Eu.L^2]**, **[Tb.bL^2]** and **[Ru.bL^2]$^{2+}$** are shown in **Table 5.8.** Lanthanide-based complex **[Tb.2]** developed by Parker *et al.* has been included for comparison.

Table 5.8 A summary of the calculated pK_a and dissociation constants of **[Eu.L^1]**, **[Eu.L^2]**, **[Tb.bL^2] and [Ru.bL^2]$^{2+}$** via fluorescence emission spectroscopy. All pK_a values are given with an error associated with the fitting. The reported binding constants following the addition of Mg^{2+}, Ca^{2+} and Zn^{2+} to **[Eu.L^1]**, **[Eu.L^2]** and **[Tb.bL^2]** are an average of 2-3 independent metal ion titrations, and are given with the experimental error given in parenthesis. Mg^{2+} saturated wavelengths are highlighted in red.† pK_a value determined from absorbance spectroscopy. * Value determined from deoxygenated solutions in both H_2O and D_2O.

Complex	q	Absorption λ_{ex} (nm)	ε / 10^3 ($M^{-1}cm^{-1}$)	Excitation λ_{max} (nm)	Emission λ_{max} (nm)	pK_a	Log K (Mg^{2+})	K_d (Mg^{2+})	Log K (Ca^{2+})	K_d (Ca^{2+})	Log K (Zn^{2+})	K_d (Zn^{2+})
[Eu.L^1]	1	316 316	11.5(2)	315 315	699 699	4.5(02)†	2.1(05)	7.5(8) mM	3.0(1)	0.9(2) mM	5.7(2)	1.8(5) μM
[Eu.L^2]	1	318 318	18.4(4)	314 314	699 699	6.7(04)	2.4(2)	3.7 (1.5) mM	3.0(05)	0.9(1) mM	5.7(04)	1.9(1) µM
[Tb.bL^2]	1*	280 280	6.2	279 274	544 544	No pH response	1.8(06)	16.9 (2.3) mM	3.1(05)	0.8(1) mM	6.3	0.5 µM
[Ru.bL^2]$^{2+}$	-	457 457	3.8(2)	454 454	629 629	6.9(01)	1.9	13.5 mM	3.2	0.6 mM	7.0	0.1 µM
[Tb.2] [6]	1	262	-	-	544 544	6.4†	3.17	0.8 mM	4.14	53.7 μM	5.0	10.5 μM

5.14 References

[1] E. Soini and I. Hemmilla, *Clin. Chem.*, 1979, **25**, 353-361.

[2] A. T. Frawley, R. Pal and D. Parker, *Chem. Commun.*, 2016, **52**, 13349-13352.

[3] J-C. G. Bünzli and C.Piguet, *Chem. Soc. Rev.*, 2005, **34**, 1048-1077.

[4] S. Shuvaev, M. Starck and D. Parker, *Chem. Eur. J.,* 2017, **23**, 1- 17.

[5] O. Reany, T. Gunnlaugsson and D. Parker, *Chem. Commun.*, 2000, 473-474.

[6] O. Reany, T. Gunnlaugsson and D. Parker, *J. Chem. Soc., Perkin Trans 2.*, 2000, **2**, 1819-1831.

[7] R. H. Laye and S. J. A. Pope, *Dalton Trans.*, 2006, 3108-3113.

[8] A. K. R. Junker, M. Tropiano, S. Faulkner and T. J. Sørensen, *Inorg. Chem.*, 2016, **55**, 12299- 12308.

[9] L. S. Natrajan, A. J. L. Villaraza, A. M. Kenwright and S. Faulkner, *Chem. Commun.*, 2009, 6020-6022.

[10] U. Brath, S. I. Swamy., A. X. Veiga., C-C, Tung., F. Van Petegem, *J. Am. Chem. Soc.*, **2015**, 137, 11391-11398.

[11] R. C. Jones, A. J. Canty, J. A. Deverell, M. G. Gardiner, R. M. Guijt, T. Rodemann, J. A. Smith and V-A. Tolhurst, *Tetrahedron.*, 2009, **65**, 7474-7481.

[12] P. Wothers, N. Greeves, S. Warren and J. Clayden, Organic Chemistry, Chapter 36, p. 943-967.

[13] B. Metten, M. Smet, N, Boens and W. Dehaen, *Synthesis.*, 2005, 1838-1844.

[14] T. Ishiyama, Y. Itoh, T. Kitano and N. Miyaura, *Tetrahedron Lett.*, 1997, **38**, 3447-3450

[15] M. Murata, T. Oyama, S. Watanabe and Y. Masuda, *J. Org. Chem.*, 2000, **65**, 778-780.

[16] J. R. Lakowicz, Principles of Fluorescence Spectroscopy, Second Edition, 1999.

[17] A. D'Aléo, A. Picot, A. Beeby, J. A. G. Williams, B. Le Guennic, C. Andraud and O. Maury, *Inorg. Chem.*, 2008, **47**, 10258-10268.

[18] J. A. G. Williams, D. Parker and P. K. Senanayake, *J. Chem. Soc. Perkin Trans 2.*, 1998, 2129.

[19] M. Soulié, F. Latzko, E. Bourrier, V. Placide, S. J. Butler, R. Pal, J. W. Walton, P. L. Baldeck, B. Le Guennic, C. Andraud, J. M. Zwier, L. Lamarque, D. Parker and O. Maury, *Chem. Eur. J.,* 2014, **20**, 8636-8646.

[20] A. Beeby, I. M. Clarkson, R. S. Dickins, S. Faulkner, L. Royle, A. S. de Sousa, J. A. G. Williams, M. Woods and D. Parker, *J. Chem. Soc. Perkin Trans 2.*, 1999, 493-503.

[21] S. Shuvaev, R. Pal and D. Parker, *Chem. Commun.*, 2017, **53**, 6724-6727.

[22] E. Harbusch-Görnert and C. Reichardt, *Liebigs Ann.*, 1983, 721-743.

[23] D. G. Smith, P. Pal and D. Parker, *Chem. Eur. J.,* 2012, **18**, 11604-11613.

[24] V. Placide, A. T. Bui, A. Grichine, A. Duperray, D. Pitrat, C. Andraud and O. Maury, *Dalton Trans.*, 2015, **44**, 4918-4924.

[25] A. T. Bui, A. Grichine, A. Duperray, P. Lidon, F. Riobé, C. Andraud and O. Maury, *J. Am. Chem. Soc.*, 2017, **139**, 7693-7696.

[26] W-S. Lo, J. Zhang, W-T. Wong and G-L. Law, *Inorg. Chem.*, 2015, **54**, 3725-3727.

[27] B. Raju, E. Murphy, L. A. Levy, R. D. Hall and R. E. London, *Am. J. Physiol.*, 1989, **256**, 540-548.

[28] Q. Lin, J. J. Gruskos and D. Buccella, *Org. Biomol. Chem.*, 2016, **14**, 11381.

[29] M. Starck, R. Pal and D. Parker, *Chem. Eu. J.,* 2016, **22**, 570-580.

[30] R. Pal, L. C. Costello and D. Parker, *Org. Biomol. Chem.*, 2009, 7, 1525-1528.

[31] R. Pal, A. Beeby and D. Parker, *J. Pharmaceut. Biomed. Anal.*, 2011, **56**, 352-358.

[32] J. H. F. Baaij, J. G. J. Hoenderop and R. J. M. Bindels, *Physiol Rev.*, 2015, **95**, 1-46.

[33] J. P. Paris and W. W. Brandt, *J. Am. Chem. Soc.,* 1959, **81**, 5001- 5002.

[34] F. P. Dwyer, H. A. Goodwin and E. C. Gyarfas, *Aust. J. Chem.,* 1963, **16**, 544-8.

[35] A. Juris, V. Balzani, F. Barigelletti, S. Campagna, P. Belser and A. Von Zelewsky, *Coord. Chem. Rev.*, 1988, **84**, 85- 277.

[36] P. D. Beer, O. Kocian, R. J. Mortimer and C. Ridgway, *J. Chem. Soc. Chem. Commun.*, 1992. **117**, 1247-1249.

[37] S. R. Stoyanov, J. M. Villegas and D. P. Rillema, *Inorg. Chem.*, 2002, **41**, 2941-2945.

[38] C. Sabatini, A. Barbieri, F. Barigelletti, K. J. Arm and J. A. G. Williams, *Photochem. Photobiol. Sci.*, 2007, **6**, 397-405.

[39] A. E. Friedman, J. C. Chambron, J. P. Sauvage and J. K. A. Barton, *J. Am. Chem. Soc.,* 1990, **112**, 4960-4962.

[40] M. R. Gill and J. A. Thomas, *Chem. Soc. Rev.*, 2012, **41**, 3179-3192.

[41] M. R. Gill, J. Garcia- Lara, S. J. Forster, C. Smythe, G. Battaglia and J. A. Thomas, *Nat. Chem.*, 2009, **1**, 662-667.

[42] M-J Li, B. W- K. Chu, N. Zhu and V. W-W. Yam, *Inorg, Chem.*, 2007, **46**, 720-733

[43] D. Wenkert and R. B. Woodward, *J. Org. Chem.*, 1983, **48**, 283-289.

[44] A. J. Wilkinson, V. L. Whittle and J. A. G. Williams, *Dalton Trans.*, 2008, 2081-2099.

[45] F. E. Lytle and D. M. Hercules, *J. Am. Chem. Soc.,* 1969, **91**, 253

[46] K. J. Arm and J. A. G. Williams, *Chem. Commun.*, 2005, 230-232.

[47] K. J. Arm, PhD thesis. Title: Cross-coupling methodology in the synthesis of luminescent metal complexes and multi-metallic assemblies, 2005. Durham University.

[48] I. Kutsche, G. Gildehaus, D. Schuller and A. Schumpe, *J. Chem. Eng. Data.,* 1984, **29**, 286-287.

6. Conclusions and Future Work

6.1 Conclusions

The aim of the work described throughout this report was to develop new ligands and complexes to study the binding of Mg^{2+} via both absorbance and luminescence spectroscopy. Originally, the work was subdivided into two main objectives. The first was to incorporate the APTRA binding group into new naphthalene, lanthanide(III) and ruthenium(II)-based systems to study the binding of Mg^{2+} and its competing divalent cations Ca^{2+} and Zn^{2+}. The APTRA binding group has been incorporated into numerous fluorophores over the years for a range of biological applications.[1-3] It remains the chelate of choice in the vast majority of Mg^{2+} sensors in the literature, even though it is universally recognised to display a higher selectivity towards Ca^{2+} over Mg^{2+}. The second and primary objective, therefore, was to develop new metal chelates containing phosphinate-based binding groups, in an attempt to increase the selectivity for the binding of Mg^{2+}.

Four pro-ligands bearing carboxylate and phosphinate groups were synthesised and characterised in **Chapter 2**, namely $\mathbf{L^1}$, $\mathbf{L^2}$, $\mathbf{L^4}$ and $\mathbf{L^6}$. These ligands were expected to form either a [5, 5, 5] ($\mathbf{L^1}$, $\mathbf{L^2}$ and $\mathbf{L^4}$) or [6, 5] ($\mathbf{L^6}$) ring chelate on the binding of divalent cations. Binding groups were introduced via a series of alkylation reactions on aminophenol precursors, with Hünig's base in acetonitrile found to be the conditions of choice. The incorporation of ligands $\mathbf{L^1}$, $\mathbf{L^2}$, $\mathbf{L^4}$ and $\mathbf{L^6}$ into fluorescent naphthalene-1-alkynylaryl (**Chapter 4**) and luminescent metal-based systems (**Chapter 5**) allowed the binding of Mg^{2+} and other biologically relevant cations to be studied in both non-competitive and competitive aqueous ionic media.

The development of the pentadentate APTRA analogue *o*-aminophenol-*N,N*-diacetic acid phosphinate (APDAP), containing one phosphinate binding group, was highlighted in **Chapter 3**. A direct comparison of the pH behaviour and the binding of divalent cations to that of its APTRA analogue, was studied via absorbance spectroscopy. Promising results were shown: a desirable lack of

sensitivity to pH in the range 6.5-7.5, and a reported 110-fold lower affinity for the binding of Ca^{2+} compared to APTRA. The enhanced selectivity for the binding of Mg^{2+} was linked to the longer C-P and P-O bonds in APDAP, generating a larger effective chelate ring size that inherently favours the binding of the smaller Mg^{2+} ion over Ca^{2+}.

The encouraging results obtained for APDAP in **Chapter 3** were carried through into **Chapter 4**, with the incorporation of the APDAP binding moiety into a naphthalene-1-alkynylaryl system to study the binding of Mg^{2+}. Phosphinate-based ligand **NapL^4** displayed a 10-fold weaker affinity for Ca^{2+} than the carboxylate-based **NapL^1** and **NapL^2**, which were seen to have values comparable to literature-based APTRA indicators.[1,3,4] Interestingly, and surprisingly, however, **NapL^4** also displayed a higher affinity for Mg^{2+}.

Tridentate ligand **NapL^6** displayed the lowest affinity for Mg^{2+} throughout the naphthalene series, suggesting that a higher denticity, i.e. pentadentate for **NapL^1**, **NapL^2** and **NapL^4**, is preferred for a low mM binding affinity of Mg^{2+}. Following the addition of Ca^{2+} and Zn^{2+}, negligible changes in the fluorescence emission and excitation spectrum were observed, suggesting a weak binding to these cations in particular. It had been thought initially that a lower denticity may favour the binding of Mg^{2+} over Ca^{2+} and Zn^{2+} because the binding of Mg^{2+} carries the greatest enthalpic cost, with the reduction in the denticity causing the biggest entropic penalty for Ca^{2+} and Zn^{2+}.[4] Such behaviour is one possible explanation for the reduced affinity observed for Ca^{2+} in the β-keto acid series.[5]

In **Chapter 5**, the APTRA binding group was incorporated into lanthanide(III)- and ruthenium(II)-based systems. It was found from luminescence spectroscopy that the Mg^{2+} / Ca^{2+} selectivity was significantly enhanced in the metal-based complexes **[Eu.L^1]**, **[Eu.L^2]**, **[Tb.L^2]** and **[Ru.bL^2]**. A low mM affinity for the binding of Ca^{2+} was observed in each complex, containing either a pyridylalkynlaryl or bi-aryl chromophore, and is significantly lower than the μM affinity seen for Ca^{2+} with **NapL^1** and **NapL^2**.

The lanthanide systems were favoured over ruthenium complexes due to their higher quantum yields in solution, 'turn-on' enhancement in the case of **[Eu.L^2]**, and the observation of larger fluorescence changes on the binding of divalent metal ions. Complexes containing pyridylalkynylaryl chromophores **[Eu.L^1]** and **[Eu.L^2]** were found to be the most selective complexes for the binding of Mg^{2+} out of all the metal-based systems studied, with low mM affinities for both Mg^{2+} and Ca^{2+}. They also displayed significantly longer excitation wavelengths than the bi-aryl lanthanide complexes, making them more suitable for future cellular studies in their present state.

The lower affinity displayed for Ca^{2+} in the metal-based complexes could in part be due to the reduced donor ability of the aniline nitrogen lone pair of electrons. Complex **[Eu.L^2]**, for example, displayed a 28-fold weaker affinity for Ca^{2+} over the model naphthalene analogue **NapL^2**. The Zn^{2+} affinity between the model naphthalene series and the metal-based systems was, however, comparable. Such behaviour could be explained by the fact that Zn^{2+} ions typically favour the binding to tertiary nitrogen donors over Mg^{2+} and Ca^{2+}.[6]

6.2 Future Work

It has been highlighted over the course of this work that the incorporation of a phosphinate binding group at the expense of a carboxylate ligating group dramatically enhances the relative Mg^{2+} / Ca^{2+} selectivity. Promising results were achieved with APDAP in **Chapter 3**, and **NapL^4** in **Chapter 4**, with the phosphinate-based ligands displaying an improved Mg^{2+} / Ca^{2+} selectivity compared to literature-based APTRA ligands. It would be interesting, therefore, to incorporate the APDAP binding group into a pyridylalkynylaryl chromophore to form phosphinate-based lanthanide complex **[Ln.L^4]** (**Figure 6.1**). A study into the pH behaviour and the binding of Mg^{2+} and its competing biologically relevant cations Ca^{2+} and Zn^{2+} to **[Ln.L^4]**, would allow a direct comparison to be made with carboxylate-based complexes **[Ln.L^1]** and **[Ln.L^2]**.

Another area of particular interest is to develop a targeted probe to study the binding of Mg^{2+} in cellular organelles such as the mitochondria. The vast

majority of mitochondrial targeting probes in the literature contain biologically stable lipophilic cations such as rhodamine and trialkylphosphonium cations (TPP^+). These cations are well known to accumulate in the mitochondria because of its negative membrane potential.[7]

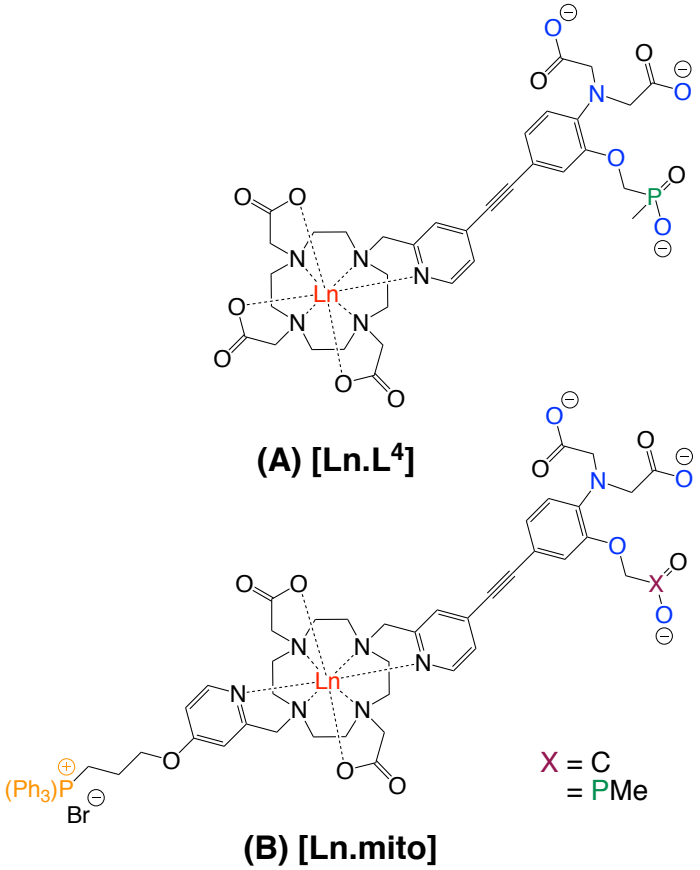

Figure 6.1 Possible structures of future lanthanide complexes containing (**A**) the APDAP binding group **[Ln.L^4]**, and (**B**) an APTRA-based mitochondria-targeted luminescence probe containing a TPP^+ group for localisation in the mitochondria **[Ln.mito]**.

Sensing Mg^{2+} in the mitochondria is of particular interest. It has been found that in HeLa cells an increase in 'free' Mg^{2+} was observed in the mitochondria in the early stages of Staurosporine-induced apoptosis.[8] Progress in the area, however, has been restricted due to the lack of selective probes available for the binding of Mg^{2+}. Many indicators, such as Mag-mito developed by Buccella *et al*, require the use of BAPTA in cellular studies to eliminate any Ca^{2+} interference.[8]

The significantly higher Mg^{2+} / Ca^{2+} selectivity observed in **Chapter 5** for lanthanide complexes **[Eu.L^1]** and **[Eu.L^2]**, in particular, may allow the *in vivo* studies to be carried out without the use of BAPTA. Complexes **[Eu.L^1]** and **[Eu.L^2]** displayed a two order of magnitude reduction in their Ca^{2+} affinity

compared with APTRA analogues in the literature (mM vs. μM). It would be expected, therefore, that in cells the Ca^{2+} interference would be greatly reduced. Slight modifications would need to be made to both the complex and the chromophore structures for mitochondria-targeted *in vivo* studies. The proposed structure of **[Ln.mito]** is shown in **Figure 6.1**. The addition of a lipophilic TPP^{+} cation onto a pyridine group should favour accumulation of the complex within the mitochondria, whilst maintaining the same affinity and selectivity for Mg^{2+} observed for **[Ln.L^2]**. The introduction of acetoxy methyl (AM) esters on the APTRA binding unit, will facilitate cell loading,[1,5] with the esters cleaved readily *in vivo* by intracellular esterases.[1,5,8]

Finally, another area of interest is to develop a metal responsive NMR-based probe that could be used to detect 'free' Mg^{2+} *in vivo*. In Durham, extensive work has been carried out to develop pH responsive ^{1}H PARASHIFT lanthanide-based MRI probes that contain a *tert*-butyl reporter group.[9,10] The *tert*-butyl group is typically 6 to 6.5 Å from the lanthanide centre, shifting the resonance away from the strong ^{1}H signals arising from water (4.7 ppm) and fat (1.3 ppm) *in vivo*, and increasing the sensitivity of the technique.[9]

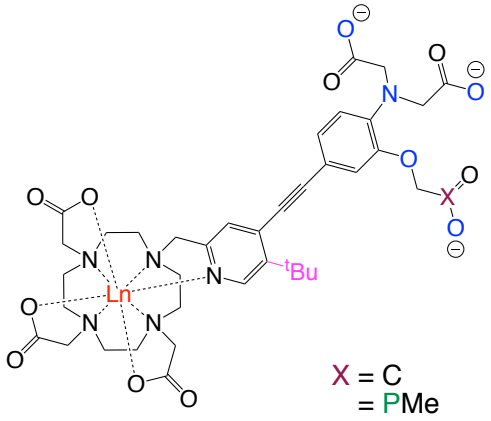

[Ln.L^7]

Figure 6.2 Possible structure of a metal-responsive PARASHIFT NMR probe **[Ln.L^7]**, to study the binding of Mg^{2+} and other divalent cations.

A PARASHIFT probe with a phosphinate-group adjacent to the *tert*-butyl reporter group has been shown to be temperature- and pH-dependent.[10] Upon a change in pH for example, a significant shift of the *tert*-butyl resonance is

reported.[10] The proposed structure of a Mg^{2+} responsive PARASHIFT probe, **[Ln.L^7]**, is shown in **Figure 6.2** with a *tert*-butyl reporter group introduced onto the pyridylalkynylaryl chromophore. It is thought that following the addition of Mg^{2+} to **[Ln.L^7]**, a shift in the *tert*-butyl resonance could occur allowing the binding of Mg^{2+} to be monitored initially by ^{1}H NMR spectroscopy. The incorporation of the APDAP binding group into a pyridylalkynylaryl chromophore **[Ln.L^7]** (X = PMe), would also allow the binding of Mg^{2+} to be studied by ^{31}P NMR.

6.3 References

[1] G. Zhang, J. J. Gruskos, M. S. Afzal and D. Buccella, *Chem. Sci.*, 2015, **6**, 6841-6846.

[2] Q.Lin, J.J Gruskos and D. Buccella, *Org. Biomol. Chem.*, 2016, **14**, 11381-11388.

[3] B. Raju, E. Murphy, L. A. Levy, R. D. Hall and R. E. London, *Am J Physiol*, 1989, **256**, 540-548.

[4] M. Brady, S. D. Piombo, C. Hu and D. Buccella, *Dalton Trans.*, 2016, 45, 12458-12464.

[5] Y. Suzuki, H. Komatsu, T. Ikeda, N. Saito, S. Araki, D. Citterio, H. Hisamoto, Y. Kitamura, T. Kubota, J. Nakagawa, K. Oka and K. Suzuki, *Anal. Chem.*, 2002, 74, 1423-1428.

[6] O. Reany, T. Gunnlaugsson and D. Parker, *J. Chem. Soc., Perkin Trans 2.*, 2000, 2, 1819-1831.

[7] J. Zielonka, J. Joseph, A. Sikora, M. Hardy, O. Ouari, J. Vasquez-Vivar, G. Cheng, M. Lopez and B. Kalyanaraman, *Chem. Rev.*, 2017, **117**, 10043-10120.

[8] G. Grynkiewicz, M. Poenie and R. Y. Tsien, *J. Biomol. Chem.*, 1985, **260**, 4041.

[9] P. Harvey, A. M. Blamire, J. I. Wilson, K-L. N. A. Finney, A. M. Funk, P. K. Senanayake and D. Parker, *Chem. Sci.*, 2013, **4**, 4251-4258.

[10] K-L. N. A. Finney, A. C. Harnden, N. J. Rodgers, P. K. Senanayake, A. M. Blamire, D. O'Hogain and D. Parker, *Chem. Eur. J.*, 2017, **23**, 7979-7989.

7. Experimental

7.1 General procedures

7.1.1 Materials

All commercially available reagents were used as received from suppliers without further purification. Solvents used were laboratory grade. Anhydrous solvents were dried over the appropriate drying agent. All moisture-sensitive reactions were carried out by Schlenk-line techniques, under an inert atmosphere of either argon or nitrogen. For air sensitive reactions, solvents were degassed using the freeze-pump-thaw cycle method. Water was purified by the 'Purite$_{STILL}$plus' system with a conductivity of $\leq 0.04\ \mu S\ cm^{-1}$.

7.1.2 Chromatography

Thin layer chromatography was performed on neutral alumina (Merck Art 5550) or silica (Merck Art 5554) and visualized under UV irradiation (254 nm) or by staining with either iodine or potassium permanganate. Column chromatography was carried out either manually using neutral alumina or silica (Merck Silica Gel, 230 – 400 mesh) or using a Teledyne Combi-flash instrument equipped with RediSep R_f silica cartridges to perform automated elution.

7.1.3 Instrumentation

NMR: Routine ^{1}H (400 MHz) and ^{13}C (101 MHz) and ^{31}P (162 MHz) NMR spectra were acquired on Bruker Avance or Varian Mercury 400 NMR spectrometers. ^{13}C NMR and ^{31}P NMR spectra were run on a proton decoupled experiment. Two-dimensional NMR spectra (COSY, NOESY, HSQC and HSBC) were carried out by the solution state NMR service at Durham University on Varian-600 (600 MHz) or VNMRS-700 (700 MHz) instruments.

Mass spectrometry: ES-MS data was acquired on a Waters TQD mass spectrometer interfaced with an Acquity UPLC system. ASAP experiments were carried out on a Waters Xevo QToF mass spectrometer. Mass spectra of **NapL^{1}**, **NapL^{2}**, **NapL^{4}**, **NapL^{6}**, **[Ln.L^{1}]** and **[Ln.L^{2}]** were recorded on a Waters Xevo

QToF instrument in an acetonitrile and ammonium bicarbonate buffered (25 mM) system.

Melting points: Melting points were measured on a Gallenkamp melting point apparatus, and are uncorrected.

7.1.4 pK_a determination

pH measurements were recorded using a Jenway 3510 pH meter in combination with a Jenway 924 005 pH electrode. The pH probe was calibrated before each independent titration using commercially available buffer solutions of pH 4, 7 and 10. Samples were prepared with a background of constant ionic strength (I = 0.1 M KCl, 298 K). Aqueous solutions were titrated to acid using 0.025 M, 0.05 M and 0.1 M concentrations of $HCl_{(aq)}$. The resulting sigmoidal curve of either absorbance or fluorescence intensity vs. pH was fitted by a non-linear least squares iterative analysis by Boltzmann using Origin 8.0 software. In each instance, pK_a values were calculated with an error associated with the fitting.

7.2 Optical techniques

7.2.1 Absorption spectroscopy

UV-Vis absorption spectra were measured using a UVIKON XS spectrometer operating with LabPower software. The sample was held in a quartz cuvette with a path length of 1 cm. Absorption spectra were recorded against pure solvent in an optically matched cuvette.

Extinction coefficients were calculated using a sample dilution method, from a linear plot of absorbance against concentration according to the Beer-Lambert law (**Equation 7.1**).

$$A = \varepsilon c l \qquad \textbf{Eq. 7.1}$$

where: A is absorbance (at λ_{max}), ε is molar extinction coefficient, l is the path length of the cuvette (1 cm), and c is the concentration of the sample.

7.2.2 Fluorescence Spectroscopy

Emission and excitation spectra were acquired on a Jobin Yvon Fluoromax-2 spectrometer, in quartz cuvettes with a path length of 1 cm. Excitation and emission wavelengths were selected according to the specific sample. An integration time of 0.5 seconds and increment of 1.0 nm was used. Emission and excitation bandpasses used were either 2:2 or 3:3 (in nm) depending on the brightness of the sample.

Lanthanide emission and excitation spectra were recorded using the appropriate glass filter (435 nm filter for Eu(III) complexes and 395 nm filter for Tb(III) complexes), to remove $2\lambda_{ex}$ light from the fluorescence emission and $\frac{\lambda_{em}}{2}$ from the excitation spectrum.

Degassed samples were measured in an adapted cuvette which can be attached to a vacuum line and degassed using the freeze-pump-thaw cycle method.

Low temperature measurements were carried out at 77 K in a smooth glass of ethanol. In each case, the complex was first dissolved in the minimum amount of water, before ethanol was added.

7.2.3 Luminescence lifetimes

Lifetime measurements were carried out using two instruments. Lifetimes of aerated samples were measured using a Perkin Elmer LS55 luminescence spectrometer. Lanthanide excited state lifetimes were measured by excitation of the sample by a short pulse of light, followed by the monitoring of the integrated intensity of light emitted during a fixed gate time t_g, after a delay time of t_d. Measurements were made for at least 30 separate decay times over a period of a minimum of three lifetimes. A gate time of 0.1 ms was selected. The decay curves were fitted to **Equation 7.2** using Origin 8.0 software.

$$I = A_0 + A_1 e^{-kt} \quad \textbf{Eq. 7.2}$$

where: I is the intensity at time t after the excitation pulse, A_0 is the background intensity after the fluorescence decay, A_1 is the pre-exponential factor and k is the rate constant for the excited state decay. The excited state lifetime, τ, can be calculated according to **Equation 7.3**.

$$\tau = \frac{1}{k} \quad \textbf{Eq. 7.3}$$

The inner sphere hydration numbers (q) of Eu^{3+} and Tb^{3+} complexes are calculated by measuring the luminescence lifetimes in both H_2O and D_2O. The q value was calculated from **Equation 7.4** for Eu^{3+} complexes and **Equation 7.5** for Tb^{3+} complexes.[1]

$$q_{Eu} = 1.2\left(k_{H_2O} - k_{D_2O} - 0.25 - 0.075n\right) \quad \textbf{Eq. 7.4}$$

$$q_{Tb} = 5.0\,(k_{H_2O} - k_{D_2O} - 0.06 - 0.010n) \quad \textbf{Eq. 7.5}$$

where: q_{Eu} / q_{Tb} is the inner sphere hydration number, k is rate constant for luminescence decay and n is the number of proximal amide –NH oscillators.

Degassed luminescence lifetimes were measured using an OB 920 Fluorimeter, using a xenon flash lamp as the excitation source. For both instruments, excitation and emission wavelengths were selected based upon the individual lanthanide complex being measured.

7.2.4 Quantum yields

The luminescence quantum yields were determined relative to a well known luminescence standard. A reference of $[Ru(bpy)_3]^{2+}$ in H_2O ($\Phi_{457} = 0.028$)[2], quinine sulphate in 0.5 M H_2SO_4 ($\Phi_{347} = 0.546$)[3] or 1,4-bis(5-phenyloxazol-2-yl) benzene (POPOP) in cyclohexane ($\Phi_{300} = 0.97$)[4] were used. The standard was chosen depending on both the fluorescence emission spectrum, and the excitation wavelength that was required. In each instance, the luminescence standard used for each quantum yield measurement is included in the table caption for reference.

Solutions of both the sample and reference were prepared so that the absorbance intensity at the excitation wavelength (λ_{ex}) was 0.1. All measurements were recorded at room temperature under both aerated and deoxygenated conditions. Absorbance and emission spectra of the reference and the sample were run consecutively with identical parameters. The quantum yield for all ligands / complexes was calculated from **Equation 7.6**.

$$\Phi_a = \left(\frac{I_a}{I_b}\right) x \left(\frac{A_b}{A_a}\right) x \left(\frac{n_a}{n_b}\right)^2 x \Phi_b \quad \textbf{Eq. 7.6}$$

where: '*a*' refers to the sample and '*b*' refers to the standard. Φ is the quantum yield, *I* is the integrated intensity of the emission spectrum, *A* is the absorbance at the excitation wavelength (λ_{ex} = ~ 0.1) and *n* is the refractive index of the solvent.

7.3 HPLC analysis

Reverse phase HPLC was performed at 295 K using a Shimadzu system consisting of a Degassing Unit (DGU-20A_{5R}), a Prominence Preparative Liquid Chromatograph (LC-20AP). An XBridge C18 10 x 100 mm, 5 μM column was used to purify the complexes on a preparative scale with a flow rate of 17 mL / minute. Analytical scale purifications were performed on a Shimadzu ShimPacl VP-ODS column, 4.6 x 150 mm, 5 μM column with a flow rate of 2 mL / min. A gradient elution was used with a total run time of 25 minutes for each individual injection. The conditions used for all preparative HPLC purifications of lanthanide complexes can be seen in **Table 7.1**.

Table 7.1 Preparative HPLC procedure for all lanthanide complexes.
Solvent A = Ammonium bicarbonate buffer (25 mM) in water, Solvent B = CH_3CN.

Time (min)	Solvent A (%)	Solvent B (%)
0	100	0
3	100	0
13	0	100
16	0	100
25	100	0

7.4 Metal ion binding studies

All divalent metal binding studies for the addition of Mg^{2+}, Ca^{2+} and Zn^{2+} ($[M^{2+}]$) were carried out in buffered solutions of 50 mM HEPES and 100 mM KCl maintained at pH 7.2. Concentrations of the ligand / complex used during the titration are stated in the Figure caption in each instance. Stock solutions of $[M^{2+}]$ contained the same concentration of the sensor in the cuvette to avoid sample dilution over the course of the titration. Small aliquots of $[M^{2+}]$ were added in each instance, with the absorbance, emission and excitation spectra run 5 minutes after each addition to ensure the sample had equilibrated.

New-born calf serum (NCS), for the titration of **NapL^4** and **EuL^2** was supplied from Thermo Fisher Scientific and stored at -20 ^oC. Small amounts of NCS were defrosted the morning prior to use. Stock solutions of $[M^{2+}]$ were also made in NCS to avoid dilution. ICP-OES was used to determine the concentrations of Ca^{2+} (2.6 mM), Mg^{2+} (0.8 mM) and K^+ (3.9 mM) in the NCS prior to the Mg^{2+} titration. 100 μL of NCS was diluted to 2 mL using 200 μL ultrapure nitric acid (70 % wt.) and 1.7 mL H_2O in a Teflon vial. The blank was prepared by an identical method with 200 μL ultrapure nitric acid (70 % wt.) and 1.7 mL H_2O. Both the sample and the blank were diluted by a factor of 5 prior to analysis with dilute nitric acid.

Dissociation constants (K_d's) for the binding of Mg^{2+} and Ca^{2+} were generated from a 1:1 binding model obtained from a least square fitting iterative from *www.supramolecular.org.*[5] Binding constants were verified with the comparison to those obtained from the linear plots of **Equation 7.7** and **Equation 7.8** for non-ratiometic indicators and **Equation 7.9** for ratiometric indicators (**See Appendix**). In the case of Zn^{2+} binding, dissociation constants were calculated from a plot of $\frac{(A-A_{min})}{(A_{max}-A)}$ in **Chapter 3**, and $\frac{(F-F_{min})}{(F_{max}-F)}$ or $\frac{(R-R_{min})}{(R_{max}-R)}$ in **Chapter 4** and **Chapter 5**, against the concentration of Zn^{2+} added. The dissociation constants were calculated from a reciprocal of the association constant obtained from the gradient of the straight line (**Equation 7.10**).

$$[M^{2+}] = K_d \frac{(A - A_{min})}{(A_{max} - A)} \qquad \textbf{Eq. 7.7}$$

$$[M^{2+}] = K_d \frac{(F - F_{min})}{(F_{max} - F)} \qquad \textbf{Eq. 7.8}$$

$$[M^{2+}] = K_d \frac{(R - R_{min})}{(R_{max} - R)} \frac{S_{f_2}}{S_{b_2}} \qquad \textbf{Eq. 7.9}$$

$$K_d = \frac{1}{K_a} \qquad \textbf{Eq. 7.10}$$

where: [M^{2+}] is the divalent cation concentration (Mg^{2+}, Ca^{2+} and Zn^{2+}), A_{min} / F_{min} are the integrated fluorescence emission / absorbance of the metal-free sensor, A_{max} / F_{max} is the integrated fluorescence emission / absorbance of the metal-saturated sensor. A / F is the integrated fluorescence emission / absorbance at concentration [M^{2+}]. R_{min} is the ratio of fluorescence excitation / emission of the 'metal-free' sensor, R_{max} is the ratio of the fluorescence excitation / emission of the metal-saturated sensor. R is the ratio at a particular concentration [M^{2+}]. S_{f2} and S_{b2} are the fluorescence intensities with 0 mM [M^{2+}] and saturating amounts of [M^{2+}] respectively.

Errors associated with the K_d values were generated from 2 or more repetitions of the binding experiments, not from the error associated with the fitting of the binding curves. In each binding figure, the number of experimental repetitions is provided.

7.5 Density Functional Theory (DFT)

All computations were carried out with the Gaussian 09 package.[6] The geometries were optimised at the hybrid-DFT B3LYP functional[7] with no symmetry constraints using the 6-311++G(d,p) basis set[8] for all atoms. The Gaussian default polarisation continuum model (IEFPCM)[9] was applied to all calculations using water as solvent. Frequency calculations on these optimised geometries revealed no imaginary frequencies.

7.6 Synthetic Procedures

7.6.1 Di-*tert*-butyl 2,2'-((2-(2-(*tert*-butoxy)-2-oxoethoxy)phenyl)azanediyl) diacetate, (1)[10]

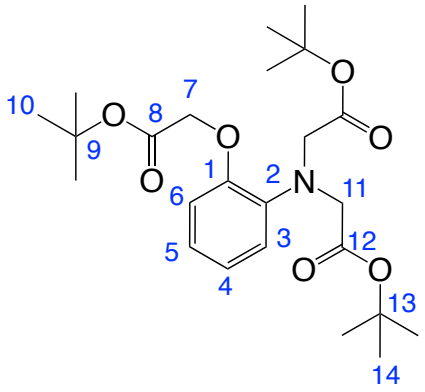

N,N-Diisopropylethylamine (15 mL, 86.1 mmol) and *tert*-butyl bromoacetate (9 mL, 60.9 mmol) were added to a solution of 2-aminophenol (1.56 g, 14.3 mmol) and sodium iodide (2.98 g, 19.9 mmol) in anhydrous acetonitrile (20 mL). The reaction was heated at 85 ^{o}C overnight under an inert atmosphere of argon before the addition of additional *N,N*- diisopropylethylamine (5 mL) and *tert*-butyl bromoacetate (4 mL). The reaction mixture was stirred for a further 3 d, before being cooled to room temperature and diluted with ethyl acetate (10 mL). Inorganic impurities were removed by filtration before the filtrate was washed with brine (10 mL) and water (20 mL). Organic extracts were combined and dried over $MgSO_4$. The solvent was then removed under reduced pressure to form a dark brown residue. Purification by silica gel column chromatography (gradient 100 % hexane to 100 % CH_2Cl_2) formed the title compound as a red oil (3.45 g, 55 %). ^{1}H NMR (400 MHz, $CDCl_3$) 6.91 – 6.85 (3 H, m), 6.80 – 6,77 (1 H, m), 4.56 (2 H, s, H^{7}), 4.08 (4 H, s, H^{11}), 1.47 (9 H, s, H^{10}), 1.44 (18 H, s, H^{14}); ^{13}C NMR (101 MHz, $CDCl_3$) 170.6 (C^{12}), 168.3 (C^{8}), 149.9 (C^{1}), 139.7 (C^{2}), 122.1 (CH), 122.0 (CH), 119.6 (CH), 116.9 (CH), 114 4 (CH), 82.0 (C^{9}), 81.0 (C^{13}), 66.6 (C^{7}), 54.6 (C^{11}), 28.1 (C^{14}), 28.0 (C^{10}); ESI-LRMS $[C_{24}H_{37}NO_7Na]^+$ (+) *m/z* 474.3; ESI-HRMS calcd for $[C_{24}H_{37}NO_7]^+$ 452.2648 found 452.2641.

7.6.2 Diethyl 2,2'-((2-(2-ethoxy-2-oxoethoxy)phenyl)azanediyl)diacetate, (2)[10]

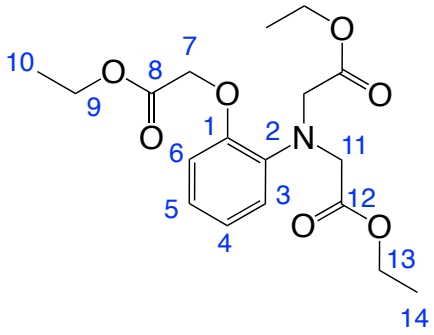

N,N-Diisopropylethylamine (22 mL, 126.3 mmol) and ethyl bromoacetate (10 mL, 90.2 mmol) were added to a solution of 2-aminophenol (2.34 g, 21.4 mmol) and sodium iodide (4.2 g, 28.0 mmol) in anhydrous acetonitrile (20 mL). The reaction was heated at 85 ^{o}C overnight under an inert atmosphere of argon before the addition of *N,N*-diisopropylethylamine (11 mL) and *tert*-butyl bromoacetate (5 mL). The reaction mixture was stirred for a further 3 d, before being cooled to room temperature and diluted with ethyl acetate (10 mL). Inorganic impurities were removed by filtration before the filtrate was washed with brine (10 mL) and water (20 mL). Organic extracts were combined and dried over $MgSO_4$. The solvent was then removed under reduced pressure to form a dark brown residue. Purification by silica gel column chromatography (gradient 100 % hexane to 100 % CH_2Cl_2) formed the title compound as an orange / red oil (4.3 g, 54 %). ^{1}H NMR (400 MHz, $CDCl_3$) 6.96 – 6.89 (3 H, m), 6.83 (1 H, d, *J* 7), 4.68 (2 H, s, H^{7}), 4.29 – 4.15 (10 H, m, H^{9} and H^{11} and H^{13}), 1.32 – 1.24 (18 H, m, H^{10} and H^{14}); ^{13}C NMR (101 MHz, $CDCl_3$) 171.3 (C^{12}), 169.0 (C^{8}), 149.8 (C^{1}), 136.7 (C^{2}), 122.6 (CH), 122.5 (CH), 120.0 (CH), 115.0 (CH), 66.3 (C^{7}), 61.2 (C^{9}, C^{11} or C^{13}), 60.7 (C^{9}, C^{11} or C^{13}), 53.8 (C^{9}, C^{11} or C^{13}), 14.2 (C^{14}), 14.1 (C^{10}); ESI-LRMS $[C_{18}H_{26}NO_7]^+$ (+) *m/z* 368.1; ESI-HRMS calcd for $[C_{18}H_{26}NO_7]^+$ 368.1709 found 368.1704.

7.6.3 {[K.18-crown-6]Br_3}$_n$, (3)[11]

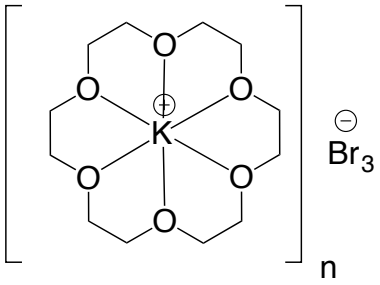

18-crown-6 (6.1 g, 23.2 mmol) was dissolved in ethanol (150 mL). Potassium bromide (4.2 g, 35.0 mmol) was added and the reaction was stirred at room temperature for 1 h. The resulting precipitate formed was isolated by filtration. Bromine (1.2 mL, 23.3 mmol) was added to the filtrate forming a yellow / orange precipitate. The precipitate was collected via filtration and re-crystallised from acetonitrile, to form the title compound as an orange crystalline solid (8.6 g, 80 %). Compound **(3)** was used in substituent steps without any further purification or characterisation.

7.6.4 Di-*tert*-butyl 2,2'-((4-bromo-2- (2-(*tert*-butoxy)-2-oxoethoxy)phenyl) azanediyl) diacetate, (4)[11]

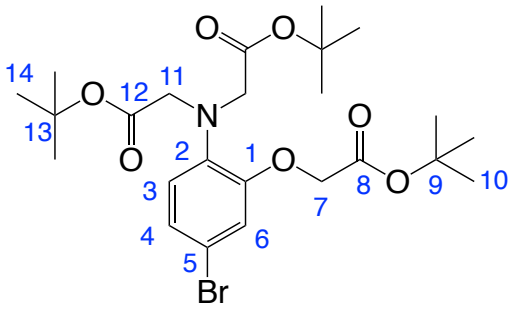

{[K.18-crown-6]Br_3}$_n$ (568.4 mg, 1.05 mmol) was added to a solution of **(1)** (398.7 mg, 0.88 mmol) in anhydrous acetonitrile (6 mL). The reaction was stirred at room temperature for 1 h under an inert atmosphere of argon. Reaction completion was confirmed via ESI mass spectrometry. The solution was diluted with ethyl acetate (10 mL) before being washed with water and dried over $MgSO_4$. The solvent was removed under reduced pressure to form a yellow residue. Purification by silica gel column chromatography (gradient hexane to 4:1 hexane / ethyl acetate) formed the title compound as a pale yellow oil (281 mg, 61 %). ^{1}H NMR (700 MHz, $CDCl_3$) 6.99 (1 H, dd, *J* 2.2, 9, H^4), 6.85 (1 H, d, *J* 2, H^6), 6.72 (1 H, d, *J* 8.6, H^3), 4.51 (2 H, s, H^7), 4.01 (4 H, s, H^{11}), 1.46 (9 H, s, H^{10}), 1.41 (18 H, s, H^{14}), ^{13}C NMR (176 MHz, $CDCl_3$) 170.2 (C^{12}), 167.6 (C^8), 150.3 (C^1), 138.8 (C^2), 124.8 (C^4), 120.7 (C^3), 117.3 (C^6), 113.6 (C^5), 82.4 (C^{13}), 81.2 (C^9), 66.5 (C^7), 54.5 9 (C^{11}), 28.1 (C^{14}), 28.0 (C^{10}); ESI-LRMS $[C_{24}H_{37}{}^{79}BrNO_7]^+$ (+) *m/z* 530.2; ESI-HRMS calcd for $[C_{24}H_{37}{}^{79}BrNO_7]^+$ 530.1755 found 530.1753.

7.6.5 Diethyl 2,2'-((4-bromo-2-(2-ethoxy-2-oxoethoxy)phenyl)azanediyl) diacetate, (5)[11]

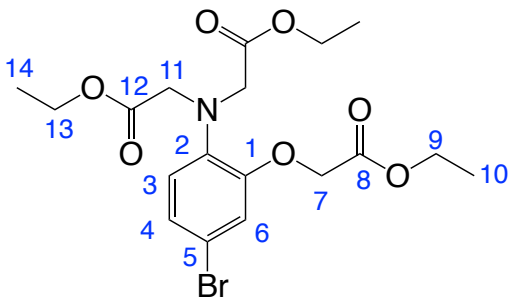

{[K.18-crown-6]Br_3}$_n$ (1.82 g, 3.36 mmol) was added to a solution of **(2)** (1.10 g, 2.99 mmol) in anhydrous acetonitrile (18 mL). The reaction was stirred at room temperature for 1 h under an inert atmosphere of argon. Reaction completion was confirmed via ESI mass spectrometry. The solution was diluted with ethyl acetate (10 mL) before being washed with brine (20 mL) and dried over $MgSO_4$. The solvent was removed under reduced pressure to form a yellow / orange residue. Purification by silica gel column chromatography (gradient hexane to 3:1 hexane / ethyl acetate) formed the title compound as a pale yellow / orange oil (1.04 g, 78 %). R_f (silica, hexane / ethyl acetate (3:1)) = 0.22; ^{1}H NMR (600 MHz, $CDCl_3$) 7.02 (1 H, dd, *J* 2, 9, H^4), 6.91 (1 H, d, *J* 2, H^6), 6.79 (1 H, d, *J* 9, H^3), 4.63 (2 H, s, H^7), 4.25 (2 H, q, *J* 7, H^9), 4.18 – 4.14 (8 H, m, H), 1.29 (3 H, t, *J* 7, H^{10}), 1.24 (6 H, t, *J* 7, H^{14}); ^{13}C NMR (151 MHz, $CDCl_3$) 170.9 (C^{12}), 168.4 (C^8), 150.3 (C^1), 138.8 (C^2), 125.4 (C^4), 121.2 (C^3), 118.0 (C^6), 114.2 (C^5), 66.24 (C^7), 61.33 (C^9), 60.75 (C^{11} or C^{13}), 53.7 (C^{11} or C^{13}), 14.2 (C^{14}), 14.1 (C^{10}); ESI-LRMS $[C_{18}H_{25}{}^{79}BrNO_7]^+$ (+) *m/z* 446.1; ESI-HRMS calcd for $[C_{18}H_{25}{}^{79}BrNO_7]^+$ 446.0814 found 446.0815.

7.6.6 Tert-butyl 2-[(5-bromo-2-hydroxyphenyl)[2-(tert-butoxy)-2-oxoethyl] amino] acetate, (6)

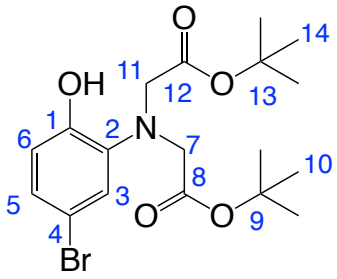

N,N-Diisopropylethylamine (1.04 g, 1.4 mL, 8.04 mmol) and *tert*-butyl bromoacetate (0.67 mL, 4.55 mmol) were added to a solution of 2-amino-4-bromophenol (372.5 mg, 1.98 mmol) and sodium iodide (388.0 mg, 2.6 mmol) in anhydrous acetonitrile (3.6 mL). The reaction was heated at 85 ^{o}C for 21 h under an inert atmosphere of argon, before the reaction mixture was cooled to room temperature and diluted with the addition of ethyl acetate (10 mL). Inorganic impurities were removed by filtration before the filtrate was washed with brine (3 x 10 mL), and water (1 x 10 mL). Organic extracts were combined and dried over $MgSO_4$, and the solvent was removed under reduced pressure to form a brown residue. Purification by silica gel column chromatography (gradient 2:1 CH_2Cl_2 / hexane to 100 % CH_2Cl_2) formed the title compound as a pale brown oil which slowly solidified as a pale brown solid on prolonged standing at room temperature (518 mg, 63 %). R_f (silica, 5:1 (hexane / ethyl acetate) = 0.75; ^{1}H NMR (700 MHz, $CDCl_3$) 6.71 (1 H, dd, *J* 2 and 8, H^5), 6.56 (1 H, d, *J* 2, H^3), 6.50 (1 H, d, *J* 8, H^6), 5.06 (1 H, br s, OH), 4.49 (2 H, s, H^7 or H^{11}), 3.78 (2 H, s, H^7 or H^{11}), 1.47 (9 H, s, H^{10}), 1.47 (9 H, s, H^{14}); ^{13}C NMR (176 MHz, $CDCl_3$) 169.5 (C^8), 167.6 (C^{12}), 144.6 (C^1), 139.0 (C^2), 119.0 (C^5), 114.9 (C^4), 113.1 (C^3), 112.6 (C^6), 82.4 (C^9), 82.0 (C^{13}), 66.5 (C^7 or C^{11}), 46.0 (C^7 or C^{11}) 28.0 (C^{10}), 28.0 (C^{14}); ASAP-LRMS $[C_{18}H_{26}NO_7{}^{79}Br]^+$ (+) *m/z* 416; ASAP-HRMS calcd for $[C_{18}H_{26}NO_7{}^{79}Br]^+$ 416.1073 found 416.1067.

7.6.7 Di-*tert*-butyl2,2'-((5-bromo-2-(2-(*tert*-butoxy)-2-oxoethoxy)phenyl) azanediyl) diacetate, (7)[10]

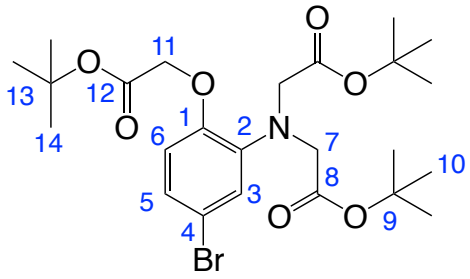

N,N-Diisopropylethylamine (0.43 g, 0.57 mL, 3.27 mmol) and *tert*-butyl bromoacetate (367 µL, 2.49 mmol) were added to a solution of 2-amino-4-bromophenol (146.1 mg, 0.78 mmol) and sodium iodide (155.6 mg, 1.04 mmol) in anhydrous acetonitrile (1.5 mL). The reaction was heated at 85 ^{o}C for 5 d under an inert atmosphere of argon, before the reaction mixture was cooled to room temperature and diluted with the addition of ethyl acetate (10 mL). Inorganic impurities were removed by filtration before the filtrate was washed with brine (3 x 10 mL), and water (1 x 10 mL). Organic extracts were combined and dried over $MgSO_4$, and the solvent was removed under reduced pressure to form a brown residue. Purification by silica gel column chromatography (gradient 2:1 CH_2Cl_2 / hexane to 100 % DCM) formed the title compound as a pale brown oil (121 mg, 29 %). R_f (silica, 100 % CH_2Cl_2) = 0.29; ^{1}H NMR (700 MHz, $CDCl_3$) 6.95 – 6.92 (2 H, m, H^3 and H^5), 6.61 (1 H, d, *J* 8, H^3), 4.49 (2 H, s, H^{11}), 4.03 (4 H, s, H^8), 1.44 (9 H, s, H^{14}), 1.43 (18 H, s, H^{10}); ^{13}C NMR (176 MHz, $CDCl_3$) 170.1 (C^{12}), 167.8 (C^8), 148.8 (C^1), 140.9 (C^2), 124.2 (C^3 or C^5), 122.5 (C^3 or C^5), 115.4 (C^4), 114.4 (C^6), 82.3 (C^{13}), 81.3 (C^9), 66.6 (C^{11}), 54.5 (C^7), 28.1 (C^{10}), 28.0 (C^{14}); ASAP-LRMS $[C_{24}H_{36}NO_7{}^{79}Br]^+$ (+) *m/z* 530.2; ASAP-HRMS calcd for $[C_{24}H_{36}NO_7{}^{79}Br]^+$ 530.1695 found 530.1700.

7.6.8 Diethyl 2,2'-((5-bromo-2-(2-ethoxy-2-oxoethoxy)phenyl)azanediyl) diacetate, (8)[10]

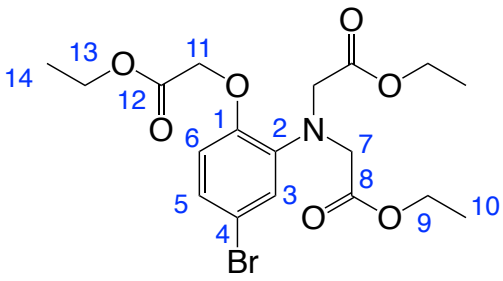

N,N-Diisopropylethylamine (8.9 g, 12 mL, 68.8 mmol) and ethyl bromoacetate (4.79 mL, 43.2 mmol) were added to a solution of 2-amino-4-bromophenol (2.0 g, 10.8 mmol) and sodium iodide (2.3 g, 15.1 mmol) in anhydrous acetonitrile (18 mL). The reaction was heated at 85 ^{o}C for 6 d under an inert atmosphere of argon, before the reaction mixture was cooled to room temperature and diluted with the addition of ethyl acetate (20 mL). Inorganic impurities were removed by filtration before the filtrate was washed with brine (3 x 20 mL), and water (1 x 10 mL). Organic extracts were combined and dried over $MgSO_4$, and the solvent was removed under reduced pressure to form a brown residue. Purification by silica gel column chromatography (gradient 2:1 DCM / hexane to 100 % DCM) formed the title compound as a pale brown oil (1.8 g, 38 %); ^{1}H NMR (700 MHz, $CDCl_3$) 6.99 – 6.97 (2 H, m, H^3 and H^5), 6.66 (1 H, d, *J* 9, H^6), 4.60 (2 H, s, H^{11}), 4.23 (2 H, q, *J* 7, H^{13}), 4.18 (4 H, q, *J* 7, H^9), 4.15 (4 H, s, H^7), 1.28 – 1.24 (9 H, m, H^{10} and H^{14}); ^{13}C NMR (176 MHz, $CDCl_3$) 170.8 (C^8), 168.6 (C^{12}), 148.9 (C^1), 141.0 (C^2), 124.9 (C^3 or C^5), 123.0 (C^3 or C^5), 116.2 (C^6), 115.0 (C^4), 66.3 (C^{11}), 61.3 (C^{13}), 60.8 (C^9), 53.6 (C^7), 14.2 (C^{10}), 14.1 (C^{14}); ESI-LRMS $[C_{18}H_{25}{}^{79}BrNO_7]^+$ (+) *m/z* 446.1; ESI-HRMS calcd for $[C_{18}H_{25}{}^{79}BrNO_7]^+$ 446.0814 found 446.0812.

7.6.9 *Tert*-butyl 2-(6-bromo-2-oxo-2*H*-benzo[*b*][1,4]oxazin-4(3*H*)-yl)acetate, (9)

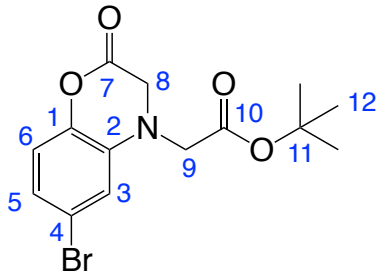

NaH (60 % wt. dispersed in mineral oil, 83.7 mg, 2.1 mmol) was added to a solution of (**6**) (240.3 mg, 0.58 mmol) and *tert*-butyl bromoacetate (0.3 mL, 396 mg, 2.0 mmol) in anhydrous THF (1 mL). The reaction was stirred at 65 ^{o}C for 19 h under an inert atmosphere of argon. The reaction mixture was cooled to room temperature, and filtered through celite to remove inorganic impurities. The solvent was removed under reduced pressure to form a dark brown residue. Purification by silica gel column chromatography (gradient 100 % hexane to 50 / 50, ethyl acetate / hexane) formed the title compound as a pale off-white solid (150 mg, 72 %); ^{1}H NMR (700 MHz, $CDCl_3$) 7.14 (1 H, dd, *J* 9, 2, H^5), 6.90 (1 H, d, *J* 9, H^6), 6.87 (1 H, d, *J* 2, H^3), 4.68 (2 H, s, H^8), 4.55 (2 H, s, H^9), 1.50 (9 H, s, H^{12}); ^{13}C NMR (176 MHz, $CDCl_3$) 166.4 (C^{10}), 164.3 (C^7), 144.2 (C^1), 130.0 (C^2), 126.7 (C^5), 118.5 (C^6), 117.5 (C^3), 114.9 (C^4), 83.1 (C^{10}), 67.3 (C^8), 43.5 (C^9), 27.9 (C^{12}); ESI-LRMS $[C_{14}H_{16}NO_4{}^{79}BrNa]^+$ (+) *m/z* 364.0; ESI-HRMS calcd for $[C_{14}H_{16}NO_4{}^{79}BrNa]^+$ 364.0174 found 364.0172.

7.6.10 Ethyl methylphosphinate, (10)[12]

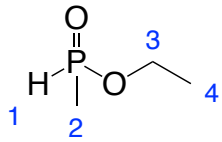

Water (264 μL, 14.7 mmol) was added to diethyl methylphosphinate (2 g, 14.7 mmol) at room temperature. The colourless solution was stirred vigorously for 18 h under an inert atmosphere of argon. Reaction completion was determined by ^{31}P NMR spectroscopy. The title compound formed with one equivalent of ethanol as a by-product and was used *in situ* in subsequent steps without any additional purification. ^{1}H NMR (400 MHz, $CDCl_3$) 7.25 (1 H, dq, *J* 538, 2, H^1), 4.17 – 3.16 (2 H, m, H^3), 1.48 (3 H, dd, *J* 16, 4, H^2), 1.24 (3 H, t, *J* 4, H^4); ^{13}C NMR (101 MHz, $CDCl_3$) 62.38 (d, *J* 24, C^3), 16.24 (d, *J* 24, C^4), 14.62 (d, *J* 97, C^2); ^{31}P NMR (176 MHz, $CDCl_3$) + 33.4; ESI-LRMS $[C_3H_9PO_2]^+$ (+) m/z 109.0; ESI-HRMS cald for $[C_3H_9PO_2]^+$ 109.0419 found, 109.0414

7.6.11 Ethyl (hydroxymethyl)(methyl)phosphinate, (11)

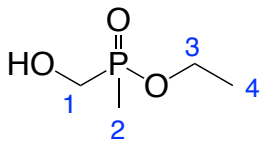

Ethyl methyl phosphinate as its EtOH adduct, (**10**) (14.7 mmol) was heated at 85 ^{o}C in anhydrous THF (5 mL) for 30 min. Paraformaldehyde (707.9 mg, 23.60 mmol) was then added. The reaction mixture was heated at 75 ^{o}C under an inert atmosphere of argon and monitored by ^{31} P NMR. After 5 h the colourless solution was cooled to room temperature before the THF was removed under reduced pressure. The residue was then dissolved in CH_2Cl_2 (20 mL) before the inorganic salts were removed by filtration. The solvent was removed under reduced pressure to form a colourless oil. Purification by silica gel chromatography (gradient from 100 % CH_2Cl_2 to 90 % CH_2Cl_2/ 10 % MeOH) formed the title compound as a pale yellow oil (747 mg, 37 %). R_f = 0.20 (silica, 95 % DCM; 5 % MeOH, visualisation with $KMnO_4$); ^{1}H NMR (400 MHz, $CDCl_3$)

4.13 (2 H, m, H^3), 3.85 (2 H, m, H^1), 3.07 (1H, br s, OH), 1.54 (3 H, d, *J* 12, H^2), 1.35 (3 H, *J* 4, H^4); ^{31}P NMR (176 MHz, $CDCl_3$) + 52.01; ^{13}C NMR (101 MHz, $CDCl_3$) 61.1 (d, *J* 7, C^3), 59.8 (d, *J* 110, C^1), 17.7 (d, *J* 6, C^4), 16.64 (d, *J* 91, C^2); ESI-LRMS $[C_6H_7{}^{79}BrN_2]^+$ (+) *m/z* 139.0; ESI-HRMS calcd for $[C_6H_7{}^{79}BrN_2]^+$ 139.0456 found, 139.0449.

7.6.12 (Ethoxy(methyl)phosphoryl)methyl methanesulfonate, (12)

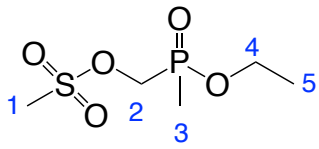

Methylsulfonyl chloride (0.65 mL, 8.4 mmol) was added to an ice cold solution of hydroxymethylmethyl phosphinic acid ethyl ester, (**11**) (808.8 mg, 5.95 mmol) and triethylamine (1.25 mL, 8.96 mmol) in anhydrous THF (5.7 mL). The solution was warmed to room temperature and stirred for an additional 1 h under an inert atmosphere of argon. After 1 h, THF was removed under reduced pressure, the dark orange residue was re-dissolved in CH_2Cl_2 (20 mL) and washed with brine (15 mL). The organic extracts were dried over $MgSO_4$, and the solvent was removed under reduced pressure to form an orange residue. Purification by silica gel column chromatography (gradient 100 % CH_2Cl_2 to 95 % CH_2Cl_2 / 5 % MeOH) formed the title compound as a yellow oil (1.03 g, 82 %). ^{1}H (400 MHz, $CDCl_3$) 4.46 – 4.34 (2 H, m, H^2), 4.25 – 4.11 (2 H, m, H^4), 3.15 (3 H, s, H^1), 1.63 (3 H, d, *J* 16, H^3), 1.39 (3 H, t, *J* 8, H^5); ^{31}P (162 MHz, $CDCl_3$) + 43.7; ^{13}C (101 MHz, $CDCl_3$) 63.0 (d, *J* 106, C^2), 61.6 (d, *J* 7, C^4), 37.8 (s, C^1), 16.5 (d, *J* 6, C^5), 12.6 (d, *J* 100, C^3). ESI-LRMS $[C_5H_{13}O_5PS]^+$ (+) *m/z* 217.3; ESI-HRMS calcd for $[C_5H_{13}O_5PS]^+$ 217.0300 found, 217.0321.

7.6.13 5-Bromo-2-((*tert*-butyldimethylsilyl)oxy)aniline, (13)

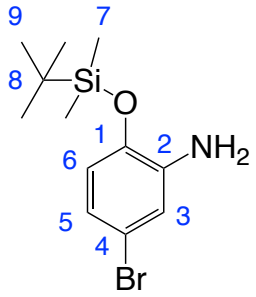

tert-Butyldimethylsilyl trifluoromethanesulfonate (TBDMS triflate) (1.38 g, 1.2 mL, 4.29 mmol) was added to a solution of 2-amino-4-bromophenol (807.3 mg, 4.29 mmol) and imidazole (490.4 mg, 7.20 mmol) in anhydrous DMF (6.5 mL) at 0 ^{o}C. The solution was gradually warmed to warm temperature and stirred at room temperature for 2 h under an inert atmosphere of argon. The reaction was quenched with aqueous ammonium chloride (10 mL, saturated solution) and extracted with ethyl acetate (3 x 20 mL). The organic extracts were combined, washed with brine (20 mL) and water (10 mL) before being dried over potassium carbonate. The solvent was removed under reduced pressure to form a brown residue. Purification by silica gel column chromatography (gradient 100 % hexane to 5:1 hexane / ethyl acetate) formed the title compound as a light red / orange oil (1.09 g, 84 %). R_f (silica, 10:1 hexane/ ethyl acetate) = 0.58; ^{1}H NMR (700 MHz, $CDCl_3$) 6.82 (1 H, d, *J* 2, H^3), 6.70 (1 H, dd, *J* 8, 2, H^6), 6.58 (1 H, d, *J* 8, H^7), 3.74 (2 H, br s, NH_2), 1.0 (9 H, s, H^9), 0.22 (6 H, s, H^8); ^{13}C NMR (176 MHz, $CDCl_3$) 142.0 (C^1), 139.7 (C^2), 120.7 (C^5), 119.8 (C^6), 117.9 (C^3), 113.9 (C^4), 25.8 (C^9), 18.2 (C^8), -4.32 (C^7); ^{29}Si NMR (139 MHz, $CDCl_3$) + 23.0; ESI-LRMS $[C_{12}H_{20}NO^{79}BrSi]^+$ (+) *m/z* 302.4; ESI-HRMS calcd for $[C_{12}H_{20}NO^{79}BrSi]^+$ 302.0576, found 302.0569.

7.6.14 Ethyl (((5-bromo-2-((*tert*-butyldimethylsilyl)oxy)phenyl)amino) methyl)(methyl)phosphinate, (14)

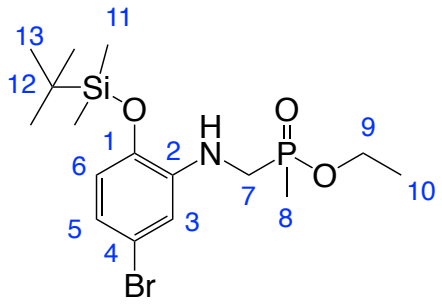

Paraformaldehyde (239.9 mg, 8 mmol) was added to a solution of **13** (406 mg, 1.35 mmol) in anhydrous THF (28 mL). The reaction was stirred at 85 ^{o}C for 10 minutes before the addition of diethyl methylphosphinite (0.72 mL, 0.65 g, 4.80 mmol). The reaction mixture was stirred at 85 ^{o}C for 19 h under an inert atmosphere of argon. The solvent was removed under reduced pressure to form an orange residue which was re-dissolved in CH_2Cl_2 (15 mL). All insoluble inorganics were then removed by filtration. The solvent was removed under reduced pressure to form a brown oil. Purification by alumina column chromatography (gradient 100 % hexane to hexane / ethyl acetate (1:1)) formed the title compound as an orange oil (84.2 mg, 15 %). ^{1}H (700 MHz, $CDCl_3$); 6.72 (1 H, dd, *J* 8, 2, H^5), 6.69 (1 H, d, *J* 2, H^3), 6.58 (1 H, d, *J* 8, H^6), 4.43 (1 H, br s, NH), 4.05 (2 H, m, H^9), 3.37 (2 H, m, H^7), 1.52 (3 H, d, *J* 14, H^8), 1.32 (3 H, t, *J* 7, H^{10}), 1.00 (9 H, s, H^{13}), 0.23 (3 H, s, H^{11} or $H^{11'}$), 0.21 (3 H, s, H^{11} or $H^{11'}$); ^{31}P (283 MHz, $CDCl_3$,) + 49.5; ^{13}C (176 Hz, $CDCl_3$) 142.0 (s, C^1), 140.8 (d, *J* 11, C^2), 120.1 (s, C^5), 118.6 (s, C^6), 114.3 (s, C^4), 113.6 (s, C^3), 60.9 (d, *J* 9, C^9), 42.4 (d, *J* 102, C^7), 25.7 (s, C^{13}), 18.1 (s, C^{12}), 16.6 (d, *J* 6, C^{10}), 13.0 (d, *J* 95, C^8), -4.4 (C^{11} or $C^{11'}$), -4.3 (C^{11} or $C^{11'}$) ; ^{29}Si (139 MHz, $CDCl_3$) + 23.5; ESI-LRMS $[C_{16}H_{29}{}^{79}BrNO_3PSi]^+$ (+) *m/z* 422.4; ESI-HRMS calcd for $[C_{16}H_{29}{}^{79}BrNO_3PSi]^+$ 422.0916 found, 422.0901.

7.6.15 Ethyl (((5-bromo-2-hydroxyphenyl)amino)methyl)(methyl) phosphinate, (15)

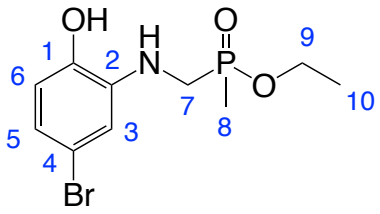

Tetrabutylammonium fluoride (TBAF) (1 M solution in THF, 0.5 mL, 0.5 mmol) was added to an ice cold solution of **14** (173.4 mg, 0.41 mmol) in anhydrous THF (3 mL). The reaction was stirred in ice for 10 minutes, before being stirred at room temperature for 1 h under an inert atmosphere of argon. The reaction was quenched with aqueous ammonium chloride (10 mL saturated solution), extracted with CH_2Cl_2 (3 x 20 mL) and dried with $MgSO_4$. The solvent was removed under reduced pressure to form a dark brown residue. Purification by silica column chromatography (gradient 100 % CH_2Cl_2 to 95 % CH_2Cl_2 / 5 % MeOH) formed the title compound as a pale brown oil (56.0 mg, 65 %). R_f (silica, 95 % CH_2Cl_2 / 5 % MeOH) = 0.24; ^{1}H (700 MHz, $CDCl_3$) 9.70 (1 H, br s, OH), 6.69 (2 H, m, H^5 and H^6), 6.63 (1 H, d, *J* 2, H^3), 4.94 (1 H, br m, NH), 4.17 (2 H, m, H^7), 3.44 (2 H, m, H^9), 1.59 (3 H, d, *J* 14, H^8), 1.34 (3 H, t, *J* 7, H^{10}); ^{31}P (283 MHz, $CDCl_3$) + 52.5; ^{13}C (176 Hz, $CDCl_3$) 144.2 (C^1), 138.0 (d, *J* 12, C^2), 120.5 (C^5 or C^6), 115.2 (C^5 or C^6), 113.1 (C^3), 111.9 (C^4), 62.0 (d, J *7*, C^9), 42.8 (d, *J* 103, C^7), 16.6 (d, *J* 6, C^{10}), 13.2 (d, *J* 95, C^8); ESI-LRMS $[C_{10}H_{15}{}^{79}BrNO_3P]^+$ (+) *m/z* 308.0; ESI-HRMS calcd for $[C_{10}H_{15}{}^{79}BrNO_3P]^+$ 308.0051 found 308.0042.

7.6.16 Ethyl methyl((2-nitrophenoxy)methyl)phosphinate, (16)

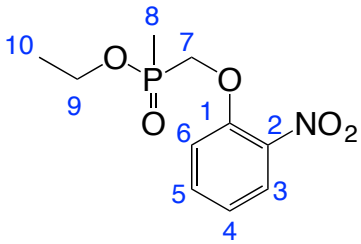

Anhydrous potassium carbonate (302.9 mg, 2.19 mmol) was added to a solution of 2-nitrophenol (98.9 mg, 0.71 mmol) and (ethoxy(methyl)phosphoryl)-

methyl methanesulfonate, (**12**) (228.2 mg, 1.05 mmol) in anhydrous acetonitrile (1.2 mL). The reaction mixture was heated at 85 °C for 48 h under an inert atmosphere of argon. The pale yellow precipitate was removed by filtration and the solvent was removed under reduced pressure to form a yellow residue. Purification by silica gel column chromatography (gradient 100 % CH_2Cl_2 to 95 % CH_2Cl_2 / 5 % MeOH) formed the title product as a pale yellow oil (115.3 mg, 63 %). ^{1}H NMR (600 MHz, $CDCl_3$) 7.88 – 7 85 (1 H, m) 7.58 – 7.54 (1 H, m), 7.13 – 7.09 (2 H, m), 4.39 – 4.26 (4 H, m, H^9 and H^7), 1.69 (3 H, d, *J* 15, H^8), 1.33 (3 H, t, *J* 7, H^{10}); ^{13}C (151 MHz, $CDCl_3$,) 151.8 (d, *J* 13, C^1), 140.1 (C^2), 134.4 (CH), 125.8 (CH), 121.9 (CH), 114.7 (C^3), 61.4 (d, *J* 7, C^9), 65.2 (d, *J* 111, C^7), 16.5 (C^9), 12.2 (C^8); ^{31}P NMR (242 MHz, $CDCl_3$) + 48.5; ESI-LRMS $[C_{10}H_{14}NO_5P]^+$ (+) *m/z* 260.1; ESI-HRMS calcd for $[C_{10}H_{14}NO_5P]^+$ 260.0701 found 260.0699.

7.6.17 Ethyl ((2-aminophenoxy)methyl)(methyl)phosphinate, (17)

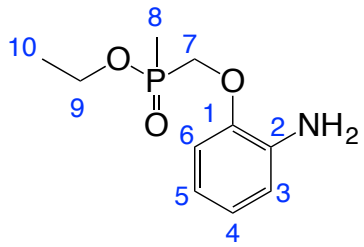

Compound (**16**) (118.1 mg, 0.46 mmol) was dissolved in ethanol (20 mL). Palladium on charcoal (10 wt. %, 51.6 mg, 0.03 mmol) was added and the reaction mixture was stirred at room temperature for 2 h under an atmosphere of hydrogen. After this time, the reaction mixture was filtered through a celite plug. The solvent was removed under reduced pressure to form a pale yellow oil (104 mg, 96 %). Compound (**17**) was used in subsequent steps without any additional purification. ^{1}H NMR (600 MHz, $CDCl_3$) 6.86 – 6.82 (2 H, m, H^3, H^4, H^5 or H^6), 6.74 – 6.70 (2 H, m, H^3, H^4, H^5 or H^6), 4.29 – 4.07 (4 H, m, H^7 and H^9), 1.64 (3 H, d, *J* 14.6, H^8), 1.34 (3 H, t, *J* 7, H^{10}); ^{31}P NMR (162 MHz, $CDCl_3$) + 47.4; ^{13}C (151 MHz, $CDCl_3$) 146.3 (d, *J* 11.9, C^1), 136.4 (C^2), 122.8 (C^3, C^4, C^5 or C^6), 118.5 (C^3, C^4, C^5 or C^6), 115.7 (C^3, C^4, C^5 or C^6), 112.2 (C^3, C^4, C^5 or C^6), 64.6 (d, *J* 111, C^7), 61.0 (d, *J* 7, C^9), 16.6 (s, C^{10}), 12.6 (d, *J* 98, C^8); ESI-LRMS

$[C_{10}H_{16}NO_3P]^+$ (+) *m/z* 230.6; ESI-HRMS calcd for $[C_{10}H_{16}NO_3P]^+$ 230.0946 found 230.0949.

7.6.18 Diethyl 2,2'-((2-((ethoxy(methyl)phosphoryl)methoxy)phenyl) azanediyl) diacetate, (18)

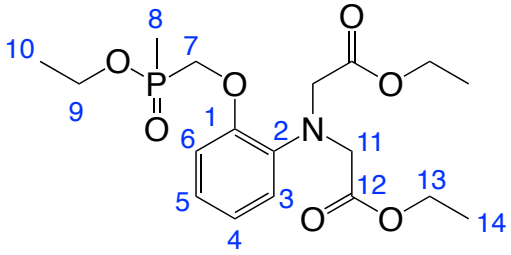

N,N-Diisopropylamine (410 μL, 2.36 mmol) and ethyl bromoacetate (158 μL, 1.42 mmol) were added to a solution of (**17**) (107.5 mg, 0.46 mmol) and sodium iodide (125.6 mg, 0.97 mmol) in anhydrous acetonitrile. The reaction was heated for 2 d at 85 °C under an inert atmosphere of argon before the addition of further *N,N*-diisopropylamine (120 μL, 0.69 mmol) and ethyl bromoacetate (50 μL, 0.45 mmol). The reaction mixture was stirred at 85 °C for a further 2 d, before being cooled and diluted with ethyl acetate (10 mL). Inorganic impurities were removed by filtration before the organic filtrate was washed with water (10 mL) and brine (10 mL). Organic extracts were combined and dried over $MgSO_4$, and the solvent was removed under reduced pressure to form a pale brown residue. Purification by silica gel column chromatography (gradient 1:1 hexane / ethyl acetate to 100 % ethyl acetate) formed the title compound as a pale brown oil (97.3 mg, 53 %). ^{1}H NMR (700 MHz, $CDCl_3$) 6.95 – 6.93 (3 H, m, H^3, H^4, H^5 or H^6), 6.90 – 6.88 (1 H, m, H^3, H^4, H^5 or H^6), 4.32 – 4.05 (14 H, m, H^7, H^9, H^{11} and H^{13}), 1.66 (3 H, d, *J* 15, H^8), 1.33 (3 H, t, *J* 7, H^{10}), 1.23 (6 H, t, *J* 7, H^{14}); ^{31}P NMR (283 MHz, $CDCl_3$) + 48.3; ^{13}C NMR (176 MHz, $CDCl_3$,) 170.9 (s, C^{12}), 150.9 (d, *J* 11, C^1), 139.4 (s, C^2), 122.9 (s, C^3, C^4, C^5 or C^6), 122.7 (s, C^3, C^4, C^5 or C^6), 120.8 (s, C^3, C^4, C^5 or C^6), 117.4 (s, C^3, C^4, C^5 or C^6), 64.8 (d, *J* 6, C^7 or C^9), 60.9 (d, *J* 7, C^7 or C^9), 60.7 (s, C^{11} or C^{13}), 53.2 (s, C^{11} or C^{13}), 16.5 (d, *J* 6, C^{10}), 14.2 (s, C^{14}), 12.5 (d, *J* 97, C^8); ESI-LRMS $[C_{18}H_{29}NO_7P]^+$ (+) *m/z* 402.6; ESI-HRMS

calcd for $[C_{18}H_{29}NO_7P]^+$ 402.1682 found 402.1694; Reverse phase HPLC (0 % - 100 % - 0% CH_3CN in ammonium bicarbonate buffer (25 mM), t_R = 9.6 min).

7.6.19 Diethyl 2,2'-((4-bromo-2-((ethoxy(methyl) phosphoryl)methoxy) phenyl) azanediyl)diacetate, (19)

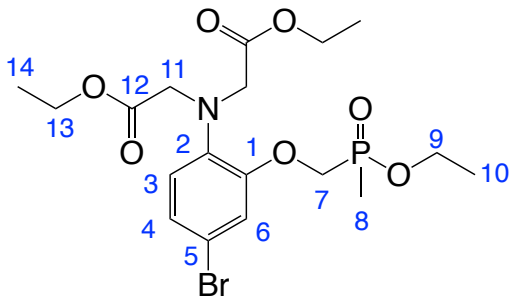

$\{[K.18\text{-crown-}6]Br_3\}_n$ (132.3 mg, 0.24 mmol) was added to a solution of ethyl-2-[(2-ethoxy-2-oxoethyl)(2-{[methoxy(methyl)phosphoryl] methoxy} phenyl) amino]acetate, **(18)** (82.5 mg, 0.21 mmol) in anhydrous acetonitrile (1.2 mL). The reaction was stirred at room temperature for 1 h under an inert atmosphere of argon. Reaction completion was confirmed via ESI mass spectrometry. The solution was diluted with ethyl acetate (10 mL) before being washed with water (10 mL) and dried over $MgSO_4$. The solvent was removed under reduced pressure to form a dark yellow / brown oil. Purification by silica gel column chromatography (gradient 100 % hexane to 100 % ethyl acetate) formed the title compound as a colourless oil. (101 mg, 82 %). ^{1}H NMR (700 MHz, $CDCl_3$) 7.05 (1 H, dd, *J* 9, 2, H^4), 7.00 (1 H, d, *J* 2, H^6), 6.81 (1 H, d, *J* 9, H^3), 4.28 – 4.06 (12 H, m, H^7, H^9, H^{11}, H^{13}), 1.64 (3 H, d, *J* 15, H^8), 1.33 (3 H, t, *J* 7, H^{10}), 1.23 (6 H, t, *J* 7, H^{14}); ^{31}P NMR (283 MHz, $CDCl_3$) + 47.2; ^{13}C NMR (176 MHz, $CDCl_3$) 170.6 (s, C^{12}), 151.4 (d, *J* 12, C^1), 138.6 (s, C^2), 125.5 (s, C^4), 122.0 (s, C^3), 117.7 (s, C^6), 114.7 (s, C^5), 65.1 (d, *J* 110, C^7), 61.0 (d, *J* 7, C^9), 60.8 (s, C^{11} or C^{13}), 53.2 (s, C^{11} or C^{13}), 16.5 (d, *J* 6, C^{10}), 14.1 (s, C^{14}), 12.5 (d, *J* 98, C^8); ESI-LRMS $[C_{18}H_{28}{}^{79}BrNO_7P]^+$ (+) *m/z* 480.1; ESI-HRMS calcd for $[C_{18}H_{28}{}^{79}BrNO_7P]^+$ 480.0787 found 480.0778.

7.6.20 (2-Nitrophenoxy)- acetic acid *tert*- butyl ester, (20)[13]

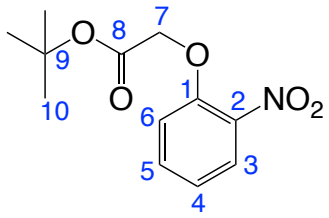

2-Nitrophenol (544.6 mg, 3.91 mmol) in anhydrous THF (3 mL) was added to a solution of NaH (60 % wt. dispersion in mineral oil, 380 mg, 9.54 mmol) in anhydrous THF (3 mL). The reaction mixture turned orange during the addition and was stirred at room temperature for 30 mins. *tert*-Butyl bromacetate (1.3 mL, 8.80 mmol) was then added and the reaction mixture was heated at reflux under an inert atmosphere of argon for a further 24 h, with the reaction turning an off-white colour. The precipitate was removed by filtration, the organic layer was washed with saturated aqueous $NaHCO_3$ solution (10 mL), HCl (1 M, 10 mL) and brine (10 mL), and dried over $MgSO_4$. The solvent was removed under reduced pressure to form a yellow oil. Purification by silica gel column chromatography (gradient hexane to 4:1 hexane / ethyl acetate) formed the title compound as a yellow oil (842 mg, 85 %). ^{1}H NMR (700 MHz, $CDCl_3$) 7.86 (1 H, dd, *J* 8, 2, H^3), 7.50 (1 H, td, *J* 10, 8, 2, H^4), 7.07 (1 H, td, *J* 9, 7, 1, H^5), 6.96 (1 H, dd, *J* 8, 1, H^6), 4.66 (2 H, s, H^7), 1.45 (9 H, s, H^{10}); ^{13}C NMR (176 MHz, $CDCl_3$) 166.7 (C^8), 151.4 (C^1), 140.3 (C^2), 133.8 (C^3), 125.8 (C^4), 121.4 (C^5), 114.8 (C^6), 83.0 (C^9), 66.7 (C^7), 28.0 (C^{10}); ESI-LRMS $[C_{12}H_{15}NO_5Na]^+$ (+) *m/z* 276.1; ESI-HRMS calcd for $[C_{12}H_{15}NO_5Na]^+$ 276.0848 found 276.0865.

7.6.21 *Tert*-butyl 2-(2-aminophenoxy)acetate, (21)

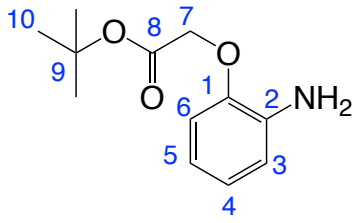

(2-Nitrophenoxy)-acetic acid *tert*-butyl ester, (**20**) (276.9 mg, 1.1 mmol) was dissolved in ethanol (20 mL). Palladium on charcoal (10 wt. %, 65.1 mg, 0.06 mmol) was added and the reaction mixture was stirred at room temperature for 5 h under an atmosphere of hydrogen. After this time, the reaction mixture was filtered through a celite plug. The solvent was removed under reduced pressure to form a pale brown oil (104 mg, 96 %). Compound (**21**) was used in subsequent steps without any further purification. ^{1}H NMR (400 MHz, $CDCl_3$) 6.87 – 6.82 (1 H, m), 6.77 – 6.67 (3 H, m), 4.55 (2 H, s, H^7), 1.51 (9 H, s, H^{10}).

7.6.22 Ethyl 2-((4-bromo-2-iodophenyl)amino)acetate, (22)

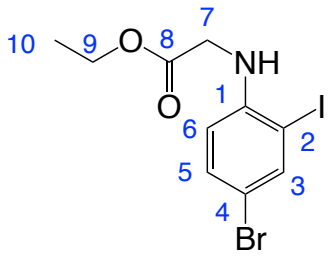

N,N-Diisopropylethylamine (0.96 g, 1.3 mL, 7.50 mmol) and ethyl bromoacetate (600 µL, 5.40 mmol) were added to a solution of 4-bromo-2-iodophenol (641.4 mg, 2.15 mmol) and sodium iodide (130.2 mg, 2.87 mmol) in anhydrous acetonitrile (3.8 mL). The reaction was heated at 85 ^{o}C for 24 h under an inert atmosphere of nitrogen, before additional *N,N*-diisopropylethylamine (1.2 mL, 6.89 mmol) and ethyl bromoacetate (470µL, 4.24 mmol) were added. The reaction mixture was stirred for a further 40 h at 85 ^{o}C. After cooling to room temperature the brown reaction mixture was diluted with ethyl acetate (15 mL), filtered through celite, and washed with water (10 mL) and brine (10 mL). Organic extracts were combined and dried over $MgSO_4$, and the solvent was removed

under reduced pressure to form a brown residue. Purification by silica gel column chromatography (gradient 100 % hexane to 80 % hexane / 20 % ethyl acetate) formed the title compound as an off white solid (565 mg, 68 %). R_f (80 % hexane / 20 % ethyl acetate) = 0.72; m.p. 77 -78 °C; ^{1}H (700 MHz, $CDCl_3$) 7.77 (1 H, d, *J* 2, H^3), 7.29 (1 H, dd, *J* 9, 2, H^5), 6.29 (1 H, d, *J* 9, H^6), 4.86 (1 H, br t, *J* 5, -NH), 4.26 (2 H, q, *J* 7, H^9), 3.89 (2 H, d, *J* 5, H^7), 1.30 (3 H, t, *J* 7, H^{10}); ^{13}C (176 MHz, $CDCl_3$) 170.0 (C^8), 145.4 (C^1), 140.6 (C^3), 132.1 (C^5), 111.4 (C^4), 109.6 (C^6), 85.3 (C^2), 61.6 (C^7), 46.0 (C^9), 14.1 (C^{10}); ESI-LRMS $[C_{10}H_{11}NI^{79}Br]^+$ (+) *m/z* 384.1; ESI-HRMS calcd for $[C_{10}H_{11}NI^{79}Br]^+$ 383.9096 found, 383.9099.

7.6.23 Ethyl 2-((4-bromo-2-(ethoxy(methyl)phosphoryl)phenyl)amino) acetate, (23)

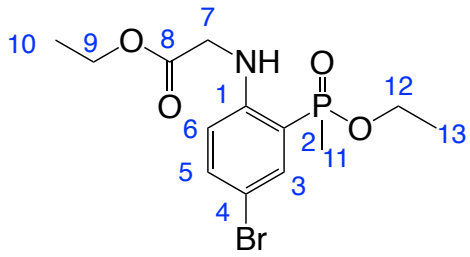

Ethyl 2-((4-bromo-2-iodophenyl)amino)acetate, (**22**) (390.2 mg, 1.02 mmol), ethyl methyl phosphinate (**10**) (as its EtOH adduct, 200.8 mg, 1.30 mmol) and triethylamine (0.58 mL, 4.16 mmol) were added to dry toluene (degassed by three freeze-pump-thaw cycles). The solution was degassed by a further three cycles before the addition of $Pd(dppf)Cl_2.CH_2Cl_2$ (19.2 mg, 0.024 mmol). The reaction mixture was stirred at 118 °C under an inert atmosphere of argon for 22 h. After cooling to room temperature the solvent was removed under reduced pressure to form a dark brown residue. Purification by silica gel column chromatography (gradient 100 % hexane to 1:1 ethyl acetate / hexane) formed the title compound as a yellow oil (137 mg, 39 %). R_f (silica, 1:1 ethyl acetate / hexane) = 0.52; ^{1}H (600 MHz, $CDCl_3$) 7.50 (1 H, br s, NH), 7.43 (1 H, dd, *J* 12, 2, H^3), 7.38 (1 H, dd, *J* 8, 2, H^5), 6.38 (1 H, dd, *J* 8, 6, H^6), 4.21 (2 H, q, *J* 7, H^9), 4.13 (2 H, m, H^{12}), 3.89 (2 H, br s, H^7), 1.66 (3 H, t, *J* 15, H^{11}), 1.32 (3 H, t, *J* 7, H^{13}), 1.25 (3 H, t, *J* 8, H^{10}); ^{13}C (151 MHz, $CDCl_3$) 170.1 (s, C^8), 150.1 (d, *J* 7, C^1), 136.5 (d, *J* 2, C^5), 134.8 (d, *J* 10, C^3), 114.1 (d, *J* 122, C^2),

113.7 (s, C), 112.9 (d, *J* 10, C^6), 108.0 (d, *J* 15, C^4), 61.3 (s, C^9), 60.9 (d, *J* 7, C^{12}), 45.1 (s, C^7), 16.4 (d, *J* 7, C^{13}), 16.3 (d, *J* 106, C^{11}), 14.2 (s, C^{10}); ^{31}P (243 MHz, $CDCl_3$) + 45.6; ESI-LRMS $[C_{13}H_{19}{}^{79}BrNO_4P]^+$ (+) *m/z* 364.5; ESI-HRMS calcd for $[C_{13}H_{19}{}^{79}BrNO_4P]^+$ 364.0313 found, 364.0320.

7.6.24 2,2'-((2-((Hydroxy(methyl)phosphoryl)methoxy)phenyl)azanediyl) diacetic acid (APDAP), (24)

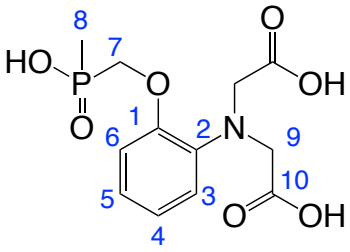

Diethyl-2,2'-((2-((ethoxy(methyl)phosphoryl)methoxy)phenyl)azanediyl) diacetate, **(18)** (82.6 mg, 0.21 mmol) was dissolved in CD_3OD (4 mL) and NaOD (0.4 M in D_2O, 1.4 mL). The pale yellow solution was stirred under an inert atmosphere of argon at room temperature for 20 h. Hydrolysis of the ethyl esters was monitored by ^{1}H NMR spectrometry, ^{31}P NMR spectrometry and ESI-LRMS. The solution was lyophilized to form the title compound as an off-white solid in a quantitative yield (62 mg, 93 %), without any further purification. ^{1}H NMR (600 MHz, D_2O) 6.95 (1 H, dd, *J* 1.8, 8, H^6), 6.83 (2 H, m, H^4 and H^5), 6.78 (1 H, br m, H^3), 3.93 (2 H, d, *J* 9, H^7), 3.71 (4 H, s, H^9), 1.29 (3 H, d, *J* 14, H^8); ^{31}P NMR (283 MHz, D_2O) + 36.54; ^{13}C NMR (176 MHz, D_2O) 179.1 (C^{10}), 150.6 (C^1) 139.4 (C^2), 121.6 (C^4 or C^5), 118.5 (C^4 or C^5), 118.1 (C^3), 113.4 (C^6), 56.5 (C^9), 14.2 (d, J 95, C^8); Reverse phase HPLC (0 % - 100 % - 0% CH_3CN in ammonium bicarbonate buffer (25 mM), t_R = 1.2 min).

7.6.25 Diethyl 2,2'-((2-(2-ethoxy-2-oxoethoxy)-4-((triisopropylsilyl)ethynyl) phenyl)azanediyl)diacetate, (25)

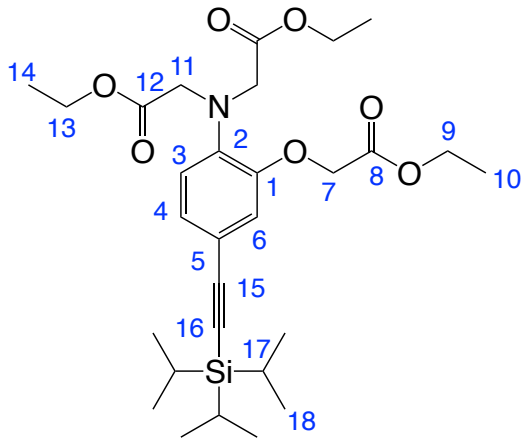

Compound (**5**) (816.0 mg, 1.83mmol) was dissolved in anhydrous THF (6 mL) and the solution was degassed via three freeze-pump-thaw cycles. (Triisopropylsilyl)acetylene (2.2 mL, 9.8 mmol), triethylamine (2.0 mL, 14.3 mmol), $Pd(dppf)Cl_2$ (147.0 mg, 0.2 mmol) and copper iodide (135.9 mg, 0.72 mmol) were added, and the solution was degassed via a further three freeze-pump-thaw cycles. The solution was stirred at 65 ^{o}C for 3 d under an inert atmosphere of argon. Reaction completion was determined by ESI mass spectrometry. The solvent was removed under reduced pressure to form a dark brown residue. Purification by silica gel column chromatography (gradient hexane to 4:1 hexane / ethyl acetate) formed the title compound as a pale yellow / orange oil which slowly solidified to an off white solid (836 g, 92 %). m.p = 69 ^{o}C – 71 ^{o}C; ^{1}H NMR (600 MHz, $CDCl_3$) 7.06 (1 H, dd, *J* 8, 2, H^4), 6.87 (1 H, d, *J* 2, H^6), 6.77 (1 H, d, *J* 8, H^3), 4.62 (2 H, s, H^7), 4.26 (2 H, q, *J* 7, H^9), 4.19 – 4.15 (8 H, m, H^{11} and H^{13}), 1.29 (3 H, t, *J* 7, H^{10}), 1.25 (6 H, t, *J* 7, H^{14}), 1.10 (21 H, br s, H^{17} and H^{18}); ^{13}C NMR (151 MHz, $CDCl_3$) 171.0 (C^{12}), 168.6 (C^8), 148.8 (C^1), 140.1 (C^2), 126.9 (C^4), 119.1 (C^3), 118.0 (C^6), 116.9 (C^5), 106.9 (C^{15}), 89.3 (C^{16}), 66.3 (C^7), 61.2 (C^{13}), 60.8 (C^9), 53.7 (C^{11}), 18.7 (C^{18}), 14.2 (C^{14}), 14.1 (C^{10}), 11.3 (C^{17}); ESI-LRMS $[C_{29}H_{46}NO_7Si]^+$ (+) *m/z* 548.3; ESI-HRMS calcd for $[C_{29}H_{46}NO_7Si]^+$ 548.3047 found 548.3044.

7.6.26 Diethyl 2,2'-((2-(2-ethoxy-2-oxoethoxy)-5-((triisopropylsilyl)ethynyl) phenyl)azanediyl)diacetate, (26)

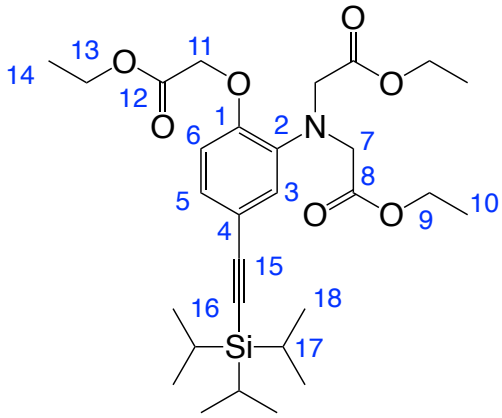

Compound (**8**) (800.8 mg, 1.8 mmol) was dissolved in anhydrous THF (6 mL) and the solution was degassed via three freeze-pump-thaw cycles. (Triisopropylsilyl)acetylene (2.0 mL, 8.9 mmol), triethylamine (1.8 mL, 12.9 mmol), $Pd(dppf)Cl_2$ (142.5 mg, 0.19 mmol) and copper iodide (135.9 mg, 0.72 mmol) were added, and the solution was degassed via a further three freeze-pump-thaw cycles. The solution was stirred at 65 ^{o}C for 3 d under an inert atmosphere of argon. Reaction completion was determined by ESI mass spectrometry. The solvent was removed under reduced pressure to form a dark brown residue. Purification by silica gel column chromatography (gradient hexane to 4:1 hexane / ethyl acetate) formed the title compound as a pale yellow oil which solidified overnight to an off white solid upon standing at room temperature (924 mg, 94 %). m.p = 64 ^{o}C – 66 ^{o}C; ^{1}H NMR (700 MHz, $CDCl_3$) 7.03 (1 H, dd, *J* 8, 2, H^5), 6.97 (1 H, d, *J* 2, H^3), 6.68 (1 H, d, *J* 8, H^6), 4.63 (2 H, s, H^{11}), 4.23 (2 H, q, *J* 7, H^{13}), 4.19 – 4.16 (8 H, m, H^7 and H^9), 1.28 – 1.24 (9 H, m, H^{10} and H^{14}), 1.09 (21 H, br s, H^{17} and H^{18}); ^{13}C NMR (176 MHz, $CDCl_3$) 171.1 (C^8), 168.5 (C^{12}), 150.1 (C^1), 139.3 (C^2), 126.6 (C^5), 123.6 (C^3), 117.6 (C^4), 114.1 (C^6), 107.0 (C^{15}), 88.9 (C^{16}), 66.0 (C^{11}), 61.3 (C^{13}), 60.7 (C^7 or C^9), 53.6 (C^7 or C^9), 18.6 (C^{18}), 14.2 (C^{10}), 14.1 (C^{14}), 11.3 (C^{17}); ESI-LRMS $[C_{29}H_{46}NO_7Si]^+$ (+) *m/z* 548.3; ESI-HRMS calcd for $[C_{29}H_{46}NO_7Si]^+$ 548.3044 found 548.3041.

7.6.27 Ethyl 2-({2-[(dimethyl phosphoryl)methoxy]-4-{2-[tris(propan-2-yl)silyl]ethynyl}phenyl}(2-ethoxy-2-oxoethyl)amino)acetate, (27)

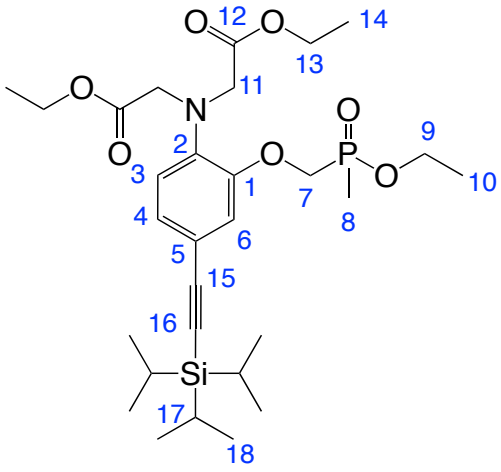

Compound (**19**) (273.9 mg, 0.57 mmol) was dissolved in anhydrous THF (1.8 mL) and the solution was degassed via three freeze-pump-thaw cycles. (Triisopropylsilyl)acetylene (0.64 mL, 2.85 mmol), triethylamine (0.56 mL, 4.02 mmol), Pd(dppf)Cl_2 (56.7 mg, 0.08 mmol) and copper iodide (22.0 mg, 0.1 mmol) were added, and the solution was degassed via a further three freeze-pump-thaw cycles. The solution was stirred at 65 ^{o}C for 6 d under an inert atmosphere of argon, reaction completion was determined by ESI mass spectrometry. The solvent was removed under reduced pressure to form a dark brown residue. Purification by silica gel column chromatography (gradient 100 % CH_2Cl_2 to 95 % CH_2Cl_2 / 5 % MeOH) formed the title compound as a pale brown oil (270.9 mg, 86 %). R_f (silica, 95 % CH_2Cl_2 / 5 % MeOH) = 0.54; ^{1}H NMR (600 MHz, $CDCl_3$) 7.08 (1 H, dd, *J* 9, 2, H^4), 6.97 (1 H, d, *J* 2, H^6), 6.81 (1 H, d, *J* 9, H^3), 4.31 – 4.07 (12 H, m, H^7, H^9, H^{11} and H^{13}), 1.65 (3 H, d, *J* 15, H^8), 1.36 (3 H, t, *J* 7, H^{10}), 1.25 (6 H, t, *J* 7, H^{14}), 1.13 (3 H, br m, H^{17}), 1.11 (18 H, s, H^{18}); ^{31}P NMR (243 MHz, $CDCl_3$) + 47.5; ^{13}C NMR (151 MHz, $CDCl_3$) 170.7 (s, C^{12}), 149.9 (s, C^1), 139.8 (s, C^2), 126.8 (s, C^4), 119.9 (s, C^3), 117.5 (s, C^6), 117.4 (s, C^5), 106.6 (s, C^{15}), 89.8 (s, C^{16}), 65.3 (d, *J* 111, C^7), 60.9 (d, *J* 7, C^9), 60.8 (s, C^{11} or C^{13}), 53.3 (s, C^{11} or C^{13}), 18.7 (s, C^{18}), 16.5 (d, *J* 6, C^{10}), 14.2 (s, C^{14}), 12.6 (d, *J* 98, C^8) 11.3 (s, C^{17}); ESI-LRMS $[C_{29}H_{49}NO_7PSi]^+$ (+) *m/z* 582.3; ESI-HRMS calcd for $[C_{29}H_{49}NO_7PSi]^+$ 582.3007 found 582.3016.

7.6.28 Ethyl 2-((2-(ethoxy(methyl)phosphoryl)-4-((triisopropylsilyl)ethynyl) phenyl)amino)acetate, (28)

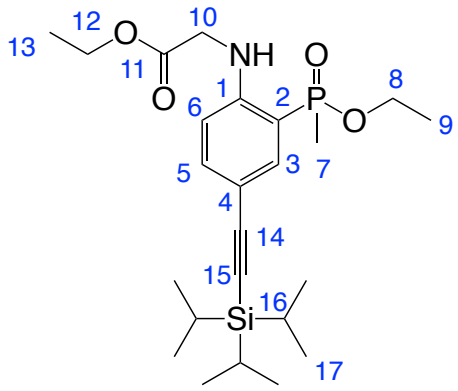

Compound (**23**) (757.0 mg, 2.09 mmol) was dissolved in anhydrous THF (7 mL) and the solution was degassed via three freeze-pump-thaw cycles. (Triisopropylsilyl)acetylene (2.4 mL, 10.7 mmol), triethylamine (2.2 mL, 15.8 mmol), Pd(dppf)Cl_2 (157.3 mg, 0.21 mmol) and copper iodide (116.3 mg, 0.61 mmol) were added, and the solution was degassed via a further three freeze-pump-thaw cycles. The solution was stirred at 65 ^{o}C for 3 d under an inert atmosphere of argon. Reaction completion was determined by ESI mass spectrometry. The solvent was removed under reduced pressure to form a dark brown residue. Purification by silica gel column chromatography (gradient 100 % hexane to 100 % ethyl acetate 4:1) formed the title compound as a pale brown oil which slowly solidified to a pale brown solid overnight (747 mg, 77 %). m.p = 82 ^{o}C – 83 ^{o}C; ^{1}H NMR (600 MHz, $CDCl_3$) 7.71 (1 H, br s, NH), 7.47 (1 H, dd, *J* 14, 2, H^3), 7.42 (1 H, dd, *J* 9, 2, H^5), 6.40 (1 H, dd, *J* 9, 6, H^6), 4.21 (2 H, q, *J* 7, H^{12}), 4.16 – 3.87 (4 H, m, H^8 and H^{10}), 1.68 (3 H, d, *J* 15, H^7), 1.32 (3 H, t, *J* 7, H^9), 1.26 (3 H, t, *J* 7, H^{13}), 1.10 (21 H, s, H^{16} and H^{17}); ^{31}P NMR (243 MHz, $CDCl_3$) + 46.6; ^{13}C NMR (151 MHz, $CDCl_3$) 170.1 (s, C^{11}), 150.8 (d, *J* 7, C^1), 137.6 (d, *J* 2, C^5), 136.5 (d, *J* 10, C^3), 113.4 (d, *J* 123, C^2), 111.3 (d, *J* 14, C^4), 110.7 (d, *J* 10, C^6), 61.3 (s, C^{12}),106.8 (s, C^{14}), 88.5 (s, C^{15}) 60.9 (d, *J*, 6, C^8), 45.0 (s, C^{10}), 18.7 (s, C^{17}), 16.5 (d, *J* 105, C^7), 16.3 (d, *J* 7, C^9), 14.2 (s, C^{13}), 11.3 (s, C^{16}); ESI-LRMS $[C_{24}H_{41}NO_4PSi]^+$ (+) *m/z* 466.2; ESI-HRMS calcd for $[C_{24}H_{41}NO_4PSi]^+$ 466.2543 found 466.2535.

7.6.29 Di-*tert*-butyl 2,2'-((2-(2-(*tert*-butoxy)-2-oxoethoxy)-5-((triisopropyl silyl)ethynyl)phenyl)azanediyl)diacetate, (29)

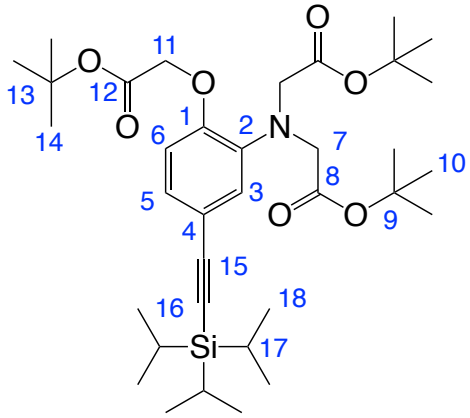

Compound (**7**) (243.7 mg, 0.46 mmol) was dissolved in anhydrous THF (1.5 mL) and the solution was degassed via three freeze-pump-thaw cycles. (Triisopropylsilyl)acetylene (0.2 mL, 0.89 mmol), triethylamine (0.35 mL, 2.5 mmol), Pd(dppf)Cl_2 (37.2 mg, 0.05 mmol) and copper iodide (21.1 mg, 0.11 mmol) were added, and the solution was degassed via a further three freeze-pump-thaw cycles. The solution was stirred at 65 ^{o}C for 5 d under an inert atmosphere of argon. Reaction completion was determined by ESI mass spectrometry. The solvent was removed under reduced pressure to form a dark brown residue. Purification by silica gel column chromatography (gradient hexane to 9:1 hexane / ethyl acetate) formed the title compound as a pale yellow oil (222 mg, 86 %). ^{1}H NMR (700 MHz, $CDCl_3$) 7.00 (1 H, dd, *J* 8, 2, H^5), 6.91 (1 H, d, *J* 2, H^3), 6.63 (1 H, d, *J* 8, H^6), 4.52 (2 H, s, H^{11}), 4.04 (4 H, s, H^7), 1.45 (9 H, s, H^{14}), 1.44 (18 H, s, H^{10}), 1.09 (21 H, br s, H^{17} and H^{18}); ^{13}C NMR (176 MHz, $CDCl_3$) 170.4 (C^{12}), 167.8 (C^8), 150.0 (C^1), 139.2 (C^2), 125.9 (C^5), 123.0 (C^3), 117.0 (C^4), 113.2 (C^6), 107.2 (C^{15}), 98.3 (C^{16}), 82.3 (C^{13}), 81.2 (C^{14}), 66.2 (C^{11}), 54.5 (C^7), 28.0 (C^{14}), 28.1 (C^{10}), 18.65 (C^{18}), 11.3 (C^{17}); ASAP-LRMS $[C_{35}H_{58}NO_7Si]^+$ (+) *m/z* 632.4; ASAP-HRMS calcd for $[C_{35}H_{58}NO_7Si]^+$ 632.3983 found 632.3983.

7.6.30 Di-*tert*-butyl 2,2'-((2-(2-(*tert*-butoxy)-2-oxoethoxy)-5-ethynylphenyl) azanediyl)diacetate, (30)

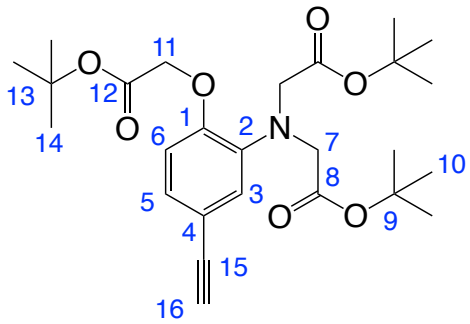

Tetrabutylammonium fluoride (TBAF, 1 M solution in THF, 0.3 mL, 0.3 mmol) was added to an ice cold solution of (**29**) in anhydrous THF (1 mL). The reaction was stirred in ice for 20 mins, before being stirred at room temperature for 1 h under an inert atmosphere of argon. The solvent was removed under reduced pressure to form a brown residue, Purification by silica gel column chromatography (gradient hexane to 4:1 hexane / ethyl acetate) formed the title compound as a colourless oil (40.2 mg, 51 %). ^{1}H NMR (600 MHz, $CDCl_3$) 7.02 (1 H, dd, *J* 8, 2, H^5), 6.97 (1 H, d, *J* 2, H^3), 6.65 (1 H, d, *J* 8, H^3), 4.54 (2 H, s, H^{11}), 4.04 (4 H, s, H^7), 2.94 (1 H, s, H^{16}), 1.45 (9 H, s, H^{14}), 1.44 (18 H, s, H^{10}); ^{13}C NMR (151 MHz, $CDCl_3$) 170.3 (C^{12}), 167.7 (C^8), 150.3 (C^1), 139.3 (C^2), 126.0 (C^5), 123.3 (C^3), 115.4 (C^4), 113.2 (C^6), 83.8 (C^{16}), 82.3 (C^9), 81.4 (C^{15}), 81.2 (C^{13}), 66.2 (C^{11}), 54.5 (C^7), 28.1 (C^{10}), 28.0 (C^{14}); ASAP-LRMS $[C_{26}H_{38}NO_7]^+$ (+) *m/z* 530; ASAP-HRMS calcd for $[C_{26}H_{38}NO_7]^+$ 476.2648 found 476.2648.

7.6.31 Diethyl 2,2'-((2-(2-ethoxy-2-oxoethoxy)-4-(naphthalen-1-ylethynyl) phenyl)azanediyl)diacetate, (31)

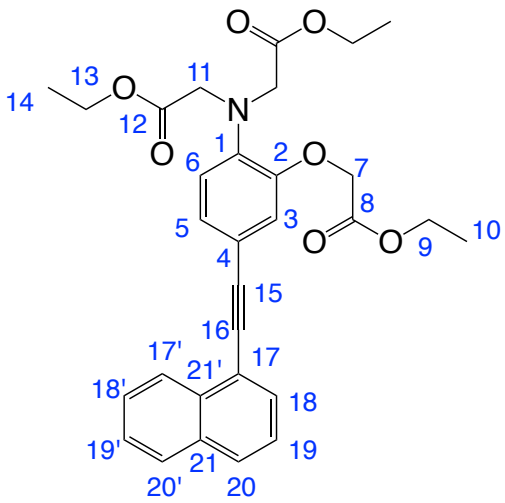

Compound (**25**) (119 mg, 0.22 mmol) and 1-bromonapthalene (29 μL, 0.22 mmol) were dissolved in anhydrous THF (1.1 mL) and the solution was degassed by three freeze-pump-thaw cycles. Triethylamine (0.6 mL), $Pd(dppf)Cl_2$ (21.2 mg, 0.03 mmol) and copper iodide (42.1 mg, 0.22 mmol) were then added and the solution was degassed once more. Tetrabutylammonium fluoride (TBAF, 1 M solution in THF, 0.3 mL, 0.3 mmol) was then added before the brown solution was degassed with three final freeze-pump-thaw cycles. The reaction mixture was stirred at 65 ^{o}C for 18 h under an inert atmosphere of argon, before the solvent was removed under reduced pressure to form a dark brown / black residue. Purification by column chromatography (gradient hexane to 1:1 hexane / ethyl acetate formed the title compound as an orange oil (23.1 mg, 20 %). ^{1}H NMR (700 MHz, $CDCl_3$) 8.39 (1 H, d, *J* 8, $H^{20'}$), 7.85 (1 H, d, *J* 8, $H^{17'}$), 7.81 (1 H, d, *J* 8, H^{20}), 7.71 (1 H, dd, *J* 2, 1, H^{18}), 7.58 – 7.56 (1 H, m, $H^{19'}$), 7.53 – 7.50 (1 H, m, $H^{18'}$), 7.45 – 7.42 (1 H, m, H^{19}), 7.22 (1 H, dd, *J* 8, 2, H^{5}), 7.05 (1 H, d, *J* 2, H^{3}), 6.85 (1 H, d, *J* 8, H^{6}), 4.68 (2 H, s, H^{7}), 4.27 (2 H, q, *J* 7, H^{9}), 4.23 (4 H, s, H^{11}), 4.20 (4 H, q, *J* 7, H^{13}), 1.30 (3 H, t, *J* 7, H^{10}), 1.27 (6 H, t, *J* 7, H^{14}); ^{13}C NMR (176 MHz, $CDCl_3$) 171.0 (C^{12}), 168.5 (C^{8}), 149.0 (C^{2}), 140.2 (C^{1}), 133.2 (C^{17}), 130.1 (C^{18}), 128.5 (C^{20}), 128.3 ($C^{17'}$), 126.2 ($C^{20'}$), 126.7 ($C^{19'}$), 126.5 (C^{5}), 126.4 ($C^{18'}$), 126.3 ($C^{21'}$), 125.3 (C^{19}), 121.1 (C^{21}), 119.2 (C^{6}), 117.5 (C^{3}), 116.5 (C^{4}),

94.3 (C^{15}), 86.6 (C^{16}), 66.2 (C^{7}), 61.3 (C^{9}), 60.8 (C^{13}), 53.8 (C^{11}), 14.2 (C^{14}), 14.1 (C^{10}) ESI-LRMS $[C_{30}H_{32}NO_7]^+$ (+) *m/z* 518.2; ESI-HRMS calcd for $[C_{30}H_{32}NO_7]^+$ 518.2173 found 518.2179.

7.6.32 Diethyl 2,2'-((2-(2-ethoxy-2-oxoethoxy)-5-(naphthalen-1-ylethynyl) phenyl)azanediyl)diacetate, (32)

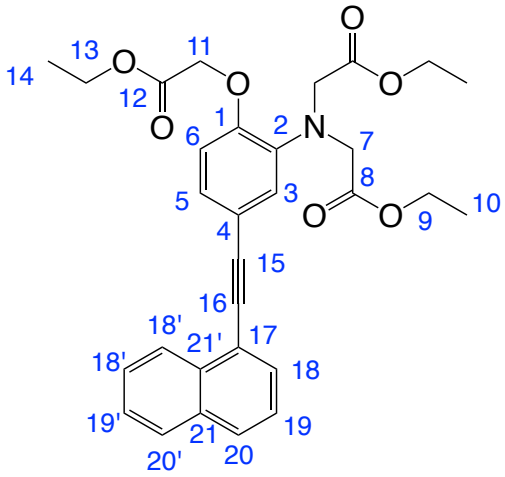

Compound (**26**) (321.7 mg, 0.59 mmol) and 1-bromonapthalene (76 μL, 0.54 mmol) were dissolved in anhydrous THF (2.4 mL) and the solution was degassed by three freeze-pump-thaw cycles. Triethylamine (1.6 mL), $Pd(dppf)Cl_2$ (49.0 mg, 0.07 mmol) and copper iodide (35 mg, 0.18 mmol) were then added and the solution was degassed once more. Tetrabutylammonium fluoride (TBAF, 1 M solution in THF, 0.8 mL, 0.8 mmol) was then added before the brown solution was degassed with three final freeze-pump-thaw cycles. The reaction mixture was stirred at 65 ^oC for 19 h under an inert atmosphere of argon, before the solvent was removed under reduced pressure to form a dark brown / black residue. Purification by silica gel column chromatography (gradient hexane to 1:1 hexane / ethyl acetate) formed the title compound as a pale yellow / orange oil (83.8 mg, 30 %).^{1}H NMR (600 MHz, $CDCl_3$) 8.40 (1 H, d, *J* 9, $H^{20'}$), 7.86 (1 H, d, *J* 8, $H^{17'}$), 7.83 (1 H, d, *J* 8, H^{20}), 7.73 (1 H, dd, *J* 7, 1, H^{18}), 7.59 – 7.56 (1 H, m, H^{19}), 7.54 – 7.51 (1 H, m, $H^{18'}$), 7.46 – 7.43 (1 H, m, $H^{19'}$), 7.22 (1 H, dd, *J* 8, 2, H^5), 7.18 (1 H, d, J 1.9, H^3), 6.80 (1 H, d, *J* 8, H^6), 4.69 (2 H, s, H^{11}), 4.28 – 4.19 (10 H, m, H^7 and H^9 and H^{13}), 1.31 – 1.25 (9 H, m, H^{10} and H^{14}); ^{13}C NMR (151 MHz, $CDCl_3$) 171.1 (C^8), 168.6 (C^{12}), 150.2 (C^1), 139.6 (C^2), 133.2 (C^{17}), 133.2 ($C^{21'}$), 130.2 (C^{20}), 128.5 (C^{18}), 128.5 ($C^{18'}$), 126.6 ($C^{19;}$), 126.3 (C^5), 126.2

($C^{20'}$), 126.2 ($C^{19'}$), 125.3 (C^{19}), 123.2 (C^{3}), 121.1 (C^{21}), 117.4 (C^{4}), 114.2 (C^{6}), 94.3 (C^{15}), 86.3 (C^{16}), 66.1 (C^{11}), 61.3 (C^{7} or C^{9} or C^{13}), 60.8 (C^{7} or C^{9} or C^{13}), 53.7 (C^{7} or C^{9} or C^{13}), 14.2 (C^{10}), 14.1 (C^{14}); ESI-LRMS $[C_{30}H_{32}NO_7]^+$ (+) *m/z* 518.2; ESI-HRMS calcd for $[C_{30}H_{32}NO_7]^+$ 518.2191 found 518.2179.

7.6.33 Diethyl 2,2'-((2-((ethoxy(methyl)phosphoryl)methoxy)-4-(naphthalen-1-ylethynyl)phenyl)azanediyl)diacetate, (33)

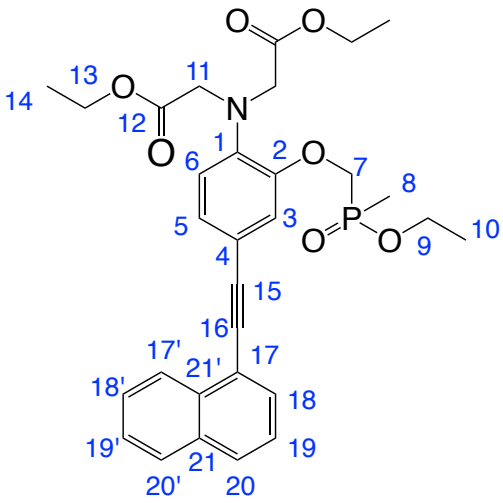

Compound (**27**) (252.5 mg, 0.434 mmol) and 1-bromonapthalene (58 μL, 0.41 mmol) were dissolved in anhydrous THF (1.8 mL) and the solution was degassed by three freeze-pump-thaw cycles. Triethylamine (1.2 mL), $Pd(dppf)Cl_2$ (43.9 mg, 0.06 mmol) and copper iodide (61.2 mg, 0.32 mmol) were then added and the solution was degassed once more. Tetrabutylammonium fluoride (TBAF, 1 M solution in THF, 0.6 mL, 0.6 mmol) was then added before the brown solution was degassed with three final freeze-pump-thaw cycles. The reaction mixture was stirred at 65 ^{o}C for 19 h under an inert atmosphere of argon, before the solvent was removed under reduced pressure to form a dark brown / black residue. Purification by column chromatography (gradient 100 % hexane to 100 % ethyl acetate) formed the title compound as a pale brown oil (24.1 mg, 10 %). ^{1}H NMR (700 MHz, $CDCl_3$) 8.39 (1 H, d, *J* 8, $H^{20'}$), 7.85 (1 H, d, *J* 9, $H^{17'}$), 7.82 (1 H, d, *J* 8, H^{20}), 7.72 (1 H, dd, *J* 7, 2, H^{18}), 7.60 – 7.57 (1 H, m, $H^{19'}$), 7.53 – 7.51 (1 H, m, $H^{18'}$), 7.46 – 7.43 (1 H, m, H^{19}), 7.25 (1 H, dd, *J* 6, 2, H^{5}), 7.15 (1 H, d, *J* 2, H^{3}), 6.90 (1 H, d, *J* 8, H^{6}), 4.36 – 4.09 (14 H, m, H^{7}, H^{9}, H^{11} and

H^{13}), 1.68 (3 H, d, *J* 15, H^{8}), 1.37 (3 H, t, *J* 7, H^{10}), 1.26 (6 H, t, *J* 7, H^{14}); ^{31}P NMR (101 MHz, $CDCl_3$) + 53.8; ^{13}C NMR (176 MHz, $CDCl_3$) 170.7 (s, C^{12}), 150.1 (s, C^{2}), 139.8 (s, C^{1}), 133.2 (s, C^{17}), 130.2 (s, C^{18}), 128.3 (s, $C^{17'}$), 128.6 (s, C^{20}), 126.7 (s, $C^{19'}$) 126.5 (s, C^{5}), 126.4 (s, $C^{21'}$), 126.3 (s, $C^{20'}$), 126.2 (s, $C^{18'}$), 125.3 (s, C^{19}), 120.9 (s, C^{21}), 120.0 (s, C^{6}) 117.1 (d, *J* 7, C^{3}) 94.0 (s, C^{15}), 87.0 (s, C^{16}), 64.6 (s, C^{7}, C^{9}, C^{11} or H^{13}), 65.2 (s, C^{7}, C^{9}, C^{11} or H^{13}), 60.9 (s, C^{7}, C^{9}, C^{11} or H^{13}), 53.3 (s, C^{7}, C^{9}, C^{11} or H^{13}), 16.6 (s, C^{10}), 14.2 (s, C^{14}), 12.6 (d, *J* 97, C^{8}); ESI-LRMS $[C_{30}H_{35}NO_7P]^+$ (+) *m/z* 552.1; ESI-HRMS calcd for $[C_{30}H_{35}NO_7P]^+$ 552.2153 found 552.2151.

7.6.34 Ethyl 2-((2-(ethoxy(methyl)phosphoryl)-4-(naphthalen-1-ylethynyl) phenyl)amino)acetate, (34)

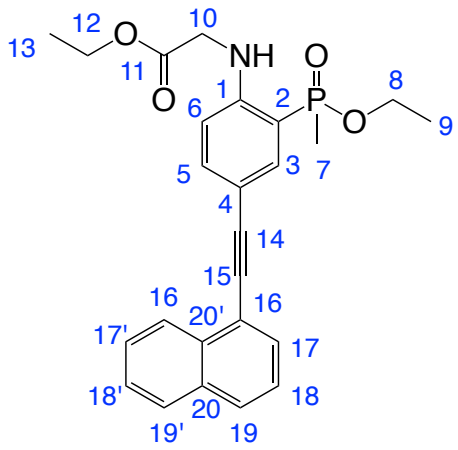

Compound (**28**) (109.7 mg, 0.24 mmol) and 1-bromonapthalene (31 μL, 0.22 mmol) were dissolved in anhydrous THF (1 mL) and the solution was degassed by three freeze-pump-thaw cycles. Triethylamine (0.7 mL), $Pd(dppf)Cl_2$ (40.6 mg, 0.06 mmol) and copper iodide (42.1 mg, 0.22 mmol) were then added and the solution was degassed once more. Tetrabutylammonium fluoride (TBAF, 1 M solution in THF, 0.35 mL, 0.35 mmol) was then added before the brown solution was degassed with three final freeze-pump-thaw cycles. The reaction mixture was stirred at 65 ^{o}C for 18 h under an inert atmosphere of argon, before the solvent was removed under reduced pressure to form a dark brown / black residue. Purification by column chromatography (gradient 100 % hexane to 100 % ethyl acetate formed the title compound as an orange oil (77.8 mg, 20 %).

^{1}H NMR (700 MHz, $CDCl_3$) 8.40 (1 H, d, *J* 8, $H^{20'}$), 7.85- 7.83 (2 H, m, $H^{17'}$ and NH), 7.80 (1 H, d, *J* 8, H^{20}), 7.71 (1 H, dd, *J* 7, 1, H^{18}), 7.65 (1 H, dd, J 15, 2, H^{3}), 7.60 – 7.56 (2 H, m, H^{5} and $H^{19'}$), 7.52 – 7.50 (1 H, m, $H^{18'}$), 7.44 – 7.42 (1 H, m, H^{19}), 6.51 (1 H, dd, *J* 9, 6, H^{6}), 4.24 (2 H, q, *J* 7, H^{12}), 4.19 – 3.93 (4 H, m, H^{10} and H^{8}), 1.73 (3 H, d, *J* 15, H^{7}), 1.35 (3 H, t, *J* 7, H^{9}), 1.28 (3 H, t, *J* 7, H^{13}); ^{13}C NMR (176 MHz, $CDCl_3$) 170.1 (s, C^{11}), 151.0 (d, *J* 6, C^{1}), 137.1 (d, *J* 2, C^{5}), 136.2 (d, *J* 10, C^{3}), 133.2 (d, *J* 14, C^{2}), 130.0 (s, C^{18}), 128.3 (s, $C^{17'}$ and C^{20}), 126.6 (s, $C^{19'}$), 126.4 (s, $C^{18'}$), 126.2 (s, $C^{20'}$), 125.3 (s, C^{19}), 121.2 (s, C^{21}), 112.5 (s, $C^{17'}$ or $C^{21'}$), 111.7 (s, $C^{17'}$ or $C^{21'}$), 111.1 (s, C^{4}), 110.0 (d, *J* 10, H^{6}), 94.1 (s, C^{14}), 86.1 (s, C^{15}), 61.4 (s, C^{12}), 60.9 (d, *J* 6, C^{8}), 45.1 (s, C^{10}), 16.44 (d, *J* 106, C^{7}), 16.4 (d, *J* 7, C^{9}), 16.1 (s, C^{13}); ^{31}P NMR (283 MHz, $CDCl_3$) + 46.7; ESI-LRMS $[C_{25}H_{27}NO_7P]^+$ (+) *m/z* 436.4; ESI-HRMS calcd for $[C_{25}H_{27}NO_7P]^+$ 436.1678 found 436.1672.

7.6.35 2,2'- ((2-(Carboxymethoxy)-4-(naphthalen-1-ylethynyl) phenyl) azanediyl)diacetic acid, NapL^{1} (35)

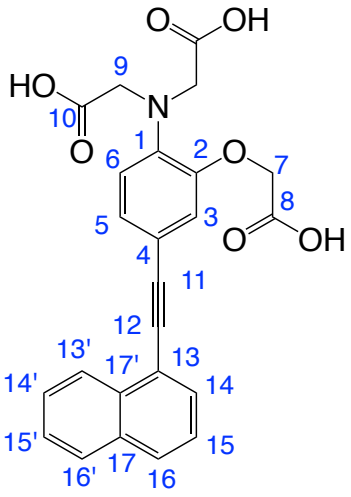

The ethyl ester of **NapL^{1}** (**31**) (51.3 mg, 0.1 mmol) was dissolved in CD_3OD (2.25 mL) and NaOD (0.4 M in D_2O, 0.75 mL). The pale yellow solution was stirred under an inert atmosphere of argon at room temperature for 19 h. Hydrolysis was confirmed by ^{1}H NMR spectrometry, and ESI-LRMS. The solution was lyophilised to form the title compound as an off white solid, in quantitative conversion 34 mg. ^{1}H NMR (700 MHz, D_2O) 8.30 (1 H, d, *J* 8, $H^{16'}$), 7.85 (1 H, d, *J* 8, $H^{13'}$), 7.82 (1 H,

d, *J* 8, H^{16}), 7.65 (1 H, dd, *J* 7, 1, H^{14}), 7.57 – 7.54 (1 H, m, $H^{15'}$), 7.51 – 7.48 (1 H, m, $H^{14'}$), 7.41 – 7.39 (1 H, m, H^{15}), 7.09 (1 H, dd, *J* 8, *2,* H^{5}), 6.87 (1 H, d, *J* 2, H^{3}), 6.65 (1 H, br. d, H^{6}), 4.35 (2 H, s, H^{7}); ^{13}C NMR (176 MHz, D_2O) 179.5 (C^{10}), 177.2 (C^{8}), 148.7 (C^{2}), 141.0 (C^{1}), 132.9 (C^{17} or $C^{17'}$), 132.5 (C^{17} or $C^{17'}$), 130.2 (C^{14}), 128.7 (C^{16}), 128.4 ($C^{13'}$), 127.2 ($C^{15'}$), 126.8 ($C^{14'}$), 125.7 ($C^{16'}$), 125.6 (C^{15}), 125.5 (C^{5}), 120.1 (C^{13}), 117.1 (C^{6}), 115.9 (C^{3}), 95.1 (C^{11}), 85.9 (C^{12}), 67.8 (C^{7}), 56.7 (C^{9}); ESI-LRMS $[C_{24}H_{20}NO_7]^+$ (+) *m/z* 434.1; ESI-HRMS calcd for $[C_{24}H_{20}NO_7]^+$ 434.1240 found 434.1247; Reverse phase HPLC (0 % - 100 % - 0% CH_3CN in ammonium bicarbonate buffer (25 mM), t_R = 7.1 min); Φ_{H_2O} = 0.3 %.

*H^{9} missing from the ^{1}H NMR spectrum because of deuterium exchange.

7.6.36 2,2'- ((2-(Carboxymethoxy)-5- (naphthalen-1- ylethynyl)phenyl) azanediyl)diacetic acid, $NapL^2$ (36)

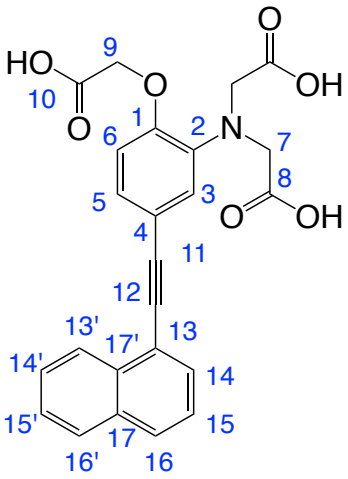

The ethyl ester of **$NapL^2$** (**32**) (41.3 mg, 0.8 mmol) was dissolved in CD_3OD (2.25 mL) and NaOD (0.4 M in D_2O, 0.75 mL). The pale yellow solution was stirred under an inert atmosphere of argon at room temperature for 19 h. Hydrolysis was confirmed by ^{1}H NMR spectrometry, and ESI-LRMS. The solution was lyophilised to form the title compound as an off white solid, in quantitative conversion (28 mg). ^{1}H NMR (700 MHz, D_2O) 8.31 (1 H, d, *J* 8, $H^{16'}$), 7.85 (1 H, d, *J* 8, $H^{13'}$), 7.83 (1 H, d, *J* 8, H^{16}), 7.67 (1 H, d, *J* 7, H^{14}), 7.55 (1 H, t, *J* 8, $H^{15'}$), 7.49 (1 H, t, *J* 8, $H^{14'}$), 7.41 (1 H, t, *J* 7, H^{15}), 7.08 (1 H, d, *J* 8, H^{5}), 6.98 (1 H, br s, H^{3}), 6.62 (1 H, d, *J* 9, H^{6}); 4.37 (2 H, s, H^{10}), 3.75 (4 H, s, H^{7}); ^{13}C NMR (176 MHz, D_2O)

179.5 (C^{8}), 177.0 (C^{10}), 150.5 (C^{1}), 139.9 (C^{2}), 132.9 (C^{17}), 132.5 ($C^{17'}$), 130.0 (C^{16}), 128.8 (C^{14}), 128.4 ($C^{13'}$), 127.2 ($C^{15'}$), 126.8 ($C^{14'}$), 125.7 (C^{4}), 125.6 (C^{15}) 125.0 (C^{5}), 120.7 (C^{3}), 120.0 (C^{13}), 114.8 (C^{4}), 113.0 (C^{6}), 94.9 (C^{11}), 85.6 (C^{12}), 67.4 (C^{10}), 55.6 (C^{7}); ESI-LRMS $[C_{24}H_{20}NO_7]^+$ (+) *m/z* 434.1; ESI-HRMS calcd for $[C_{24}H_{20}NO_7]^+$ 434.1240 found 434.1247; Reverse phase HPLC (0 % - 100 % - 0% CH_3CN in ammonium bicarbonate buffer (25 mM), t_R = 6.6 min); Φ_{H_2O}= 1.3 %.

7.6.37 2,2'-((2-((Hydroxy(methyl)phosphoryl)methoxy)-4-(naphthalen-1-ylethynyl)phenyl)azanediyl)diacetic acid, NapL^4 (37)

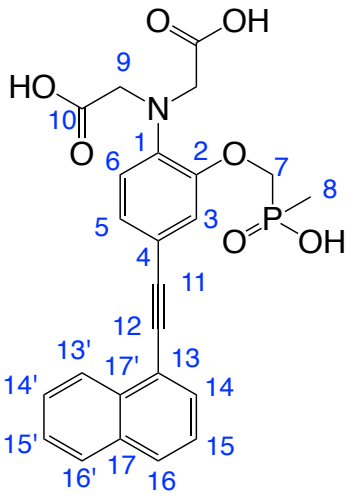

The ethyl ester of **NapL^4** (**33**) (11 mg, 0.02 mmol) was dissolved in CD_3OD (2 mL) and NaOD (0.4 M in D_2O, 0.5 mL). The pale yellow solution was stirred under an inert atmosphere of argon at room temperature for 48 h. Ester hydrolysis was confirmed by ^1H NMR spectrometry, and ESI-LRMS. The solution was lyophilised to form the title compound as a pale brown solid, in quantitative conversion (7 mg). QToF-LRMS $[C_{24}H_{21}NO_7P]^-$ (-) *m/z* 466.1; ESI-HRMS calcd for $[C_{24}H_{21}NO_7P]^-$ (-) 466.1056 found 466.1044. Reverse phase HPLC (0 % - 100 % - 0% CH_3CN in ammonium bicarbonate buffer (25 mM), t_R = 7.1 min); Φ_{H_2O} = 0.7 %.

7.6.38 2-((2-(Hydroxy(methyl)phosphoryl)-4-(naphthalen-1-ylethynyl) phenyl)amino)acetic acid, NapL^6 (38)

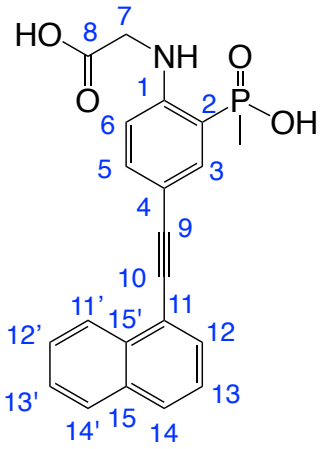

The ethyl ester of **NapL^6** (**34**) (46.0 mg, 0.10 mmol) was dissolved in CD_3OD (1.8 mL) and NaOD (0.4 M in D_2O, 0.2 mL). The pale yellow solution was stirred under an inert atmosphere of argon at room temperature for 4 d. Ester hydrolysis was confirmed by ^{1}H NMR spectrometry, and ESI-LRMS. The solution was then lyophilised to form the title compound as a pale brown solid, in quantitative conversion (30 mg). QToF-LRMS $[C_{21}H_{17}NO_4P]^-$ (-) *m/z* 466.1; ESI-HRMS calcd for $[C_{21}H_{17}NO_4P]^-$ (-) 378.0905 found 378.0895. ^{1}H NMR (400 MHz, D_2O) 8.19 (1 H, d, *J* 8), 7.69 – 7.60 (3 H, m), 7.48 – 7.47 (1 H, d, *J* 7), 7.43 (1 H, t, *J* 7), 7.36 – 7.21 (4 H, m), 6.27 (1 H, m), 1.32 (3 H, d, *J* 14); ^{31}P (176 MHz, D_2O) + 31.7; Reverse phase HPLC (0 % - 100 % - 0% CH_3CN in ammonium bicarbonate buffer (25 mM), t_R = 6.6 min); Φ_{H_2O} = 0.8 %.

7.6.39 [1, 4, 7- Tris(ethoxycarbonylmethyl)] 1, 4, 7, 10- tetraazacyclodecane hydrobromide, (39)[14]

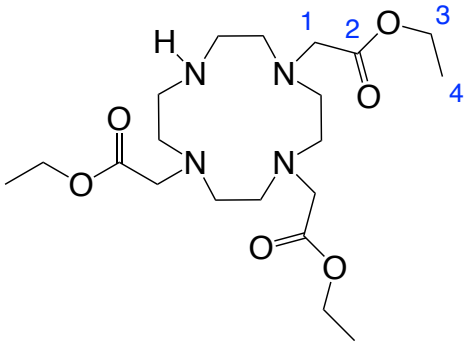

Ethyl bromoacetate (2 mL, 18.1 mmol) was added dropwise to an ice cold suspension of sodium hydrogen carbonate (1.64 g, 19.52 mmol) and 1,4,7,10-tetraazacyclododecane (0.99 g, 5.73 mmol) in anhydrous acetonitrile (35 mL). The reaction mixture was slowly left to warm to room temperature and stirred for 48 h under an inert atmosphere of argon. Inorganic material was removed by filtration and the solvent was removed under reduced pressure to form a yellow oil. Purification by column chromatography (gradient CH_2Cl_2 to 90 % CH_2Cl_2 / 10 % MeOH) formed the title compound as a pale yellow oil that slowly solidified to an off white solid (1.63 g, 66 %). m.p. 94-96 ^oC (lit. 92-94 ^oC)[14]; ^1H NMR (400 MHz, $CDCl_3$) 10.05 (2 H, br s, NH_2), 4.19 (6 H, q, *J* 7, H^3), 3.50 (6 H, s, H^1), 3.42 – 2.89 (16 H, br m, cyclen -H), 1.29 (9 H, t, *J* 7, H^4); ^{13}C NMR (101 MHz, $CDCl_3$) 171.1 (C^2), 60.8 (C^3), 57.3 (C^1), 51.7, 51.4, 49.4, 47.4 (4 x cyclen –CH_2), 14.3 (C^4); ESI-LRMS $[C_{20}H_{39}N_4O_6]^+$ (+) *m/z* 431.1; ESI-HRMS calcd for $[C_{20}H_{39}N_4O_6]^+$ 431.2870 found 431.2865.

7.6.40 [1, 4, 7- Tris(tert-butylcarbonylmethyl)]1,4,7,10- tetraazacyclodecane hydrobromide, (40)[15]

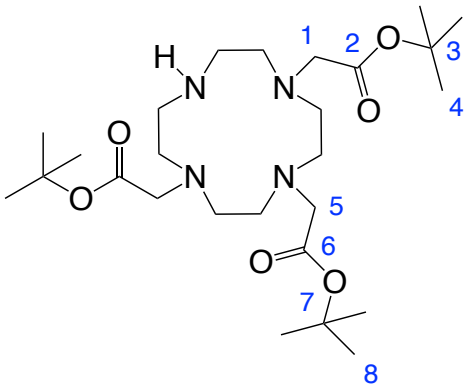

tert-Butyl bromoacetate (2.0 mL, 13.6 mmol) was added to a solution of 1,4,7,10-tetraazacyclododecane (0.9 g, 5.1 mmol) and sodium hydrogen carbonate (1.4 g, 17.0 mmol) in anhydrous acetonitrile (30 mL). The reaction mixture was stirred at room temperature overnight for 19 h under an inert atmosphere of argon. Inorganic impurities were removed by filtration before the solvent was removed under reduced pressure to form an off white solid. Purification by recrystallisation from a minimum amount of hot toluene formed the title compound as a white solid (1.3 g, 43 %). m.p. = 182-184 ^{o}C (lit. 183-184 ^{o}C)[15]; ^{1}H NMR (400 MHz, $CDCl_3$) 10.62 (2 H, br s, NH_2), 3.38 (4 H, s), 3.28 (s, 2H), 3.16- 3.06 (2 H, br s), 2.75 – 2.92 (12 H, m), 1.52 (9 H, s, H^8), 1.45 (18 H, s, H^4); ^{13}C NMR (101 MHz, $CDCl_3$) 170.4 (C^2 and C^6), 85.08 (C^3 or C^7), 82.74 (C^3 or C^7), 54.3, 52.5, 50.4, 48.1, 28.2 (C^8), 28.1 (C^4); ESI-LRMS $[C_{26}H_{51}N_4O_6]^+$ (+) *m/z* 515.4; ESI-HRMS calcd for $[C_{26}H_{51}N_4O_6]^+$ 515.3809 found 513.3798.

7.6.41 4-Bromo-2-methyl pyridine-N-oxide, (41)[16]

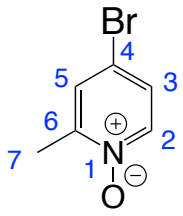

m-CPBA (12.09 g, 46.2 mmol) was added to an ice-cold solution of 4-bromo-2-methyl pyridine (4.2 mL, 35.6 mmol) in anhydrous $CHCl_3$ (110 mL).

The solution was stirred at room temperature for 17 h under an inert atmosphere of argon. The inorganic impurities were removed by filtration, before the organic layer was washed with $NaHCO_3$ (30 mL). The aqueous layer was washed with CH_2Cl_2 (3 x 20 mL). Organic extracts were combined and dried over $MgSO_4$, and the solvent was removed under reduced pressure to form a yellow oil. Purification by alumina gel column chromatography (gradient CH_2Cl_2 to 95 % CH_2Cl_2 / 5 % MeOH) formed the title compound as a pale yellow oil (5.4 g, 81 %). ^{1}H NMR (400 MHz, $CDCl_3$) 8.10 (1 H, d, *J* 7, H^2), 7.42 (1 H, d, *J* 3, H^5), 7.29 (1 H, dd, *J* 7, 3, H^3), 2.50 (3 H, s, H^7); ^{13}C NMR (101 MHz, $CDCl_3$) 150.4, 140.1, 129.4, 126.8, 118.4, 17.8.

7.6.42 4-Bromo-2-(hydroxymethyl)pyridine, (42)[16]

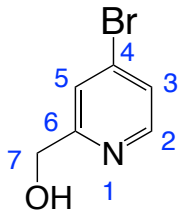

Trifluoroacetic anhydride (16 mL, 115.0 mmol) was added to a solution of 4-bromo-2-methyl pyridine-N-oxide (2.2 g, 11.5 mmol) in anhydrous $CHCl_3$ (32 mL). The solution was heated at 60 °C for 20 h under an inert atmosphere of argon. The reaction mixture was then cooled to room temperature, and the solvent was removed under reduced pressure for form a light brown oil. The brown residue was dissolved in CH_2Cl_2 (20 mL) before NaOH (2 M) was added and the reaction mixture was stirred at room temperature under argon for 16 h. The organic layer was extracted with CH_2Cl_2 (3 x 30 mL) and dried over $MgSO_4$. The solvent was removed under reduced pressure to form a dark brown oil. Purification by silica gel column chromatography (gradient 100 % CH_2Cl_2 to 95 % CH_2Cl_2 / 5 % CH_3OH) formed the title compound as a pale brown oil, that slowly solidified to a fluffy off-white solid on standing at room temperature (1.4 g, 64 %). m.p. 34-36 °C; ^{1}H NMR (700 MHz, $CDCl_3$) 8.37 (1 H, d, *J* 5, H^2), 7.49 (1 H, d, *J* 1, H^5), 7.39 (1 H, dd, *J* 5, 1, H^3), 4.75 (2 H, s, H^7), ^{13}C NMR (176 MHz, $CDCl_3$) 160.8 (C^6), 149.1 (C^2), 133.7 (C^4), 125.8 (C^3), 124.0 (C^5), 63.8 (C^7); ESI-LRMS

$[C_6H_7NO^{79}Br]^+$ (+) *m/z* 188.1; ESI-HRMS calcd for $[C_6H_7NO^{79}Br]^+$ 187.9711 found 187.9688.

7.6.43 Diethyl 2,2'-((2-(2-ethoxy-2-oxoethoxy)-4-((2-(hydroxymethyl) pyridine-4-yl)ethynyl)phenyl)azanediyl)diacetate, (43)

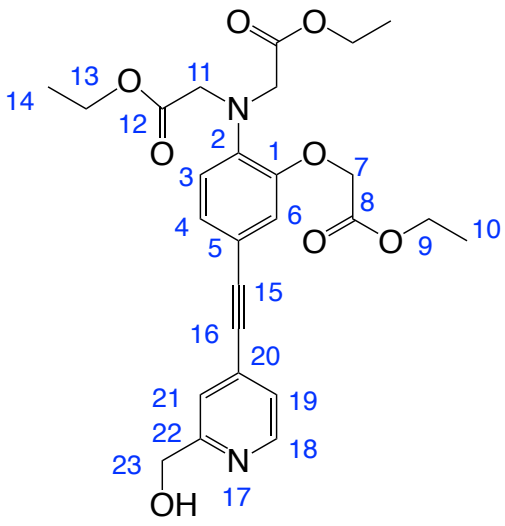

Compound (**25**) (973.0 mg, 1.80 mmol) and 4-bromo-2-(hydroxymethyl) pyridine (**42**) (310.7 mg, 1.66 mmol) were dissolved in anhydrous THF (8 mL) and the solution was degassed by three freeze-pump-thaw cycles. Triethylamine (4.8 mL), $Pd(dppf)Cl_2$ (132.4 mg, 0.018 mmol) and CuI (110.6 mg, 0.58 mmol) were then added and the solution was degassed once more. Tetrabutylammonium fluoride (TBAF, 1 M solution in THF, 0.5 mL, 0.5 mmol) was then added before the brown solution was degassed with three final freeze-pump-thaw cycles. The reaction mixture was stirred at 65 ^oC for 3 h under an inert atmosphere of argon, before the solvent was removed under reduced pressure to form a dark brown / black residue. Purification by column chromatography (gradient hexane to ethyl acetate (with 1 % triethylamine)) formed the title compound as a yellow / brown oil (580.2 mg, 65 %). ^1H NMR (700 MHz, $CDCl_3$,) 8.53 (1 H, br s, H^{18}), 7.29 – 7.69 (2 H, br m, H^{19} and H^{21}), 7.12 (1 H, dd, *J* 9, 2, H^4), 6.94 (1 H, d, *J*, 2, H^6), 6.79 (1 H, d, *J* 8, H^3), 4.76 (2 H, br s, H^{23}), 4.63 (2 H, s, H^7), 4.24 (2 H, q, *J* 7, H^9), 4.21 (4 H, s, H^{11}), 4.19 (4 H, q, *J* 7, H^{13}), 1.29 (3 H, t, *J* 7, H^{10}), 1.25 (6 H, t, *J* 7, H^{14}); ^{13}C NMR (176 MHz, $CDCl_3$) 170.9 (C^{12}), 168.4 (C^8), 148.7 (C^1), 141.0 (C^2), 131.3 (C^{19} or C^{21}), 128.3 (C^{19} or C^{21}), 126.8 (C^4),

118.9 (C^3), 117.5 (C^6), 66.2 (C^7), 61.33 (C^9), 60.89 (C^{13}), 53.8 (C^{11}),14.2 (C^{14}), 14.1 (C^{10}); ESI-LRMS $[C_{26}H_{31}N_2O_8]^+$ (+) *m/z* 499.2; ESI-HRMS calcd for $[C_{26}H_{31}N_2O_8]^+$ 499.2080 found 499.2080.

*Protons from the pyridine spin system are very broad, carbons (C^{18}, C^{19}, C^{20}, C^{21} and C^{22}) are missing from the spectrum.

7.6.44 Diethyl 2,2'-((2-(2-ethoxy-2-oxoethoxy)-4-((2-(((methylsulfonyl)oxy) methyl)pyridin-4-yl)ethynyl)phenyl)azanediyl)diacetate, (44)

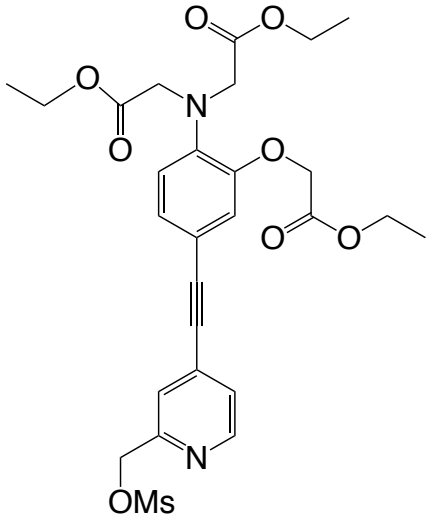

Mesyl chloride (39 μL, 0.5 mmol) was added to an ice cold solution of (**43**) (169.0 mg, 0.339 mmol) and triethylamine (0.15 mL, 1.1 mmol) in anhydrous THF (2 mL). The orange solution was stirred in ice for 20 mins before being gradually warmed to room temperature and stirred for a further 1 h under argon. The reaction mixture was diluted with CH_2Cl_2 (20 mL) and washed with brine. Organic extracts were combined and dried over $MgSO_4$. The solvent was removed under reduced pressure to form the title compound as a brown oil, which was used in subsequent steps without any additional purification. ESI-LRMS $[C_{27}H_{33}N_2O_{10}S]^+$ (+) *m/z* 577.2; ESI-HRMS calcd for $[C_{27}H_{33}N_2O_{10}S]^+$ 577.1858 found 577.1856.

7.6.45 Diethyl 2,2'-((4-((2-(bromomethyl)pyridin-4-yl)ethynyl)-2-(2-ethoxy-2-oxoethoxy)phenyl)azanediyl)diacetate, (45)

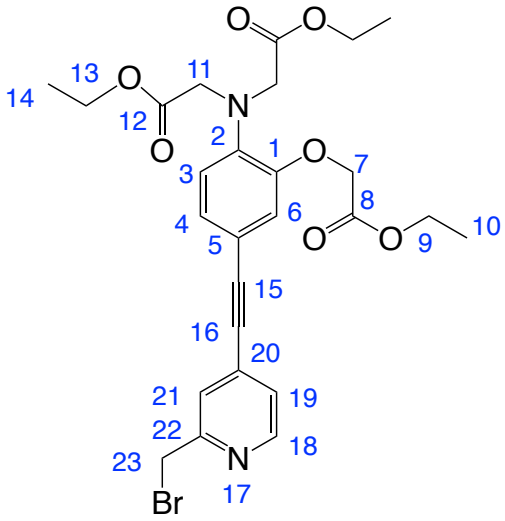

Phosophorus tribromide (PBr_3) (71 μL, 0.75 mmol) was added to an ice cold solution of (**43**) (338.3 mg, 0.68 mmol) in anhydrous CH_2Cl_2 (6 mL). The reaction was warmed to room temperature and stirred at room temperature for 1 h under an inert atmosphere of argon. Reaction completion was determined by ESI-MS. The solvent was removed under reduced pressure to form the title compound as a pale brown oil which was used in subsequent steps without any further purification. ESI-LRMS $[C_{26}H_{30}N_2O_8{}^{79}Br]^+$ (+) *m/z* 561.1; ESI-HRMS calcd for $[C_{26}H_{30}N_2O_8{}^{79}Br]^+$ 561.1238 found 561.1241.

7.6.46 Triethyl-2,2',2''-(10-((4-((4-(bis(2-ethoxy-2-oxoethyl)amino)-3-(2-ethoxy-2-oxoethoxy)phenyl)ethynyl)pyridin-2-yl)methyl)-1,4,7,10-tetraaza-cyclododecane-1,4,7-triyl)triacetate, (46)

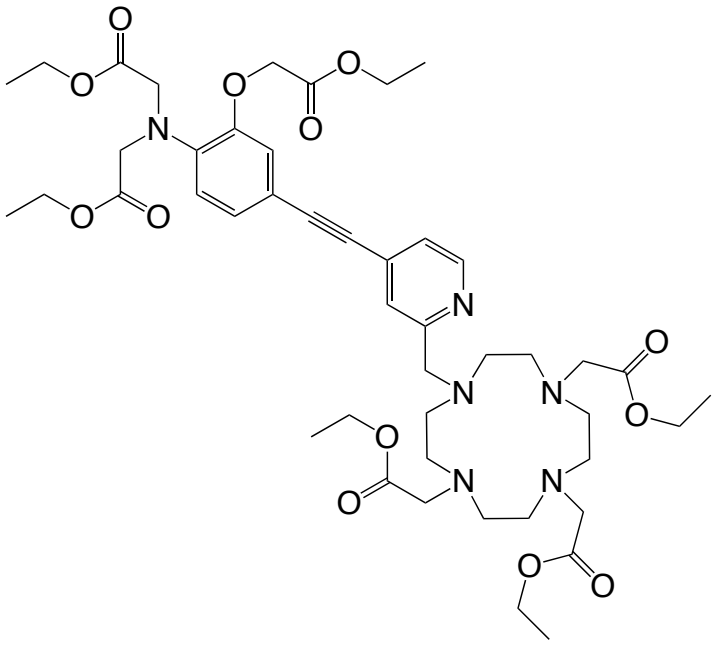

Caesium carbonate (632.4 mg, 1.94 mmol) and sodium iodide (73.8 mg, 0.49 mmol) were added to a solution of (**45**) (154.1 mg, 0.275 mmol) and [1,4,7-tris(ethoxycarbonylmethyl)]-1,4,7,10-tetraazacyclodecane hydrobromide (139.2 mg, 0.273 mmol) in anhydrous acetonitrile (3 mL). The reaction mixture was stirred at 60 ^{o}C for 16 h under an inert atmosphere of argon. After reaction completion, the suspension was diluted with ethyl acetate, and all inorganic impurities were collected by filtration. The solvent was removed under reduced pressure to form a dark brown residue. Purification by silica gel column chromatography (gradient 100 % CH_2Cl_2 to 90 % CH_2Cl_2 / 10 % MeOH) formed the title compound as a pale yellow oil (160 mg). ESI-LRMS $[C_{46}H_{66}N_6O_{13}]^+$ (+) *m/z* 910.9; ESI-HRMS calcd for $[C_{46}H_{66}N_6O_{13}]^+$ 911.4766 found 911.4774.

7.6.47 [Eu.L^1(H_2O)]

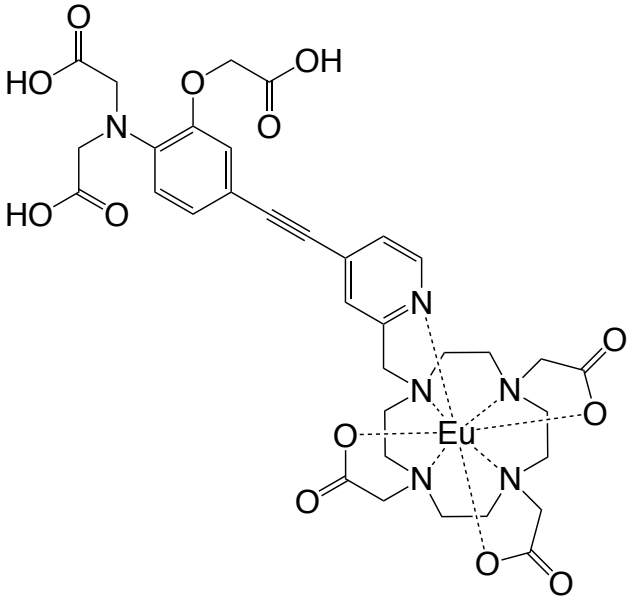

Compound (**46**) (64.3 mg, 0.07 mmol) was dissolved in CD_3OD (3 mL) and NaOD (0.4 M in D_2O, 0.80 mL). The pale yellow solution was stirred under an inert atmosphere of argon at room temperature for 18 h, ester hydrolysis was confirmed by ^{1}H NMR spectrometry, and ESI-LRMS. The solution was lyophilised to form the title compound as a white solid (61.4 mg), which was used in subsequent steps without any further purification. ESI-LRMS $[C_{34}H_{43}N_6O_{13}]^+$ (+) *m/z* 743.2. The ethyl ester hydrolysed product (61.4 mg, 0.029 mmol) was dissolved in H_2O (3 mL). The pH was adjusted to 5.5 using HCl (aq, 1 M) and $EuCl_3.6H_2O$ (42.8 mg, 0.12 mmol) was added. The resulting yellow solution was stirred at 65 ^oC for 18 h under an inert atmosphere of argon. The pH was adjusted to pH 8 and precipitated $Eu(OH)_3$ was removed by syringe filtration. Purification was achieved by reverse phase HPLC (0 % - 100 % - 0% CH_3CN in ammonium bicarbonate buffer (25 mM), t_R = 1.13 min). The solvent was lyophilised to form the title compound as a pale yellow solid (13 mg); ESI-LRMS $[C_{46}H_{39}N_6O_{13}{}^{151}Eu]^-$ (-) *m/z* 890.3; ESI-HRMS calcd for $[C_{46}H_{39}N_6O_{13}{}^{151}Eu]^+$ 890.1774 found 890.1767; Φ_{H_2O}= 13.0 %.

7.6.48 Diethyl 2,2'-((2-(2-ethoxy-2-oxoethoxy)-5-((2-(hydroxylmethyl)-pyridin-4-yl)ethynyl)phenyl)azanediyl)diacetate, (47)

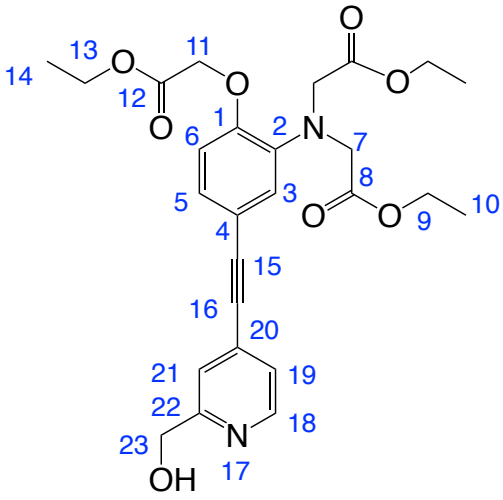

Compound (**26**) (185.6 mg, 0.34 mmol) and 4-bromo-2-(hydroxymethyl) pyridine (63.8 mg, 0.34 mmol) were dissolved in anhydrous THF (1.6 mL) and the solution was degassed by three freeze-pump-thaw cycles. Triethylamine (1 mL), $Pd(dppf)Cl_2$ (26.2 mg, 0.036 mmol) and copper iodide (22.4 mg, 0.11 mmol) were then added and the solution was degassed once more. Tetrabutylammonium fluoride (TBAF, 1 M solution in THF, 0.5 mL, 0.5 mmol) was then added before the brown solution was degassed with three final freeze-pump-thaw cycles. The reaction mixture was stirred at 65 ^{o}C for 3 h under an inert atmosphere of argon, before the solvent was removed under reduced pressure to form a dark brown / black residue. Purification by column chromatography (gradient hexane to ethyl acetate (with 1 % triethylamine)) formed the title compound as a yellow oil (73.4 mg, 42 %). R_f (silica, 100 % ethyl acetate) = 0.38. ^{1}H NMR (700 MHz, $CDCl_3$) 8.57 (1 H, br s, H^{18}), 7.38 (2 H, br s, H^{19} and H^{21}), 7.10 (1 H, dd, *J* 8, 2, H^{5}), 7.08 (1 H, d, *J* 2, H^{3}), 6.73 (1 H, d, *J* 8, H^{6}), 4.78 (2 H, br s, H^{23}), 4.66 (2 H, s, H^{11}), 4.24 (2 H, q, *J* 7 H^{13}), 4.17 – 4.21 (8 H, m, H^{7} and H^{9}), 1.24 – 1.28 (9 H, m, H^{10} and H^{14}); ^{13}C NMR (700 MHz, $CDCl_3$) 171.0 (C^{8}), 168.3 (C^{12}), 150.7 (C^{1}), 139.5 (C^{2}), 126.5 (C^{5}), 123.4 (C^{3}), 113.9 (C^{6}), 65.8 (C^{11}), 61.2 (C^{13}), 60.8 (C^{7} or C^{9}), 53.6 (C^{7} or C^{9}), 14.2 (C^{10}), 14.1 (C^{14}); ESI-LRMS $[C_{26}H_{31}N_2O_8]^+$ (+) *m/z* 499.2; ESI-HRMS calcd for $[C_{26}H_{31}N_2O_8]^+$ 499.2080 found 499.2068.

*Protons from the pyridine spin system are very broad, carbons (C^{18}, C^{19}, C^{20}, C^{21} and C^{22}) are missing from the spectrum.

7.6.49 Diethyl 2,2'-((5-((2-(bromomethyl)pyridin-4-yl)ethynyl)-2-(2-ethoxy-2-oxoethoxy)phenyl)azanediyl)diacetate, (48)

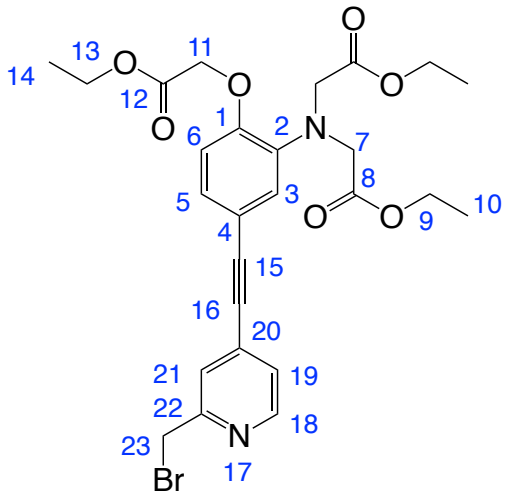

Phosphorus tribromide (PBr_3) (38 μL, 0.40 mmol) was added to an ice cold solution of (**47**) (132.7 mg, 0.27 mmol) in anhydrous CH_2Cl_2 (3 mL). The solution was stirred at 0 °C for 1 h before being stirred at room temperature for 2 h under an inert atmosphere of argon. The solvent was removed under reduced pressure to form a yellow residue. Purification by column chromatography (gradient 100 % CH_2Cl_2 to 95 % CH_2Cl_2 / 5 % MeOH) to form the title compound as a yellow oil (88.6 mg, 59 %). ^{1}H NMR (700 MHz, $CDCl_3$) 8.55 (1 H, br s, H^{18}), 7.57 (1 H, br s, H^{21}), 7.35 (1 H, br d, *J* 5, H^{19}), 7.10 – 7.13 (2 H, m, H^3 and H^5), 6.74 (1 H, d, *J* 8, H^6), 4.68 (2 H,s, H^{11}), 4.62 (2 H, s, H^{23}), 4.17 – 4.21 (8 H, m, H^7 and H^9), 1.24 – 1.29 (9 H, m, H^{10} and H^{14}); ^{13}C NMR (176 MHz, $CDCl_3$) 170.9 (C^8), 168.2 (C^{12}), 155.8 (C^{22}), 151.1 (C^1), 147.8 (C^{18}), 139.6 (C^2), 126.8 (C^3 or C^5), 126.0 (C^{21}) 125.1 (C^{19}), 123.7 (C^{20}), 123.6 (C^3 or C^5), 115.2 (C^4), 113.8 (C^6), 97.0 (C^{15}), 85.2 (C^{16}), 65.8 (C^7 or C^9), 61.4 (C^{13}), 60.8 (C^{11}), 53.6 (C^7 or C^9), 31.6 (C^{23}), 14.21 (C^{10}), 14.11 (C^{14}); ESI-LRMS $[C_{26}H_{29}N_2O_7{}^{79}Br]^+$ (+) *m/z* 561.1; ESI-HRMS calcd for $[C_{26}H_{29}N_2O_7{}^{79}Br]^+$ 561.1236 found 561.1236.

7.6.50 Triethyl-2,2',2''-(10-((4-((3-(bis(2-ethoxy-2-oxoethyl)amino)-4-(2-ethoxy-2-oxoethoxy)phenyl)ethynyl)pyridin-2-yl)methyl)-1,4,7,10-tetraaza-cyclododecane-1,4,7-triyl)triacetate, (49)

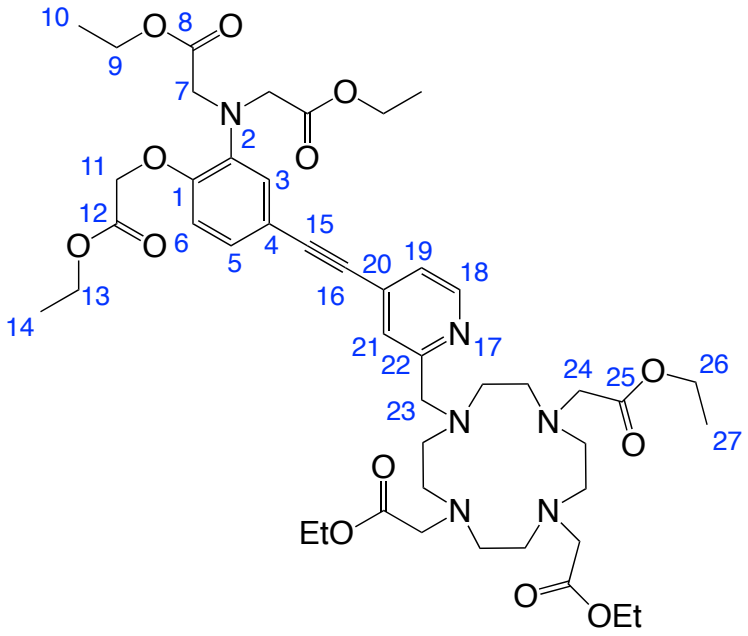

Caesium carbonate (341.8 mg, 1.05 mmol) and sodium iodide (32.2 mg, 0.21 mmol) were added to a solution of (**48**) (97.5 mg, 0.17 mmol) and [1,4,7-tris(ethoxycarbonylmethyl)]-1,4,7,10-tetraazacyclodecane hydrobromide (81.8 mg, 0.158 mmol). The reaction mixture was stirred at 60 ^{o}C for 16 h under an inert atmospgere of argon. After completion the solution was diluted with ethyl acetate and all inorganic impurities were collected by filtration. The solvent was removed under reduced pressure to form a dark brown residue. Purification by silica gel column chromatography (gradient 100 % CH_2Cl_2 to 90 % CH_2Cl_2 / 10 % MeOH) formed the title compound as a pale yellow oil (42.1 mg, 29 %). ^{1}H NMR (400 MHz, $CDCl_3$) 8.20 (1 H, d, *J* 5, H^{18}), 7.31 (1 H, br s, H^{21}), 7.23 (1 H, dd, *J* 5, 2, H^{19}), 7.14 – 7.12 (2 H, m, H^{3} and H^{5}), 6.77 (1 H, d, *J* 9, H^{6}), 4.70 (2 H, s, H^{23}), 4.30 – 4.16 (22 H, m), 1.30 (18 H, m, H^{10}, H^{14} and H^{27}); ESI-LRMS $[C_{46}H_{66}N_6O_{13}]^+$ (+) *m/z* 910.9; ESI-HRMS calcd for $[C_{46}H_{66}N_6O_{13}]^+$ 911.4766 found 911.4794.

7.6.51 [Eu.L^2(H_2O)]

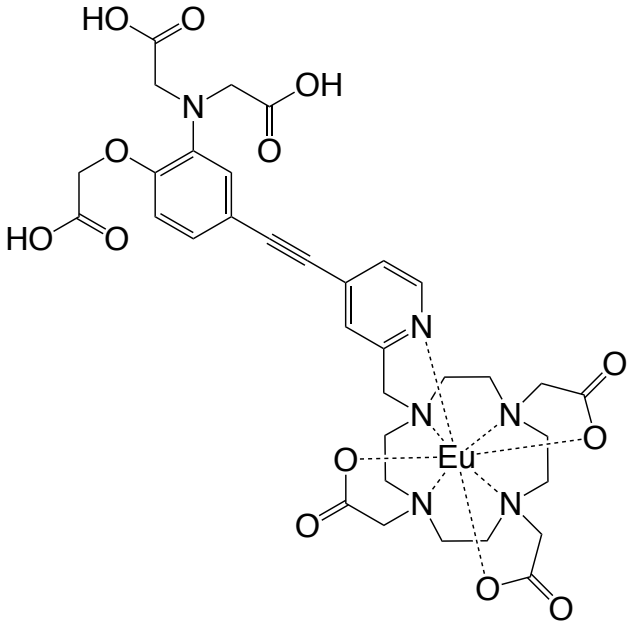

Compound (**49**) (41.5 mg, 0.046 mmol) was dissolved in CD_3OD (2 mL) and NaOD (0.4 M in D_2O, 0.70 mL). The pale yellow solution was stirred under an inert atmosphere of argon at room temperature for 20 h, ester hydrolysis was confirmed by ^{1}H NMR spectrometry, and ESI-LRMS. The solution was lyophilised to form the title compound as a white solid (35 mg), which was used in subsequent steps without further purification. ESI-LRMS $[C_{34}H_{43}N_6O_{13}]^+$ (+) *m/z* 743.2; ESI-HRMS calcd for $[C_{34}H_{43}N_6O_{13}]^+$ 743.2888 found 743.2893. The ethyl ester hydrolysed product of (**49**) (22 mg, 0.029 mmol) was dissolved in H_2O (2 mL). The pH was adjusted to 5.5 using HCl (aq, 1 M) and $EuCl_3.6H_2O$ (21.7 mg, 0.069 mmol) was added. The resulting yellow solution was stirred at 65 ^oC for 18 h under an inert atmosphere of argon. The pH was adjusted to pH 8 and the $Eu(OH)_3$ precipitate was removed by syringe filtration. The solvent was lyophilised to form a pale yellow solid. Purification by reverse phase HPLC (0 % - 100 % - 0% CH_3CN in ammonium bicarbonate buffer (25 mM), t_R = 5.6 min) to form the title compound as a pale yellow solid (8 mg); ESI-LRMS $[C_{46}H_{39}N_6O_{13}{}^{151}Eu]^-$ (-) *m/z* 890.3; ESI-HRMS calcd for $[C_{46}H_{39}N_6O_{13}{}^{151}Eu]^+$ 890.1774 found 890.1778; Φ_{H_2O} = 11.2 %.

7.6.52 [Tb.L^2(H$_2$O)]

The complex **[Tb.L^2(H$_2$O)]** was synthesised in a procedure analogous to that used for the synthesis of **[EuL^2(H$_2$O)]**, using (**49**) (18.9 mg, 0.025 mmol) and $TbCl_3.6H_2O$ (16.4 mg, 0.04 mmol) in H_2O (1.8 mL). Purification by reverse phase HPLC (0 % - 100 % - 0% CH_3CN in ammonium bicarbonate buffer (25 mM), t_R = 5.7 min) to form the title compound as a pale yellow solid (4 mg); ESI-LRMS $[C_{46}H_{39}N_6O_{13}Tb]^+$ (+) *m/z* 900.4; ESI-HRMS calcd for $[C_{46}H_{39}N_6O_{13}Tb]^+$ 900.1907 found 900.1937.

7.6.53 *tert*-Butyl 2-(2-{bis[2-(tert-butoxy)-2-oxoethyl]amino}-5-(4,4,5,5-tetramethyl-1,3,2-dioxaborolan-2-yl)phenoxy)acetate, (50)[17]

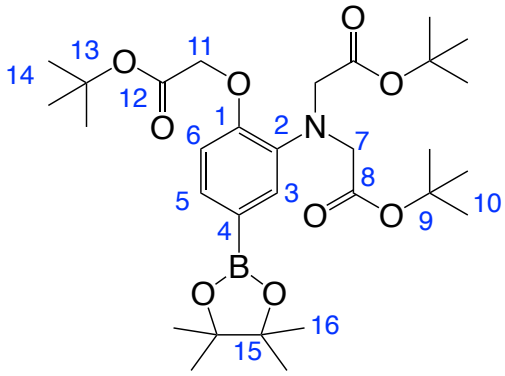

Pd(dppf)Cl_2 (11.8 mg, 0.016 mmol) was added to a solution of **7** (264.2 mg, 0.5 mmol), bis(pinacolato)diboron (B_2pin_2) (155.2 mg, 0.61 mmol) and potassium acetate (158.4 mg, 1.61 mmol) in 1,4-dioxane (1.4 mL). The solution was degassed via four freeze-pump-thaw cycles, and heated in a microwave reactor for 30 mins at 120 ^oC. The reaction mixture was suspended between CH_2Cl_2 (20 mL) and water (10 mL) and the aqueous layer was extracted with CH_2Cl_2 (3 x 10 mL). The organic extracts were combined, dried over $MgSO_4$, and the solvent was removed under reduced pressure to form a dark brown residue. Purification by silica gel column chromatography (gradient hexane to 80 / 20 (hexane / ethyl acetate)) formed the title compound as a pale yellow solid (203.1 mg, 70 %). R_f (silica, 80 / 20 (hexane / ethyl acetate)) = 0.36; m.p = 136-138 ^oC; ^1H ($CDCl_3$, 700 MHz) 7.30 (1 H, dd, *J* 8, 2, H^5), 7.27 (1 H, d, *J* 2, H^3), 6.70 (1 H, d, *J* 8, H^6), 4.53 (2 H, s, H^{11}), 4.07 (4 H, s, H^7), 1.44 (18 H, s, H^{10}), 1.43 (9 H, s,

H^{14}), 1.28 (12 H, s, H^{16}); ^{11}B ($CDCl_3$, 128 MHz) + 30.7; ^{13}C ($CDCl_3$, 176 MHz) 170.8 (C^8, C^{12}), 167.9 (d, *J* 1, C^4),152.1 (C^1), 138.8 (C^2), 129.0 (C^5), 125.8 (C^3), 112.4 (C^6), 83.4 (C^{15}), 82.1 (C^{13}), 80.9 (C^9), 66.0 (C^{11}), 54.5 (C^7), 28.1 (C^{10}), 28.0 (C^{14}), 24.9 (C^{16}); ASAP-LRMS $[C_{30}H_{48}BNO_9]^+$ (+) *m/z* 578.3; ASAP-HRMS calcd for $[C_{30}H_{48}BNO_9]^+$ 577.3511 found 577.3537.

7.6.54 Di-*tert*-butyl 2,2'-((2-(2-(*tert*-butoxy)-2-oxoethoxy)-5-(2-(hydroxyl-methyl)pyridin-4-yl)phenyl)azanediyl)diacetate, (51)

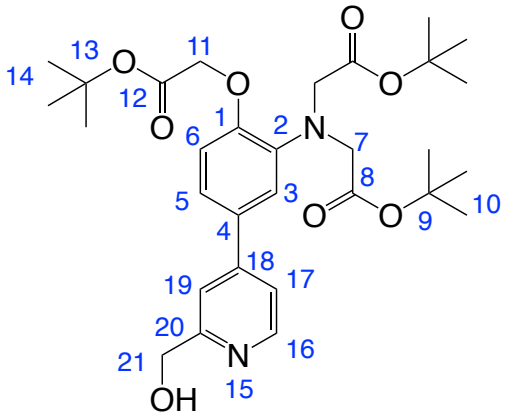

Compound (**50**) (205.2 mg, 0.35 mmol), 4-bromo-2-(hydroxymethyl) pyridine (**42**) (69.1 mg, 0.37 mmol) and sodium carbonate (151.3 mg, 1.48 mmol) were dissolved in a mixture of DME (1.4 mL) and water (0.6 mL). The solution was degassed by three freeze-pump-thaw cycles, before the addition of $Pd(PPh_3)_4$ (41.8 mg, 0.036 mmol). The reaction mixture was stirred at 85 ^oC for 18 h, before the solvent was removed under reduced pressure to form a dark brown / black residue. Purification by column chromatography (gradient hexane to ethyl acetate (with 1 % triethylamine)) formed the title compound as a yellow oil (111.6 mg, 51 %). ^1H NMR (600 MHz, $CDCl_3$) 8.53 (1 H, d, *J* 5.22, H^{16}), 7.36 (1 H, br s, H^{19}), 7.34 (1 H, dd, *J* 5, 1, H^{17}), 7.17 (1 H, dd, *J* 8, 2, H^5), 7.12 (1 H, d, *J* 2, H^3), 6.82 (1 H, d, J 8, H^6), 4.78 (2 H, s, H^{21}), 4.58 (2 H, s, H^{11}), 4.12 (4 H, s, H^7), 1.47 (9 H, s, H^{14}), 1.43 (18 H, s, H^{10}); ^{13}C NMR (151 MHz, $CDCl_3$) 170.4 (C^8), 167.8 (C^{12}), 159.3 (C^{20}), 150.7 (C^1), 148.9 (C^{18}), 148.7 (C^{20}), 140.0 (C^2), 131.4 (C^4), 120.4 (C^{17}), 120.0 (C^5), 118.0 (C^3), 117.7 (C^{19}), 113.9 (C^6), 82.4 (C^{13}), 81.2 (C^9), 66.3 (C^7), 64.2 (C^{11}), 54.6 (C^{21}), 28.1 (C^{10} and C^{14}); ESI-LRMS $[C_{30}H_{43}N_2O_8]^+$ (+) *m/z* 599.3; ESI-HRMS calcd for $[C_{30}H_{43}N_2O_8]^+$ 559.3019 found 599.2999.

7.6.55 Di-*tert*-butyl 2,2'-((5-(2-(bromomethyl)pyridin-4-yl)-2-(2-(*tert*-butoxy)-2-oxoethoxy)phenyl)azanediyl)diacetate, (52)

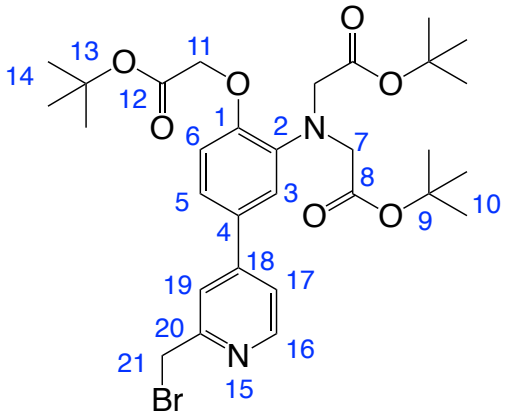

Phosphorus tribromide (PBr_3) (52 μL, 0.55 mmol) was added to an ice cold solution of (**51**) (252.3 mg, 0.45 mmol) in anhydrous CH_2Cl_2 (3 mL) The reaction was warmed to room temperature and stirred at room temperature for 1 h, reaction completion was determined by ESI-MS by the disappearance of the starting material peak. The solvent was removed under reduced pressure to form the title compound as a yellow oil which was used in subsequent steps without any further purification. ESI-LRMS $[C_{30}H_{42}N_2O_7{}^{79}Br]^+$ (+) *m/z* 621.2; ESI-HRMS calcd for $[C_{30}H_{42}N_2O_7{}^{79}Br]^+$ 621.2175 found 621.2165.

7.6.56 Tri-tert-butyl 2,2',2''-(10-((4-(3-(bis(2-(tert-butoxy)-2-oxoethyl) amino)–4-(3,3-dimethyl-2-oxobutoxy)phenyl)pyridin-2-yl)methyl)-1,4,7,10-tetraazacyclododecane-1,4,7-triyl)triacetate, (53)

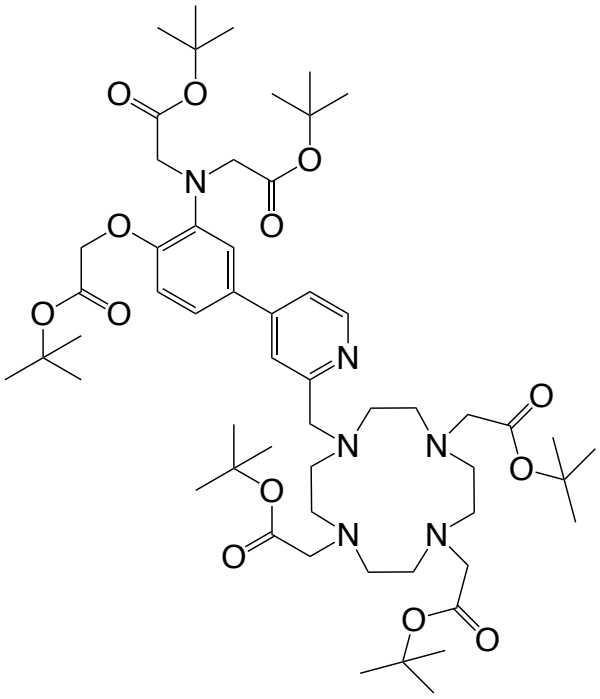

Caesium carbonate (620.0 mg, 1.9 mmol) and sodium iodide (120.2 mg, 0.8 mmol) were added to a solution of (**52**) (201.1 mg, 0.32 mmol) and [1,4,7-tris(ethoxycarbonylmethyl)]-1,4,7,10-tetraazacyclodecane hydrobromide, (**40**) (81.8 mg, 0.158 mmol) in anhydrous acetonitrile (2 mL). The reaction mixture was stirred at 60 ^{o}C for 17 h under an inert atmospgere of argon. After completion the solution was diluted with ethyl acetate (15 mL) and all inorganic impurities were collected by filtration. The solvent was removed under reduced pressure to form a dark brown residue. Purification by silica gel column chromatography (gradient 100 % CH_2Cl_2 to 90 % CH_2Cl_2 / 10 % MeOH) formed the title compound as a pale yellow oil (118.3 mg). ESI-LRMS $[C_{56}H_{91}N_6O_{13}]^+$ (+) *m/z* 1056.8; ESI-HRMS calcd for $[C_{56}H_{91}N_6O_{13}]^+$ 1055.6644 found 1055.6678.

7.6.57 [Eu.bL^2(H$_2$O)]

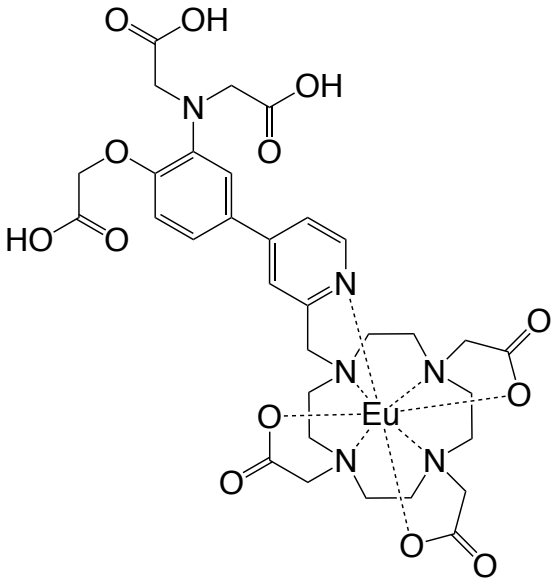

Compound (**53**) (47.1 mg, 0.045 mmol) was dissolved in CH_2Cl_2 (1 mL) and TFA (1 mL). The pale brown solution was stirred under an inert atmosphere of argon at room temperature for 20 h, ester hydrolysis was confirmed by ^{1}H NMR spectrometry, and ESI-LRMS. The solvent was lyophilised to form the title compound as a white solid (39 mg), which was used in subsequent steps without further purification. The *tert*-butyl ester hydrolysed product (39 mg, 0.029 mmol) was dissolved in H_2O (4 mL). The pH was adjusted to 5.5 using NaOH (aq, 1 M) and $EuCl_3.6H_2O$ (21.7 mg, 0.069 mmol) was added. The resulting yellow solution was stirred at 65 ^oC for 18 h. The pH was adjusted to pH 8 and $Eu(OH)_3$ was removed by filtration. The solvent was lyophilised to form a pale yellow solid. Purification by reverse phase HPLC (0 % - 100 % - 0% CH_3CN in ammonium bicarbonate buffer (25 mM), t_R = 1.06 min) to form the title compound as a pale yellow solid (21 mg); ESI-LRMS $[C_{32}H_{40}N_6O_{13}{}^{151}Eu]^+$ (-) *m/z* 867.1; ESI-HRMS calcd for $[C_{32}H_{40}N_6O_{13}{}^{151}Eu]^+$ 867.1840 found 867.1852.

7.6.58 [Tb.bL^2(H$_2$O)]

The complex **[Tb.bL^2(H$_2$O)]** was synthesised in a procedure analogous to that used for the synthesis **[Eu.bL^2(H$_2$O)]**, using **(53)** (30.2 mg, 0.04 mmol) and $TbCl_3.6H_2O$ (35.5 mg, 0.09 mmol) in H_2O (3.0 mL). Purification by reverse phase HPLC (0 % - 100 % - 0% CH_3CN in ammonium bicarbonate buffer (25 mM),

t_R = 1.63 min) to form the title compound as a white solid yellow solid (4 mg); ESI-LRMS $[C_{32}H_{40}N_6O_{13}Tb]^+$ (+) *m/z* 875.2; ESI-HRMS calcd for $[C_{32}H_{39}N_6O_{13}Tb]^+$ 875.1908 found 875.1907; Φ_{H_2O}= 3.4 % (aerated), Φ_{H_2O}= 5.4 % (deoxygenated).

7.6.59 [Gd.bL^2(H$_2$O)]

The complex **[Gd.bL^2(H$_2$O)]** was synthesised in a procedure analogous to that used for the synthesis **[Eu.bL^2(H$_2$O)]**, using **(53)** (79 mg, 0.11 mmol) and $GdCl_3.6H_2O$ (8 mg, 0.22 mmol) in H_2O (5.0 mL). Purification by reverse phase HPLC (0 % - 100 % - 0% CH_3CN in ammonium bicarbonate buffer (25 mM), t_R = 1.48 min) to form the title compound as a white solid yellow solid (11 mg); ESI-LRMS $[C_{32}H_{40}N_6O_{13}{}^{155}Gd]^+$ (+) *m/z* 871.2; ESI-HRMS calcd for $[C_{32}H_{40}N_6O_{13}{}^{155}Gd]^+$ 871.1908 found 871.1907.

7.6.60 2, 2'-Bipyridine-N-oxide, (54)[18]

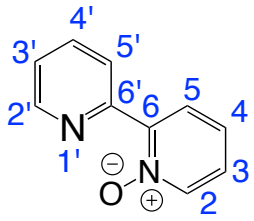

3-Chloroperoxybenzoic acid (3.1 g, 77%, 13.8 mmol) was dissolved in $CHCl_3$ (55 mL) and added dropwise to a solution of 2,2'-bipyridine (2.0 g, 12.8 mmol) in $CHCl_3$ (7 mL) at 0 °C. The pale yellow solution was stirred at room temperature for 20 h. The reaction mixture was washed with Na_2CO_3 (5 %, 3 x 20 mL), the aqueous extracts were then combined and washed with $CHCl_3$ (3 x 50 mL). The organic extracts were combined, dried over $MgSO_4$, the solvent was removed under reduced pressure to form a yellow oil. Purification by alumina column chromatography (gradient 100 % CH_2Cl_2 to 95 % CH_2Cl_2 / 5 % MeOH) formed the title compound as an off while solid (1.54 g, 71 %). m.p. 56-57 °C (Lit 56-57 °C)[19]; ^{1}H (700 MHz, $CDCl_3$,) 8.87 (1 H, d, *J* 8, H$^{2'}$), 8.70 (1 H, d, *J* 5, H$^{5'}$), 8.29 (1 H, d, *J* 7, H^2), 8.16 (1 H, dd, *J* 8, 2, H^5), 7.81 (1 H, td, *J* 8, 2, H$^{3'}$), 7.33 (2 H, m, H$^{4'}$ and H^4), 7.25 (1 H, m, H^3); ^{13}C (176 MHz, $CDCl_3$,) 149.6 (C^6), 149.4 (C$^{5'}$), 147.3 (C$^{6'}$), 140.7 (C^2), 136.2 (C$^{3'}$), 127.9 (C^5), 125.6 (C^4 / C$^{4'}$),

125.5 ($C^{2'}$), 125.2 ($C^{3'}$), 124.2 (C^{4} / $C^{4'}$); ESI-LRMS $[C_{10}H_8N_2O]^+$ (+) *m/z* 174.0; ESI-HRMS calcd for $[C_{10}H_8N_2O]^+$ 173.0707 found, 173.0715.

7.6.61 4-Nitro-2, 2'-bipyridine-N-oxide, (55)[18]

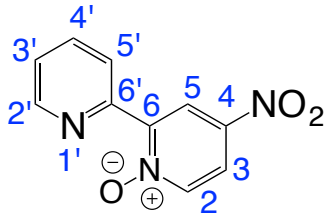

2, 2'-Bipyridine-N-oxide (3.409 g, 19.8 mmol) and potassium nitrate (10.9 g, 107.8 mmol) were dissolved in H_2SO_4 (97 %, 26 mL). The solution was stirred at 80 ^oC for 24 h before the addition of further KNO_3 (6 g, 59.3 mmol) and H_2SO_4 (97 %,10 mL). The solution was stirred for a further 24 h, cooled to room temperature, poured onto ice, and basified to pH 10 with NaOH (2 M). The pale yellow precipitate formed was extraction into CH_2Cl_2 (3 x 100 mL) and dried over $MgSO_4$. The solvent was removed under reduced pressure to form the title compound as a pale yellow solid (2.05 g, 48 %) and was used in subsequent steps without further purification. m.p. 184-185 ^oC (Lit = 184-186 ^oC)[19]; ^1H (400 MHz, $CDCl_3$) 9.19 (1 H, d, *J* 3, H^5), 8.91 (1 H, dt, *J* 8, 1, $H^{5'}$), 8.81 (1 H, ddd, *J* 5, 2, 1, $H^{2'}$), 8.38 (1 H, d, *J* 7, H^2), 8.09 (1 H, ddd, *J* 7, 4, H^3), 7.88 (1 H, td, *J* 8, 2, $H^{4'}$), 7.45 (1 H, ddd, *J* 8, 5, 4, $H^{3'}$); ^{13}C (101 MHz, $CDCl_3$) 149.8 ($C^{2'}$), 148.0 ($C^{6'}$), 147.6 (C^6), 142.8 (C^4), 142.0 (C^2), 136.7 ($C^{4'}$), 125.3 ($C^{5'}$), 125.1 ($C^{3'}$), 122.6 (C^5), 118.8 (C^3); ESI-LRMS $[C_{10}H_8N_3O_3]^+$ (+) *m/z* 218.1; ESI-HRMS calcd for $[C_{10}H_8N_3O_3]^+$ 218.0566 found, 218.0574.

7.6.62 4-Bromo-2, 2'-bipyridine-N-oxide, (56)[18]

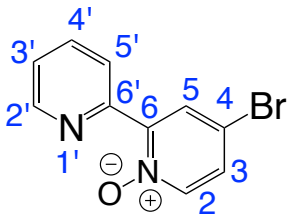

Acetyl bromide (10 mL, 0.135 mol) was added to a solution of 4-nitro-2,2'-bipyridine-N-oxide (1.40 g, 6.45 mmol) in glacial acetic acid (17 mL) and heated at 120 ^{o}C for 7 h under an inert atmosphere of argon. Once cooled to room temperature, the reaction mixture was poured onto ice and basified to pH 12 with NaOH (2 M). The reaction mixture was extracted into $CHCl_3$ (3 x 200 mL) and dried over $MgSO_4$. The solvent was removed under reduced pressure to form an off white solid (1.49 g, 90 %). The title product, from ^{1}H NMR was a mixture of 4-bromo-2,2'-bipyridine-N-oxide and the de-oxygenated product 4-bromo-2,2'-bipyridine, and was used in the subsequent step without any purification. ESI-LRMS $[C_{10}H_7{}^{79}BrN_3O_3]^+$ (+) *m/z* 251.1.

7.6.63 4-Bromo-2, 2'-bipyridine [bpyr-Br], (57)[18]

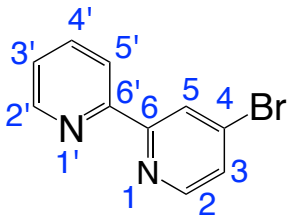

Phosphorus tribromide (PBr_3) (11.4 g, 4 mL, 42.0 mmol) was added to a solution of 4-bromo-2,2'-bipyridine-N-oxide (1.49 g, 5.96 mmol) in anhydrous $CHCl_3$ (24 mL) at 0 ^{o}C. The yellow solution was heated at 65 ^{o}C for 3 h under an inert atmosphere of argon. After cooling to room temperature the solvent was removed under reduced pressure to form a dark brown residue, and was cautiously quenched with NaOH (2 M, 100 mL). The resulting solution was extracted into CH_2Cl_2 (3 x 100 mL) and dried over $MgSO_4$. The solvent was removed under reduced pressure to form the title compound as an off-white solid

(1.31 g, 92 %) that was used in subsequent steps without any further purification. m.p. 52-54 ^{o}C (Lit = 51-53 ^{o}C)[19]; ^{1}H (400 MHz, $CDCl_3$) 8.71 (1 H, ddd, *J* 5, 2, 1, $H^{2'}$), 8.65 (1 H, dd, *J* 2, 1, H^{5}), 8.51 (1 H, dd, *J* 5, 1, H^{2}), 8.41 (1 H, dt, *J* 8, 1, $H^{5'}$), 7.85 (1 H, td, *J* 8, 2, $H^{4'}$), 7.50 (1 H, dd, *J* 5, 2, H^{3}), 7.36 (1 H, ddd, *J* 8, 5, 1, $H^{3'}$); ^{13}C (400 MHz, $CDCl_3$) 157.4 (C^{6}), 154.8 ($C^{6'}$), 149.8 (C^{2}), 149.3 ($^{2'}$), 137.0 ($C^{4'}$), 134.0 (C^{4}), 126.9 (C^{3}), 124.5 (C^{5}), 124.4 (C^{3}), 121.4 ($C^{5'}$); ESI-LRMS $[C_{10}H_7{}^{79}BrN_2]^+$ (+) *m/z* 235.3; ESI-HRMS calcd for $[C_{10}H_7{}^{79}BrN_2]^+$ 234.9871 found 234.9878.

7.6.64 [Ru(2,2'-bipyridine)2(4-bromo-2,2'-bipyridine)][PF_6]$_2$, (58)[20]

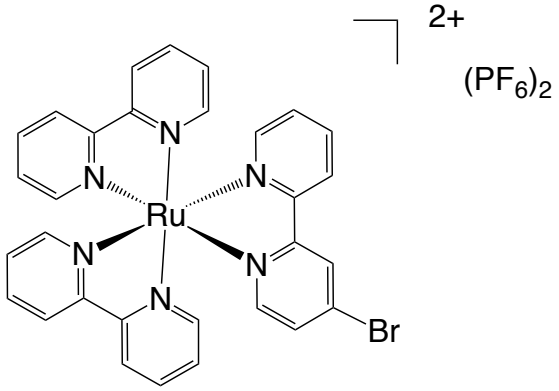

$AgNO_3$ (51.4 mg, 0.30 mmol) was added to a solution of $Ru(bpy)_2Cl_2.2H_2O$ (61.9 mg, 0.12 mmol) in anhydrous methanol (5 mL). The reaction mixture was stirred at room temperature in the dark for 3 h under an inert atmosphere of argon. The suspension was filtered through a celite plug and the filtrate was added to 4-bromo-2-2'-bipyridine, (**57**) (32.2 mg, 0.14 mmol). The dark red solution was heated at 65 ^{o}C in the dark for 21 h under an intert atmosphere of argon. The solution was removed under reduced pressure, dissolved in the minimum amount of acetonitrile and dropped onto a saturated solution of KPF_6. The precipitate was isolated by centrifuge and washed with water and ether to form the title compound as a orange / red solid (40.9 mg, 49 %);^{1}H (700 MHz, $(CD_3)_2CO$) 9.03 (1 H, t, *J* 2), 8.92 (1 H, d, *J* 8), 8.81 – 8.79 (4 H, m), 8.23 – 8.18 (6 H, m), 8.07 (1 H, d, *J* 6), 8.04 – 8.01 (3 H, m), 7.94 (1 H, dd, *J* 6, 2), 7.75 – 7.73 (1 H, m), 7.61 – 7.55 (5 H, m); ^{13}C ($CDCl_3$, 176 MHz) 158.4, 157.3, 157.2, 157.1, 157.0, 156.2, 152.3, 152.0, 151.9, 151.8, 151.7, 138.1, 138.0, 133.8, 130.8, 128.4, 127.7, 125.1,

124.2; ESI-LRMS $[C_{30}H_{23}{}^{79}BrN_6Ru]^{2+}$ (+) *m/z* 324.2; ESI-HRMS calcd for $[C_{30}H_{23}{}^{79}BrN_6Ru]^{2+}$ 324.0107 found, 324.0091.

7.6.65 $[Ru(bpy)_2(bpy\text{-}^tBu\text{-}APTRA)][PF_6]_2$, (59)

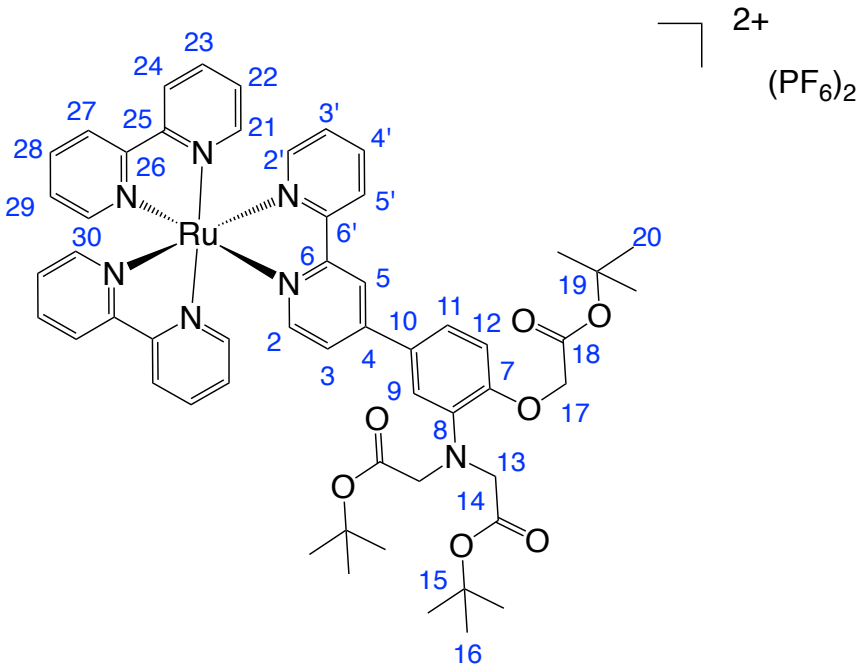

$Pd(PPh_3)_4$ (10.4 mg, 0.009 mmol) was added to a solution of $[Ru(bpy)_2(bpyBr)][PF_6]_2$ (64.9 mg, 0.069 mmol), (**50**) (48.3 mg, 0.084 mmol) and Na_2CO_3 (44.5 mg in 280 μL H_2O, 0.42 mmol) in DMSO (5.3 mL). The reaction mixture was degassed by three free-pump-thaw cycles, and heated under an inert atmosphere of argon at 85 °C for 22 h. After cooling to room temperature the solution was diluted with acetonitrile (3 mL), an insoluble black precipitate was removed by centrifuge, and washed with acetonitrile. The combined yellow filtrates were added to a saturated solution of KPF_6, the precipitate formed was isolated using a centrifuge and washed with water and ether. Recrystallisation from methanol / diethyl ether formed the title compound as an orange / red solid (38.7 mg, 43 %); ^1H (700 MHz, $(CD_3)_2CO$) 8.98 – 8.96 (2 H, m), 8.82 – 8.80 (4 H, m), 8.23 – 8.19 (5 H, m), 8.16 (1 H, d, *J* 5), 8.05 – 8.04 (4 H, m), 7.98 (1 H, d, *J* 6), 7.76 (1 H, dd, *J* 6, 2), 7.59 – 7.56 (5 H, m), 7.52 (1 H, dd, *J* 8, 2) 7.39 (1 H, d, *J* 2), 7.06 (1 H, d, *J* 9), 4.74 (2 H, s), 4.18 (4 H, s), 1.47 (9 H, s), 1.39 (18 H, s); ^{13}C ($CDCl_3$, 151 MHz) 170.0 (C^{18}), 167.5 (C^{14}), 157.4 (Cq), 157.3 (Cq), 157.2 (Cq), 157.2 (Cq), 157.2 (Cq), 157.2 (Cq), 151.8 (Cq), 151.7 (CH), 151.7 (CH),

151.5 (CH), 149.5 (CH), 140.4 (Cq), 138.0 (CH), 137.9 (CH), 128.6 (Cq), 127.8 (CH), 124.4 (CH), 124.3 (CH), 121.1 (CH), 121.1 (CH), 120.5 (-CH), 118.2 (CH), 114.2 (CH), 81.6 (C^{15}), 80.4 (C^{19}), 65.7 (C^{17}), 54.2 (C^{13}), 27.4 (C^{20}), 27.3 (C^{16}); ESI-LRMS $[C_{54}H_{57}N_6O_7Ru]^{2+}$ (+) *m/z* 509.7; ESI-HRMS calcd for $[C_{54}H_{57}N_6O_7Ru]^{2+}$ 509.6768 found, 509.6731.

7.6.66 $[Ru(bpy)_2(bpy\text{-}APTRA)][PF_6]_2$, $[Ru.bL^2]$, (60)

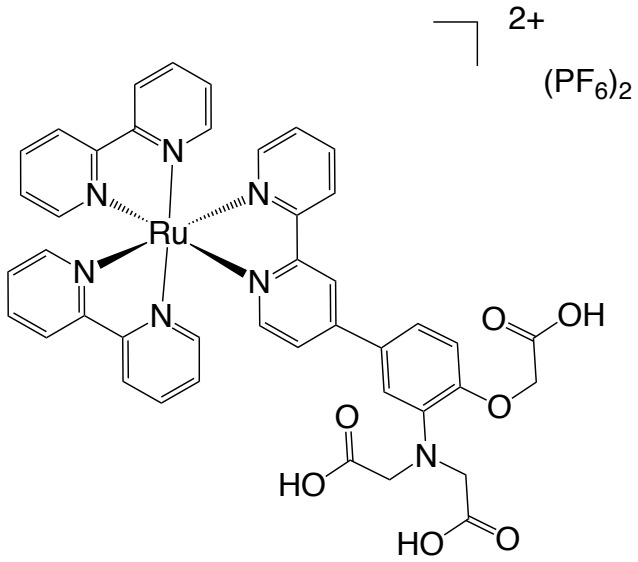

$[Ru(bpy)_2(bpy\text{-}^tBu\text{-}APTRA)][PF_6]_2$, (**59**) (38.2 mg, 0.05 mmol) was dissolved in anhydrous CH_2Cl_2 (1 mL) and TFA (1 mL) and stirred at room temperature for 24 h under an inert atmosphere of argon. The solvent was removed under reduced pressure. CH_2Cl_2 was added and the solvent was removed under reduced pressure to form an orange residue. The complex was dissolved in the minimum amount of CH_3OH and precipitated out of a saturated solution of KPF_6, to form the title compound in quantitative conversion.

7.6.67 $[Ir(ppy)_2(bpy\text{-}Br)]PF_6$, (61) [21]

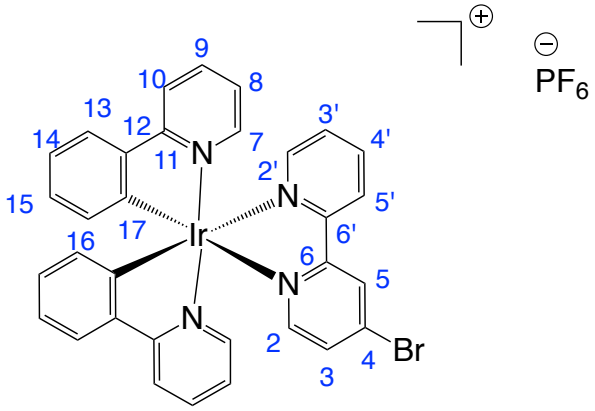

$[Ir(ppy)_2(\mu Cl)]_2$ (121.2 mg, 0.11 mmol) was suspended in methanol (7.8 mL), before 4-bromo-2,2'-bipyridine, (**57**) (58.7 mg, 0.25) was added in a solution of CH_2Cl_2 (6 mL). The reaction mixture was heated at 65 ^oC for 2 h, before being cooled to room temperature. The solvent was removed under reduced pressure to form an orange solid which was dissolved in the minimum amount of acetonitrile / water (1:1) and added drowse to a saturated solution of KPF_6. The orange precipitate formed was collected using a centrifuge and washed with water. The solvent was removed under reduced pressure to form the title compound as a yellow solid. ^1H (400 MHz, $(CD_3)_2CO$) 9.10 (1 H, s), 8.97 (1 H, d, *J* 8), 8.34 (1 H, td, *J* 8,2), 8.25 (2 H, m), 8.12 (1 H, d, *J* 6), 8.01 – 7.94 (5 H, m), 7.91 (2 H, d, *J*, 8), 7.85 (1 H, d, *J* 6), 7.76 (1 H, m), 7.20 – 7.15 (2 H, m), 7.07 – 7.03 (2 H, m, H), 6.95 – 6.91 (2 H, m), 6.35 (2 H, d, *J*, 8); ESI-LRMS $[C_{32}H_{24}{}^{79}Br^{191}IrN_4]^+$ (+) *m/z* 733.1; ESI-HRMS calcd for $[C_{32}H_{24}{}^{79}Br^{191}IrN_4]^+$ 733.0712 found, 733.0709.

7.6.68 [Ir(ppy)$_2$(bpy-^{t}BuAPTRA)]PF$_6$, (62)

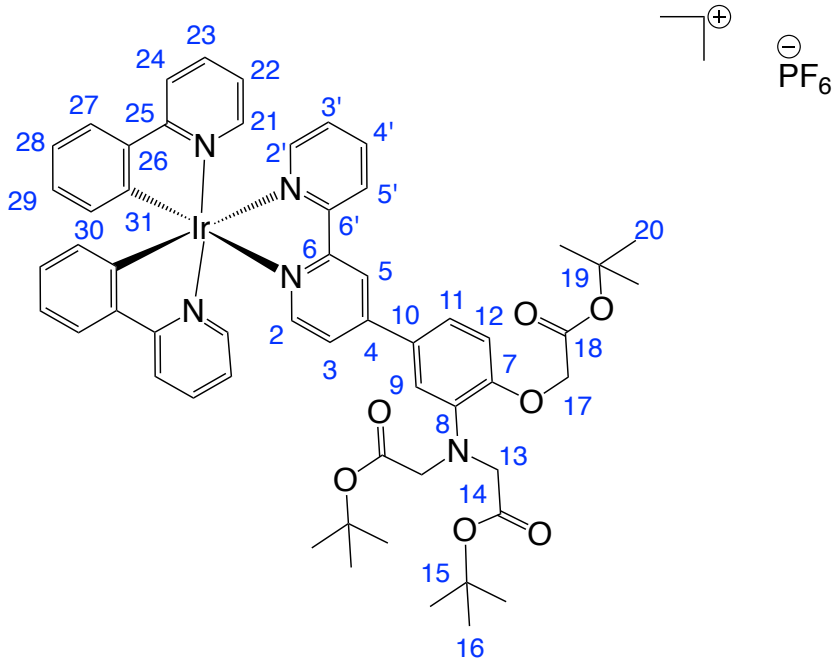

$(PdPPh_3)_4$ (16.9 mg, 0.015 mmol) was added to a solution of $[Ir(ppy)_2(bpy\text{-}Br)]PF_6$ (**61**) (112.8 mg, 0.12 mmol) (119.4 mg, 0.2 mmol) and Na_2CO_3 (78 mg in 480 μL H_2O, 0.74 mmol) in DMSO (9 mL). The reaction mixture was degassed by three free-pump-thaw cycles, and heated at 85 ^oC under an inert atmosphere of argon for 20 h. After cooling to room temperature the solution was diluted with acetonitrile (4 mL), an insoluble black precipitate was removed by centrifuge, and washed with acetonitrile. The combined yellow filtrates were added to a saturated solution of KPF_6, the precipitate formed was isolated using a centrifuge and washed with water. Purification by alumina column chromatography (gradient 100 % hexane to 100 % ethyl acetate) formed the title compound as a bright yellow solid (40 mg, 25 %) R_f (silica, ethyl acetate) = 0.7; ^1H (600 MHz, CH_3OD) 8.80 (2 H, m,), 8.15 (1 H, t, *J* 8,), 8.10 (2 H, t, *J* 8), 8.02 (1 H, d, *J* 5), 7.94 (1 H, d, *J* 6), 7.82 (4 H, m), 7.71 (1 H, d, *J* 6), 7,67 (1 H, br m), 7.63 (1 H, d, *J* 6), 7.52 (1 H, br t, *J* 5), 7.46 (1 H, dd, *J* 2, 8), 7.34 (1 H, d, *J* 2), 7.04 (2 H, t, *J* 7), 7.00 (3 H, m), 6.87 (2 H, td, *J* 7, 2), 6.30 (2 H, dd, *J* 4, 8), 4.68 (2 H, s), 4.12 (4 H, s), 1.47 (9 H, s), 1.40 (18 H, s); ^{13}C (151 MHz, MeOD) 171.1, 168.0, 167.8, 156.2, 151.7, 151.2, 150.5, 150.2, 150.1, 148.6, 148.5, 143.8, 140.0, 139.1, 138.2, 131.4, 130.1, 129.0, 128.0, 124.7, 124.6, 124,5, 123.1, 122.2, 121.3, 121.0, 119.6, 118.3, 113.8, 82.2, 81.2, 65.5, 54.5, 26.9, 26.9;

ESI-LRMS $[C_{55}H_{59}{}^{191}IrN_5O_7]^+$ (+) *m/z* 1108.6; ESI-HRMS calcd for $[C_{55}H_{59}{}^{191}IrN_5O_7]^+$ 1104.4021 found, 1104.4031.

7.6.69 $[Ir(ppy)_2(bpy\text{-}APTRA)]PF_6$, (63)

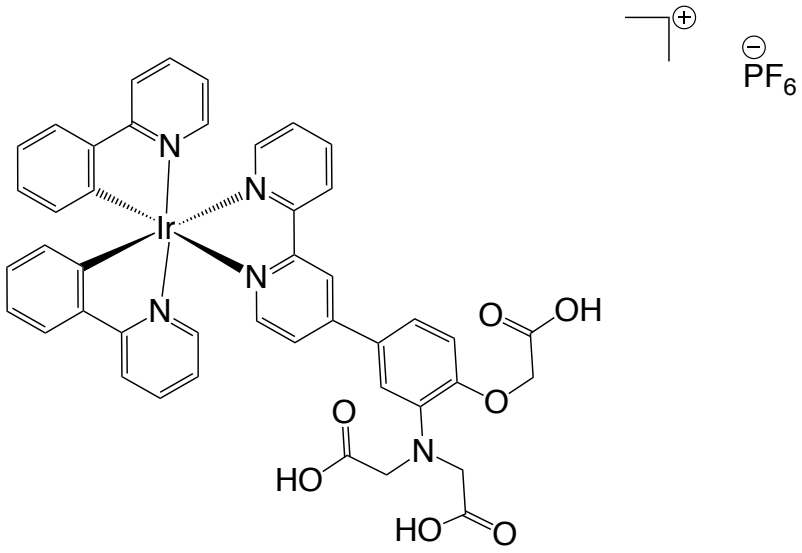

$[Ir(ppy)_2(bpy\text{-}tBu\text{-}APTRA)]PF_6$, (**62**) (40.0 mg, 0.04 mmol) was dissolved in anhydrous CH_2Cl_2 (1 mL) and TFA (1 mL) and stirred at room temperature for 24 h under an inert atmosphere of argon. The solvent was removed under reduced pressure. CH_2Cl_2 was added and the solvent was removed under reduced pressure to form an orange residue. The complex was dissolved in the minimum amount of CH_3OH and precipitated out of a saturated solution of KPF_6. to form the title compound in quantitative conversion.

7.7 References:

[1] A. Beeby, I. M. Clarkson, R. S. Dickins, S. Faulkner, L. Royle, A. S. de Sousa, J. A. G. Williams, M. Woods and D. Parker, *J. Chem. Soc., Perkin Trans. 2.*, 1999, 493-503.

[2] K. Nakamaru, *Bull, Chem. Soc. Jpn.*, 1982, **55**, 2697-2705.

[3] B. Gelerent, A. Findeisen, A. Stein and J. A. Poole, *J. Chem. Soc. Faraday Trans II.*, 1973, **70**, 939.

[4] A. M. Brouwer, *Pure Appl. Chem.,* 2001, **83**, 2213-2228.

[5] *www.supramolecular.org*

[6] M. J. Frisch, G. W. Trucks, H. B. Schlegel, G. E. Scuseria, M. A. Robb, J. R. Cheeseman, G. Scalmani, V. Barone, B. Mennucci, G. A. Petersson, H. Nakatsuji, M. Caricato, X. Li, H. P. Hratchian, A. F. Izmaylov, J. Bloino, G. Zheng, J. L. Sonnenberg, M. Hada, M. Ehara, K. Toyota, R. Fukuda, J. Hasegawa, M. Ishida, T. Nakajima, Y. Honda, O. Kitao, H. Nakai, T. Vreven, Jr., J. A. Montgomery, J. E. Peralta, F. Ogliaro, M. Bearpark, J. J. Heyd, E. Brothers, K. N. Kudin, V. N. Staroverov, R. Kobayashi, J. Normand, K. Raghavachari, A. Rendell, J. C. Burant, S. S. Iyengar, J. Tomasi, M. Cossi, N. Rega, J. M. Millam, M. Klene, J. E. Knox, J. B. Cross, V. Bakken, C. Adamo, J. Jaramillo, R. Gomperts, R. E. Stratmann, O. Yazyev, A. J. Austin, R. Cammi, C. Pomelli, J. W. Ochterski, R. L. Martin, K. Morokuma, V. G. Zakrzewski, G. A. Voth, P. Salvador, J. J. Dannenberg, S. Dapprich, A. D. Daniels, O. Farkas, J. B. Foresman, J. V. Ortiz, J. Cioslowski, D. J. Fox, *Gaussian 09*, Revision A.02, Gaussian, Inc., Wallingford CT, 2009.

[7] (a) A. D. Becke, *J. Chem. Phys.,* 1993, **98**, 5648-5652; (b) C. Lee, W. Yang, R. G. Parr, *Phys. Rev. B.,* 1988, **37**, 785-789.

[8] (a) G. A. Petersson, M. A. Al-Laham, *J. Chem. Phys.* 1991, **94**, 6081-6090; (b) G. A. Petersson, A. Bennett, T. G. Tensfeldt, M. A. Al-Laham, W. A. Shirley, J. Mantzaris, *J. Chem. Phys.* 1988, **89**, 2193-2218; (c) M. J. Frisch, J. A. Pople, J. S. Binkley, *J. Chem. Phys.* 1984, **80**, 3265-3269; (d) A. D. McLean, G. S. Chandler*, J. Chem. Phys*. 1980, ***72***, 5639-5648.

[9] J. Tomasi, B. Mennucci, E. Cancès, *J. Mol. Struct. (Theochem)*, 1999, **464**, 211-226.

[10] R. Hata, H. Nonaka, Y. Takakusagi, I. Yoichi, K. Ichikawa and S, Sando, *Chem. Commun.*, 2015, **51**, 12290-12292.

[11] M. A. Zolfigol., G. Chehardoli., S. Salehzadeh., H. Adams., M. D. Ward, *Tett Lett.*, 48, **2007**, 7969 – 7973.

[12] J. W. Walton, PhD thesis. Title: Highly Emissive Europium Complexes, 2012. Durham University.

[13] WO2010 / 139481 A1, 2010.

[14] L. S. Natrajan, A. J. L. Villaraza, A. M. Kenwright and S. Faulkner, *Chem. Commun.*, 2009, 6020-6022.

[15] U. Brath, S. I. Swamy., A. X. Veiga., C-C, Tung., F. Van Petegem, *J. Am. Chem. Soc.*, **2015**, 137, 11391-11398.

[16] R. C. Jones, A. J Canty, J. A. Deverell, M. G. Gardiner, R. M. Guijt, T. Rodemann, J. A. Smith and V-A. Tolhurst, *Tetrahedron.*, 2009, **65**, 7474- 7481.

[17] B. Metten, M. Smet, N. Boens and W. Dehaen, *Synthesis.*, 2005, **11**, 1838-1844.

[18] D. Wenkert and R. B. Woodward, *J. Org. Chem.*, 1983, **48**.

[19] K. Kodama, A. Kobayashi, T. Hirose, *Tett Lett.*, 2013, **54**, 5514-5517.

[20] P. Farras, H. Waller and A. C. Benniston, *Chem. Eur. J.,* 2016, **22**, 1133-1140.

[21] K. J. Arm, PhD thesis. Title: Cross-coupling methodology in the synthesis of luminescent metal complexes and multi-metallic assemblies, 2005. Durham University.

8. Appendix

8.1 pK_a and binding studies

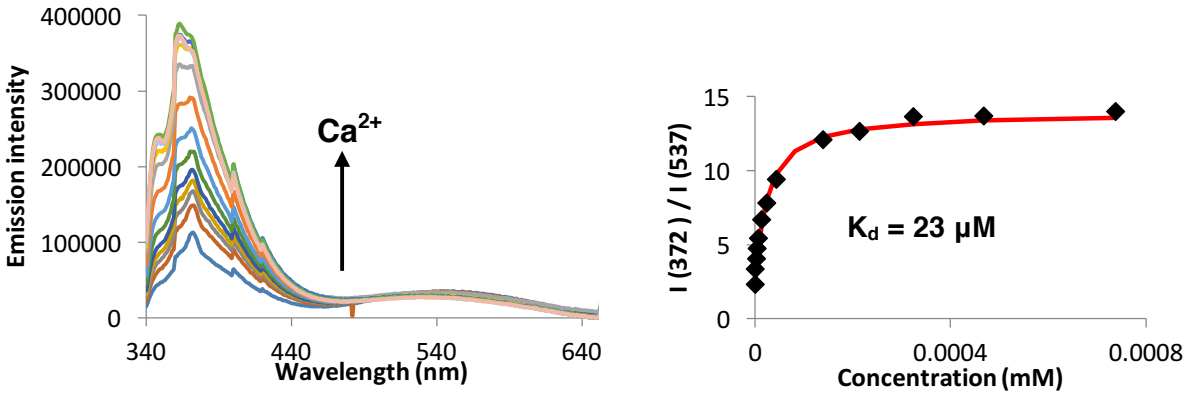

Figure A.1 (Left) emission spectrum of **NapL**[1]; (right) fitting of the emission intensity against the added concentration addition of Ca^{2+} (λ_{ex} = 330 nm). Ligand concentration = 5 µM in 50 mM HEPES, 100 mM KCl, pH 7.21, 298 K

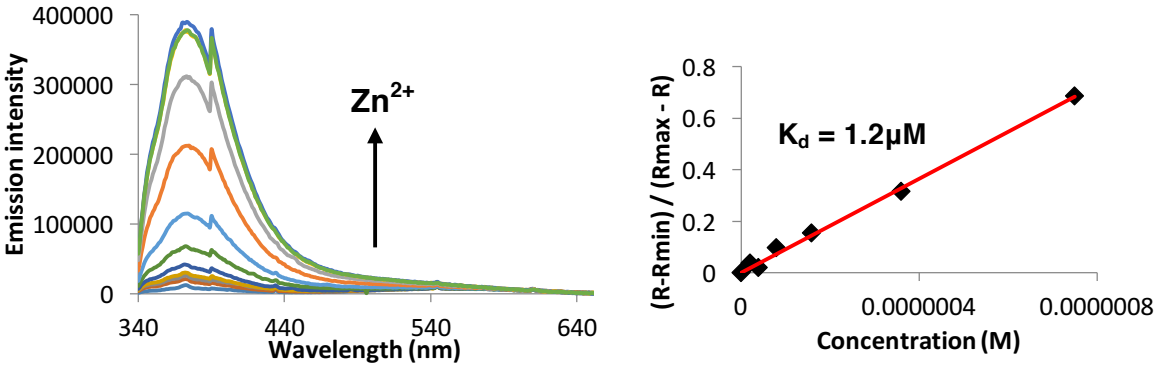

Figure A.2 (Left) emission spectrum of **NapL**[1]; (right) fitting of the emission intensity against the added concentration of Zn^{2+} (λ_{ex} = 330 nm). Ligand concentration = 5 µM in 50 mM HEPES, 100 mM KCl, pH 7.21, 298 K.

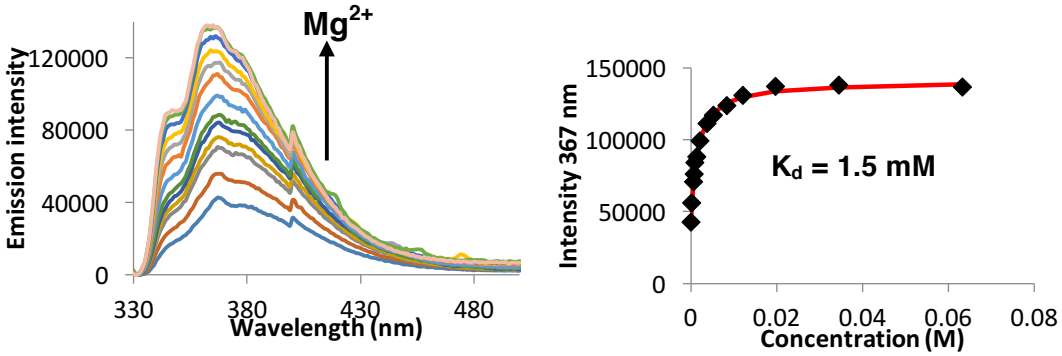

Figure A.3 (Left) emission spectrum of **NapL^2**; (right) fitting of the emission intensity against the added concentration of Mg^{2+} (λ_{ex} = 326 nm). Ligand concentration = 10 μM in 50 mM HEPES, 100 mM KCl, pH 7.21, 298 K

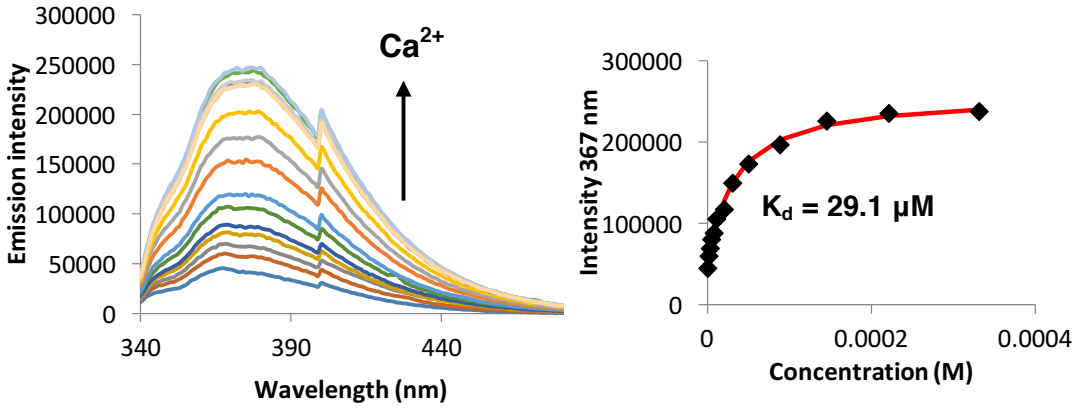

Figure A.4 (Left) emission spectrum of **NapL^2**; (right) fitting of the emission intensity against the added concentration of Ca^{2+} (λ_{ex} = 326 nm). Ligand concentration = 10 μM in 50 mM HEPES, 100 mM KCl, pH 7.21, 298 K

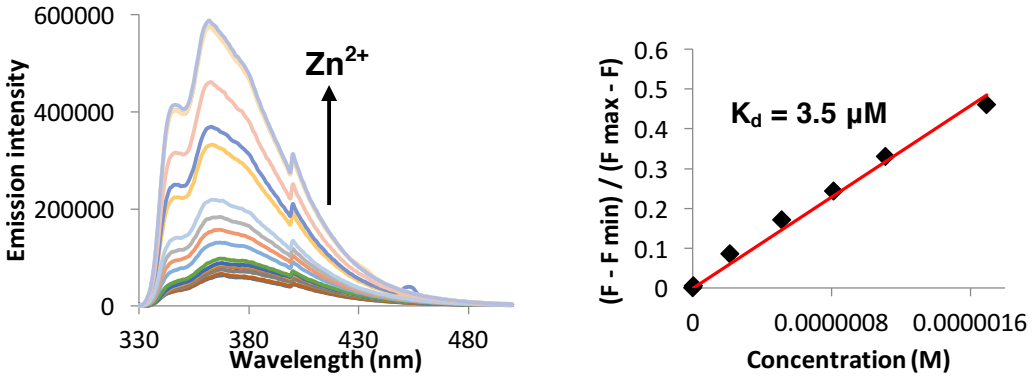

Figure A.5 (Left) emission spectrum of **NapL^2**; (right) fitting of the emission intensity against the added concentration of Zn^{2+} (λ_{ex} = 326 nm). Ligand concentration = 10 μM in 50 mM HEPES, 100 mM KCl, pH 7.21, 298 K.

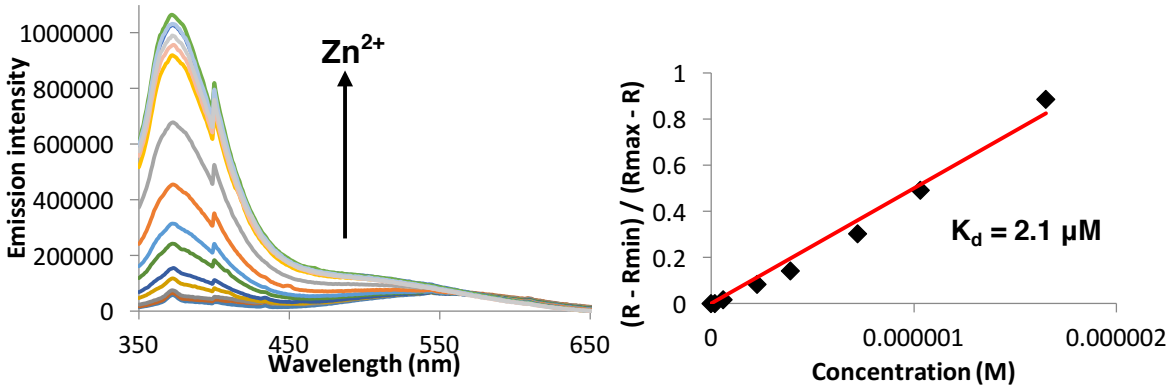

Figure A.6 (Left) emission spectrum of **NapL**^{4}; (right) fitting of the emission intensity against the added concentration of Zn^{2+} (λ_{ex} = 330 nm). Ligand concentration = 10 µM in 50 mM HEPES, 100 mM KCl, pH 7.21, 298 K.

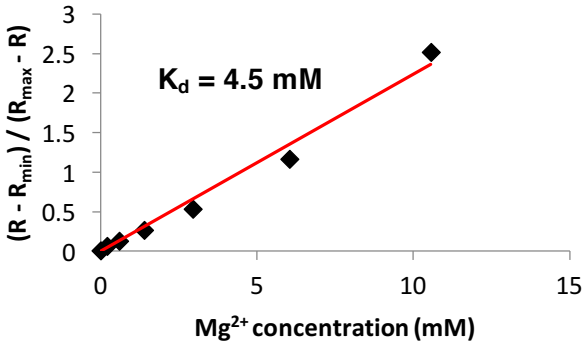

Figure A.7 The calculation for the dissociation constant based on **Equation 7.8** (**Section 7.4**). Comparable dissociation constants were calculated for the binding of Mg^{2+} to **NapL**^{1}, to that measured from www.supramolecular.org in a 1:1 binding model.

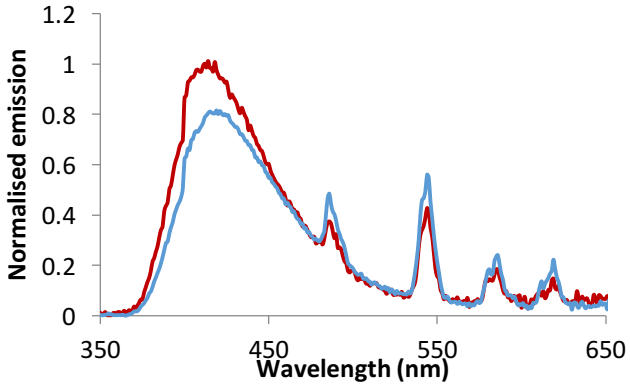

Figure A.8 Normalised emission spectrum of **[Tb.L^2]** in aerated and deoxygenated solutions. λ_{ex} = 315 nm, 298 K in H_2O.

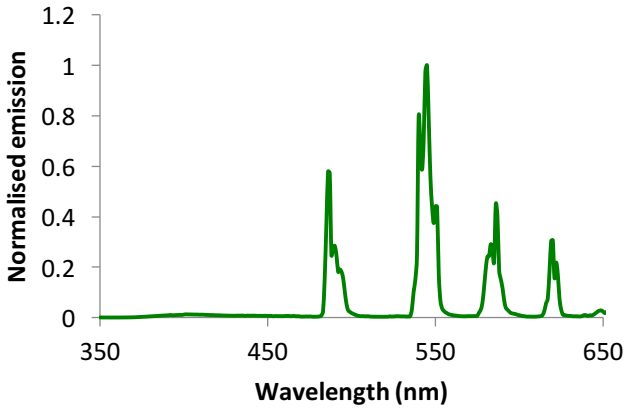

Figure A.9 Normalised emission spectrum of **[Tb.L^2]** in an ethanol glass at 77 K. λ_{ex} = 315 nm.

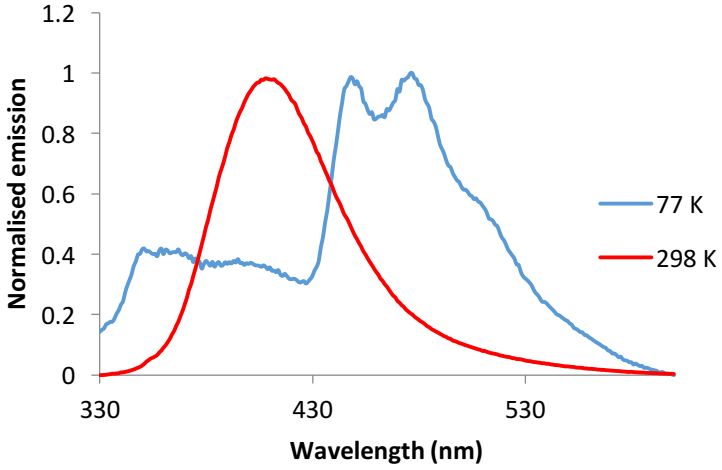

Figure A.10 Normalised emission spectra of of **[Gd.L^1]** in ethanol at room temperature (298 K, red) and 77 K (transparent glass, blue). The shortest-wavelength phosphorescence band was assumed to be the 0-0 transition, λ_{ex}= 320 nm. $\tau_{77\ K}$= 14 ms (λ_{ex}= 320 nm, λ_{em}= 450 nm).

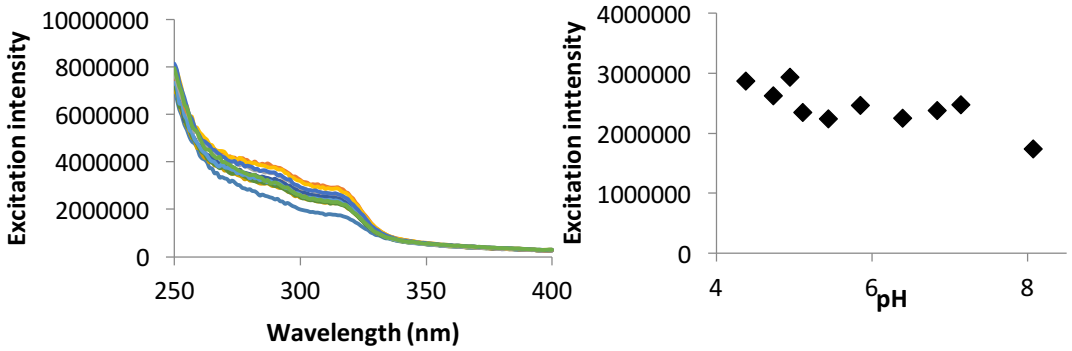

Figure A.11 (Left) excitation spectrum of **[Eu.L^1]**; (right) fitting of the excitation at 313 nm against the pH. **[Eu.L^1]** concentration = 5 µM in 100 mM KCl, 298 K, λ_{em} = 613 nm.

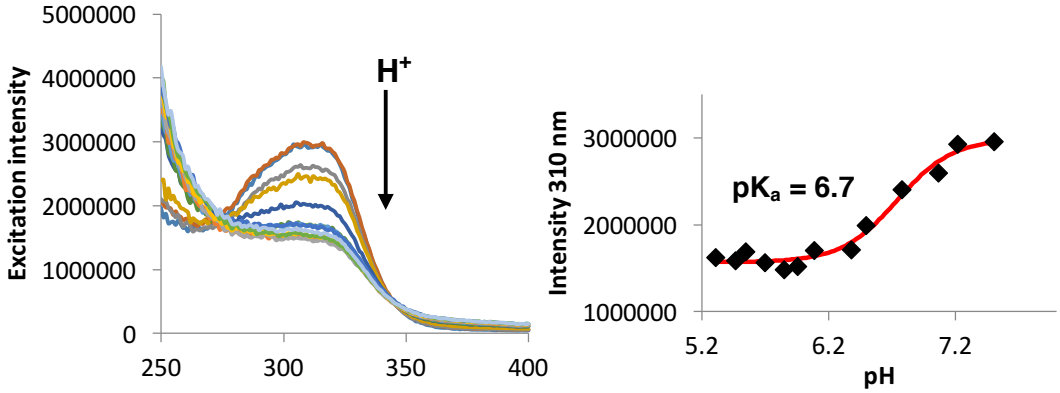

Figure A.12 (Left) excitation spectrum of **[Eu.L^2]**; (right) fitting of the excitation at 305 nm against the pH. **[Eu.L^1]** concentration = 5 µM in 100 mM KCl, 298 K, (λ_{em} = 613 nm).

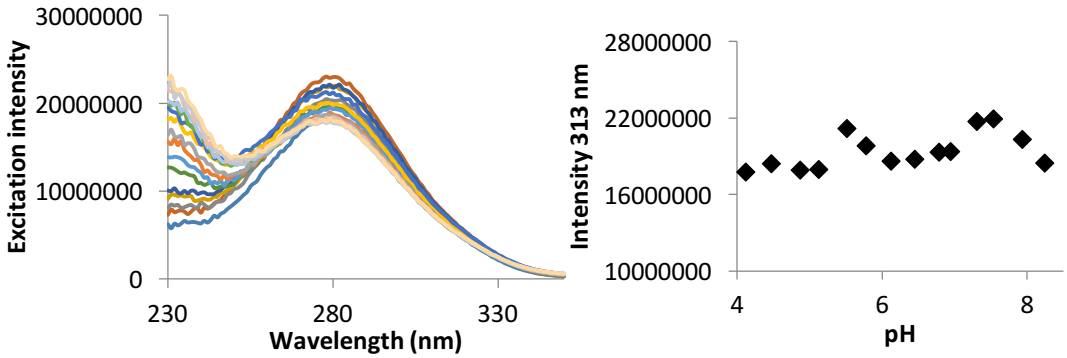

Figure A.13 (Left) excitation spectrum of **[Tb.bL^2]**; (right) fitting of the excitation at 313 nm against the pH. **[Eu.L^1]** concentration = 5 µM in 100 mM KCl, 298 K, (λ_{em} = 544 nm).

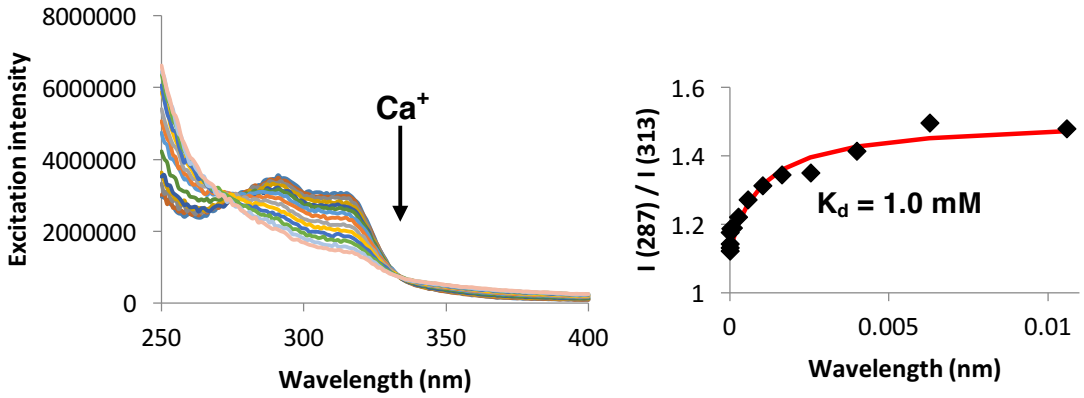

Figure A.14 (Left) excitation spectrum of **[Eu.L^1]**; (right) fitting of the excitation ratio at 287 nm and 313 nm against the added concentration of Ca^{2+} (λ_{em} = 613 nm). Complex concentration = 5 µM in 50 mM HEPES, 100 mM KCl, pH 7.21, 298 K.

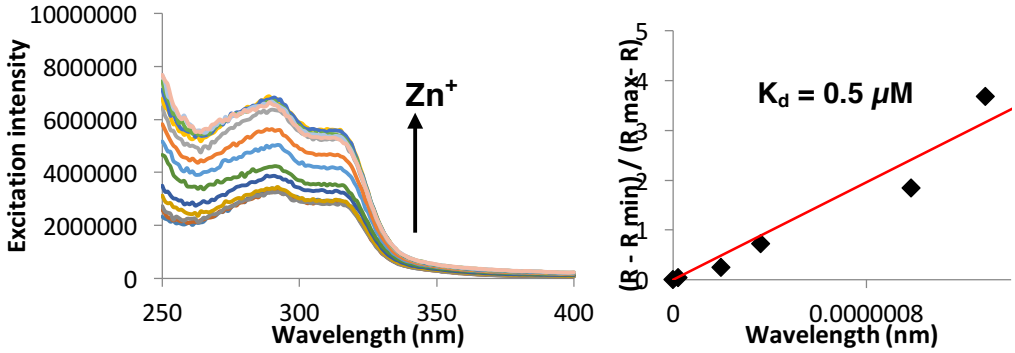

Figure A.15 (Left) excitation spectrum of **[Eu.L^1]**; (right) fitting of the excitation ratio at 287 nm and 313 nm against the added concentration of Zn^{2+} (λ_{em} = 613 nm). Complex concentration = 5 µM in 50 mM HEPES, 100 mM KCl, pH 7.21, 298 K.

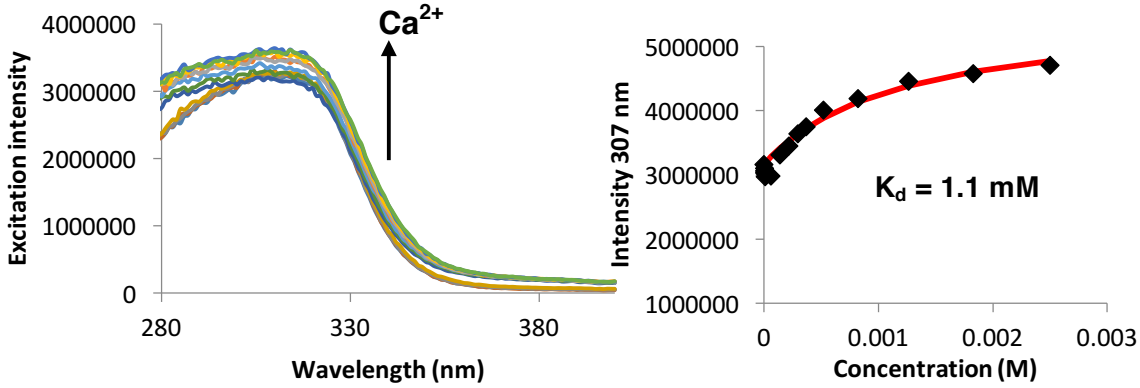

Figure A.16 (Left) excitation spectrum of **[Eu.L^2]**; (right) fitting of the excitation ratio at 307 nm against the added concentration of Ca^{2+} (λ_{em} = 613 nm). Complex concentration = 5 µM in 50 mM HEPES, 100 mM KCl, pH 7.21, 298 K.

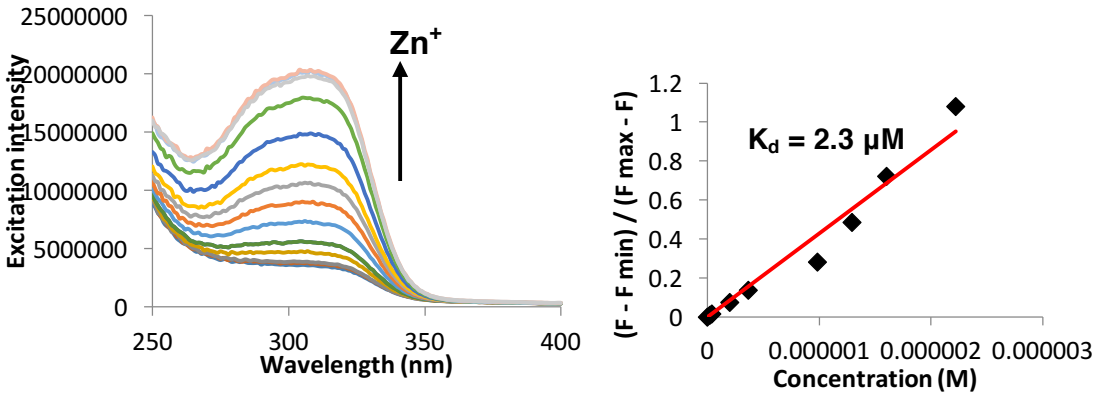

Figure A.17 (Left) excitation spectrum of **[Eu.L^2]**; (right) fitting of the excitation ratio at 307 nm against the added concentration of Zn^{2+} (λ_{em} = 613 nm). Complex concentration = 5 µM in 50 mM HEPES, 100 mM KCl, pH 7.21, 298 K.

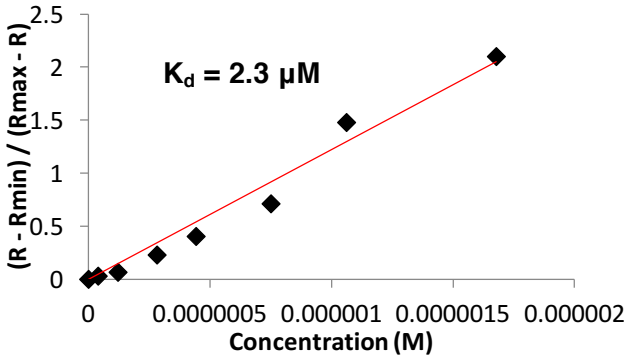

Figure A.18 The ratiometric emission response following the addition of Zn^{2+} to **[Tb.bL^2]**. The dissociation constant was calculated from a ratio of the ΔJ = 2 (486 nm) and ΔJ = 1 (544 nm) emission bands. **[Tb.bL^2]** concentration = 5 µM in 50 mM HEPES, 100 mM KCl, pH = 7.21, λ_{ex} = 280 nm, 298 K.

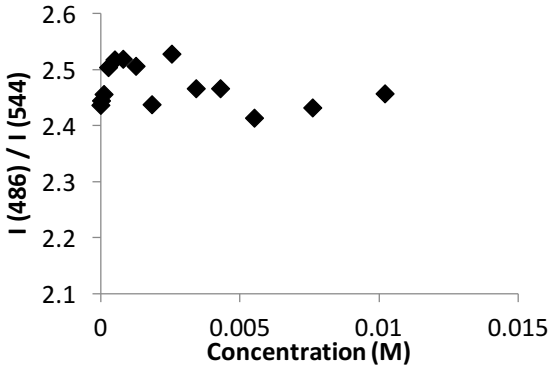

Figure A.19 The non-ratiometric emission response following the addition of Ca^{2+} to **[Tb.bL^2]**. **[Tb.bL^2]** concentration = 5 µM in 50 mM HEPES, 100 mM KCl, pH = 7.21, λ_{ex} = 280 nm, 298 K.

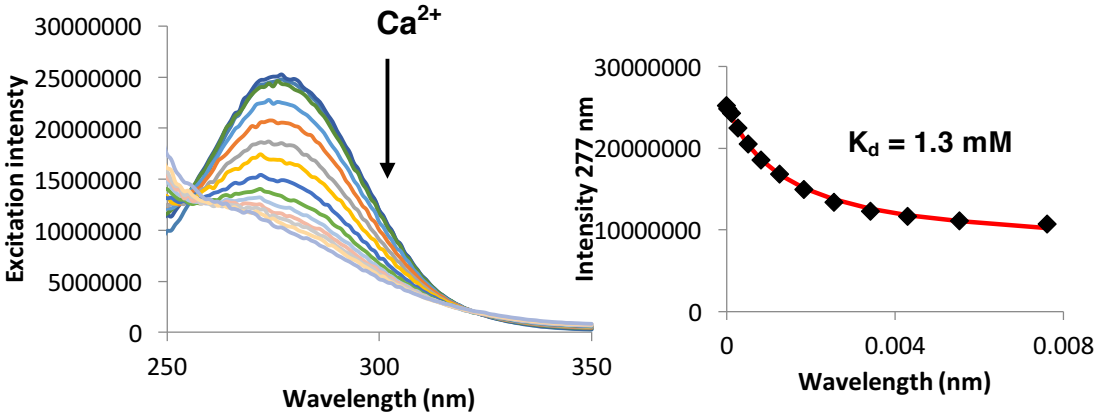

Figure A.20 (Left) excitation spectrum of **[Tb.bL^2]**; (right) fitting of the excitation ratio at 277 nm against the added concentration of Ca^{2+} (λ_{em} = 544 nm). Complex concentration = 5 µM in 50 mM HEPES, 100 mM KCl, pH 7.21, 298 K.

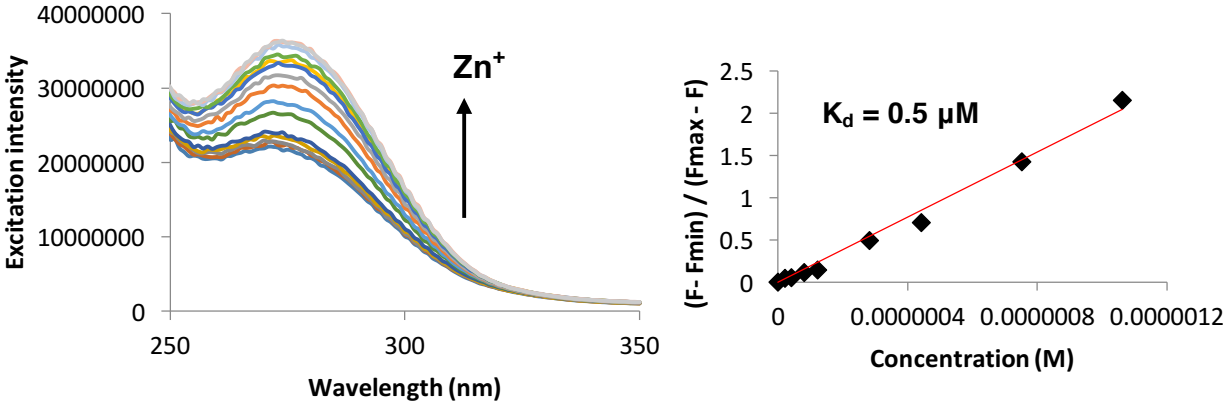

Figure A.21 (Left) excitation spectrum of **[Tb.bL^2]**; (right) fitting of the excitation ratio at 277 nm against the added concentration of Zn^{2+} (λ_{em} = 544 nm). Complex concentration = 5 µM in 50 mM HEPES, 100 mM KCl, pH 7.21, 298 K

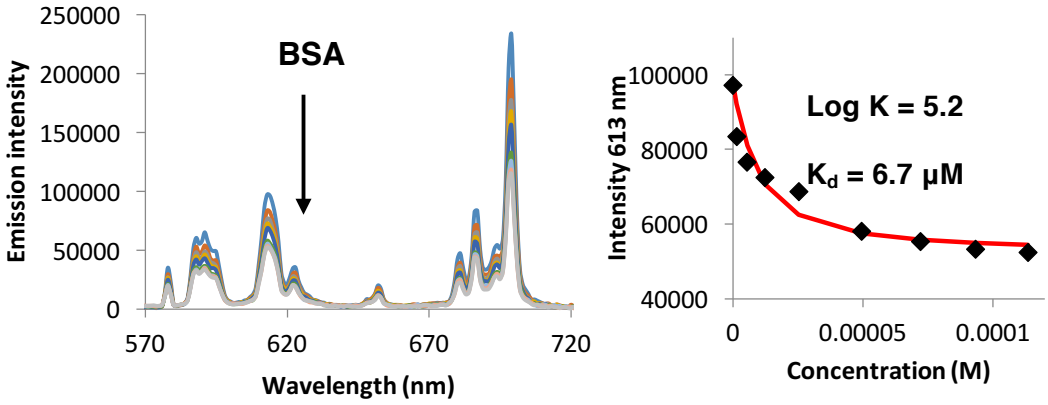

Figure A.22 (Left) emission spectrum of **[Eu.L^2]**; (right) fitting of the emission intensity against the added concentration of BSA, λ_{ex} = 318 nm, 298 K.

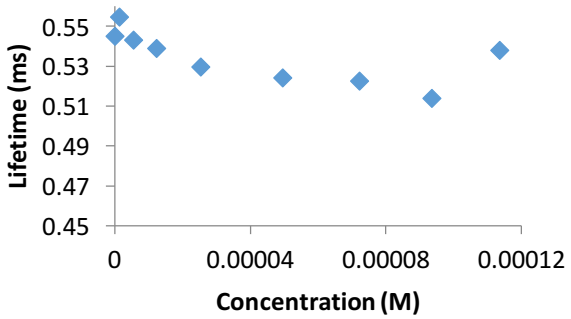

Figure A.23 The effect of the luminescence lifetime of **[Eu.L^2]**, following the addition of BSA. λ_{ex} = 318 nm, λ_{em} = 613 nm 298 K.

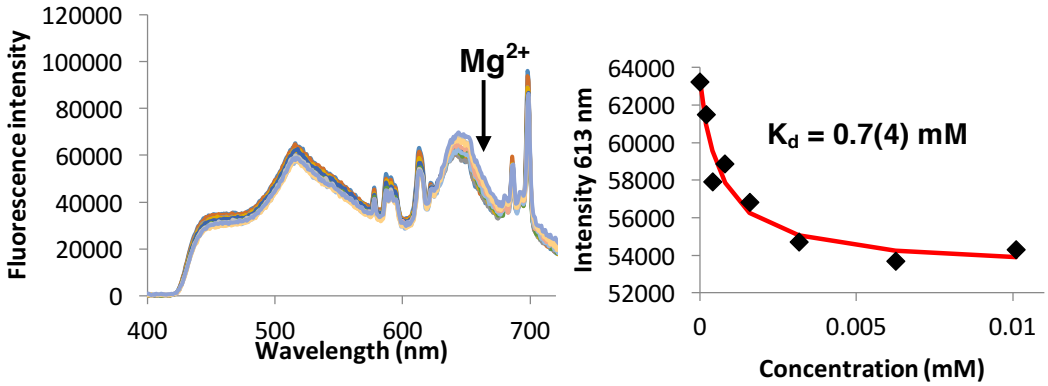

Figure A.24 (Left) The emission spectrum of **[Eu.L^2]** in NCS following the addition of Mg^{2+}. (Right) the fitting of the emission intensity against the concentration of Mg^{2+}. **[Eu.L^2]** concentration = 5 μM, λ_{ex} = 343 nm,298 K.

8.2 Analytical reverse-phase HPLC traces

Reverse phase HPLC was performed at 295 K using a Shimadzu system consisting of a Degassing Unit (DGU-20A_{5R}), a Prominence Preparative Liquid Chromatograph (LC-20AP).

Analytical column 1: Shimadzu ShimPacl VP-ODS.

Analytical column 2: Chromolith RP-18

Table 8.1 Method used for all analytical and semi-preparative HPLC analysis

Time (min)	Solvent A (%)	Solvent B (%)
0	100	0
3	100	0
13	0	100
16	0	100
25	100	0

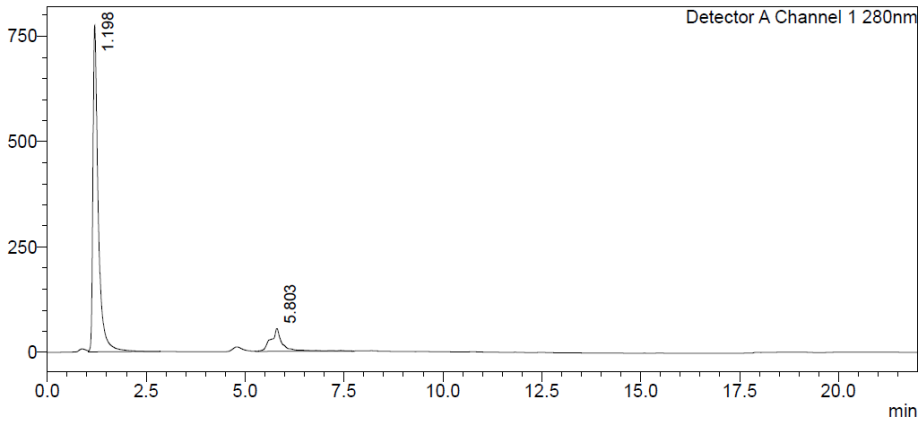

Figure A.25 The analytical reverse-phase HPLC trace for APDAP. Column 1, conditions are shown in **Table 8.1**. λ_{abs} = 280 nm.

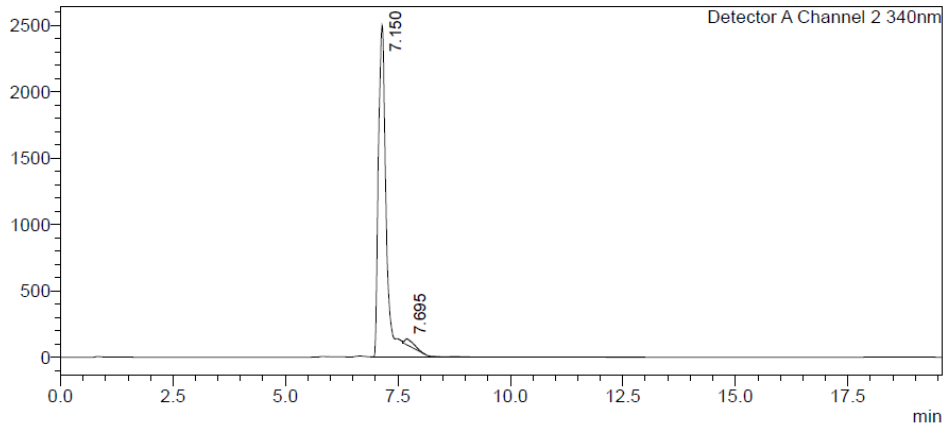

Figure A.26 The analytical reverse-phase HPLC trace for NapL[1]. Column 1, conditions are shown in **Table 8.1**. λ_{abs} = 340 nm.

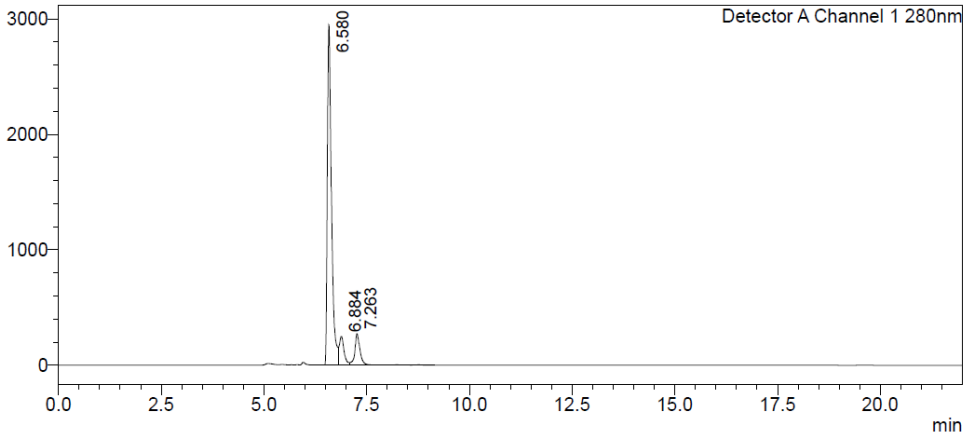

Figure A.27 The analytical reverse-phase HPLC trace for NapL[2]. Column 2, conditions are shown in **Table 8.1**. λ_{abs} = 280 nm.

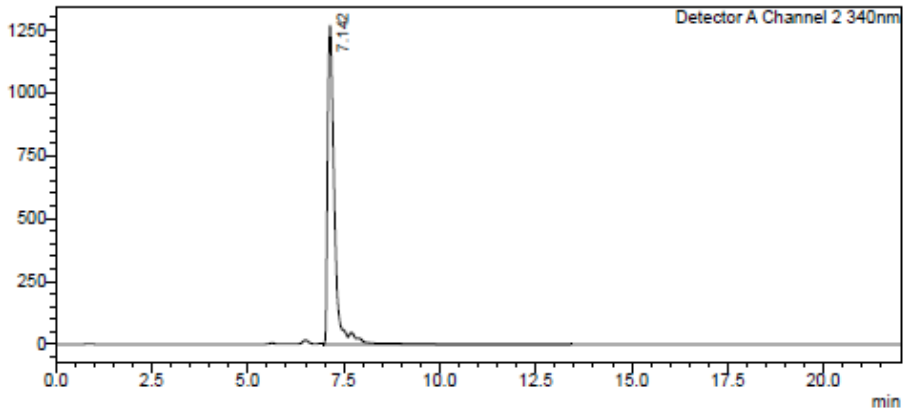

Figure A.28 The analytical reverse-phase HPLC trace for NapL[4]. Column 1, conditions are shown in **Table 8.1**. λ_{abs} = 340 nm.

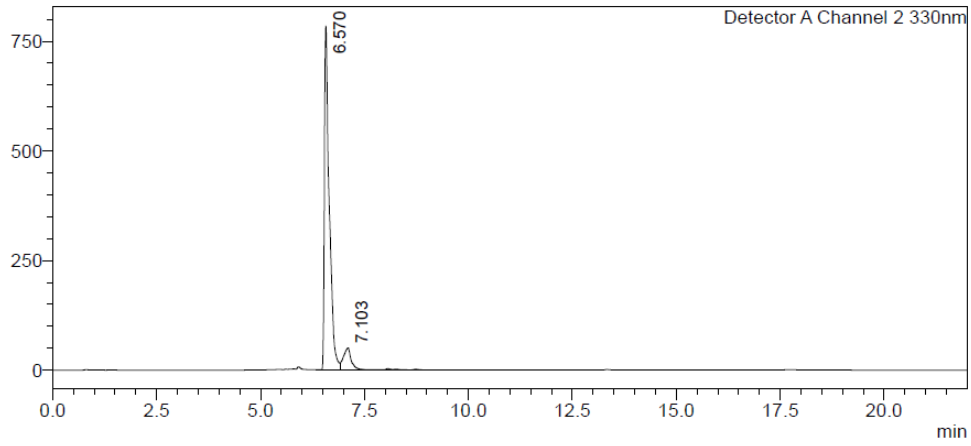

Figure A.29 The analytical reverse-phase HPLC trace for NapL[6]. Column 2, conditions are shown in **Table 8.1**. λ_{abs} = 330 nm.

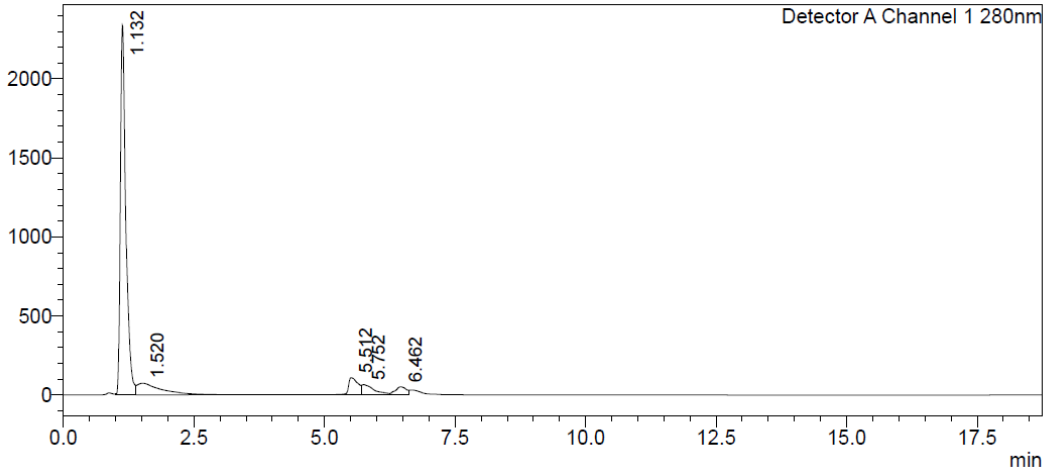

Figure A.30 The analytical reverse-phase HPLC trace for **[Eu.L[1]]**. Column 1, conditions are shown in **Table 8.1**. λ_{abs} = 280 nm.

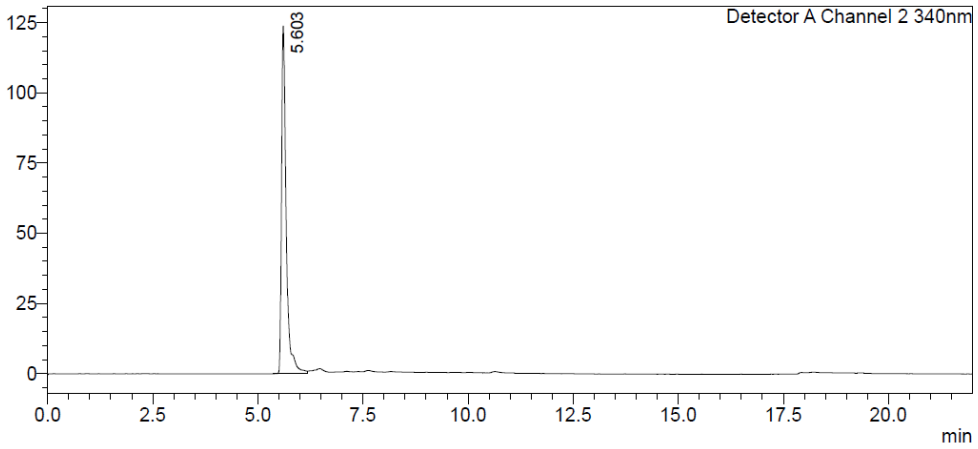

Figure A.31 The analytical reverse-phase HPLC trace for **[Eu.L[2]]**. Column 1, conditions are shown in **Table 8.1**. λ_{abs} = 340 nm.

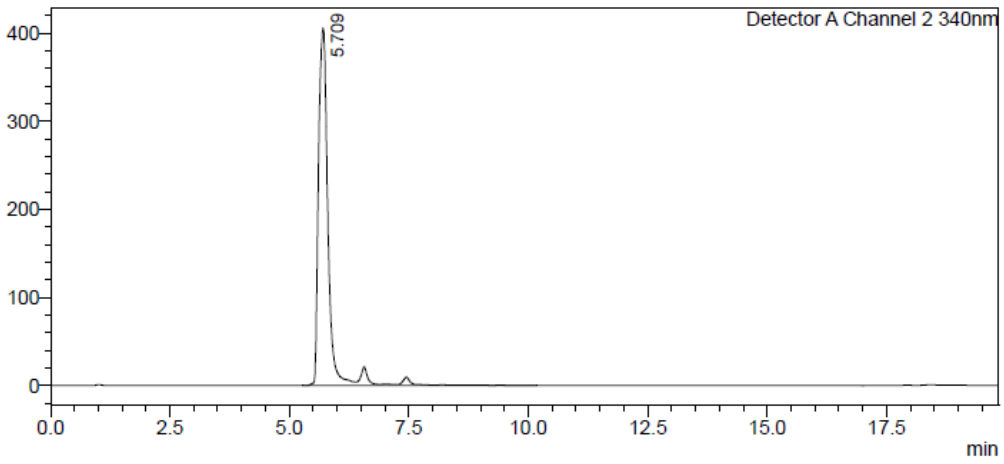

Figure A.32 The analytical reverse-phase HPLC trace for **[Tb.L^2]**. Column 1, conditions are shown in **Table 8.1**. λ_{abs} = 340 nm.

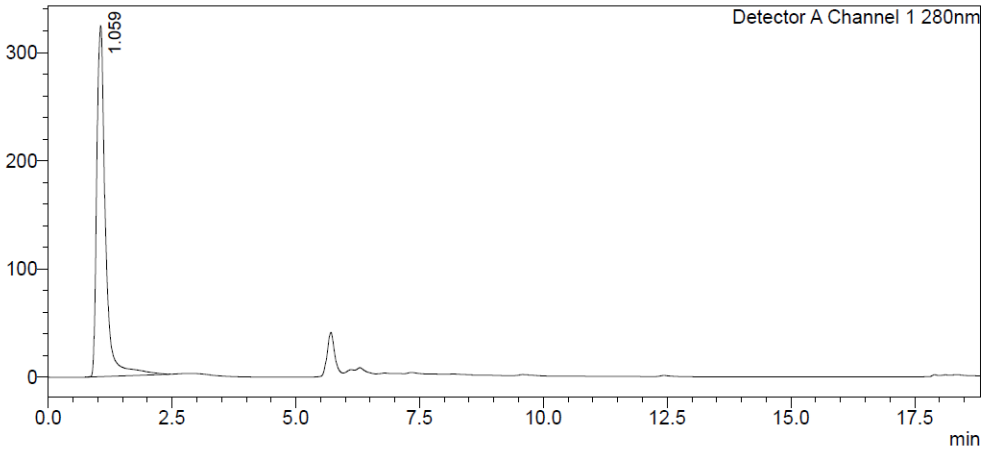

Figure A.33 The analytical reverse-phase HPLC trace for **[Eu.bL^2]** . Column 1, conditions are shown in **Table 8.1**. λ_{abs} = 280 nm.

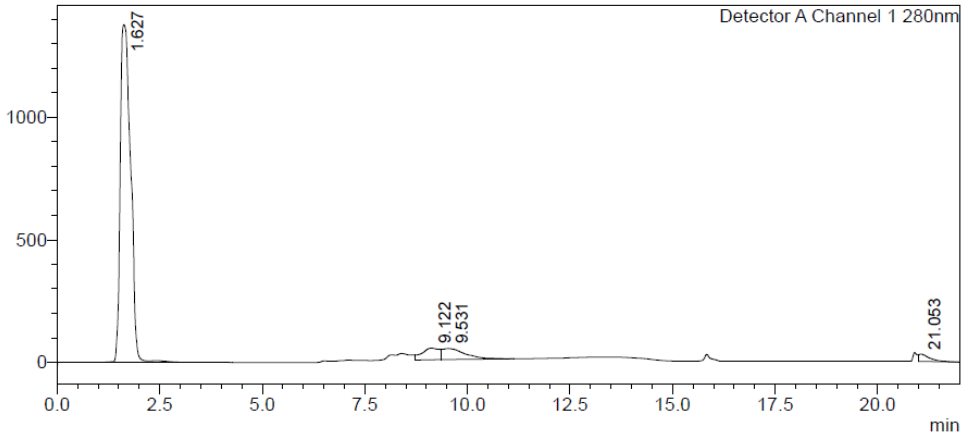

Figure A.34 The analytical reverse-phase HPLC trace for **[Tb.bL^2]**. Column 1, conditions are shown in **Table 8.1**. λ_{abs} = 280 nm.

8.3 Key ligands and complexes

8.3.1 APDAP

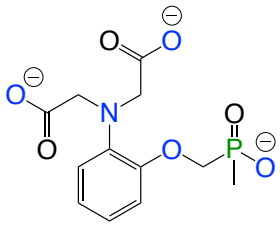

8.3.2 The naphthalene series

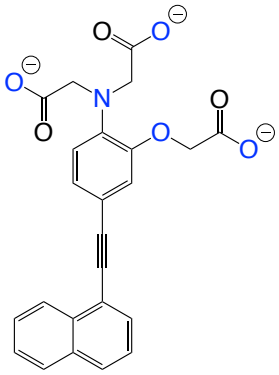

NapL^1

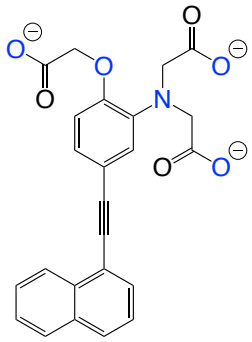

NapL^2

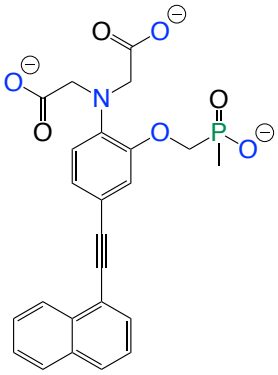

NapL^4

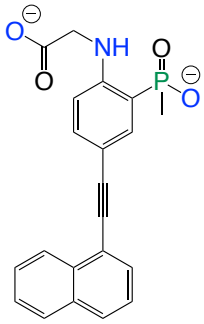

NapL^6

8.3.3 Key lanthanide complexes

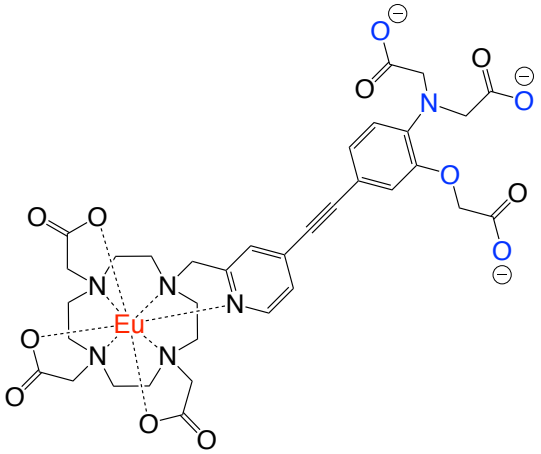

[Eu.L^1]

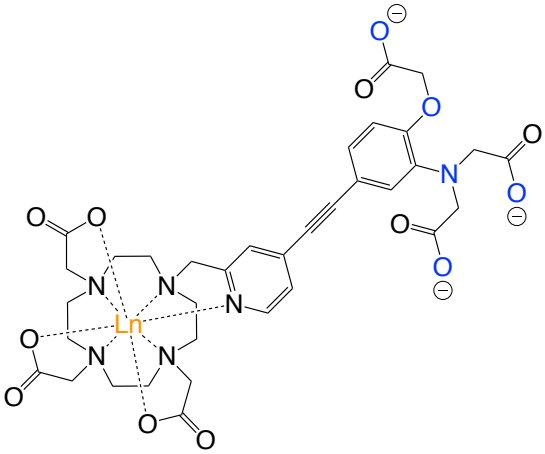

[Eu.L^2]

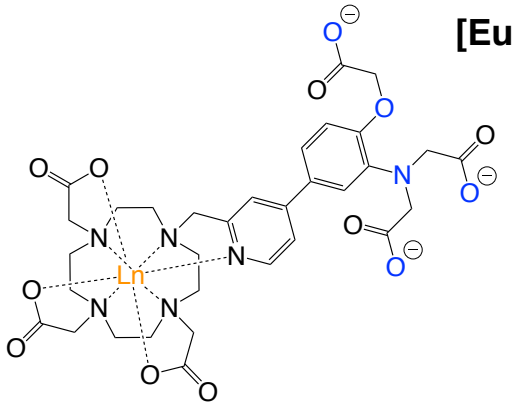

(Ln = Eu^{3+}, Tb^{3+})

[Tb.bL^2]

8.3.4 Ruthenium(II) and Iridium(III) complexes

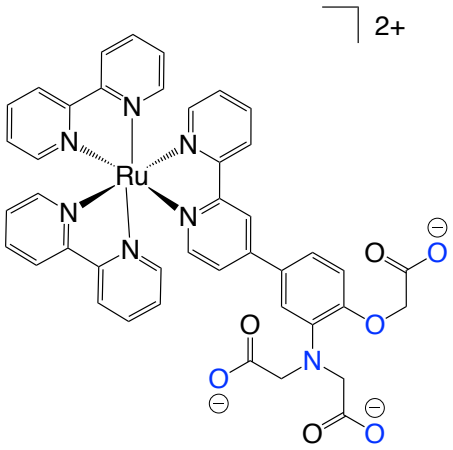

[Ru.bL^2]$^{2+}$

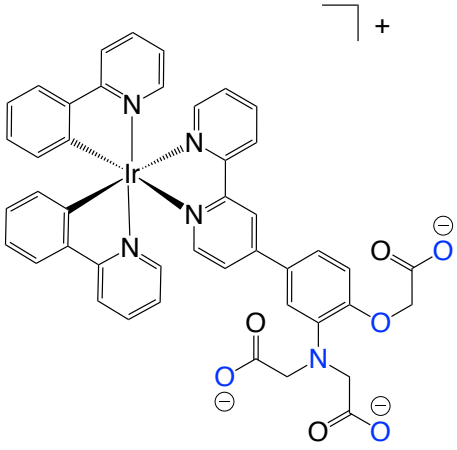

[Ir.bL^2]$^{+}$

8.4 Conferences Attended

- Molecular Photophysics Conference I, Newcastle, 2015.
- 42nd International Conference of Coordination Chemistry (ICCC), Brest, France 2016. Poster presentation 'Synthesis of magnesium-selective ligands and the incorporation into fluorescence-based sensors'.
- Rennes-Durham Symposium, Durham, May 2017.

8.5 Departmental Seminars attended

8.5.1 First year

- Bacterial superglue, spontaneous amide bond formation, and polymers to fish for cancer cells. Dr M. Howarth. University of Oxford, 2014.
- Protein Reactions with Anticancer Metallodrugs. Prof. Peter O'Connor. University of Warwick, 2014.
- Time-resolved radiation chemistry; interaction of excess electrons with water and nucleobases. Prof. D. Neumark. University of California, Berkeley, 2014.
- Design of New Chemical Tools for Cancer. Dr. John Spencer. University of Sussex, 2014.
- Surprising 'twist and turns' in supramolecular self-assembly formations. Prof. T. Gunnlaugsson. Trinity College Dublin, 2015.
- π-Conjugated organophosphorus oligomers for optoelectronic applications. Prof. M. Hissler. Institute des Sciences Chimique de Rennes, 2015.
- New peptide ligands for metal ions: from MRI contrast agents to DNA binding proteins. Dr A. Peacock. University of Birmingham, 2015
- Durham Lecture 1; Carbon Materials, Devices, Medicine and Nanocars. Prof. James Tour Rice University, Texas, 2015.
- Durham Lecture 2; Graphene, Composites and Devices. Prof. James Tour Rice University, Texas, 2015.

- Durham Lecture 3: Nanomedicine for Stroke, Traumatic Brain Injury, Autoimmune disease and drug delivery. Prof. James Tour. Rice University, Texas, 2015.

8.5.2 Second year

- Musgrave Lecture 2016, Prof Steven V Ley FRS University of Cambridge.
- 'Chemical Probes for Epigenetic Targets', Prof Paul Brennan, University of Oxford.
- 'Using Chemical Biology to Manipulate the Peroxisome', Dr Stuart Warriner, University of Leeds.
- 'Targeted Design of Photoactive Organic- Inorganic Hybrid Materials for Energy and Lighting Applications', Dr Rachel C Evans, Trinity College Dublin.
- 'New Main Group Metal Mediated Strategies for Ring Functionalisation', Prof. Eva Hevia, University of Strathclyde.
- 'Catalysis on Gold', Prof. Graham Hutchings FRS, Cardiff University.
- 'Targeting the Tumour Microenvironment', Dr Robert Elmes, Maynooth University.
- 'Versatility of Tetrazole Ligands in Luminescence Metal Complexes for Applications in Life Sciences', Dr Max Massi, Curtin University, Perth.
- 'Using Organometallics as catalysts; from drug precursors to little black dresses', Dr Patrick McGowan, University of Leeds.
- Durham Lecture Series 2016: Presented by Sir J Fraser Stoddart.

8.5.2 Third year

- 'Strategies for the Development of Lanthanide-Based Chemosensors', Prof. Kellie Tuck, Monash University, 2017.
- 'Lanthanide Based MRI Probes for A-beta-Amloid', Prof. Carlos FGC Geraldes, Coimbra, 2017.
- 'Ionic Liquids: Solvents for Sustainable Chemistry' Prof. Tom Welton, Imperial College London, 2017.

- Imposter Syndrome: ‘ Floating to Professor on a Magic Carpet of Success’, Prof. Tom Welton, Imperial College London, 2017.
- Development of gold and palladium catalysed reactions, D. Ai-Lan Lee, Herriot-Watt University, 2016.
- ‘Metal-based chemical entities for applications in chemical biology and medicine’, Prof. Angela Casini, Cardiff University, 2016.
- ‘Synthesis of conjugated polymers for organic electronics: Making use of triplet excited states’, Dr Hugo Bronstein, University College London, 2016.